DOCTOR OF PHILOSOPHY

Development of Electronic Systems for Ultrasonic Particle Manipulation

Wang, Han

Award date:
2015

Development of Electronic Systems for Ultrasonic Particle Manipulation

By

Han Wang

A thesis submitted in fulfilment of the requirements for the degree of Doctor of Philosophy to the School of Engineering, Physics and Mathematics, University of Dundee, Scotland, UK

August 2015

DECLARATION OF ORIGINALITY

I hereby certify that the thesis entitled, "**Development of Electronic Systems for Ultrasonic Particle Manipulation**", submitted to University of Dundee for the degree of Doctor of Philosophy represents the original work of the author. All references cited have been consulted by me; no part of the work referred to in this thesis has been supported in application of another degree or qualification of this university or any other university or institute of learning.

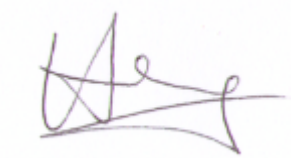

Signature: Date: 11th May, 2015

CERTIFICATE

This is to certify that Mr. Han Wang has done this research under my supervision and complied with all the requirements for the submission of this Doctor of Philosophy thesis to the University of Dundee.

Signature: 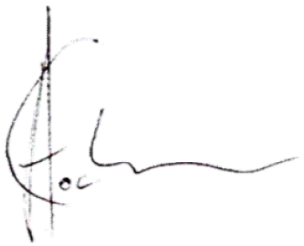 Date: 11th May, 2015

ACKNOWLEDGEMENTS

I would like to express my sincerely thankfulness to my supervisors Prof. Sandy Cochran and Dr. Christine Démoré, for their guidance, support and encouragement during my research. Prof. Sandy Cochran has been providing preciously valuable and timely advice that guided me through my PhD, both in science and management of research progress. Dr. Christine Démoré has always been very helpful for giving me advice and encouragement in all aspects that helped me complete my research.

I would like to express my gratitude to my collaborators, Dr. Yongqiang Qiu, Dr. Peter Glynne-Jones and Dr. Sylvia Gebhardt for providing transducer devices and useful advice for experiments. I would like to thank Mr. Romans Poltarjonoks for the assistance in the electronics fabrication, and Mr. Aleksandrs Bolhovitins for the help in the experiments. I would also like to thank Mr. Graeme Casey for the help in the acoustic chamber fabrication.

I would like to give my gratefulness to Martin Curran-Gray, Tony Kirkham and Gerry Owen in Agilent Technologies, for their valuable suggestions and supports for the electronics design in my research. Especially I would like to thank Gerry Owen for providing me a precious opportunity to visit the Agilent headquarters in the USA.

I would like to offer my gratitude to Prof. Tony Jun Huang at the Pennsylvania State University for inviting me to visit his Acoustofluidics laboratory for two months. It was a great pleasure to work in the group.

I would like to thank other Sonotweezers project collaborators for the useful suggestions and supports in my research. And I extend my appreciation to all the members in the ultrasound lab and IMSaT. It has always been joyful to work with you.

Finally, I would like to dedicate my deeply thankfulness to my parents. Your persistent understanding and encouragement has been a great support, and your endless love has always been my source of momentum to keep going.

Han Wang

The research presented in this thesis was funded by Scottish Universities Physics Alliance (SUPA) INSPIRE Studentship.

TABLE OF CONTENTS

LIST OF FIGURES

LIST OF TABLES

GLOSSARY

Symbols

β	Compressibility
c	Speed of sound
ε	Energy density
$\langle E_{kin} \rangle$	Averaged kinetic energy
$\langle E_{pot} \rangle$	Averaged potential energy
F_{agg}	Agglomeration force for single particles
f_c	Cut-off frequency
F_d	Stokes' drag force
$F_{lateral}$	Acoustic lateral force
F_{manip}	Agglomerate manipulation force
FREQ_OUT	Output signal frequency
FREQ_REF	FPGA reference frequency
FREQ_SYN	Output of the frequency synthesizer
I_{out}	Output current
$I_{quiescent}$	Quiescent current
$J_m(x)$	*m*th order Bessel function of the first kind
k	Wave number
λ	Acoustic wavelength
μ	Dynamic viscosity
$N\frac{K}{M}$	Fractional factor
$\emptyset$	Diameter
$\Phi\ (\beta, \rho)$	Acoustic contrast factor
ϕ_n	Phase of driving signals for transducer elements in the circular array
PHA_RES_BIT	Phase resolution-in-bits
PHA_RES_DEG	Phase-resolution-in-degrees
P_{out}	Output power
$P_{quiescent}$	Quiescent current
r	Particle / agglomerate diameter
ρ	Density
R_{on}	On resistance of ADG5434
(r_n, θ_n)	Polar coordinate of each transducer element in the circular array
r_{nT}	Relative distance between each transducer element and the target Bessel-function field centre in the circular array
(r_T, θ_T)	Target Bessel-function field origin in the circular array
SR	Slew rate

τ	RC circuit time constant
θ	Azimuthal angle
v	Particle / agglomerate velocity
V_{out}	Output voltage

Acronyms

AC	Alternating current
ADC	Analogue to digital converters
AFM	Atomic force microscopy
AOD	Acousto-optic deflectors
API	Application program interfaces
ASIC	Application-specific Integrated Circuit
BAW	Bulk acoustic waves
BGA	Ball grid array
BJT	Bipolar junction transistors
CLB	Configurable logic block
CMUT	Capacitive MUTs
CPU	Central processing unit
CW	Continuous wave
DAC	Digital to analogue converter
DC	Direct current
DDS	Direct Digital Synthesis
DFF	D-type flip-flops
DMD	Dual-modulus-divider
DSP	Digital signal processors
EDA	Electronic design automation
FACS	Fluorescence-activated cell sorting
FIFO	First in, first out
FluidFM	Fluidic force microscopy
FPGA	Field-programmable gate array
GPIB	General purpose instrumentation bus
GUI	Graphical user interface
HDL	Hardware description language
HIFU	High intensity focused ultrasound
IC	Integrated circuits
IOB	I/O blocks
IP	Intellectual properties
LDV	Laser Doppler Vibrometry
LED	Light emitting diode
LOC	Lab-on-chip
LSB	Least significant bit
LUT	Look-up table
MCU	Microcontroller units
MOSFET	Metal-oxide-semiconductor field-effect transistors
MSB	Most significant bit
OAM	Orbital angular momentum
OET	Optoelectronic tweezers
PC	Personal computer
PCB	Printed circuit boards
PLL	Phase-locked loops
PMUT	Piezoelectric MUTs

PROM	Programmable read-only memories
PSU	Power supply unit
QFP	Quad Flat Pack
RAM	Random-access-memory
RC	Resistor-capacitor
RF	Radio-frequency
RMS	Root-mean-square
ROM	Read-only-memory
RTL	Register transfer level
SAW	Surface acoustic standing waves
SFR	Special function registers
SLM	Spatial light modulators
SoC	System-on-chip
SPAD	Single photon avalanche diode
SPI	Serial Peripheral Interface
SPICE	Simulation Program with Integrated Circuit Emphasis
SSAW	Standing surface acoustic wave
STM	Scanning tunnelling microscope
TSSOP	Thin Shrink Small Outline Package
UART	Universal asynchronous receiver and transmitter
USW	Ultrasound Standing Wave
UTW	Ultrasound travelling wave
VCO	Voltage-controlled oscillators

ABSTRACT

Demands to handle individual particles or particle agglomerates have been emerging in the fields of biology and chemistry, and particle trapping and manipulation with mechanical waves generated from ultrasound sources, known as “acoustic tweezing”, has gained great interest by researchers and been proved useful for its unique advantages. With an analogy to optical tweezing, research has demonstrated the possibility to use modulated acoustic fields generated by ultrasound arrays for trapping individual particles and groups of particles at length scales from hundreds of μm to a few mm.

This thesis explores and demonstrates particle trapping and manipulation with electronically-controlled miniaturized ultrasound arrays (element pitch around 500 μm or less), focusing on the development of dexterous electronic systems. Generally, in acoustic manipulation applications, low voltage outputs with continuous mode operation are required to create stable acoustic energy potential “landscapes” for trapping without damaging particles or cells.

The research work of this thesis is oriented towards integration of control electronics with miniaturized ultrasound arrays. Test fixtures have been carefully designed and fabricated for the characterization of transducer arrays developed by collaborating researchers and array-controlled particle manipulation experiments have been demonstrated with customized fluorescence microscopy equipment.

Most importantly, this thesis has established two versions of prototype Field-programmable gate array (FPGA) based electronics to drive ultrasound arrays. One is a computer-controlled 16-channel system, with adjustable output frequencies, phases and amplitudes. Another is a 40-channel switching electronics for manual-controlled output switching or time-shared output multiplexing. The electronic systems that have been developed are highly scalable and easily adapted for different acoustic tweezing applications.

In conclusion, this thesis has proposed prototype electronic toolkits as research platforms to explore diverse possibilities for acoustic tweezing with miniaturized ultrasound arrays.

CHAPTER 1 INTRODUCTION

The work described in this thesis formed part of the UK Engineering and Physical Sciences Research Council (EPSRC) Sonotweezers research programme. Collaborative investigators came from four UK universities: Bristol, Dundee, Glasgow and Southampton. The programme targeted the exploration of devices that incorporate electronically-controlled ultrasound transducer arrays as well as bespoke fluid chambers for trapping and manipulation of microparticles and biological cells. This thesis is focused particularly on the electronic system development and experimental characterization of typical array-based Sonotweezer devices, thus having a central place in the overall programme.

1.1 Thesis Background

1.1.1 Ultrasonic Particle Manipulation

In the field of chemistry, pharmaceuticals and life sciences research there have been increasing demands for suitable technologies to handle microparticles and nanoparticles, or particle groups, with applications including single cell analysis (Lu et al., 2004) and sorting (Andersson and van den Berg, 2003) , intercellular study (Guo et al., 2013) and tissue engineering (Smith and Gerecht, 2014).

In terms of the approaches to how the particles are handled, the technology can be classified into “contact” and “contactless” categories. The contact methods involve widely used approaches such as micropipette aspiration (Oh et al., 2012), atomic force microscopy (AFM) (Afrin et al., 2009, 2012) and microelectromechanical systems (MEMS) based micro-tweezers (Wester et al., 2011). On the other hand, the technologies for contactless particle handling are rapidly emerging, based on the advantage of reducing mechanical damage to the particles. There have been extensive studies of handling microparticles with different non-contact methods, such as hydrodynamic methods

(Dziubinski, 2012; Wheeler et al., 2003), optical beams (Ashkin et al., 1987; Grier, 2003), magnetic fields (Lee et al., 2004; Pamme and Manz, 2004), electric fields (Voldman, 2006; Yang et al., 2000), and acoustic fields (Dual and Möller, 2012; Glynne-Jones et al., 2012; Hawkes and Radel, 2013; Nilsson et al., 2009; Qiu et al., 2014; Wiklund et al., 2013). Each technology has its unique advantages and weaknesses (Qiu et al., 2014).

Among the contactless methods, particle trapping and manipulation with acoustic fields are addressed in this thesis, as they can potentially provide large forces, in the range of pN – nN to handle particles or particle groups with diameters (Ø) ranging from less than 1 µm to over 50 µm, and within a relatively large working area, with dimensions of a few mm. Acoustic methods are also of interest because of the possibilities to integrate the acoustic devices with control electronics in miniaturized systems.

The term "acoustic tweezers" was first introduced by Wu (1991) in the use of two counter-facing 3.5 MHz, Ø1.2 cm focused ultrasound transducers to form potential wells which successfully trapped Ø270 µm latex particles and frog's eggs. The acoustic potential wells or hills are created by localized minima or maxima of the acoustic force potentials. The trapped particles positioned in the potential wells were manipulated by physically moving the transducers (Wu, 1991). Particle trapping at pressure nodal planes or antinodal planes with standing waves in single transducer planar resonators had also been proved promising for particle focusing and sorting applications (Cousins et al., 2000; Harris et al., 2003; Lilliehorn et al., 2005; Petersson et al., 2005). It is also possible to create 2-D standing wave fields for particle immobilization (Haake et al., 2005). These early research efforts have demonstrated that particles or particle groups with sizes from a few µm to hundreds of µm can be trapped with standing waves created by transducers working in the MHz range.

In this context, it is of particular interest that it is possible to create and alter standing wave acoustic fields with multiple transducers, and dynamically change the driving signals to the transducers which acting as the ultrasound sources. Hence an acoustic "potential landscape" is possibly to be created, either with repeated patterns of localized potential maxima and minima, or with dynamically spatially varied potential wells or hills. Microparticles can be trapped and manipulated in such acoustic "potential landscapes".

1.1.2 Motivation and Objectives

Inspired by the previous research into ultrasonic particle manipulation, the Sonotweezers programme aimed to develop electronically-controlled ultrasound devices to dynamically modify potential energy landscapes for particle trapping, manipulation and patterning. As part of this work, the main motivations of the research described in this thesis can be generalized as follows.

- Ultrasonic arrays working in the MHz range were chosen as the active device instead of using single element transducers, allowing additional flexibility in control of particles at μm scale within acoustic chambers.

- Knowledge from related research fields such as medical imaging and high intensity focused ultrasound (HIFU) was useful to facilitate the electronics development and characterization with Sonotweezer devices.

- Programmable microelectronic technologies including microcontroller units (MCUs), FPGAs and application-specific integrated circuits (ASICs) provide possibilities to develop customized electronic systems with high dexterity.

- The electro-mechanical characteristics of piezoelectric transducers make them suitable to integrate with board-level electronics or silicon-level integrated circuits (IC), the latter in an approach termed “more than Moore” (Brillouët et al., 2011), as the developing microelectronic technology that integrating the analogue domain such as radio-frequency (RF) circuits, sensors, MEMS devices with standard digital electronics, towards system in package (SiP) or system on chip (SoC).

- The theory and applications of acoustic tweezing demonstrated by other researchers indicate the potentials and demands of developing a compact electronic system as a control toolkit.

- Analogous mature technologies such as spatial light modulators (SLM) have motivated the development of reconfigurable electronics to control transducer arrays for dynamic acoustic field modulation.

The main focus of this thesis is on the development of electronic systems suitable for driving Sonotweezer prototypes constructed by other researchers in a collaborative process. The main objectives can be generalized as follows.

- To develop electronics that meet the demands of different types of Sonotweezer devices, and demonstrate their functionality experimentally.

- To provide an electronic toolkit with versatile functionality which will facilitate ultrasonic device characterization, and also allow exploration of future applications with electronic controlled Sonotweezers.

A detailed discussion of electronics development considerations for Sonotweezers will be further presented in Chapter 3.

1.2 Contributions to Knowledge of the Field

This thesis successfully demonstrates the possibility to build customized FPGA-based programmable electronic systems that can drive array-based acoustic tweezing devices. The main work includes setting up essential experimental facilities such as customized fluorescent microscope, and microfluidic system such as fluid circulator and test chambers for experimental verification of Sonotweezer devices and bespoke electronics. For the electronics, the work mainly involves the development of control logic in reconfigurable FPGA cores to meet the demands of a variety of Sonotweezer applications, and the development of appropriate analogue driving electronics that provide sufficient power to actuate the piezoelectric transducers. The highlights can be described as follows.

- Demonstrated the possibility of using a customized scalable multichannel electronic driving system with circular array Sonotweezer (Wang et al., 2014) for dynamically shape the acoustic field for particle trapping and manipulation under

a programmable manner, by the accurate control of the frequencies and phases of the driving signals. Such system can be proved useful for diverse acoustic tweezing applications.

- Demonstrated the possibility of using a mechanism of switching the array actuation signals to control a linear-array-based planar resonator device (Wang et al., 2012) with customized electronics. And the switching mechanism can be further applied to complex 2-D arrays (Qiu, Wang, et al., 2014).

- Demonstration of the reconfigurability of the electronics as a "Sonotweezer toolkit" by providing a system-level GUI-based PC interface for circular array Sonotweezer (Acoustofluidics 2014, Prato, Italy, poster).

- Providing electronic testing and driving platform for packaging the thick-film PZT ultrasound arrays as planar resonator Sonotweezers, and demonstrate the feasibility of using such arrays for particle manipulation and patterning (Qiu, Wang, et al., 2015).

1.3 Thesis Structure

Chapter 2 gives a review of the diverse technologies available for microparticle manipulation. The origin and fundamental concepts of different technologies are introduced, followed by more detailed descriptions of the experimental setups and associated applications. Acoustic tweezing technology is highlighted in this chapter, with detailed discussion of the key materials, theories and applications reported by other researchers.

Chapter 3 explores the electronic technologies that are suitable for Sonotweezer devices. The chapter first gives a general review of acoustic tweezing devices developed in the project and requirements for the electronic design, then provides a wide review of the field of electronics for ultrasound to source the most appropriate technology.

Chapter 4 describes briefly the methods and equipment involved in this thesis for electronics development and experimental characterization with Sonotweezer devices.

Chapters 5 and 6 describe in detail the development of two versions of electronics for typical Sonotweezer devices within the domain of the present project. The functionalities of the electronics are verified and demonstrated with experimental studies.
Finally, Chapter 7 summarizes the work that has been reported for electronics development and device characterization. This chapter focus on future possibilities to extend the functionality of the electronics for complex acoustic field modulation, and also emphasizes the potential to develop integrated Sonotweezer devices with programmable electronics.

1.4 List of Publications

Peer-reviewed Journal Publications

Qiu, Y., **Wang, H.**, Gebhardt, S., Bolhovitins, A., Démoré, C.E.M., Schönecker, A. and Cochran, S. (2015), "Screen-printed Ultrasonic 2-D Matrix Array Transducers for Microparticle Manipulation", *Ultrasonics*, Elsevier B.V., in press.
doi:10.1016/j.ultras.2015.05.010.

Y. Qiu, **H. Wang**, C. Demore, D. Hughes, P. Glynne-Jones, S. Gebhardt, A. Bolhovitins, R. Poltarjonoks, K. Weijer, A. Schönecker, M. Hill, and S. Cochran, "Acoustic Devices for Particle and Cell Manipulation and Sensing", *Sensors*, vol. 14, no. 8. 2014, pp. 14806–14838.

S. Kotopoulis, **H. Wang**, S. Cochran, M. Postema, "Lithium Niobate Transducers for MRI-Guided Ultrasonic Microsurgery", *IEEE Transactions on Ultrasonics, Ferroelectrics and Frequency Control*, Vol. 58, No.8, pp. 1570-1576, Aug, 2011.

Conference Proceedings

H. Wang, Y. Qiu, C. Demore, and S. Cochran, "FPGA embedded system for ultrasound particle manipulation with Sonotweezers," in *2014 IEEE International Ultrasonics Symposium*, 2014, pp. 1440–1443.

Paul O'Mahoney, Graham W. Brodie, **Han Wang**, et al., "Hybrid optical and acoustic force based sorting", *Proceedings of SPIE*, Vol. 9164, 916421 (2014).

Y. Qiu, **H. Wang**, A. Bolhovitins, C. Démoré, S. Cochran, S. Gebhardt, and A. Schönecker, "Thick Film PZT Transducer Arrays for Particle Manipulation," in *Proc. IEEE Ultrasonics Symposium*, 2013, pp. 1911–1914.

H. Wang, Y. Qiu, C. Demore, S. Cochran, P. Glynne-Jones, and M. Hill, "Planar Particle Trapping and Manipulation with Ultrasonic Transducer Arrays," in *Optics in the Life Sciences, OSA Technical Digest (online) (Optical Society of America, 2013)*, paper TW4D.2.

H. Wang, Y. Qiu, C. Demore, S. Cochran, P. Glynne-Jones, M. Hill, "Particle Manipulation in a Microfluidic Channel with an Electronically Controlled Linear Piezoelectric Array", in *Proc. IEEE Ultrasonics Symposium*, Dresden, Germany, 2012, pp. 1998-2001.

C. Demore, Z. Yang, A. Volovick, **H. Wang**, S. Cochran, M. MacDonald, G. Spalding, "A sonic screwdriver: Acoustic angular momentum transfer for ultrasonic manipulation", in *Proc. IEEE Ultrasonics Symposium*, Orlando, Florida, U.S.A., 2011, PP. 180-183.

Spiros Kotopoulis, **Han Wang**, Sandy Cochran, Michiel Postema, "Lithium Niobate Ultrasound Transducers for High-Resolution Focused Ultrasound Surgery", in Proc. IEEE Ultrasonics Symposium, San Diego, California, U.S.A., 2010, pp.72-75.

Conference Presentations

H. Wang, Y. Qiu, C. Demore, S. Cochran, "Electronic Sonotweezers – Ultrasonic particle manipulation with FPGA embedded systems", presented at Acoustofluidics 2014, Prato, Italy, 2014 (Poster).

H. Wang, Y. Qiu, C. Demore, S. Cochran, P. Glynne-Jones, M. Hill, "Electronic Controlled Piezoelectric Array for Ultrasonic Particle Manipulation in an Acoustic Resonator", presented at Acoustofluidics 2013, Southampton, U.K., 2013 (Oral).

H. Wang, Y. Qiu, C. Demore, S. Cochran, P. Glynne-Jones, M. Hill, “Electronic Control of Ultrasonic Transducer Arrays for Particle Trapping and Manipulations”, presented at The long arm of microelectronics – satellite meeting, The Royal Society at Chicheley Hall, Buckinghamshire, U.K., 2013 (Poster).

Han Wang, Spiros Kotopoulis, Sandy Cochran, Michiel Postema, "Ultrasound Transducers Made with Lithium Niobate for High Frequency HIFU", presented at 2011 International Congress on Ultrasonics, Gdansk, Poland, 2011 (Oral).

CHAPTER 2 REVIEW OF MICROPARTICLE MANIPULATION TECHNOLOGIES

2.1 Introduction

This chapter will review the technologies for microparticle manipulation and patterning. The techniques are classified here as “contact”, for the cases that the apparatus is in direct contact with the sample, or “contactless”, as for the cases of controlling the particles through different force fields.

2.2 Contact Manipulation Technologies

Generally the contact microparticle manipulation methods is intuitive as it operates. With various sensors integrated the system could be used for diverse sample characterisation purposes. This section will list the maturely developed and widely used technologies include micropipette aspiration, AFM and microfabricated mechanical manipulators. Typical apparatus for different technologies will be discussed as well.

2.2.1 Micropipette Aspiration

Micropipette aspiration (Microaspiration) technology was first invented for transporting liquids in accurate quantities in biology and chemistry research, and later developed as an approach to study the mechanical properties of cells. Early explorations feature the experiments with micropipettes to study the sea urchin egg cell membrane (Mitchison and Swann, 1954). Microaspiration is performed with a very small tip with diameter 2 - 50 μm which made it ideal for single cell studies (Oh et al., 2012). As shown in Figure 2.1, the mechanical properties of cells can be studied by the deformation of cell membranes with negative pressure introduced at a micropipette tip attached to the cell surface (Hochmuth, 2000). This technology can measure very small forces, at the piconewton

level, so it can be used for measuring molecular bond forces (Evans et al., 1995). Recently, as shown in Figure 2.2, the technology was developed into sophisticated systems for robotic controlled cell manipulation and positioning (Anis et al., 2010; Shojaei-Baghini et al., 2013; Zhang, Leung, et al., 2012).

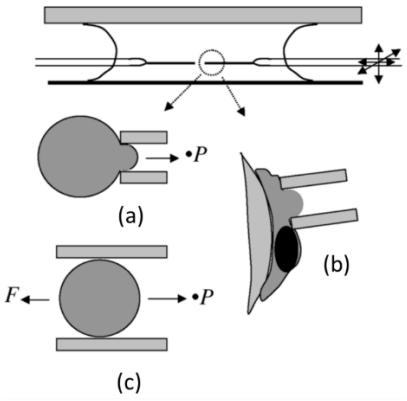

Figure 2.1 A schematic of typical micropipette aspiration techniques for cell study (from Hochmuth, 2000). (a) Cell partially aspirated into the pipette tip. (b) Cell being aspirated while attached to a bead. (c) Cell moving freely in a pipette like a piston in a cylinder.

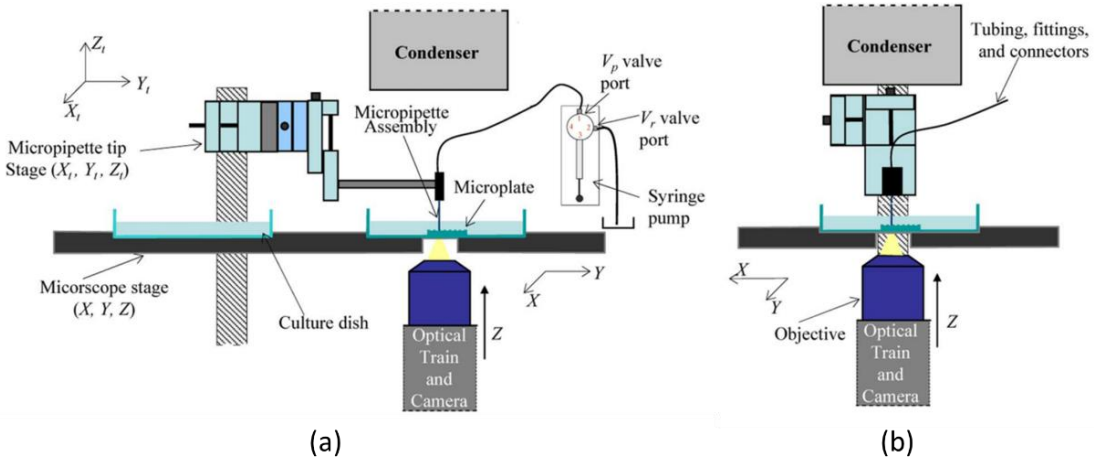

Figure 2.2 Schematic of a six-axis robotic microaspiration workstation for cell transfer and positioning, using computer vision based feedback control (from Anis et al., 2010). (a) Front view of the main hardware. (b) Side view of the main hardware.

2.2.2 AFM

The AFM was invented as an improvement over the scanning tunnelling microscope (STM), which could be used for profiling three dimensional (3-D) contours of both conductive and insulating samples (Binnig et al., 1986). Demonstrated as in Figure 2.3, a

modern commercial AFM consists of a cantilever with a tip of radius of curvature in the order of nanometres which is brought into the proximity with the sample surface. A small ionic repulsive force from the surface applied to the tip causes a deflection of the cantilever, which is recorded through a laser diode photo-detection system, and the force is measured through Hooke's law. A piezoelectric scanner is used together with the feedback mechanism to maintain a constant tip-to-sample force, while the tip moves across the sample to create the 3-D contours.

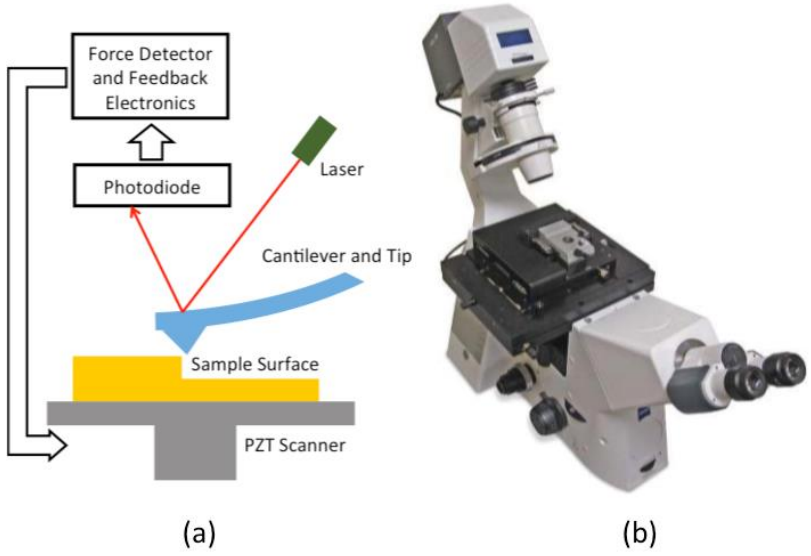

Figure 2.3 (a) Diagram of typical modern atomic force microscope. (b) A commercial atomic force microscope that combines AFM and direct optical imaging on an inverted light microscope (7500ILM AFM, Keysight Technologies, Inc., Santa Rosa, CA, USA).

AFM has the advantage of measuring almost all kinds of surfaces in different environments, including air, liquid, vacuum and special gas. Commercialized AFM systems have made this technology an ideal tool for single cell studies. Organic materials such as amino acid crystals can be imaged with molecular level resolution (Hansma et al., 1988), and inner cell structure such as filamentous actin can be revealed by AFM imaging (Henderson et al., 1992). In addition, the cell membrane can be indented by an AFM probe tip to study its elastic properties (Daily et al., 1984; Kuznetsova et al., 2007). Research of using AFM for direct nanoparticle manipulation by the precise control of the cantilever tip has also been reported (Junno and Deppert, 1995; Tong et al., 2008). One example demonstrated as in Figure 2.4, with modified AFM cantilever tips, researchers have successfully created small holes at defined loci in single cells and have performed intracellular imaging and genetic studies (Afrin et al., 2009, 2012).

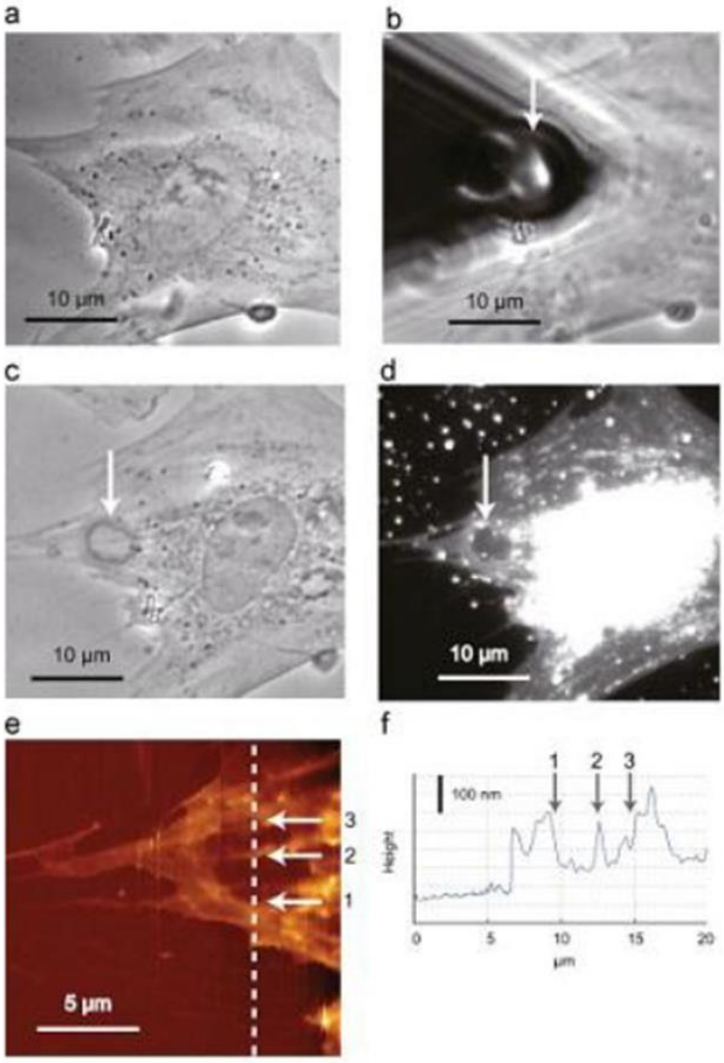

Figure 2.4 Hole (~ 5 µm in diameter) created at cell surface using phospholipase A2 coated beads attached to AFM probe tip, observed by phase contrast microscopy (from Afrin et al., 2009).

2.2.3 Microfabricated Mechanical Manipulators

As the development of micro- and nano-fabrication technologies has improved, demonstrated as in Figure 2.5, various mechanical manipulation device have been designed and fabricated at the micrometre level based on microelectromechanical systems (MEMS). Based on various actuation mechanisms, such as shape memory alloys, electrostatic forces, or piezoelectric forces, these devices can "pick-up and place" objects with size ranges from hundreds of micrometres to tens of micrometres with accuracy (Jia and Xu, 2013). With sensors integrated, these tools can measure and deliver real-time force feedback, which makes them useful for telemanipulation of micrometre-sized

objects (Bolopion and Régnier, 2013), minimally invasive surgery (Menciassi et al., 2003) and manipulation of biological samples (Beyeler et al., 2007; Zhang, Chu, et al., 2012).

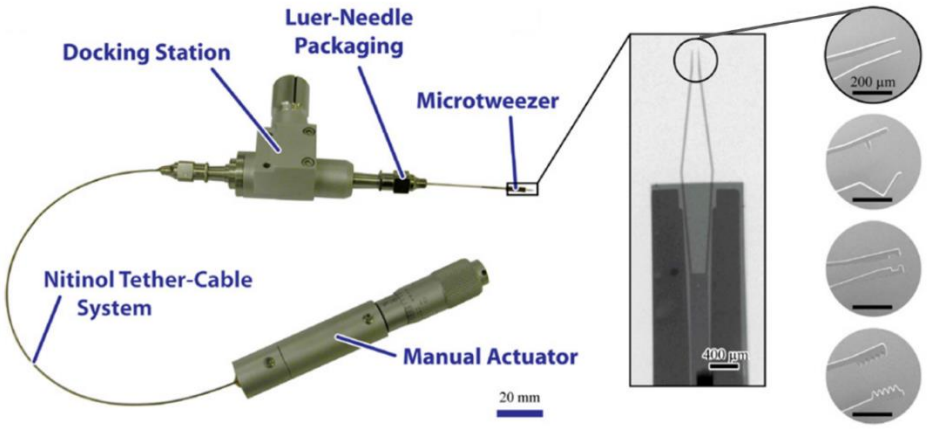

Figure 2.5 A manually-controlled mechanical microtweezer system (from Wester et al., 2011).

2.3 Contactless Manipulation Technologies

This section will discuss the mainstream non-contact manipulation technologies, including hydrodynamic methods, electrophoresis and dielectrophoresis, magnetic tweezing, optical tweezing and, the main focus of this thesis, acoustic tweezing. The technology developed nowadays can meet the demands for handling either large quantities of samples or single cells. Particularly in biology, these techniques are useful for cell or molecule trapping and sorting as well as manipulation, which prepare samples in specific ways for future treatment and analysis (Andersson and van den Berg, 2003). In the past twenty years there has been increased interest in the field of micro total analysis systems (µTAS) or lab-on-chip (LOC), based on microfluidic devices that incorporate contactless manipulation technologies.

2.3.1 Hydrodynamic Methods

A particle suspended in a fluid is subject to hydrodynamic forces. Depending on the mechanical properties of the fluid, such as density and speed, the technology can be used for particle focusing. As shown in Figure 2.6 (a), a typical hydrodynamic focusing set-up consists of four microchannels intersecting with two channels of sheath flow squeezing

the sample flow into a thin, focused layer (Dziubinski, 2012). In early research, Shuler et al. demonstrated that hydrodynamic focusing could improve particle sizing results within a Coulter counter (Shuler et al., 1972). Later, as shown in Figure 2.6 (b), the technology gained wide utilization in flow cytometry, which represents an improved version of the Coulter counter and is extensively used for biological cell analysis. The technology has also gained numerous applications in microfluidics, such as fluorescence-activated cell sorting (FACS) (Bang et al., 2006; Nawaz et al., 2014).

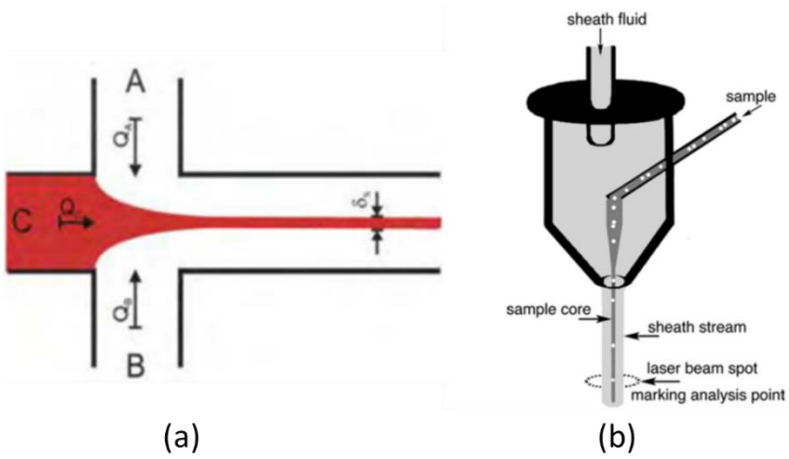

Figure 2.6 (a) An illustrative schematic of a hydrodynamic focusing set-up (from Givan, 2011). A and B are sheath flow channels and C is the sample channel. (b) An illustration of a typical application of hydrodynamic focusing in flow cytometry (from Dziubinski, 2012).

Through the development of micro- and nano-fabrication technologies, chambers with micro-channels and other structures were developed for capture, manipulation and analysis of biological samples. In early exploration, Carlson et al. demonstrated using microfabricated lattices with a flow of whole blood to perform self-sorting of red blood cells and different types of white blood cells based on a combination of different cell mechanical properties (Carlson et al., 1997). Wheeler et al. demonstrated the possibility to perform single-cell analysis in a multilayer PDMS microfluidic chamber with integrated valves and pumps, as shown in Figure 2.7. The devices could separate single cells from bulk cell suspension as well as deliver nanolitre volumes of reagents to the cell for analysis (Wheeler et al., 2003).

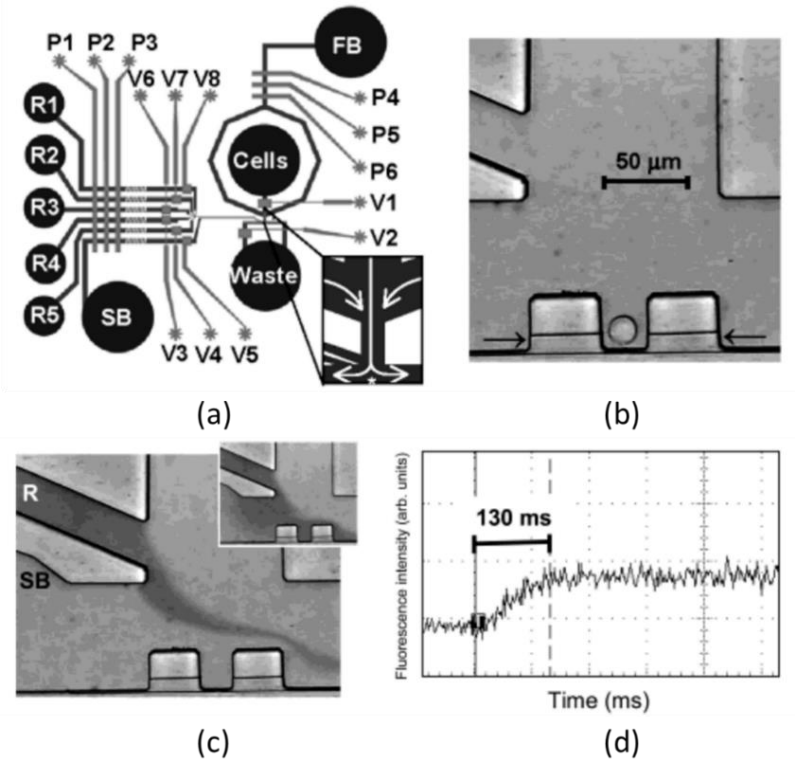

Figure 2.7 Single cell analysis device (from Wheeler et al., 2003). (a) Schematic of the device. The fluidic channels are dark, control channels are light. R1 - R5 are reactant inlets, SB and FB are shield and focusing buffer inlets respectively. Valves are controlled by applying pressures to valve V1 – V8, and pumps are controlled by actuating pump P1 – P3 or P4 – P6 in series. (b) CCD image of an individual Jurkat T cell trapped in cell dock. (c) Image of "load" (main picture) and "perfuse" (inset) states. In load state, the reagent shield buffer is turned on and the reagent flows over the dock; in perfuse state, SB is off so the reagent flows onto the dock. (d) Oscilloscope screen capture showing the dye-marked solution change during load and perfuse states, illustrating that the changeover is achieved in ~100 ms.

2.3.2 Electrophoresis and Dielectrophoresis

Microparticles can be transported in an electric field based on their electrical properties and field gradients. Electrophoresis (EP) is the movement of charged objects in electric fields while, in dielectrophoresis (DEP), polarized dielectric objects are manipulated because of the forces generated in spatially non-uniform electric fields. Figure 2.8 is a diagram illustrating the mechanisms of and the main differences between EP and DEP. Both can be used in biology for cell characterization and handling.

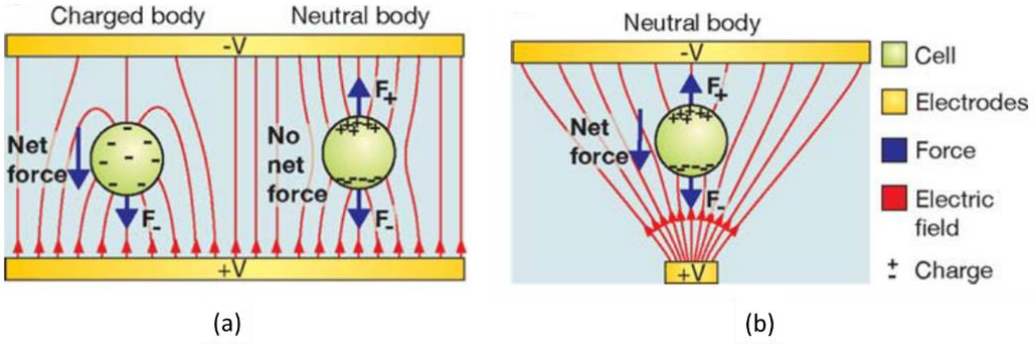

Figure 2.8 Illustration of EP and DEP (from Voldman, 2006). (a) Charged and neutral particles in a uniform electric field. The charged particle experiences a net force and the neutral particle experiences zero net force. (b) A neutral particle in a non-uniform electric field. The particle will be moved to the electric field maximum as a result of the unbalanced field magnitude.

A. Electrophoresis

For EP, the dominant force is Coulomb force given by $\boldsymbol{F} = q\boldsymbol{E}$, where q is net charge on the object and $\boldsymbol{E}$ is the intensity of the electric field. The electrophoretic mobility (EPM) is given by $\mu = \varepsilon_m \xi / \eta$, where ε_m is the permittivity of the liquid, η is the liquid viscosity, and ξ is the "zeta potential", which is primarily related to the particle's charge density and the ionic strength of the liquid. The zeta potential varies over diverse cell types, which leads to the difference in electrophoretic mobility, so EP can be used to differentiate cells with different zeta potentials (Voldman, 2006). EPM data is also an important parameter to characterize the electrical properties of the cell surface.

Most cells in multicellular organisms except some bacteria, are covered with negative charges as they are alive within their natural environments (Mehrishi and Bauer, 2002). Early research publications of using EP to study biological cells can be traced back from the 1920's (Coulter, 1921). Since then, EPM data measured from numerous types of cells has contributed greatly to the knowledge of the electrical properties of cell membrane surfaces, which is important to understand cell behaviours under different conditions (Mehrishi and Bauer, 2002).

The conventional EP experiments require rather large chambers and analytical instruments, but the development of miniaturized capillary EP has significantly reduced the amount of buffer solution needed and also simplified the cooling equipments needed to deal with Joule heating generated because of the large spaces between the electrodes.

Figure 2.9 (a) shows an example of conventional gel EP equipment for DNA separation and (b) is a schematic of a commercial system for DNA sequencing by capillary array EP.

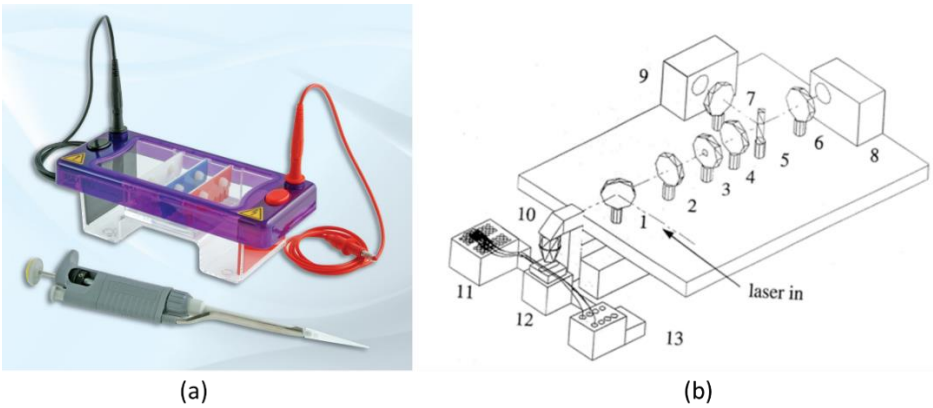

(a) (b)

Figure 2.9 (a) A commercial low-cost gel EP instrument (dimensions: 9 × 21 × 9 cm^3) with replaceable sample tank (MultiSUB Mini, Cleaver Scientific, Ltd., Warwickshire, UK). (b) A schematic of capillary array EP equipment MegaBASE 1000 by Molecular Dynamics, as shown in (Bashkin et al., 1996). Components: (1) to (7) optical lenses and filters for the detection in the optical beam path, (8) and (9) photomultiplier (PMT) tubes, (10) objective mounted on translation stage, (11) cathode manifold, (12) capillary detection window mount, (13) anode pressure manifold.

EP could also be used for cell handling and positioning, including reports of using EP for cell transportation over large distances (in centimetres) in microchannels (Li and Harrison, 1997). Other examples include bacteria concentration with EP and isoelectric focusing in a multilayer polymeric device (Cabrera, 2001). However, the main disadvantage of EP is that the direct current (DC) electric fields used are harmful to cells (Voldman, 2006).

B. Dielectrophoresis

For DEP, the force on a particle is generated by the particle dipole moment and the spatial gradient of the electric field, which can be expressed as $\boldsymbol{F}_{dep} = \boldsymbol{p} \cdot \nabla \boldsymbol{E}$. The dipole moment, $\boldsymbol{p}$, is induced by the electric field, $\boldsymbol{E}$, and the dipole contribution factors which could be free or polarization charge. At DC and low frequency alternating current (AC) electric fields free-charge dipoles dominate, while, at high frequency AC fields polarization charge dipoles dominate. An AC field is typically used for DEP as it will reduce the EP-induced motion, and minimize the physiological impact on cells and electrochemical reactions at the electrodes.

If the relative polarizability of the cell is higher than that of the medium, known as positive DEP (pDEP), the force will be directed towards the field gradient maximum while, if the cell has lower polarizability than that of the medium, known as negative DEP (nDEP), the force will be directed towards the field gradient minimum (Voldman, 2006).

Whether DEP can be used for cell characterization and separation depends on the polarizability of the cell electrical phenotype, which is primarily related to the cell wall, membrane and/or cytoplasmic electrical properties, as well as the applied electric field frequency (Voldman, 2006). For cells with very different electrical phenotypes, a specific AC field frequency and medium conductivity can be found so that one type of cells experience pDEP while the rest experience nDEP. This technique has been used for differentiation of live and dead cells and different cell types, and also to identify cancer cells from whole blood (Huang et al., 2002; Markx, 1994; Markx et al., 1994). For cells with similar electric phenotypes, techniques like field flow fraction DEP (DEP-FFF), as shown in Figure 2.10, levitate cells via DEP forces which balance the weights of the cells, and a side parabolic flow can separate them into different bands while the cells are experiencing different side drag forces (Yang et al., 2000).

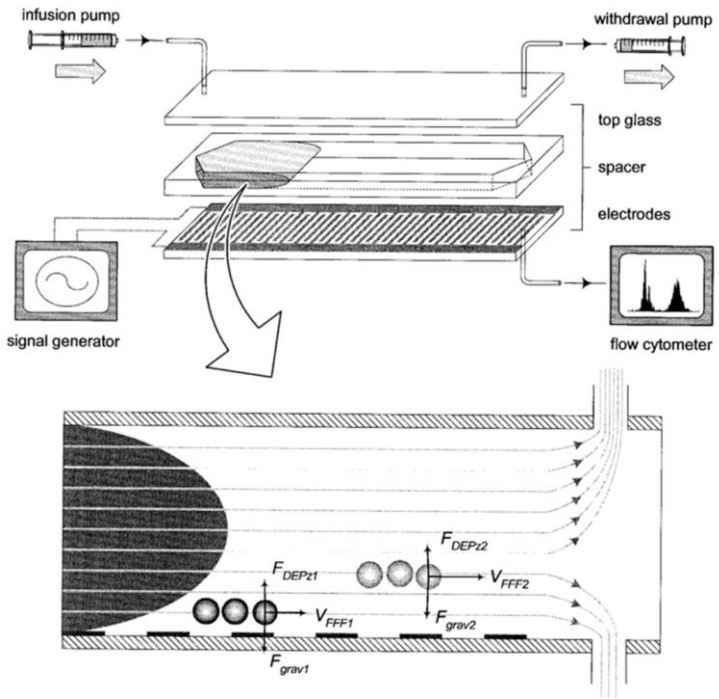

Figure 2.10 DEP-FFF principle and system setup (from Yang et al., 2000). Cells experience different DEP forces induced by bottom interdigitated electrodes. The DEP forces are balanced with gravity and the cells are held at different vertical positions. A parabolic flow is used to separate cells into regions.

DEP has also been extensively used for cell trapping and manipulation based on various techniques. One example, as shown in Figure 2.11 use two layers of patterned electrode arrays placed orthogonally to create a localized field maximum to trap a cell and manipulate it by changing the voltages of adjacent electrodes (Suehiro and Pethig, 1998). Another example features an adaption of CMOS technology for creating a large array of 102,400 electrodes for cell caging and manipulation, as well as sensing through integrated optical sensors on-chip (Manaresi et al., 2003).

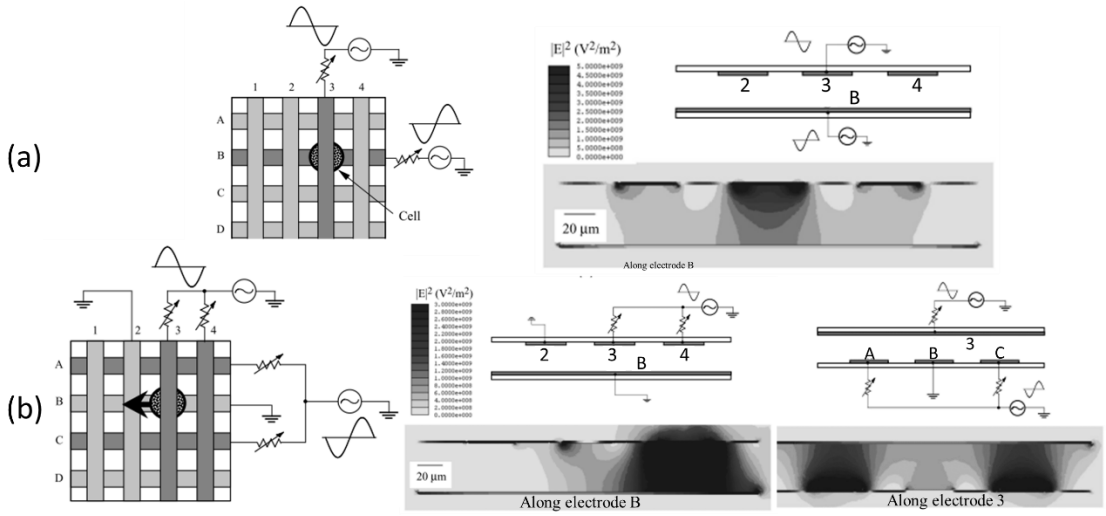

Figure 2.11 Electrode grids for cell trapping and manipulation with DEP (from Suehiro and Pethig, 1998). (a) The "capture" operation via pDEP. Top Electrode 3 and bottom Electrode B are connected to 2.8 V_{pp} AC signals while other electrodes are floating. The local highest field region at grid position 3-B captures a cell by pDEP. (b) The "release" operation via nDEP. Top Electrodes 2 is grounded, Electrode 3 is connected to 2.8 V_{pp} AC and Electrode 4 is connected to 11.2 V_{pp} AC. Bottom Electrode A and C are connected to 2.8 V_{pp} while B is grounded. The cell is moved towards Electrode 2 and a potential well is created between A and C to confine the cell movement along Electrode B.

2.3.3 Magnetic Tweezers

The magnetic field is another phenomenon being widely researched for microfluidic applications for biology and chemistry studies. The magnetic field can be coupled into microchannels in various ways, either from outside the channel, using permanent magnets or electromagnets, or inside the device, with microfabricated magnets. The latter has been thoroughly investigated with the development of microfabrication technology. Like EP and DEP, in microfluidic devices, particles can be manipulated because of their size and electromagnetic properties compared with surrounding medium.

The force is given by $\boldsymbol{F} = \frac{V \cdot \Delta \chi}{\boldsymbol{\mu_0}} (\boldsymbol{B} \cdot \boldsymbol{\nabla}) \boldsymbol{B}$, where V is the particle size, and $\boldsymbol{B}$ is the magnetic field strength. The term $\Delta\chi = \chi_p - \chi_m$ is defined as the difference between the susceptibility of the particle, χ_p, and that of the buffer medium, χ_m (Pamme, 2006). For a homogeneous field, the force on the particles is zero. Although particles are not pulled or pushed into any directions, this is still useful for magnetohydrodynamic (MHD) pumps, which require a static field for operation (Zhong et al., 2002). A more commonly used method is to generate an inhomogeneous field. The large gradients created can manipulate particles into local field minima or maxima, and, determined by Δ_{χ}, the particles could be either diamagnetic (repelled from magnetic fields), paramagnetic (experience small force towards field maxima) or ferromagnetic (strongly attracted to the field maxima) (Pamme, 2006).

For magnetic tweezing, usually magnetic micro- or nano-particles are attached to biological samples such as cells or DNA molecules (Pankhurst et al., 2003). Only two types of cells are naturally magnetic: red blood cells and magnetotactic bacteria (Šafařík and Šafaříková, 1999); other types of cells should be labelled with magnetic particles as noted. Ferrofluids, suspension of magnetic nanoparticles in carrier liquid, are another type of material that can be used in applications like pumping (Hatch and Kamholz, 2001).

Diverse applications of magnetic tweezing technology have been published, such as pumping and mixing (Ryu et al., 2004; Zhong et al., 2002), cell manipulation and sorting (Lee et al., 2004; Watarai and Namba, 2002), bioassay support (Choi et al., 2002; Fan et al., 1999; Liu et al., 2004) , sensing in microfluidic devices (Ferreira et al., 2005) and nuclear magnetic resonance on-chip for analysis at molecule level (Trumbull et al., 2000). Specifically, for cell handling applications as shown in Figure 2.12, like EP, cells tagged with magnetic microparticles can be separated in a laminar flow within a field gradient generated by a strong magnet (Pamme and Manz, 2004). As shown in Figure 2.13, magnetically-labelled particles can also be transported by spatially varying magnetic fields created by microwire matrices (Lee et al., 2004).

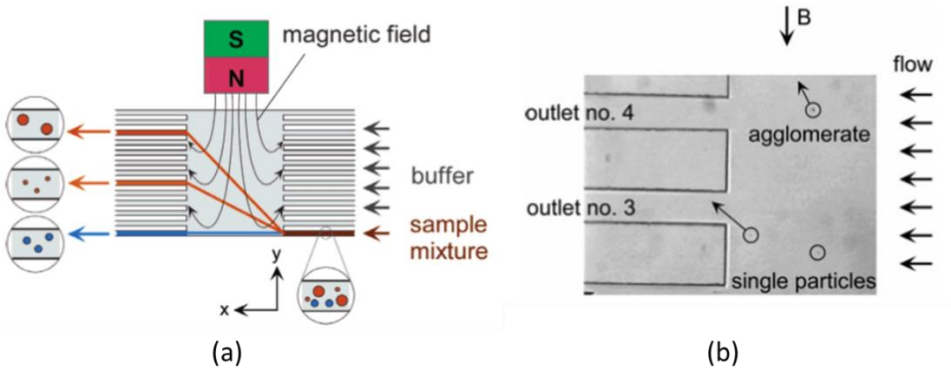

Figure 2.12 Free flow magnetophoresis (from Pamme and Manz, 2004). (a) Conceptual diagram of separation of particles based on their size and susceptibility. (b) A photograph showing that a larger agglomerate is deflected further than the smaller single particle in a field gradient.

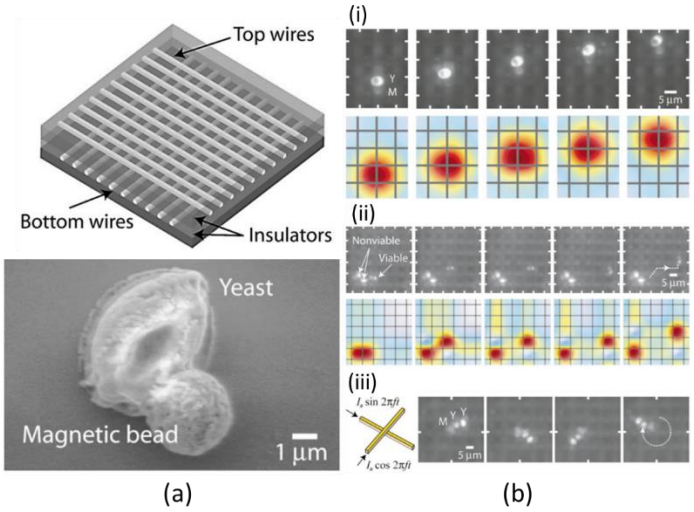

Figure 2.13 A matrix consists of electromagnetic microwires (from Lee et al., 2004). (a) Microwire matrix and a yeast cell attached to a magnetic bead for manipulation. (b) (i) Cell manipulation by moving the magnetic field maxima. (ii) Viable and non-viable cell sorting with two individually controlled field maxima. (iii) Cell rotation with time-varying magnetic field.

2.3.4 Optical Tweezers

Optical tweezing of microparticles was pioneered by Arthur Ashkin while working in Bell Laboratories in the 1970s. He found that, with an unfocused laser beam, objects with high refractive index could be drawn towards the axial centre of the beam and repelled along the beam propagation direction (Ashkin, 1970). Later, he found that a single tightly-focused laser beam could trap and hold a dielectric object in 3-D (Ashkin et al., 1986) and this technology has been recognized as “optical tweezers” ever since.

Ashkin himself gave a detailed analysis of the force origin of radiation pressure on particles induced by the laser light, calculated in the ray optics regime, as demonstrated in Figure 2.14. For a transparent particle with high refractive index, the light refraction as it passes through the object results in a change of photon momentum, inducing a force on the particle. For a slightly focused laser beam, the net force can be resolved in two forms as scattering force, F_{scat}, and gradient force F_{grad}. F_{scat} will push the particle along the beam axis while F_{grad} will drag the particle towards intensity maxima. For a tightly focused laser beam, in addition to keeping the particle at the lateral centre, the momentum change of the focused rays causes a restoring force towards the beam focus in the axial direction, and as a result, the particle can be trapped in 3-D.

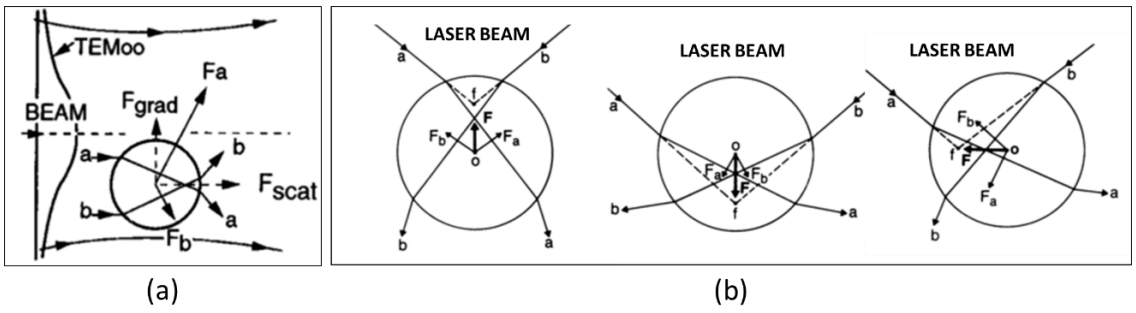

Figure 2.14 Ray optic schematic diagram showing the origins of light-induced radiation forces on transparent particles with high refractive index. (a) When a slightly focused Gaussian laser beam passes a particle that is off the beam axis, the gradient force, F_{grad}, pushes the particle into the beam axis and the scattering force, F_{scat}, drives the particle along the beam (from Ashkin, 1992). (b) A tightly focused laser beam generates a restoration force, *F*, which can fix the particle towards the beam focus (labelled as "f" in (b))(from Ashkin, 1997).

Since they were firstly invented, optical tweezers have gained important applications in atom trapping (Ashkin, 1978) and manipulation of biological particles(Ashkin et al., 1987, 1990). One highlight of early biological applications was that Ashkin et al. performed trapping of colloidal tobacco mosaic virus. Later they proved the ability to use infrared lasers to manipulate cells without damage by trapping *E. coli* bacteria and yeast cells for hours, while observing cell reproduction within the trap (Ashkin et al., 1987). Another important biological applications that emerged is the study of molecular motors, both *in vitro* (Svoboda et al., 1993) and *in vivo* (Ashkin et al., 1990), including the action of the mechano-enzymes and actin filaments of the cell which are responsible for cell motion and organelle movement within cells (Svoboda et al., 1993; Finer et al., 1994; Molloy et al., 1995; Nishizaka et al., 1995). Still another important study with optical tweezers has been the measurement of force generated by RNA polymerase enzyme as it pull itself

along a DNA molecule during RNA transcription (Yin et al., 1995). Other biological applications include study of cell mechanical properties (Dai and Sheetz, 1995), separation of bacteria from mixed sample (Huber et al., 1995), and investigation of the mechanism of cell motility (Burkhardt et al., 1993). In general, optical tweezers have become a very useful tool for biochemical research at the molecular level.

Another important phenomenon in optics is that light beams can carry angular momentum. Gaining interest from researchers, as shown in Figure 2.15, the possibility of rotating mechanical objects by light beams was investigated. Rubinsztien-Dunlop et al. first demonstrated the use of a forked diffraction grating to implement orbital angular momentum (OAM) in helically phased optical tweezers, with the absorption of the light and OAM causing rotation of the affected particle (He and Friese, 1995; He et al., 1995). The arrangement was later called “optical spanners” (Simpson et al., 1997).

As Ashkin’s conventional setup of optical tweezer has the limitation that it traps only particles with refractive index higher than the surrounding medium, helically shaped Laguerre-Gaussian beams can overcome the limitation by confining the low refractive index particles at the centre of the beam annulus due to the scattering forces (Gahagan and Swartzlander, Jr., 1996). O’Neil et al. also demonstrated that a large Laguerre-Gaussian beam can trap particles that are small compared to the beam size into a ring that circulates (O’Neil et al., 2002). Light-induced rotation has been adapted in various biological studies. For example, Parkin et al. used self-developed highly birefringent vaterite particles spun by optical tweezers to probe the viscosity of picolitre fluid volumes such as internal cell environments (Parkin et al., 2007, 2009).

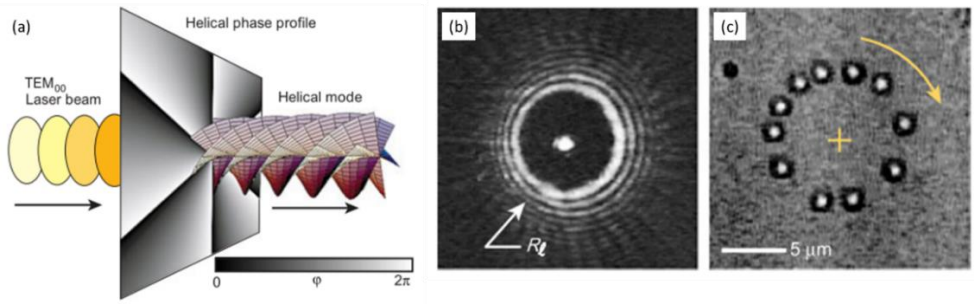

Figure 2.15 Optical vortices created from a helical light mode (from Grier, 2003). (a) The helical phase profile converts a TEM00 laser beam into a beam with a rotational wavefront. (b) Image of resulting optical vortex with annular beam focus. (c) Time lapse image of a single 800 nm colloidal particle travelling in circulation driven by the OAM of the helical beam.

With the implementation of the SLM, optical tweezers gained great flexibility by using computer-addressed optical holograms. Termed as “holographic optical tweezers”, as shown in Figure 2.16, the SLM enabled trapping and manipulation of hundreds of objects simultaneously and dynamically (Curtis et al., 2002; Grier, 2003). Also, the wavefront of each trap can be modulated individually, allowing independent rotation of trapped particles (Curtis and Grier, 2003; Preece et al., 2008).

Another popular approach to create multiple laser trap sites is with an acousto-optic deflectors (AOD) (Milne et al., 2007). An AOD consists of a transparent piezoelectric crystal which can produce an optical diffraction grating that associated with the frequency and amplitude of the acoustic waves propagating inside the crystal (Neuman and Block, 2004). The gratings can be dynamically configured so the optical beam can be steered. If the beam steering is faster than 10 kHz, the trapped particles will not undergo of Brownian diffusion over an uncontrollable distance due to the damped nature of the fluid medium. An AOD can switch very fast so a single laser beam can be multiplexed across the focal plane to create multiple optical traps.

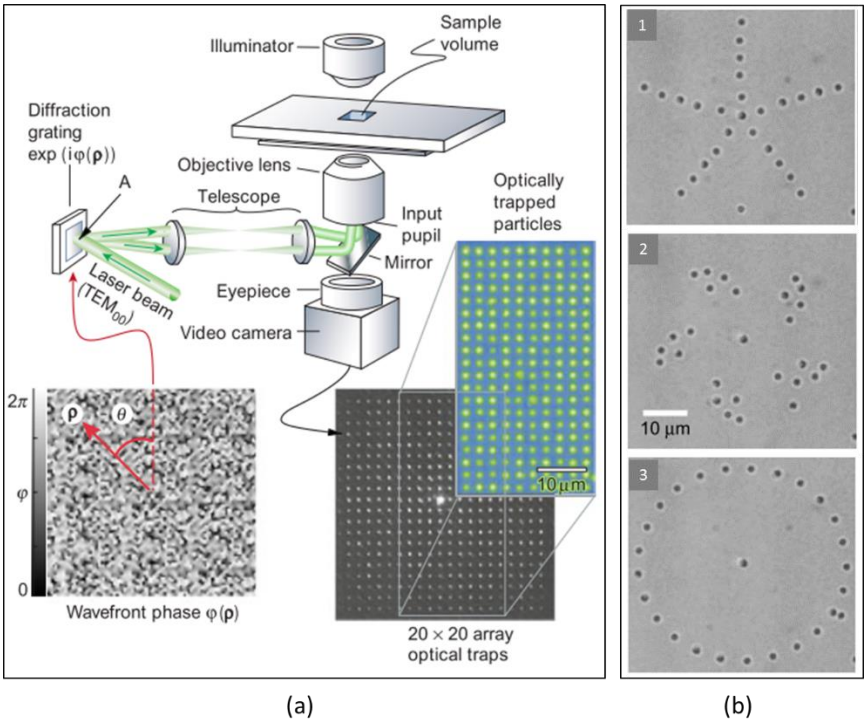

Figure 2.16 Holographic optical tweezers (from Grier, 2003). (a) Creation of large number of traps by computer generated holograms. The example phase grating creates a 20 × 20 array of traps of 800 nm diameter polystyrene spheres. (b) 1-3 shows 36 water-borne polystyrene spheres with 800 nm in diameter trapped in a plane with dynamic configurations.

Invented over 30 years ago, and benefitting from development over the most recent 10 years, there is now a handful of companies have already commercialize optical tweezer technology, mostly for single cell and molecular level biological studies (Matthews, 2009). Globally, numerous research groups are building their own sophisticated optical tweezing system based on previous research (Chen et al., 2012; Grier, 2003; He et al., 1995; MacDonald et al., 2010; Padgett and Di Leonardo, 2011; Smith, 1999; Stevenson et al., 2014).

2.3.5 Acoustic Tweezers

Using ultrasound for microparticle and cell manipulation in microfluidic devices has gained great interest in the past 30 years. The appeal of this technology lies in: the ability of MHz-frequency ultrasound with correspondingly small wavelength, to manipulate micrometre-size particles; the ease of integration with conventional microfluidic devices; the ease of control of the field geometry by adjusting the dimensions of the microfluidic devices and / or the ultrasound transducers; the simplicity of creating field gradients; and the strong trapping forces ranging from pN to nN, able to manipulate large particles or particle clusters with size ranges from a few micrometres to hundreds of micrometres, and large objects such as liquid droplets with dimensions in millimetres.

In this section, a brief review of the fundamentals of acoustic field generation will be given in Subsection A, followed by a summary of typical biological applications in Subsection B. Subsection C will provide an insight into the acoustic field shaping methodologies from the perspectives of transducer geometries and / or acoustic chamber geometries, and with modulated transducer excitation signals.

A. Ultrasound Basics for Particle Manipulation

a. Piezoelectricity

Acoustics is the interdisciplinary science that studies the mechanical wave propagation in media such as gases, liquids and solids. The majority of the theoretical basis of linear and non-linear acoustics was established in the 19th century, a highlight being the treatise by

Lord Rayleigh (John William Strutt), *The Theory of Sound*. The discovery of piezoelectricity in 1880 by the Curie brothers, (Pierre and Jacques) opened the gate to modern ultrasonics. Ultrasound is an acoustic wave with a frequency higher than the range of human hearing, normally 20 Hz – 20 kHz. As piezoelectricity is induced as a result of dipole rotations in the materials, piezoelectric materials must have anisotropic structures (Cobbold, 2007a). A detailed illustration of the piezoelectric and inverse piezoelectric phenomena is shown in Figure 2.17. It can be noted that the inverse piezoelectric effect is particularly useful for generating ultrasound waves if an AC electric field is applied on two conductive surfaces of the material. The energy is transformed from electricity into mechanical waves and this acts as the basic principle for the operation of ultrasonic transducers.

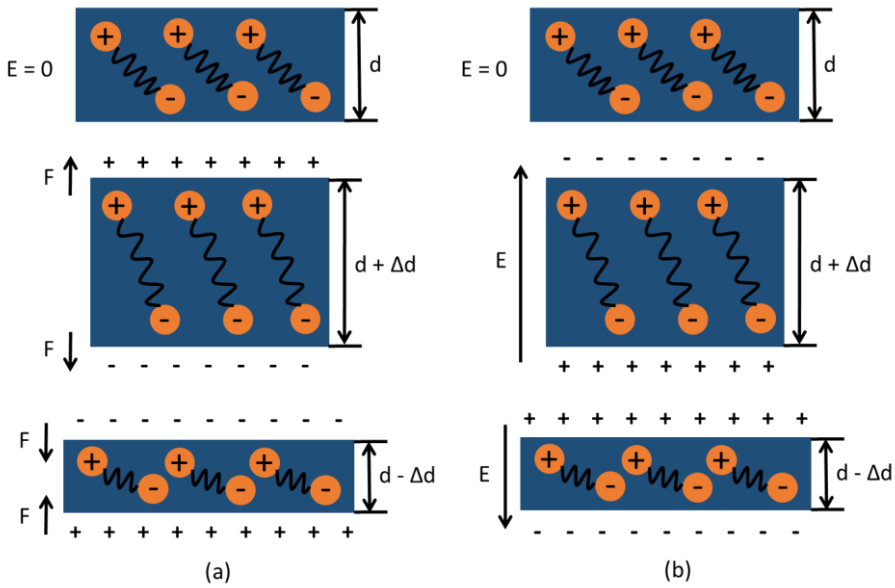

Figure 2.17 Simplified illustration of piezoelectricity and inverse piezoelectricity (adapted from Cobbold, 2007a). The piezoelectric material is polarized and the resulting dipole is oriented by the strong electric field in poling process. (a) Piezoelectricity: if tensile stress is applied, the voltage appears at the two surface electrodes would be in the opposite polarity to the poling voltage and, if the compressive stress is applied, the resulting voltage is in the same direction as the poling voltage. (b) Inverse piezoelectricity: if the applied electric field is in the same direction as the poling voltage, the material will expand and, if the applied electric field is in the opposite direction of the poling voltage, the material will contract.

b. Acoustic Wave Propagation

A mechanical pressure wave induced by the vibration of a piezoelectric transducer may travel in a coupling medium, either inside the medium (body waves), or along the surface of the medium (surface waves). For body waves, there are two basic types of wave motion

for mechanical waves: longitudinal (compressional) waves and transverse (shear) waves, as illustrated in Figure 2.18 (a) and (b). In a longitudinal wave, the particle displacement is parallel to the direction of wave propagation; while in a transverse wave, the particles are moving perpendicular to the direction of wave propagation. Longitudinal wave are generally more important for most acoustic tweezing applications. However, these two forms of waves can be combined in more complex particle displacement profiles, especially for the case of surface waves. There are many types of surface waves, and a typical class of surface wave found in solid is Rayleigh surface waves, as illustrated in Figure 2.18 (c). The particles near a solid surface through which the Rayleigh wave propagates move in elliptical paths, with the major axis perpendicular to the surface of the solid. As the depth into the solid increases, the amplitude of particle displacement decay rapidly. Surface waves as a method for acoustic tweezing has also been widely investigated.

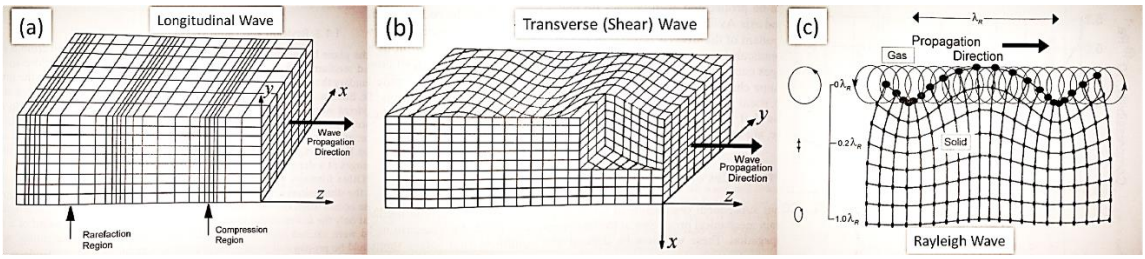

Figure 2.18 Snapshot views of particle displacements in different wave propagation forms (from Cobbold, 2007a). (a) A plane longitudinal wave. (b) A y-polarized shear wave. (c) A Rayleigh surface wave

Ultrasound Standing Wave (USW)

Acoustic discontinuities such as microparticles in an ultrasound field will experience small forces, and such forces are generally stronger in USW fields than ultrasound travelling wave fields (UTWs) (Hill and Harris, 2007). For a USW, a straightforward illustration is use an air pipe model sealed at one end, as shown in Figure 2.19. Consider this air pipe with one opening closed and, a piston oscillating at the other end. The air molecules vibrate in a periodic pattern, with local displacement maxima (displacement antinode) and local displacement minima, nearly zero (displacement node). At the displacement antinode, the air molecules are moving back and forth, the local densities do not change, and these positions can be recognized as pressure nodes. At the displacement nodes, the local densities either increase or decrease, causing local pressure

varying between maximum-positive and maximum-negative. These positions can be recognized as pressure antinodes. It can be found from Figure 2.19 that the pressure and air molecule displacement variations in the longitudinal standing wave are 90° out of phase.

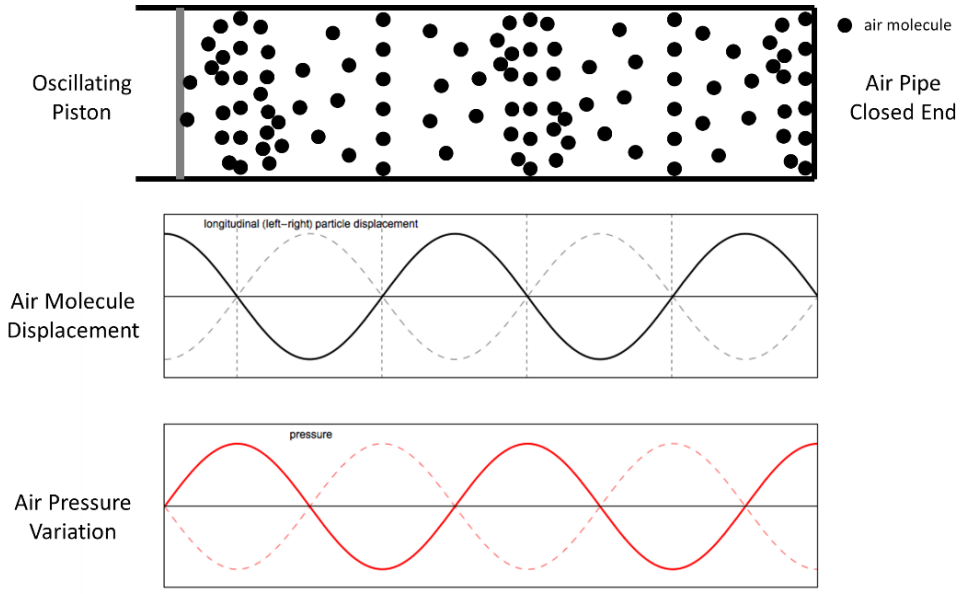

Figure 2.19 Longitudinal standing wave illustration with an air pipe model, showing the air molecule displacement and pressure variation in the pipe with a piston oscillating at one end of the pipe (from Russell, 2012).

Radiation Forces in USW: Primary Forces and Secondary Forces

Relevant parts of the review by Hill and Harris of USW radiation force theory development forms the major content of this section (Hill and Harris, 2007).

Acoustic radiation forces or acoustic radiation pressure as a phenomenon was first described by Kundt and Lehman in 1874, and later, in detail by Lord Rayleigh. These descriptions indicated that sound wave can exert time-averaged directed pressure on objects (Lord Rayleigh, 1902). In 1903 Altberg was the first to report measurements of the radiation pressure produced by acoustic waves. The first comprehensive calculation of acoustic radiation forces on small particles within standing wave fields was presented by King. He considered that, in an inviscid fluid, rigid spheres would be moved towards pressure nodes or antinodes, depending on the ratio of the particle density to the fluid density (King, 1934). The error for compressible spheres (such as air bubbles) in USW

field was corrected by Yosioka and Kawasima (Yosioka and Kawasima, 1955). They derived an expression for one-dimensional (1-D) time-averaged acoustic radiation force on a sphere of radius, *a*, at position, *x*, within an USW field of time-averaged energy density, $\langle\varepsilon\rangle$, as

$$F(x) = 4\pi k\langle\varepsilon\rangle a^3 \Phi(\beta,\rho)\sin(2kx), \quad \textbf{(2.1)}$$

where the term $\Phi(\beta,\rho)$, defined as acoustic contrast factor, is given by

$$\Phi(\beta,\rho) = \frac{\rho_p + \frac{2}{3}(\rho_p - \rho_f)}{2\rho_p + \rho_f} - \frac{\beta_p}{3\beta_f}, \quad \textbf{(2.2)}$$

where β and ρ are the compressibility and the mass density of the fluid (indicated by f) and the particle (indicated by p). k is the wave number, and compressibility, β, is relative to the speed of sound, *c*, according to $\beta = {}^{1}/_{\rho c^2}$. Figure 2.20 is a plot of the compressibility ratio ${}^{\beta_p}/_{\beta_f}$ against the density ratio ${}^{\rho_p}/_{\rho_f}$, for the function $\Phi(\beta,\rho) = 0$. The curve trend indicates that particles positioned at pressure nodes or antinodes as a result of the radiation forces are actually determined by both the compressibilities and densities of the fluid and particles. Particles that are denser and less compressible than the fluid medium tend to be moved towards pressure nodes in an USW field (Hill and Harris, 2007).

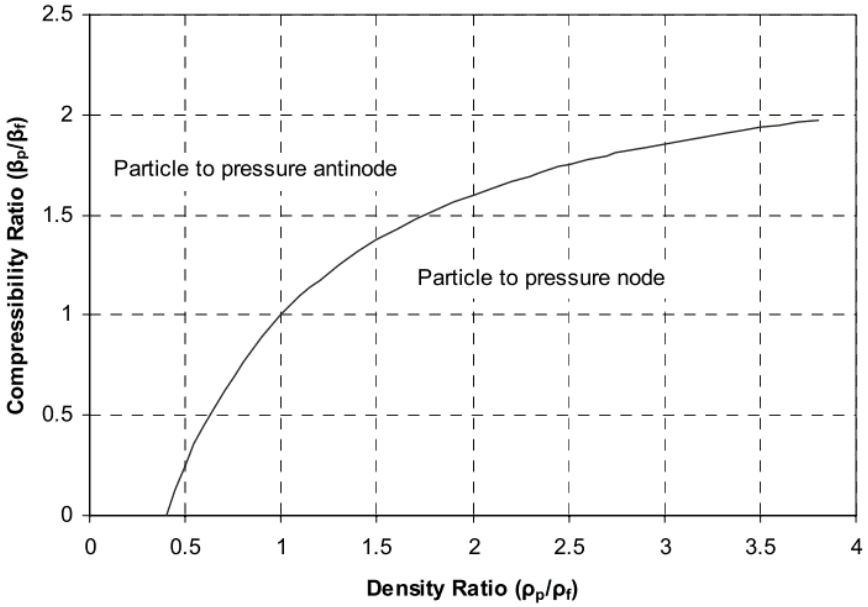

Figure 2.20 Plot of $\Phi(\beta, \rho) = 0$ as a function of density and compressibility ratios (from Hill and Harris, 2007).

As an alternative, Gor'kov (Gor'kov, 1962) demonstrated the acoustic radiation forces on a particle from the energy stored in a 1-D plane standing wave, with the form of the time averaged kinetic energy term $\langle \varepsilon_{kin}(x) \rangle$, and potential energy term $\langle \varepsilon_{pot}(x) \rangle$, being

$$F(x) = -\frac{\partial}{\partial x}\left(\frac{4\pi a^3}{3}\left(\left(1-\frac{\beta_p}{\beta_f}\right)\langle \varepsilon_{pot}(x)\rangle - \frac{3(\rho_p-\rho_f)}{2\rho_p+\rho_f}\langle \varepsilon_{kin}(x)\rangle\right)\right) \qquad \textbf{(2.3)}$$

For a plane standing wave of energy density, ε, with a rigid boundary at $x = 0$, **(2.3)** has the same form as **(2.1)**, with (Gröschl, 1998)

$$\langle \varepsilon_{kin}(x)\rangle = \langle \varepsilon \rangle sin^2(kx) \qquad \textbf{(2.4)}$$
$$\langle \varepsilon_{pot}(x)\rangle = \langle \varepsilon \rangle cos^2(kx) \qquad \textbf{(2.5)}$$

If substituting **(2.4)** and **(2.5)** into **(2.3)**, the radiation force can be expressed as the same form in **(2.1)** (Hill and Harris, 2007). Gor'kov also derived the expression of $\langle \varepsilon_{kin}(x)\rangle$ and $\langle \varepsilon_{pot}(x)\rangle$ as functions of velocity field, u, and potential field, p (Glynne-Jones, Démoré, et al., 2012; Gor'kov, 1962):

$$\langle \varepsilon_{kin}(x) \rangle = \frac{1}{2} \rho_f u^2(x) \quad \textbf{(2.6)}$$

$$\langle \varepsilon_{pot}(x) \rangle = \frac{1}{2\rho_f {c_f}^2} p^2(x) \quad \textbf{(2.7)}$$

where ρ_f and c_f are the density and the sound speed in the fluid.

The radiation forces discussed above are normally termed "primary radiation forces", and can be decomposed into "axial forces", associated with the potential energy field, and "lateral forces", associated with the kinetic energy field. The axial forces are responsible for transporting particles toward pressure nodes / antinodes in the axial direction, and the lateral forces, as combinations from many different contributing factors such as source inhomogeneity, geometric interference, and 2-D or 3-D dimensional acoustic modes (Hill and Harris, 2007), will move particles to lateral nodal planes. It has been determined by modelling and experimental measurement that the lateral forces are generally a factor × 100 smaller than the axial forces (Glynne-Jones, Démoré, et al., 2012).

Another form of acoustic radiation forces that is responsible for forming the particle clusters at the pressure nodes or antinodes is termed "secondary radiation force" and has been reviewed in detail by Gröschl (Gröschl, 1998). This force is generated due to the scattering field interactions between particles and is usually negligible until the particles are closely spaced. Bjerknes calculated the attractive and repulsive forces between oscillating spheres, without considering the primary field (Bjerknes, 1906). Thus the force is also termed "Bjerknes force". Weiser et al. investigated the theoretical origins of secondary radiation force in the context of red blood cells in USW field (Weiser et al., 1984). Zheng and Apfel expressed the total radiation force as the sum of the primary radiation force and the particle interaction force, with the latter reducing to Bjerknes force in the case of $kd \ll 1$, where d is the distance between the particles (Zheng and Apfel, 1995). A diagram illustrating the primary radiation force, F_{PRF}, and the secondary radiation force, F_{SRF}, on particles in an USW field is shown in Figure 2.21.

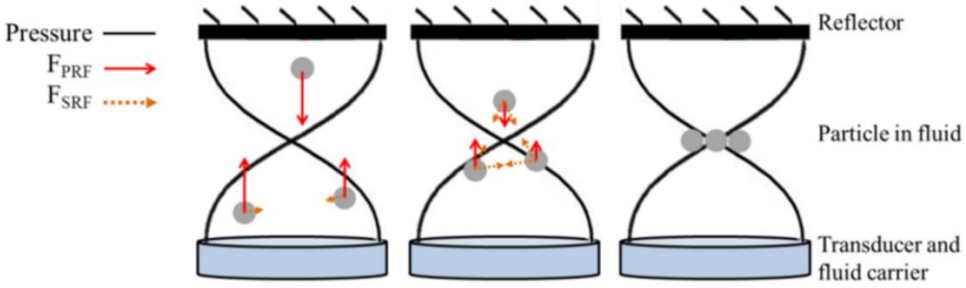

Figure 2.21 Schematic showing the pressure distribution in an USW field, and F_{PRF} and F_{SRF} for creation of a particle cluster at a pressure node (from Qiu et al., 2014).

B. Applications of Ultrasound Particle Manipulation in Biology and Chemistry

Early publications dating from the 1900s to 1980s focused on the development of the theory of acoustic radiation forces, which built the foundations for the succeeding experimental studies. Starting from the 1990s, a boom in publications began on exploration of USW in diverse biological applications. Differing in the principle of the wave origin, one kind of USW tweezing devices is based on the creation of plane standing waves from bulk acoustic waves (BAW) which propagate inside the medium, and another kind operates based on surface acoustic standing waves (SAW), which are generated and conducted along the surfaces of piezoelectric and other solids. Applications for particle manipulation with UST were also explored, but significantly less, mainly because of smaller forces generated on particles compared with USW.

Qiu et al. recently published a review (Qiu et al., 2014) of acoustic particle manipulation technology development in most recent 25 years for handling biological cells, microbubbles and other types of microparticles, using both USW (BAW and SAW) and UST. A summary of the main applications is given below:

- Microparticle filtration, washing and sorting (Cousins et al., 2000; González et al., 2010; Harris et al., 2003; Hawkes, Barber, et al., 2004; Laurell et al., 2007; Petersson et al., 2005)
- Microparticle patterning and immobilization (Bernassau, Gesellchen, et al., 2012; Chen et al., 2014; Courtney et al., 2010; Ding, Shi, et al., 2012; Lee et al., 2011; Li et al., 2014; Qiu et al., 2014; Raiton et al., 2012)

- Cell culturing and proliferation in USW field (Bazou et al., 2008; Gesellchen et al., 2014; Hultström et al., 2007)
- Sensitivity improvement of biosensors and bioassays (Glynne-Jones, Boltryk, Hill, et al., 2010; Hawkes, Long, et al., 2004; Martin et al., 2005; Wiklund et al., 2013)
- *In vitro* cell sonoporation enhancement (Carugo et al., 2011; Khanna et al., 2006; Kinoshita and Hynynen, 2007)

C. Acoustic Field Shaping Methodologies

a. Field Shaping with Transducer Geometries or Acoustic Chamber Geometries

Field Shaping with Physically Focused Transducers

Lee et al. reported an approach for single cell immobilization and manipulation (Lee et al., 2011), as shown in Figure 2.22. They used a high frequency (200 MHz) single element focused ultrasound transducer to perform trapping and manipulation of a single 10 µm leukaemia cell. Similar to optical tweezers, the cell was trapped at the focus of the ultrasound microbeam, and was manipulated with transducers by a mechanical stage.

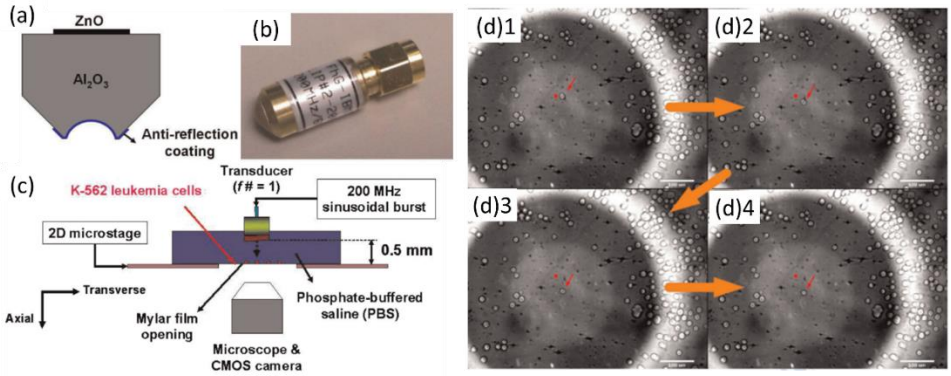

Figure 2.22 High frequency focused ultrasound for cell manipulation (from Lee et al., 2011). (a) An illustrative diagram of a focused transducer made from 6 µm thick ZnO piezoelectric film sputtered onto an Al_2O_3 buffer rod. (b) A photo of the fabricated high frequency transducer. (c) Experimental setup. (d)1 – (d)4 A cell was picked up and manipulated by the focused ultrasound microbeam.

Qiu and Hughes et al. reported another approach, using a curved ultrasound transducer working at 3.4 MHz, for trapping and manipulating aggregates of polystyrene particles and Dictyostelium cells with a focused USW field (Hughes et al., 2012; Qiu et al., 2014).

As shown in Figure 2.23, a quarter-ring transducer was placed against a petri dish with its surface as the reflector to create a quasi-USW with the pressure node placed a half wavelength away from the reflector surface in the fluid medium. The particles were concentrated and picked up at the pressure nodes near the reflector surface, and manipulated with a mechanical stage that was holding the transducer.

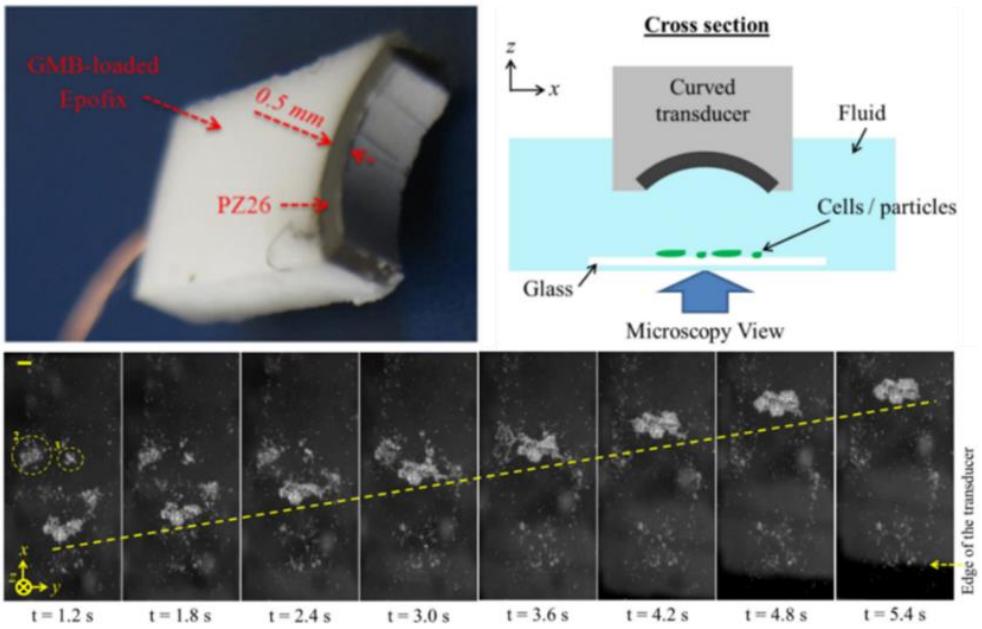

Figure 2.23 A focused quasi-USW field created by a curved transducer for trapping and manipulation of an agglomerate of 10 μm polystyrene particles (from Qiu et al., 2014).

Field Shaping with Acoustic Chamber Geometry

For USW devices that using pressure nodal planes for particle trapping, the positions of the pressure nodes are highly dependent on the chamber geometry. A popular approach is using a half-wavelength thick fluid layer to create a single pressure node for particle focusing (Glynne-Jones et al., 2012; Lenshof et al., 2012). A group of researchers in Lund University reported a resonator setup for effective particle focusing and acoustophoresis, as shown in Figure 2.24(a), using etched silicon microchannels with defined channel widths that matched half the acoustic wavelength in the buffer fluid.

An alternative setup is a multilayer resonator, with the fluid channel sandwiched between the transducer and the reflector layers, as shown in Figure 2.24(b). But the USW field in such devices is very sensitive to the fluid and reflector layer thickness. With reduced fluid

layer thickness and matched reflector thickness the pressure node can also be placed at the reflector surface for enhanced biosensor behaviour (Hawkes et al., 2004; Martin et al., 2005). Hill and Glynne-Jones et al. published comprehensive studies of the influence of the reflector layer thickness over the positioning of the acoustic pressure nodes (Glynne-Jones et al., 2012; Hill, 2003).

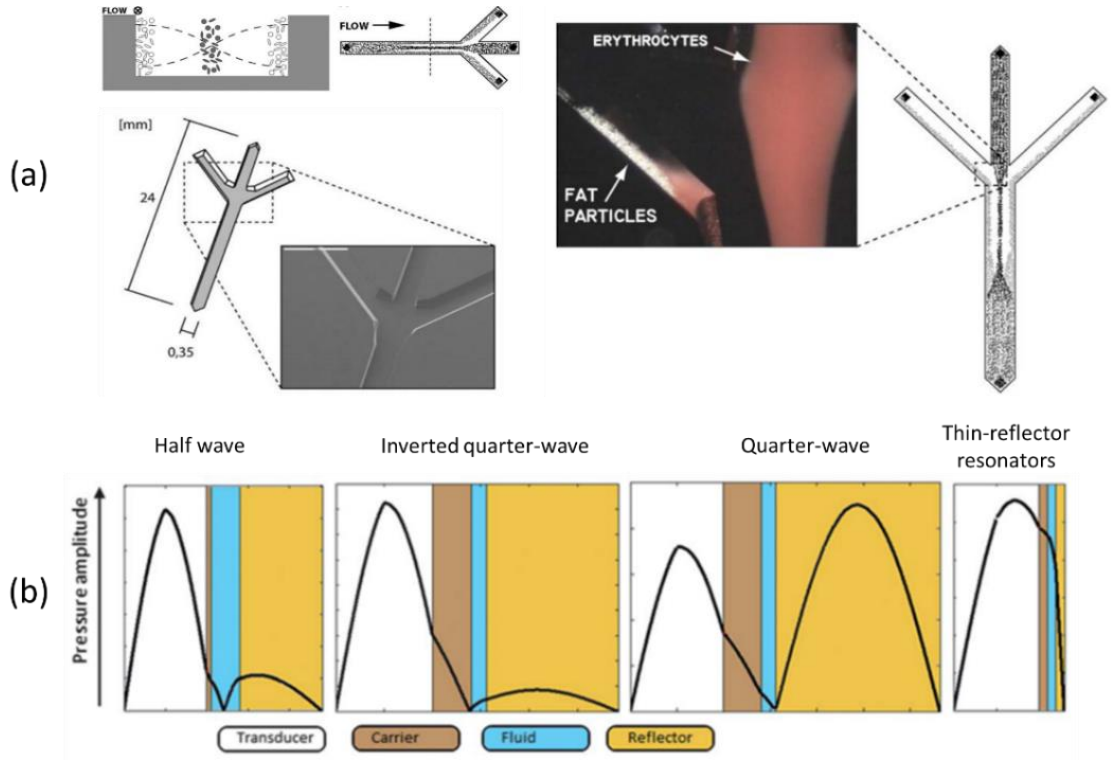

Figure 2.24 Different USW resonators. (a) Experimental setup of a silicon etched half-wavelength-wide channel for continuous flow separation of red blood cells focused at pressure nodes, and lipid particles focused at pressure antinodes (from Petersson et al., 2004). (b) Normalized pressure amplitude variation in different multilayer resonator setup. The pressure nodes in the fluid layer (blue) can be placed at different positions (from Glynne-Jones, Boltryk, et al., 2012).

b. Field Shaping with Modulated Transducer Excitation Signals

As discussed in Section 2.3.5 A, the ultrasound pressure wave is generated by the piezoelectric transducers that excited with AC signals. In the past 10 years, quite a few research programmes have been conducted in acoustic field shaping via modulated excitation signals. This subsection will discuss the examples of particle manipulation within both USW and UTW fields based on modulation of transducer driving signals with particular attention to signal frequency, phase and amplitude.

Field Shaping with Excitation Signal Frequency Modulation

Ding et al. reported the manipulation of microparticles and cells in 2-D within a polydimethylsiloxane (PDMS) microchamber using a frequency-modulated standing SAW field (Ding, Lin, Kiraly, et al., 2012). With the same method they also performed SAW-activated particle flow guidance in PDMS microchannels (Ding, Lin, Lapsley, et al., 2012). The operational principles and experimental results are illustrated in Figure 2.25. SAWs were generated by chirped interdigitated transducers (IDT) which are interlocking comb-shaped electrodes coated on $LiNbO_3$ piezoelectric substrates. The counter-propagating SAWs interfered with each other and formed a stable pattern of pressure nodes and antinodes in a 2-D field. Particles trapped at the pressure nodes could be manipulated by varying the excitation frequencies of the chirp IDTs to change the SAW wavelength, in order to move the positions of the pressure nodal planes.

Glynne-Jones et al. proposed an FM technique for pressure nodal plane manipulation within multilayer resonators (Glynne-Jones, Boltryk, Harris, et al., 2010), as shown in Figure 2.26. Typically, the transducers in multilayer resonators are excited at fixed frequencies, allowing the device to work at half-wavelength or quarter-wavelength modes in which the acoustic pressure nodes are placed at the axial centre of the fluid or very close to the reflector layer. However the pressure nodal plane can be manipulated to any arbitrary position between the half-wave node and the quarter-wave node by fast switching between the device half-wave and quarter-wave resonance frequencies, with different fractions of each in every switching period.

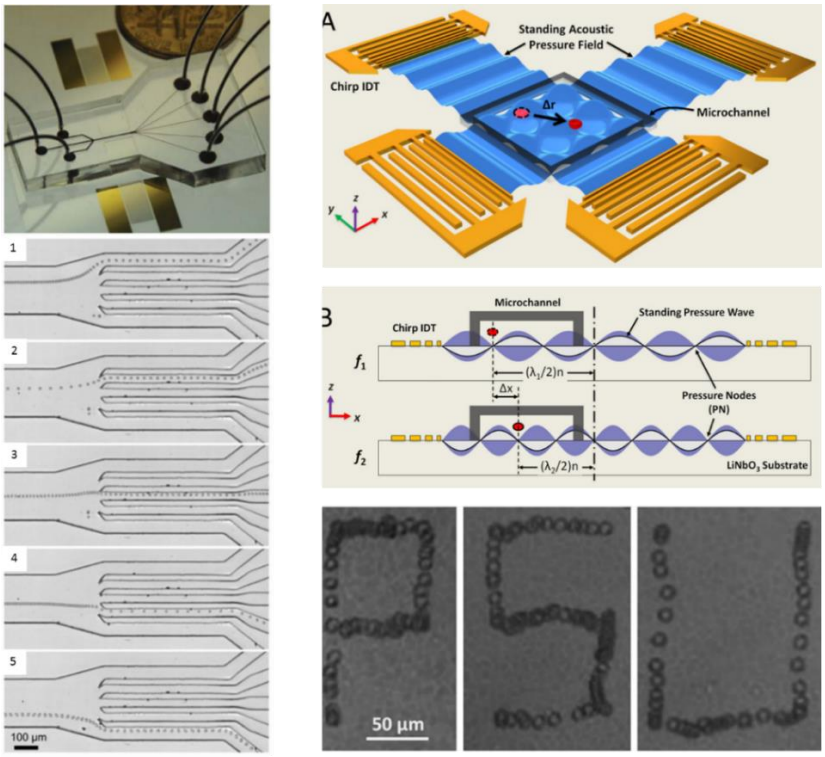

Figure 2.25 Frequency-modulated standing SAW for particle manipulation. (a) A flow of human white blood cells (HL-60 human promyelocytic leukemia cells) diverges into five different channels with two paired chirp IDTs working at frequencies of 9.8, 10.0, 10.2, 10.6 and 10.9 MHz, from inset 1-5 (from Ding, Lin, Lapsley, et al., 2012). (b) 2-D manipulation of a single bovine red blood cell with four paired IDTs; the stacked images trace out the cell movements as "PSU" (from Ding, Lin, Kiraly, et al., 2012).

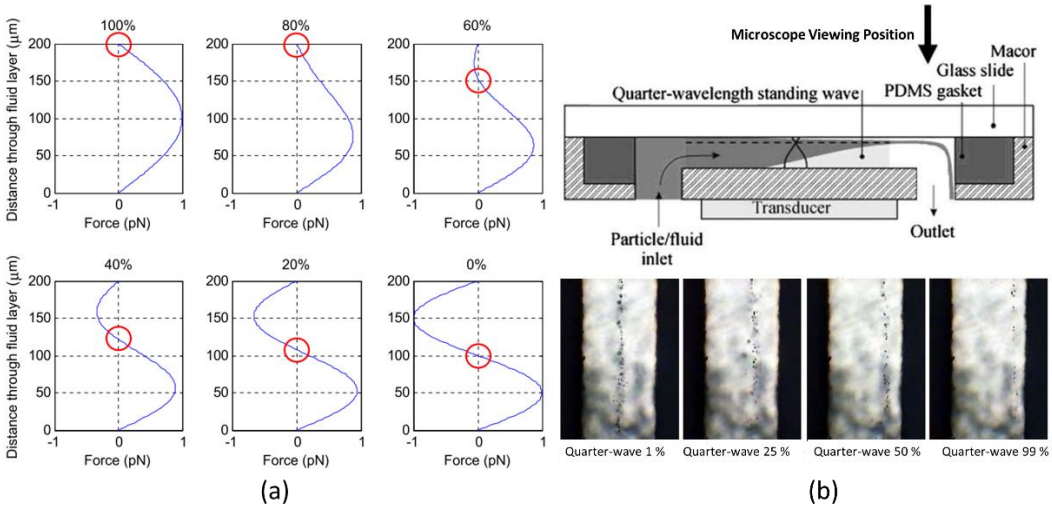

Figure 2.26 Mode-switching for pressure node positioning in USW multilayer resonator (from Glynne-Jones, et al., 2010). (a) Modelling results showing time-averaged force profiles with different fractions of quarter-wave mode. (b) Experimental verification of positioning a focused flow of polystyrene particles in the positions between the half-wave and the quarter-wave nodes.

Field Shaping with Excitation Signal Phase Modulation

Pressure nodes and antinodes within USW fields can also be manipulated by variation of the phases of the excitation signals. Courtney et al. reported a study with phase-controllable USWs to manipulate particles in a 2-D microfluidic chamber (Courtney et al., 2010, 2011). Four counter-facing piezoelectric transducers with matching and backing layers were placed at every other adjacent side of an octagonal fluidic chamber, with a piezoelectric plate at the bottom as a particle levitation stage. An illustration of the setup and experimental results are shown in Figure 2.27. The excitation signals for the four transducers were synchronized with defined relative phase difference in both x- and y-directions, and the resulting pressure node / antinode patterns could be manipulated in 2-D. If the phases of the excitation signals for transducers numbered 1 – 4 in Figure 2.27 (a) are defined as ϕ_1, ϕ_2, ϕ_3, and ϕ_4 respectively, and:

$$\begin{cases} \phi_x = \dfrac{\phi_1 + \phi_2}{2} \\ \Delta\phi_x = \phi_1 - \phi_2 \\ \phi_y = \dfrac{\phi_3 + \phi_4}{2} \\ \Delta\phi_y = \phi_3 - \phi_4, \end{cases} \tag{2.8}$$

then 2-D manipulation can be achieved, within a plane of regular grid of traps (regions of zero pressure shown in Figure 2.27 (b)), when $\phi_y = \phi_x + {}^{\pi}/_{2}$, and the in-plane (x, y) values are defined as:

$$\begin{cases} x = (2n_x - 1)\dfrac{\lambda}{2} + \dfrac{\Delta\,\phi_x}{2\pi}\dfrac{\lambda}{2} \\ y = \left(2n_y - 1\right)\dfrac{\lambda}{2} + \dfrac{\Delta\,\phi_y}{2\pi}\dfrac{\lambda}{2}, \end{cases} \tag{2.9}$$

where n_x and n_y are independent integers.

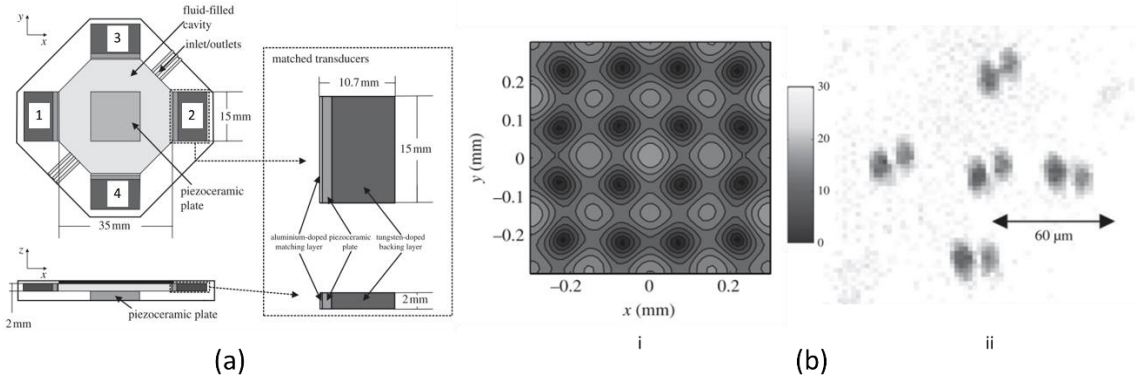

Figure 2.27 Phase-controllable 2-D USW particle manipulation device (from Courtney et al., 2011). (a) Schematic of the device setup with four paired counter-facing ultrasound transducers and a bottom transducer plate for acoustic levitation (b) i. The simulated plane with alternating pressure nodes and antinodes. ii. A stacked image showing trapping and manipulation of 10 μm polystyrene particles in the field, with the condition $\phi_y = \phi_x + \pi/2$, and with additional phase delays $\pm \pi/2$ applied over each pair of counter-facing transducers in turn.

Very recently Ochiai et al. demonstrated three-dimensional USW acoustic manipulation in air with four counter-facing 2-D ultrasound matrix arrays (Ochiai et al., 2013, 2014), as shown in Figure 2.28. Each transducer array consists of 285 ultrasound transducers with 10 mm diameter circular aperture operating at 40 kHz arranged in a 190-mm × 190-mm 2-D matrix. Each transducer matrix was controlled by standalone, FPGA-based driving electronics that consist of FPGA circuitry and power amplifiers. All four transducer matrices were synchronized and controlled by a PC via a USB interface. With the ultrasound array positioned as shown in Figure 2.28(a), counter-propagating acoustic waves created a USW field, and the field could be focused and dynamically configured based on computer-addressed algorithms. The spatial resolution was 0.5 mm, and the acoustic field refresh rate was 1 kHz. Small objects like polystyrene spheres of diameter 0.6 mm and large objects like paper models with size in centimetres could be levitated and manipulated in the USW field.

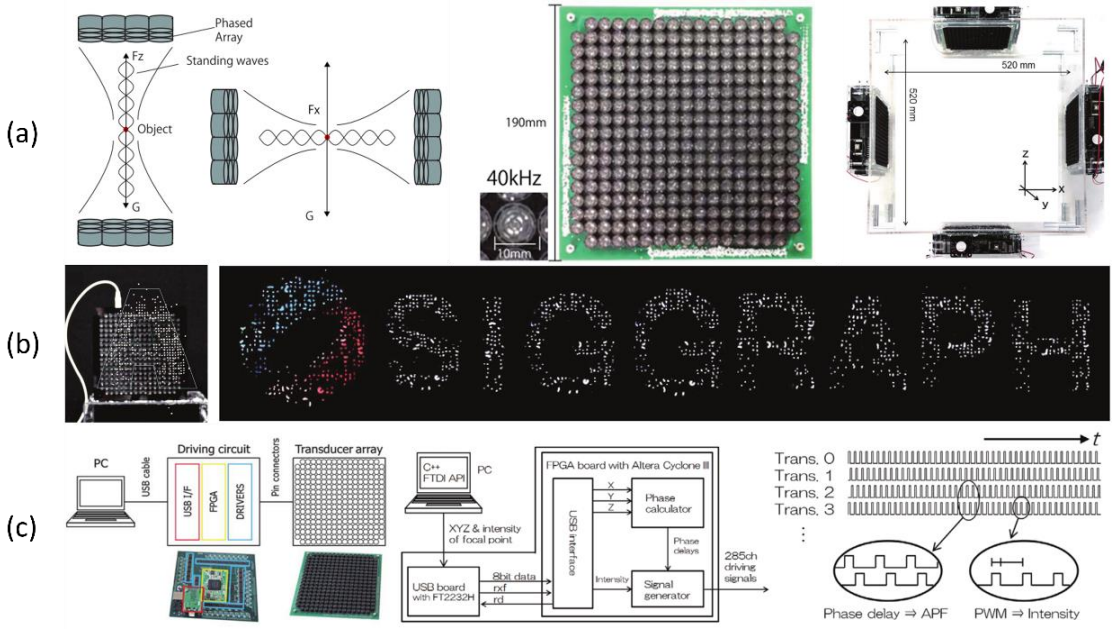

Figure 2.28 3D acoustic manipulation matrix array (from Ochiai et al., 2013, 2014). (a) An illustration of focused USW field generated with counter-facing 2D transducer arrays, and the experimental setup of four array matrices arranged in a 520 mm × 520 mm square. (b) Dynamic patterning of 1 mm diameter polystyrene particles. (c) System schematic for the electronics of each 2D transducer matrix. Dynamic control of signal intensity and relative phase delay between each transducer is configured by an FPGA via PC addressed algorithms.

Field Shaping with Complex Excitation Signal Modulation

There have been reports of complex acoustic field shaping with ultrasonic arrays for manipulation of both small particles and large objects. Démoré et al. reported the creation of helical acoustic beams with an adapted commercial ultrasonic array system for levitating and rotating a disk made of acoustic absorbing material with diameter 100 mm, weighing 87 g. This experiment was successfully and for the first time directly validate the theoretically predicted ratio of the OAM to the linear momentum in a propagating beam (Démoré et al., 2011, 2012).

Originally designed for HIFU surgery, the ExAblate 2100 ultrasound instrument (InSightec, Haifa, Israel) is capable of generating high power, continuous wave (CW) ultrasound beams. In the experiments of Démoré et al., acoustic power was varied between 23 W and 55 W, by adjusting the voltage amplitudes of the excitation signals for transducer elements. The transducer probe comprises a 550 kHz matrix array with over one thousand elements. The array elements are individually addressable through a computer-based system, which is able to adjust the excitation AC signal phase with $\pi/4$

discretized resolution, allowing transmission beam forming such as focusing and steering. Exploiting the versatility of this system, helical ultrasound beams can be created with modulated wavefronts from specified relative phases between the array elements. An illustration of the experimental setup and beam wavefront measurements is shown in Figure 2.29. Helical beams can be generated with a wave source spiral profile defined as $\varphi = l\theta$, where l is an integer named as topological charge which defines the vorticity and θ is the azimuthal angle when looking into the source wave plane.

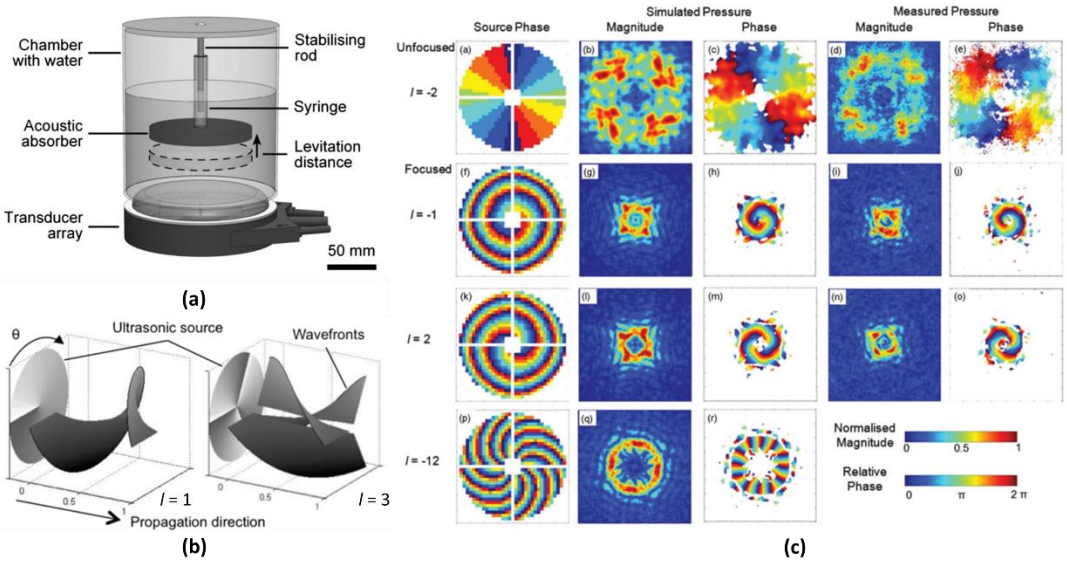

Figure 2.29 Spiral acoustic beams for levitation and rotation of a macroscopic object in an UTW field (from Démoré et al., 2011, 2012). (a) Setup of the one-thousand-element high power transducer array and the acoustic absorber disk within a chamber filled with water. (b) An illustration of the beam vorticity defined by different topological charge l. (c) Simulated and direct measured pressure of helical beam wavefronts with different l at a plane approximately 60 mm above the transducer surface.

Another very recent report from Zhang et al., as shown in Figure 2.30, for the first time demonstrates the possibility of engineering acoustic wavefronts to create self-bending and bottle beams, with linear and 2-D ultrasound transducer arrays respectively (Zhang et al., 2014). Their approach is a new alternative to generate directed acoustic beams in homogenous media without acoustic metamaterials as a spatially-varying medium for manipulation of acoustic beams. According to their theory, with a linear ultrasound array it is possible to create a bending acoustic beam that propagates along any prescribed arbitrary convex trajectory in 2-D, and also possible to construct an acoustic bottle beam that comprises an axial symmetric feature in 3-D from a 2-D ultrasound matrix array. The bending beam trajectory following a caustic curve is a result of constructive waves emitted from an engineered wavefront from the transducer sources.

To create the acoustic self-bending beam in 2-D and bottle beam in 3-D, at the wave sources, the phase and amplitude profiles of the excitation signals for all transducers in the array are obtained as an asymptotic solution of Helmholtz equation, for a given beam trajectory. The resulting self-bending beam has uniqueness as a non-diffracting beam that can reconstruct itself after the main lobe is blocked by an obstacle, which may be useful for ultrasound imaging and therapeutic ultrasound. It was also demonstrated that a 3-D bottle beam could generate a pulling force on a rigid ball inside the beam bottle with direction opposite to the beam propagation. This offers the potential for acoustic trapping and manipulation.

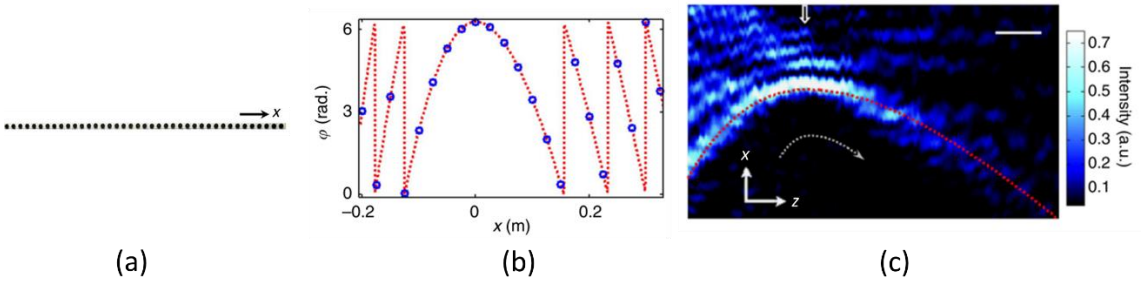

Figure 2.30 Acoustic self-bending beam generated in air from a 1-D array consisted of 10-kHz transducers (1.5 cm in diameter with 2.5 cm spacing) (from Zhang et al., 2014). (a) The linear array consists of 40 speakers. (b) The theoretical (red dotted line) and quantized (blue circles) phase (φ) profile for the transducer array. (c) Experimentally-measured acoustic intensity distribution of a self-bending beam generated from the design in (b). The measurement was taken at x-z plane. Scale bar in the picture is 0.1 m.

2.4 Conclusions

This chapter gave a summary of the major particle manipulation technologies for both contact and contactless modalities. In studies in biology that require single cell handling, a micropipette is still the most robust and widely used apparatus; however, it does require skill for operation with accuracy. As a mature and efficient technology, AFM is still an important tool for single cell studies. Contactless manipulation technologies include hydrodynamic methods, EP and DEP, magnetic tweezers, optical tweezers and acoustic tweezers. These offer diverse alternatives for non-contact handling from microscopic objects to large objects with dimensions in millimetres. In biological studies these technologies have many potential benefits such as reducing cell damage during manipulation, label-free cell sorting, massively parallel cell studies, and automatic cell assembly for tissue engineering. More importantly, they all have their own benefits and

drawbacks, and each has some superior properties for different applications (Qiu, Wang, et al., 2014).

As the main interest of this thesis, acoustic tweezers has the advantages as a tool for label-free cell handling, with relatively large forces to manipulate cell agglomerates over a large working volume while maintaining good cell viability over long operating time periods for hours and days (Vanherberghen et al., 2010). However, compared to other contactless technologies, the limitations of acoustic tweezers include poor ability to handle single cells and sub-micrometre particles because of the low spatial resolution of ultrasound waves (Wiklund and Önfelt, 2012), and side effects such as cavitation (Marmottant and Hilgenfeldt, 2003), excessive transducer heating (Augustsson et al., 2011) and acoustic streaming (Wiklund et al., 2012). The acoustic streaming can be recognized as a steady fluid flow formed by the attenuation of an acoustic wave in the viscous fluid (Riley, 2001). The streaming effects are induced mostly by the boundary confinement of the chamber (Frampton et al., 2003; Nyborg, 1958) or by the absorption of acoustic energy by the bulk fluid (Cosgrove et al., 2001; Eckart, 1948). The streaming effects can be problematic for ultrasound trapping if left uncontrolled (Bernassau, Glynne-Jones, et al., 2013). An overview summary of non-contact particle handling techniques is listed in Table 2.1 (adapted from Qiu, Wang, et al., 2014).

To compensate for intrinsic limitations of different manipulation technologies, as well as to explore new possibilities, research has been conducted on combining different particle handling methods. One typical example is the technology developed as fluidic force microscopy (FluidFM) that combining hydrodynamic methods with conventional AFM. The key apparatus is an altered hollow AFM cantilever with a sub-micrometre size aperture at the tip, controlled by a pressure addressed fluid delivery system. The FluidFM technique is able to pick and place single cells, and inject fl volumes of liquid directly into the cells (Guillaume-Gentil et al., 2014). Another example, combining optical tweezer and DEP, is optoelectronic tweezers (OET) that produce optically-addressed DEP force for dynamic manipulation of particles following complex patterns. The technology uses photosensitive electronics to create a dynamic, localized DEP field for particle manipulation while using the optical beam with intensity 100,000 times smaller than conventional optical tweezers to reduce the photo-toxicity of the light beams (Ohta et al., 2007).

Table 2.1 Comparison of major non-contact particle handling technologies.

	Hydrodynamic Methods	EP	DEP	Magnetic Tweezers	Optical Tweezers	Acoustic Tweezers
Typical particle sizes for handling	Less than 1 µm to hundreds of µm	Tens of µm	Tens of µm	Less than 1 µm to tens of µm	Less than 1 µm to tens of µm	Tens of µm to hundreds of µm
Typical force scale	pN	pN	pN	pN - nN	fN - pN	pN - nN
Label-free	Yes	Yes	Yes	No	Yes	Yes
Key physical parameters for particle differentiation	Hydro-dynamic focusing force	Particle charge density	Electric permittivity / Frequency of AC electric field / Electric field strength	Suscepti-bility / Magnetic field strength	Refractive index	Density and compressi-bility
Manipulation spatial resolution	Low	Medium	Medium	Medium	High	Low
Operating field range	Long	Short	Short	Short	Short	Long
Challenge of system integration	Low	Low	Low	Low	High	Low

Because of the advantage of operating robustness and ease of integration, acoustic tweezers have gained great interest to provide a field complementary to other force fields for enhanced device behaviour. Glynne-Jones et al. summarised the combination of acoustic fields with other non-contact manipulation technologies, such as gravity forces, hydrodynamic forces, DEP, magnetic forces and optical forces for particle differentiation and manipulation (Glynne-Jones and Hill, 2013).

Incorporating conventional ultrasound array technology into acoustic tweezers has greatly enhanced the controllability of the acoustic gradient field for complex particle patterning and manipulation. Dynamic, reconfigurable acoustic fields can be created and controlled by direct modulation of excitation signals applied to individual transducer elements in a source array. Computer-addressed electronics such as microcontrollers or

FPGAs are competent for this task, allowing the flexible adjustment of transducer signal frequency, phase and amplitude for acoustic field shaping. As such a project, “Electronic Sonotweezers” aimed to create electronically controlled, ultrasonic transducer array-based acoustic tweezers for particle trapping and manipulation. The necessary signal modulation methods will be discussed in detail in Chapter 3.

CHAPTER 3 ELECTRONICS CONSIDERATIONS FOR SONOTWEEZERS

3.1 Introduction

The purpose of this chapter is to give a review and discussion of the technologies relevant to the electronics design involved in this thesis. The chapter starts with a general view of Sonotweezer and the requirements for the electronic design, followed by a review of conventional electronic technologies that are relevant to Sonotweezer devices. The review includes array technologies in ultrasonic imaging, programmable electronics, and ultrasound pulse generators. Consideration of ways to select the proper digital and analogue electronics is discussed as well.

3.2 Sonotweezer Devices and Electronics

3.2.1 Sonotweezer Devices Taxonomy

The concept of Sonotweezers cover a wide range of piezoelectric devices generating BAW for diverse microparticle manipulation applications, hence it is useful to summarize different type in a collective fashion, as shown in Table 3.1, in which the categorization is based on the piezoelectric device complexity (single element or array) and manipulation dimensionality (from 0.5-D to 3-D). This taxonomy, developed originally by Démoré (Démoré, 2010) is a helpful reference for designing the electronics, considering the complexity of the transducers and device functionalities. It should be noticed that in Table 3.1, 0.5-D manipulation dimensionality refers to the simple phenomenon of particle concentration at pressure nodes in an USW field.

Table 3.1 Taxonomy of Sonotweezer devices. Lateral axis represents the device complexity and horizontal axis represents the manipulation dimensionality. The transducer arrays used for electronics demonstration are highlighted with dashed lines.

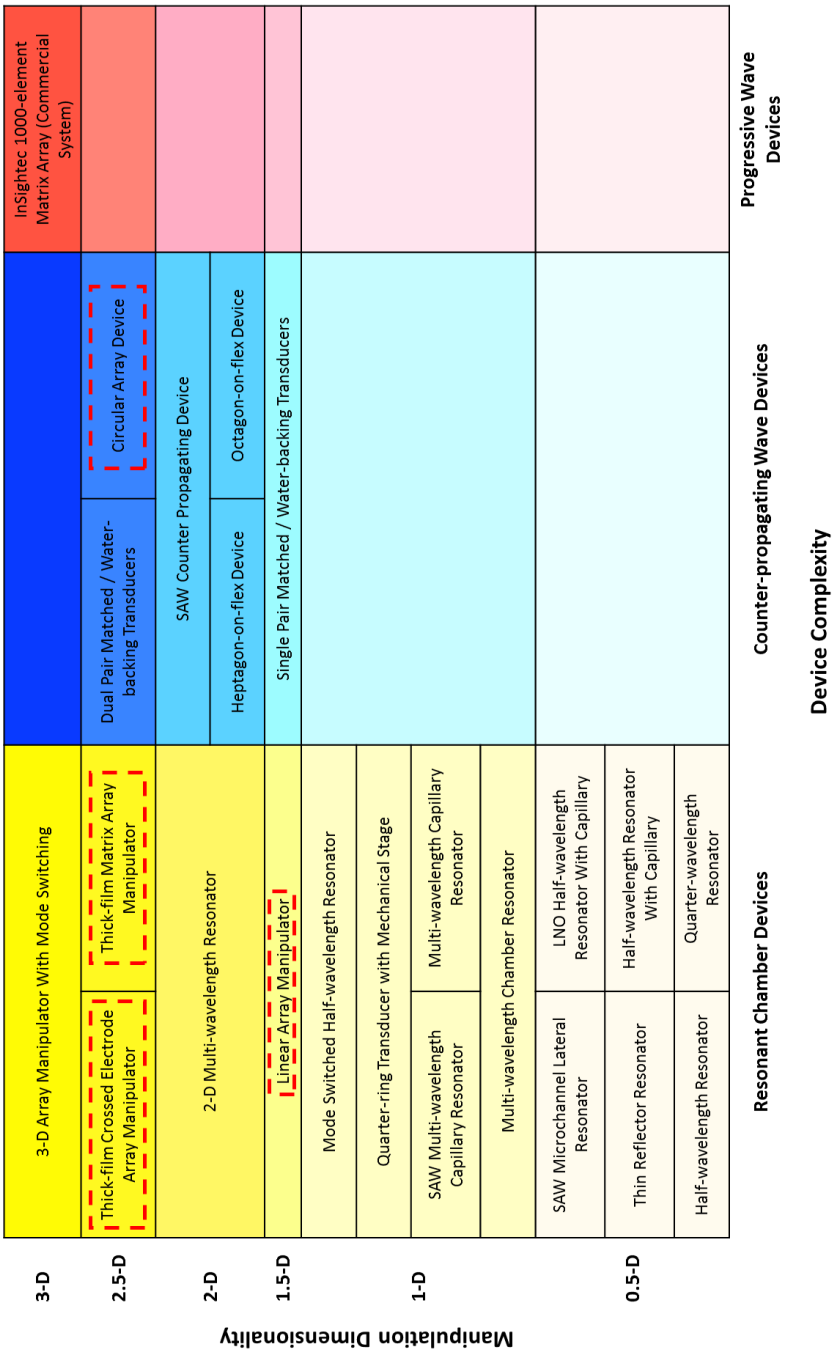

In this thesis, the design of the electronic system was based on the investigation of specific devices with representative functionality, discussed in detail in Chapter 5 and 6. The typical devices considered in the thesis are listed as following:

- Circular array (2.5-D, Counter-propagating Device), discussed in Chapter 5.

- Linear array lateral manipulator (1.5-D, resonant chamber device), discussed in Chapter 6. 2-D matrix array (2.5-D, resonant chamber device), discussed in Appendix D.
- 2-D Crossed-electrode array (2.5-D, resonant chamber Device), discussed in Chapter 6.

3.2.2 System Level Design Considerations

The ultrasonic transducers of Sonotweezer devices are either single element or arrays. Although single element transducers are easy to implement for trapping (0.5-D manipulation), they lack the ability to direct the particles freely in 1-D or 2-D. Hence the ultrasonic array structure is preferred and the primary consideration for electronics is the capability to generate multi-channel outputs. Moreover, for the purpose of developing "all-singing-all-dancing" Sonotweezer devices, ultrasound arrays with the control electronics should allow for great dexterity for configuring all the transducer elements simultaneously under a programmable manner. In addition, sufficient power is required to excite the transducer piezoelectric elements to create USW field with high enough acoustic energy gradient to allow Sonotweezing. Considering these contributing factors, an architecture of the electronic system to complement Sonotweezer devices is proposed and illustrated in Figure 3.1.

The key structures of the electronic system in Figure 3.1 are the digital and analogue electronics. As the requirements include array driving dexterity, a digital logic stage is essential to perform various controls. At a higher level, the electronics will be configured for different functions based on the specific acoustic models of different Sonotweezer devices. At the top level, the user will interact with the device via customized control panels realised within personal computer (PC) software, and typically observe real-time particle manipulation through microscope cameras. Common application program interfaces (APIs) are used between the layers to translate the commands from the users into the necessary parameters for different physical layers. Moreover, there could be sensors added at each layer to provide feedback to allow control correction and automation. Detailed discussion of the system development for different Sonotweezer devices can be found in Chapters 5 and 6.

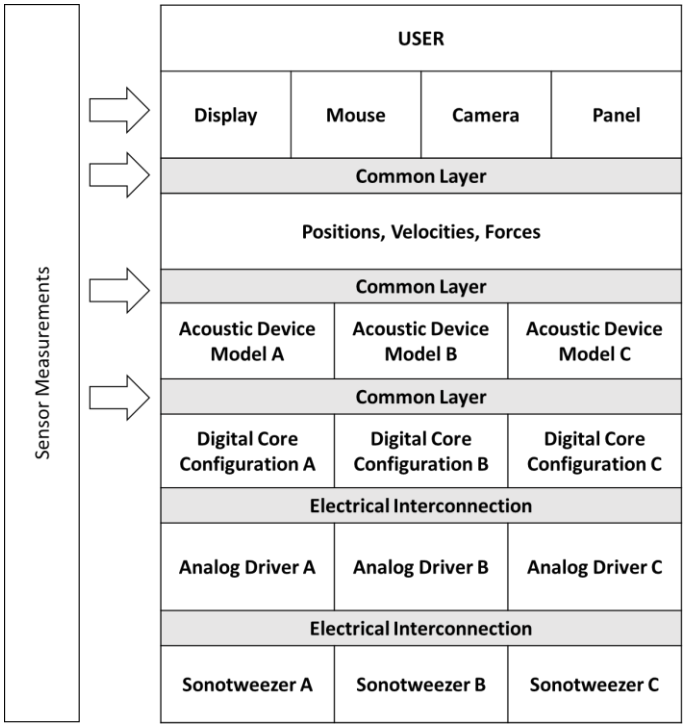

Figure 3.1 Top level system architecture for electronic Sonotweezer devices. Design courtesy of Martin Curran-Gray.

3.3 Ultrasound Transducer Array Technology

3.3.1 Ultrasound Transducer Arrays

Ultrasound imaging arrays enable acoustic images to be obtained without the need of movement of single element transducers, and they can also work at high frame rates to avoid distortion of rapidly moving objects such as those in the heart (Cobbold, 2007b). Generally, a 1-D array can offer real time 2-D images, and a 2-D array can offer real time 3-D images, through with the associated cost of increased element population and signal processing complexity. There are also intermediate steps between 1-D and 2-D arrays, with some control of the focus in the elevation plane, without requiring a large number of active elements (Whittingham and Martin, 2010). Commonly used array structures for ultrasound imaging are shown in Figure 3.2. Depending on the ability to perform beam steering, focusing, apodization and aperture control, the array geometry can be classified as 1-D, 1.x-D and 2-D (Cobbold, 2007b). As microparticles can be picked up and

manipulated by ultrasound beams, the features of beam control with arrays are important for Sonotweezer applications.

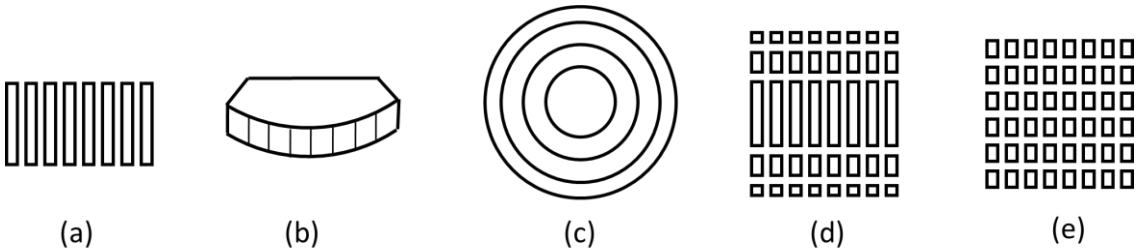

Figure 3.2 Illustrations of conventional 1-D and 2-D ultrasound array geometries (adapted from Qiu, 2014a): (a) 1-D linear (b) 1-D curvilinear array (c) annular array (d) 1.x-D array (e) 2-D array.

In Figure 3.2 (a), a linear array consists of transducer elements arranged in a 1-D line with the element pitch usually less than one wavelength of the ultrasound that propagates in the medium to which it is coupled. The curvilinear array in Figure 3.2 (b) is similar to a linear array, with the elements arranged along a contour either convex or concave. The annular array in Figure 3.2 (c) is another type of 1-D array consisting of concentric ring-shape elements, each with the same area to aid electrical impedance matching. Both linear and curvilinear 1-D arrays are able to perform electronic beam steering, but this is not possible for the annular array. Figure 3.2 (d) shows a 1.x-D array, which allows control of the focus in the beam elevation plane. In Figure 3.2 (d) the 2-D array offers flexibility for steering the beam in 2-D, allowing 3-D ultrasound imaging. However this type usually requires a large element count, as well as an increased cost for fabrication because of the difficulty of electrical connection, and complex control electronics.

3.3.2 Ultrasound Beamforming

Ultrasound arrays as shown in Subsection 3.3.1 are widely used for medical imaging. In ultrasound imaging, the ability to steer and focus the ultrasound beam during both transmission and reception is essential for obtaining high quality real-time images. The highest resolution is obtained when the ultrasound waves from all the elements are focused at a single point. Both transmitting and receiving beams can be focused and steered, by implementing delays in the electrical signals applied to or recorded from the array elements (Lay, 2011).

A. Transmitter Beamforming

Transmitter beamforming refers to focusing and steering the beam generated by the ultrasound transducer array. Principles for beamforming can be illustrated as shown in Figure 3.3. Initially the array elements are assumed as point sources. As shown in Figure 3.3 (a), if each element of the active aperture is pulsed simultaneously, the resultant wavefront is planar and parallel to the transducer surface. To steer the beam, if the excitation pulse for each element is delayed by a constant period of time after preceding element (equivalent to phase delay in CW), the transmitted wavefront will propagate at an azimuthal steering angle, as shown in Figure 3.3 (b). Beam focusing along the axis perpendicular to the array aperture can be achieved by adding delays mirrored symmetrically around the central element, as shown in Figure 3.3 (c). Combining the steering and focusing techniques, the ultrasound beam can be controlled to scan the target area sequentially, as shown in Figure 3.3 (d).

B. Receiver Beamforming

Similarly to transmitter beamforming, a receiver beamforming system is required to focus the backscattered signals received by a transducer array. The receiver beamforming algorithm is typically known as “delay-and-sum”, or “dynamic focusing”, to steer and focus the received beam. The basic idea of dynamic focusing is that, as the scattered wave arrives at array receive aperture, the signal recorded at each transducer element has a delayed applied corresponding to the exact amount that could focus the receive aperture at the scatterer where the signal originated (Cobbold, 2007b). The significant advances in high speed ADCs and parallel computing hardware such as FPGAs and digital signal processors (DSPs) in recent twenty years have allowed digital beamforming to be implemented for ultrasound image reconstruction at high frame rates. Figure 3.4 illustrates an architecture of a typical commercial system available in the 1990s with 128 channels for receiver beamforming.

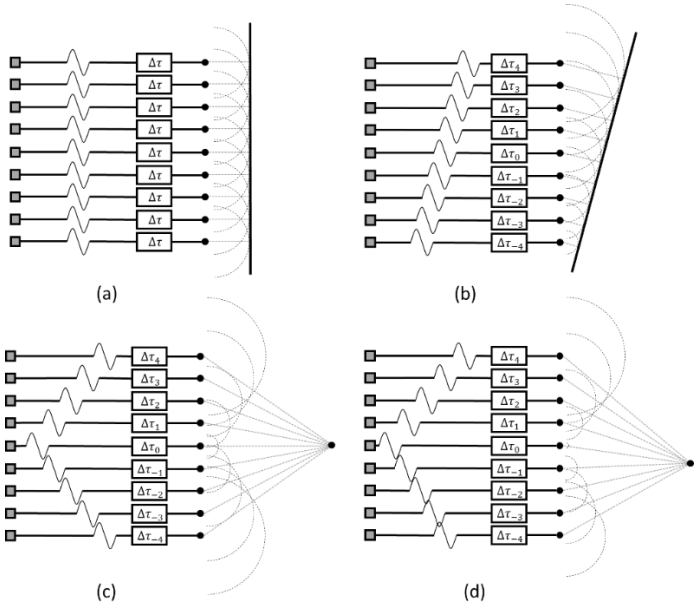

Figure 3.3 Diagram illustrating diagrams of ultrasound array transmitter beamforming (adapted from Cobbold, 2007). (a) Excitation signals with no delay between elements generate a wavefront parallel to the array aperture. (b) A plane wavefront is steered at an angle to the array aperture with constant delays between elements. (c) The beam can be focused with symmetric delay patterns for successive array elements. (d) The beam can be focused as well as steered when techniques (b) and (c) are combined.

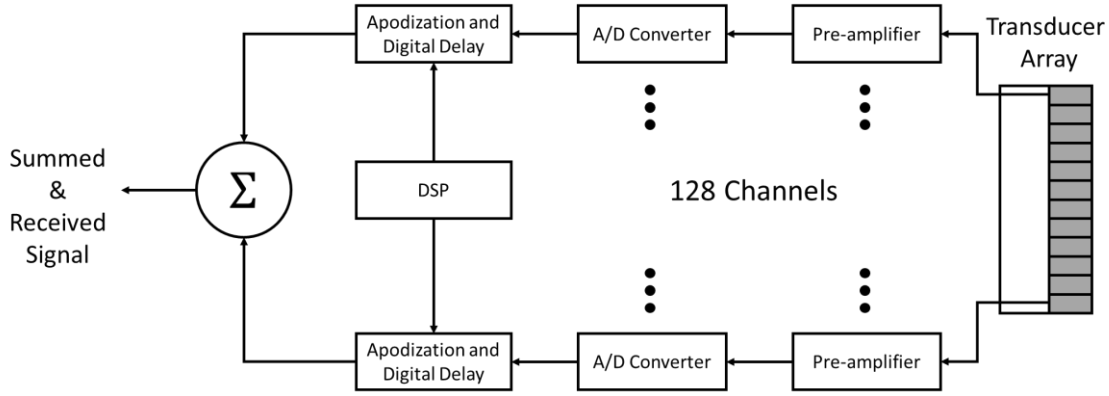

Figure 3.4 Simplified block diagram illustrating a digital beamforming receiver system with a low-noise preamplifier, a high speed analogue to digital converters (ADC) (40 MHz, ⩾ 12 bit), and a digital delay line (shift register) controlled by a DSP (adapted from Cobbold, 2007).

3.4 Digital Programmable Electronics

3.4.1 MCU

MCU is a term used to describe the use of a microprocessor as a central processing unit (CPU), with other assorted functional circuitry like timers, memories and configurable

input/output (I/O) ports, for dedicated purposes such as process management and instrument control (Horowitz and Hill, 1989a). An illustrative diagram of the internal function blocks of an MCU is shown in Figure 3.5. The major blocks in a typical MCU include CPUs, memories such as read-only-memory (ROM) and random-access-memory (RAM), I/O ports and oscillators. The CPU is the central unit for monitoring and controlling all the data processing within the MCU. ROM permanently stores a program to be executed, and a program counter can access the instructions stored in the ROM in a serial manner. RAM is a volatile memory unit to temporarily store the data and intermediate results generated during MCU operations. For the I/O ports, each MCU has one or more registers connected to the relevant pins. These I/O ports are configured as input or output by internally-connected special function registers (SFRs). Integrated oscillators are the sources of clocks for synchronizing the MCU operation. Modern, inexpensive but versatile MCUs are the cores of many electronic systems including dedicated embedded solutions for industrial control, automobiles, handheld electronic devices, medical instruments and many others.

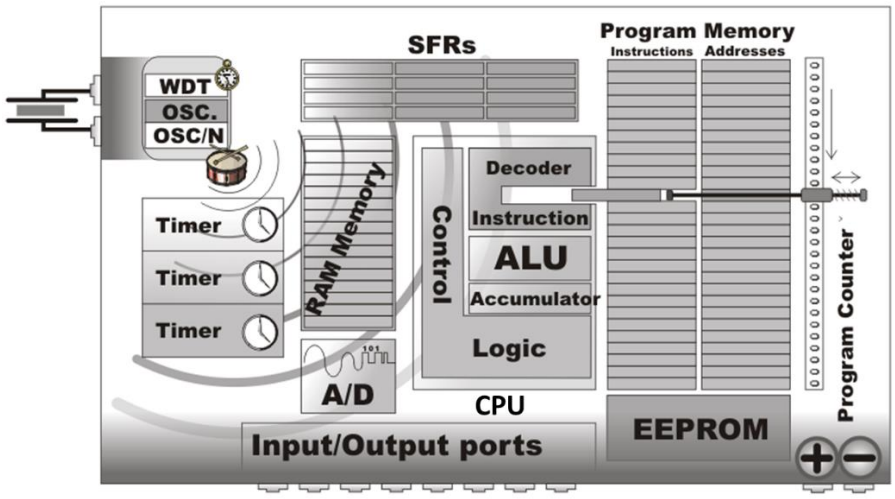

Figure 3.5 Functional block diagram of a typical microcontroller architecture (from Verle, 2014).

3.4.2 ASIC

ASICs are ICs designed for particular applications in specified systems. A modern ASIC can include an entire subsystem as a system-on-chip (SoC), including a MCU, memories, peripherals, other custom logic, etc. There are four major generally accepted categories of ASICs with increasing complexity: gate array devices, standard cell devices, structural

ASICs and full custom parts (Maxfield, 2008). The gate array ASICs provides arrays of unconnected, dedicated logic cells, and the interconnections can be defined by synthesis tools, and realized by metallization process. Standard cell ASICs can be created from vendor provided libraries with dedicated functional blocks as intellectual properties (IPs), including software- and hardware-based "macros", such as RAM and ROM blocks, clock generators, boundary scan logic, etc. Structural ASICs are similar to the gate array ASICs, providing a much smaller non-recurring expenditures (NRE). The structural ASIC tile has a higher level of sophistication, by predefining the majority of the metallization layers (Maxfield, 2008). A full-customized ASIC design defines all the photolithographic layers of the device. This approach is pursued if there is no suitable existing cell libraries meet the design specification. The benefits usually include reduced circuit area, integration of analogue and digital components, and controlled power consumption. However the disadvantages can include increased NRE, more complexity in the design tools and higher design skill requirement (Or-Bach, 2014).

3.4.3 FPGA

An FPGA is a kind of programmable logic device that could be reconfigured after fabrication with user-defined logic. FPGAs are generally configured with the hardware description language (HDL), which is similar to that used for the ASICs. An FPGA is a highly flexible device as it contains programmable logic components recognized as "logic blocks", and reconfigurable interconnections to wire the blocks together. The FPGA industry started with devices such as programmable read-only memories (PROMs) and programmable logic devices (PLDs) ("History of FPGAs"). The first commercially available FPGA was invented in 1985 ("History of Xilinx, Inc."), and since then, the FPGA industry has gain rapid growth with applications in many fields. Although the functionalities of the devices are similar, different FPGA vendors have their own technical nomenclatures. As a Xilinx FPGA is used in this thesis, the technical terms in the following text are based on Xilinx terminology.

A. FPGA Device Internal Structures

The basic structure of an FPGA typically has three types of element, as shown in Figure 3.6:

- **Logic blocks (called configurable logic blocks by Xilinx)**: For Xilinx FPGAs, typically a configurable logic block (CLB) contains a few slices, and each slice incorporates a few logic cells. Each logic cell consists of a look-up table (LUT), a flip-flop (FF), and some other logic devices such as multiplexers ("Spartan-3A FPGA Family: Data Sheet", 2010). The logic cell structure is equivalent to that of the SRAM (Static random-access memory) (Horowitz and Hill, 1989b).
    - LUT: This element is a truth table that stores different output values for the associated input combinations. In FPGAs typically there are 4-input or 6-input 1-bit LUTs.
    - Flip-Flop (FF): This register element stores the results of the LUT.
- **I/O blocks (IOB)**: These physically available components are used as ports to transfer data in and out of the FPGA.
- **Programmable Interconnects**: These components are used to make interconnections between CLBs and IOBs.

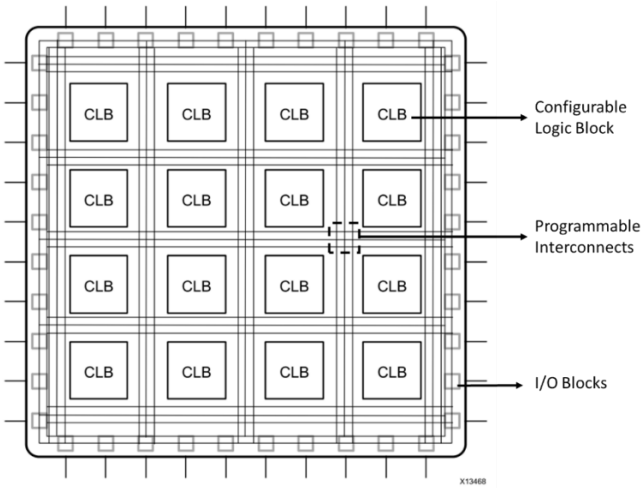

Figure 3.6 An illustration of the basic FPGA internal structure (adapted from "Introduction to FPGA Design with Vivado High-Level Synthesis", 2013).

It should be noted that the LUT-based logic cells in CLBs are the most basic logic components for FPGA functionality. An LUT can be configured as the equivalent of a

wide range of combinational logic, ranges from a simple inverter (one gate) to a complex logic circuit containing many logic gates.

B. Circuit Design and Implementation with FPGA

Modern FPGA designs and implementations are realized with software toolkit provided by the commercial vendors. The typical process, which was followed for creating the FPGA projects involved in this thesis, can be summarized as below ("Xilinx Synthesis and Simulation Design Guide", 2010):

- **Design creation**: Define the behaviour of the circuit by providing HDL source codes or schematic designs. Popular HDLs are VHDL and Verilog.
- **Synthesis**: Within an electronic design automation (EDA) tool, the design is synthesized at register transfer level (RTL) level, which is an abstraction level that models the synchronous digital circuit in terms of the flow of signals through hardware registers and combinational logic components.
- **Implementation**: A technology-mapped netlist is generated specifically for the physical FPGA device being used, through a process called place-and-route. A bit stream file is generated when the process is completed.
- **Configuration**: The FPGA can be configured as the bit stream file is transferred into the FPGA in real-time, or it can be configured after power-up if the bit stream file is transferred into an external memory device such as a PROM.
- **Simulation**: A functional simulation needs to be carried out after the design is created to verify the circuit functionality, and a timing simulation is an important process to verify circuit performance after the worst case place-and-route delays are calculated.

3.4.4 Strengths and Weaknesses of Using MCUs, ASICs and FPGAs

ASICs can provide a full customized circuit design capability with controlled circuit area and power consumption. But the development process is incredibly expensive, time-consuming, lack of flexibility and resource-intensive (Maxfield, 2014). Both MCUs

and FPGAs are good candidates for developing Sonotweezer driving systems, with the key issue being that all these devices are programmable for fast prototyping. Generally MCUs are cheaper and easier to use. However considering the requirements of multichannel CW signal generation, and the need of reconfigurable electronics to work with different types of Sonotweezers, FPGAs have important advantages. Firstly, as shown in Figure 3.6, the internal architecture of an FPGA consists of many similar functional blocks distributed in a nearly repeated manner. This structure allows the FPGA to work in a concurrent mode, in which multiple circuits carry out their functions simultaneously in different places in the FPGA. This concurrent nature makes the FPGA ideal for parallel operations, with the advantage of high I/O pin-counts for multichannel outputs. Secondly, because of concurrent processing with many simple circuit blocks, FPGAs can operate at very high clock speeds, from tens of megahertz up to gigahertz. Thirdly, differently than MCUs with their fixed internal hardware, FPGAs are highly flexible, and can be implemented into almost any digital hardware configuration with a wide range of complexities (Bishop, 2009).

On the other hand, its versatility makes the FPGA a relatively complex device to use (Sarwar, 2012). With high pin-counts, unlike the easy-to-solder TSSOP (Thin Shrink Small Outline Package), SOIC (Small Outline Integrated Circuit) and QFP (Quad Flat Pack) packages used for MCUs, contemporary FPGAs are normally supplied in BGA (ball grid array) packages, which are difficult to implement on printed circuit boards (PCBs), instead requiring expensive equipment for circuit construction. Another issue is that unlike MCUs using a global +5 V power supply for the whole IC, an FPGA requires different voltage levels for different internal components. This means that voltage regulation ICs must usually be associated with FPGA implementation. Moreover, though reconfigurable, FPGAs are volatile so external memory is essential to store the configuration data. Also there are no internal oscillators embedded in the FPGA, so external oscillators are required.

All these extra requirements increase the complexity of FPGA implementation. However, there are development boards with embedded FPGAs available to reduce the difficulty of the set-up process, to allow the user to focus specifically on the circuit configuration itself. At time of writing, there are also advanced options supplied by FPGA vendors integrating MCUs and FPGAs as SoC FPGAs (Zynq-7000, Xilinx Inc., San Jose, CA, USA). There

are also HDL-based MCUs packaged into soft IP cores (MicroBlaze Soft Processor Core, Xilinx Inc., San Jose, CA, USA), which can be implemented directly within HDL designs.

3.5 Ultrasound Pulse Generators

This section reviews of the technologies involved in the design of electronic ultrasound pulse generators, or ultrasound pulsers. One widely-adopted circuit topology is the "push-pull" structure that can generate pulses with both high positive and negative voltages. In this thesis, considering the high channel-count of the array driving system, the fact that it mush run in CW mode to maintain the USW field, and that the required excitation voltages are low, the ultrasound pulse generation circuitry is maximally simplified into an array of operational amplifiers (op-amps). Finally, analogue and digital approaches for AC signal generation and transformation are discussed.

3.5.1 Pulsers for Ultrasound Transducers

For driving ultrasound transducers for applications such as imaging, a high peak power electrical signal is required to make the piezoelectric element vibrate with a high surface displacement. Normally this is achieved by generating the pulses with a high voltage swing and sufficient output current for the load impedance. In practice, there are already established circuit architectures optimized for the purpose. They are often recognized as the "push-pull" circuits using two complementary bipolar junction transistors (BJTs) or metal-oxide-semiconductor field-effect transistors (MOSFETs) to source and sink current from a positive and a negative voltage supply respectively. A bipolar voltage can be generated with the amplitude approaching the full power supply voltage rail range.

A typical example is the output circuit used in conventional op-amps. Figure 3.7 shows the schematic of the widely used op-amp LM741. In the output stage, the BJT Q14 and Q20 comprise a class AB push-pull emitter-follower amplifier that can generate output voltage within V^+ and V^-.

The same design has been adopted to create unipolar or bipolar pulsers for ultrasound applications. Consideration of ultrasound pulser design focuses on two factors: output

voltage and frequency. The generated pulse has a certain voltage amplitude, measured $V_{peak\text{-}peak}$, and a centre frequency, $f = 1/2T$, for a bipolar pulse, where T is the length of a half pulse. Normally, discrete transistors are used, allowing full control of the degree of amplification and switching time for high-frequency ultrasound applications, which usually require the switching time to be under 10 ns (Lay, 2011). One popular circuit shown in Figure 3.8 (a), as a push-pull amplifier, comprises two complementary MOSFET switches which drive the load in turn with precise timing by control logic. Single-chip pulsers have become available commercially in recent years, allowing minimum external circuitry and guaranteed performance. A typical example is the HV738 (Microchip Technology, Chandler, AZ, USA) four-channel high speed ultrasound pulser IC, as shown in Figure 3.8 (b). It offers up to ± 65 V output and a maximum 20 MHz frequency, with ± 750 mA and ± 110 mA source and sink current for pulse mode and CW mode respectively. This IC comprises a pair of current source drivers charging the gate capacitors of N-channel MOSFETs (NMOS) and P-channel MOSFETs (PMOS) to allow fast switching between positive and negative voltages at the outputs.

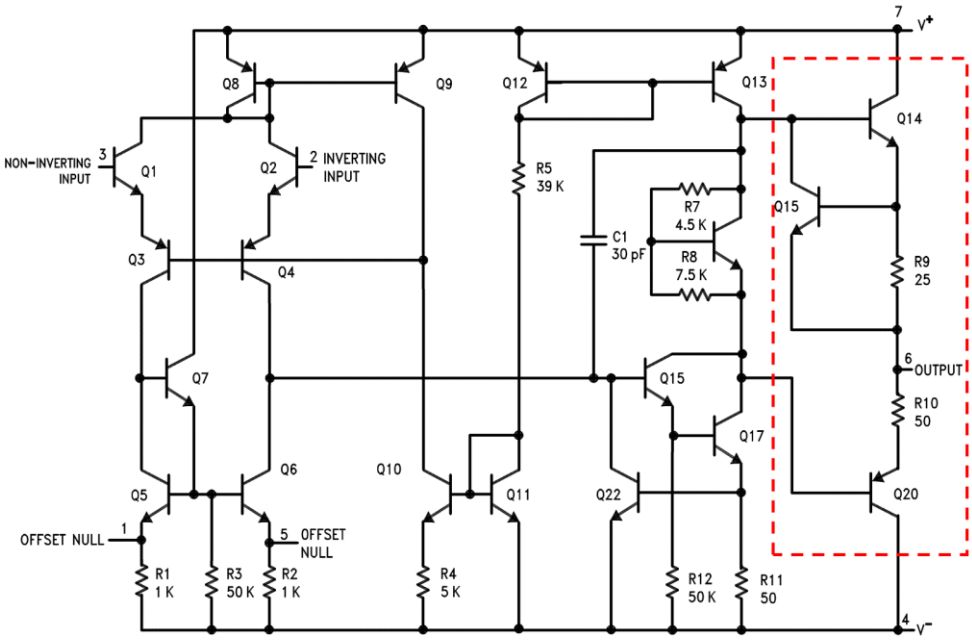

Figure 3.7 The Schematic of op-amp LM741 (from "LM741 Operational Amplifier", 2013). The red dashed-line surrounds the "push-pull" configuration output stage.

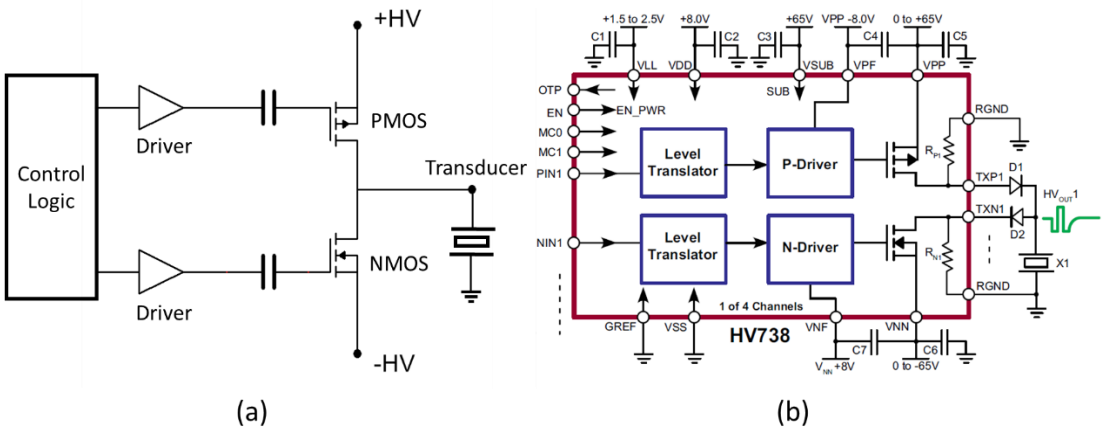

Figure 3.8 Examples of ultrasound pulser circuitry. (a) Typical ultrasound pulser topology. (b) HV738 application circuitry and internal circuit diagram (from "Four-Channel, High Speed, ±65V 750mA Ultrasound Pulser", 2011).

3.5.2 Operational Amplifiers

Op-amps are often used in electronic systems to amplify small signals received from sensors. Originating from analogue computers, they are also still widely used to perform mathematical operations with signals, such as summing, subtraction, differentiation and integration for linear and non-linear circuits.

Ideally, the open loop gain of an op-amp is considered infinite, with practical gain values in the range 10^5 – 10^6, so they are used with negative feedback loops with specific gain to maintain stable behaviour. In this thesis, op-amps are utilised as power amplifying devices for ultrasound transducer excitation. Ideal op-amps are considered as having the following characteristics (Horowitz and Hill, 1989c):

- Infinite input impedance (differential or common mode);
- Zero output impedance;
- Infinite voltage gain;
- Zero common-mode voltage gain;
- Zero output for zero offset voltage at the inputs;
- The potential for instantaneous changes in output (i.e. infinite slew rate).

Depending on which connection is used as the signal input, typical op-amp circuits can be classified as inverting and non-inverting amplifiers, with the circuit routing and gain

equations shown in Figure 3.9. The gain of the amplifier is dependent only on the values of the closed-loop feedback resistors.

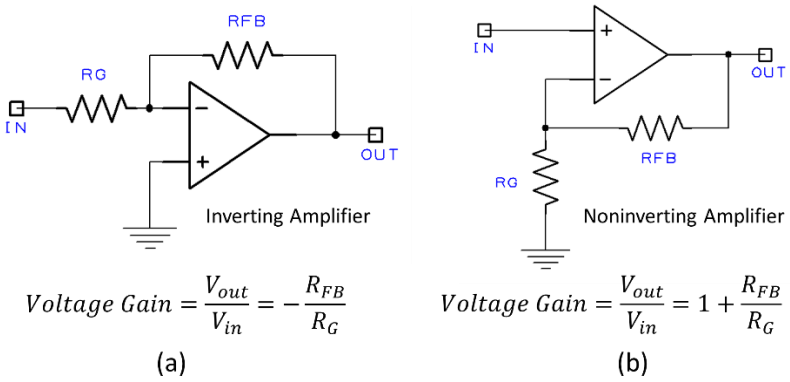

Figure 3.9 (a) Inverting amplifier and the gain equation. (b) Noninverting amplifier and the gain equation.

The above ideal conditions are very useful when sketching rough designs of op-amp circuits. In reality, these ideal conditions are impaired because of non-ideal op-amp intrinsic characteristics, and the effects of these limitations must be considered. A practical op-amp model is shown in Figure 3.10, which includes a dependent voltage source with an open-loop voltage gain, A, non-negligible input offset voltage, V_d, an input resistance, R_i, and an output resistance, R_o.

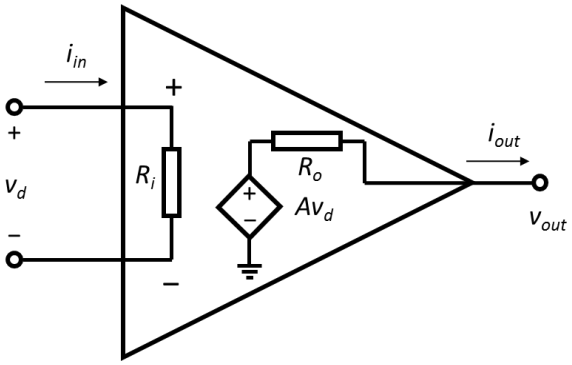

Figure 3.10 Detailed model of an realistic op-amp (from Hayt Jr. et al., 2002).

For Sonotweezers applications, relatively high output voltages are required up to 30 V_{pp}, and high maximum operating frequency, a few to tens of MHz, are required. Thus one of the most important practical parameters to look at is the slew rate. Because of limited slew rate, the maximum undistorted sine-wave output amplitude drops over a certain frequency, and the amplitude is limited to $A_{peak-peak} \leq SR/\pi f$, for a sine-wave with

frequency *f*, and slew rate *SR*. Another parameter is the maximum output current, which can reduce the voltage output for small load resistances (Horowitz and Hill, 1989c). More detailed discussions of the op-amp output current and slew rate are given in Chapter 5. Issues such as non-zero input offset voltage, input bias current and input offset current relate most strongly to the output amplitude precision and are less relevant for the applications in this thesis.

3.5.3 Waveform Generation and Transformation Methods

For nearly every electronic instrument, it is essential to have an oscillator or a waveform generator. Examples include regulated DC power supplies, digital multimeters, oscilloscopes, and almost all kinds of digital instruments such as counters and timers (Horowitz and Hill, 1989d). This subsection briefly reviews waveform generation and transformation methods that can be adapted for Sonotweezers applications.

A. Analogue Approaches – Oscillators

Analogue electronics for waveform generation can be in simple forms such as resistor-capacitor (RC) oscillators, inductor-capacitor (LC) oscillators and quartz-crystal oscillators, or in more complex forms such as 555 timer ICs and voltage-controlled oscillators (VCOs) with better accuracy and tunability.

RC and LC oscillators are easy to implement with discrete components, however they are lack of accuracy. On the contrary, highly accurate quartz-crystal oscillators lack tunability. Timer ICs like 555 timers use external resistors and capacitors to control the output signal frequency. They are widely used as compact devices with reasonable stability, e.g. 1%, and a wide voltage supply range from 4.5 V to 16 V (Horowitz and Hill, 1989d). However, they depend on the accuracy and stability of the external discrete components. Contemporary IC oscillators are available as VCOs, with the output frequency variable in some range according to an input DC control voltage. The VCOs normally use LC or RC oscillators for nominal frequency generation, and the frequency is changed with reverse-biased diodes or special purpose voltage-controlled capacitors in response to a tuning DC voltage. VCO ICs are widely used in telecommunication systems, however

they also rely on the precision of external components as well as voltage sources. There are also more advanced analogue technologies like phase-locked loops (PLLs) that use VCOs as the key component. They can offer very precise frequency tuning, but the circuitry is very complex and difficult to implement, especially for multichannel applications required in this thesis.

B. Digital Approaches

Fully digital frequency synthesizers have gained great interest because they are cost-competitive, high-performance, functionally-integrated and in small package with performance competitive with analog frequency synthesizers. A typical example is the direct digital synthesis (DDS) technology that can be implemented with programmable digital electronics. In the following text, DDS technology is discussed in detail, including advantages and disadvantages, as a potential candidate technology in a Sonotweezer system, is discussed in a great detail for its own advantages and disadvantages. A simpler alternative, i.e. an algorithm-based digital frequency divider, requires less hardware resources than DDS implementation, and is finally used for Sonotweezers. This approach will be introduced in the later text and fully discussed in Chapter 5.

a. DDS

DDS is a technique using digital data processing blocks as the means to generate frequency- and phase-tunable output signals referenced to a fixed-frequency precision clock source. The basis of the DDS architecture is that a reference clock is divided down by a scaling factor set from a programmable binary tuning word. As an alternative to the agile analogue frequency synthesizer, DDS has its own advantages, which can be understood as general advantages of digital-based frequency synthesizers (“A Technical Tutorial on Digital Signal Synthesis”, 1999):

- With the normal binary tuning word length of 24 – 48 bit, a DDS can achieve micro-hertz tuning resolution of the output frequency and sub-degree phase tuning capacity, all under digital control.

- Extremely fast switching (hopping) speed is possible in tuning of the output frequency and phase, without over/under-shoot or analogue-related loop settling time anomalies.
- Full-digital architecture eliminates the efforts of component aging and temperature shift found in analogue synthesizers.

The implementation of DDS technology can be understood as based on LUTs. The simplest form of a direct digital synthesizer can be implemented from a precision reference clock, an address counter, a PROM and a digital to analogue converter (DAC). The digital amplitude values that correspond to a complete cycle of a sine-wave are stored in the PROM. Hence the PROM acts as the sine-wave amplitude LUT (Figure 3.11). The address counter steps through each address of the PROM successively and the contents are read out into a DAC. The DAC then generates an analogue sine wave from the digital contents of the PROM. Practical DDS devices normally utilize mapping logic that synthesizes a complete sine wave from a 1/4 cycle of a complete sine period which is read back and forth through the sine wave LUT.

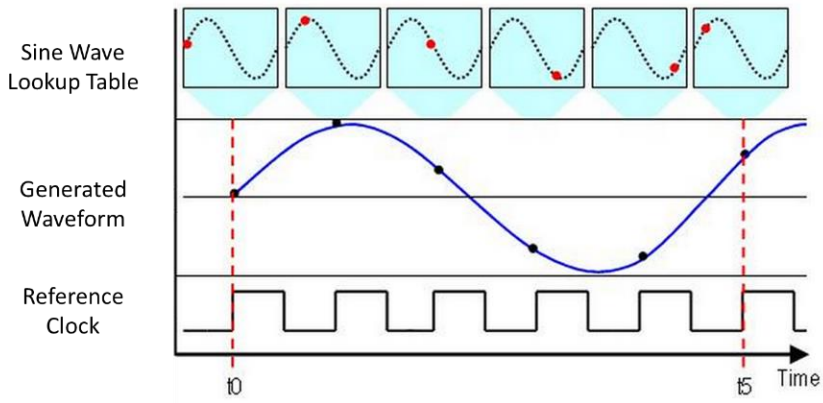

Figure 3.11 An illustrative diagram of the sine-wave LUT theory for DDS implementation (from "Understanding Direct Digital Synthesis (DDS)", 2013).

The output frequency from the DDS implementation depends on the frequency of the reference clock, and the sine wave step size stored in the PROM. Adjusting the reference clock is not easy for high speed switching between frequencies. Instead, it is useful to introduce a phase accumulator function into the digital signal chain, and the DDS core becomes a highly flexible numerically controlled oscillator for frequency tuning.

Figure 3.12 illustrates a frequency-tunable DDS system. An N-bit variable-modulus counter and a phase register combined in a tunable phase accumulator are implemented before the sine wave LUT. For a fixed reference clock frequency, the output frequency from the DDS is determined by the size of the address counter used to read the contents from the PROM. The phase accumulator function can be understood as reading a "phase wheel" in the DDS, as shown in Figure 3.13. The number of discrete phase points in the wheel is 2^N, determined by the phase accumulator resolution, N. The mode-M address counter designates the step size when reading the phase value, via the modulus parameter, M, and then a phase-to-amplitude LUT is used to convert the selected phases into sine-wave amplitudes. The digitized amplitude data are transformed into an analogue waveform through a DAC.

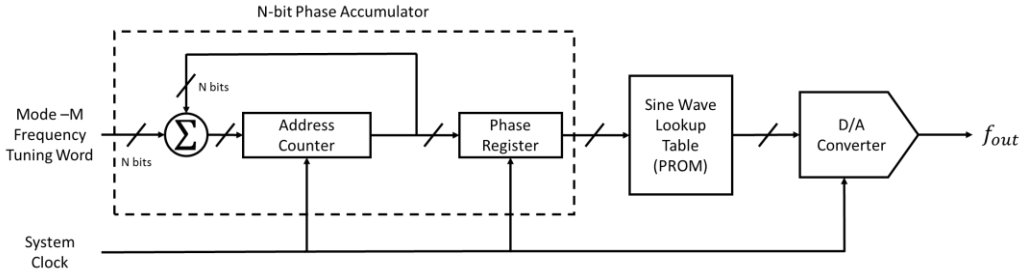

Figure 3.12 Block diagram of basic DDS architecture (adapted from "A Technical Tutorial on Digital Signal Synthesis", 1999).

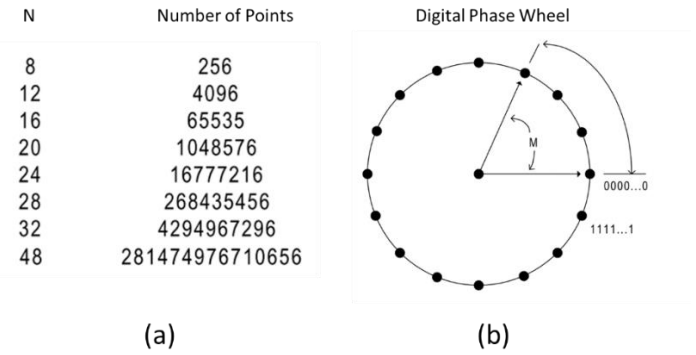

Figure 3.13 (a) Maximum frequency resolution is determined by the size of the N-bit phase accumulator. (b) Digital phase wheel representation. The parameter, M, controls the step size when reading the sine-wave LUT that, in turn, determines the output frequency (from "A Technical Tutorial on Digital Signal Synthesis", 1999).

With a mode-M counter implemented in the N-bit phase accumulator, sampling from a reference clock frequency, f_c, the DDS output frequency, f_{out}, can be expressed by:

$$f_{out} = \frac{M \times f_c}{2^N} \quad \textbf{(3.1)}$$

The size of *M* in the address counter can be controlled entirely through digital signals, hence the DDS architecture has very high "frequency hopping" speed for dynamic tuning. Moreover, a phase tuning word of a given size can be added to the phase accumulator to determine the phase shift of the output signal. As the shape of the output waveform is based on the amplitude values stored in the pre-programmed PROM, DDS can be easily implemented for arbitrary waveform generation, which is hard to realize with an analogue frequency synthesizer. It is also useful to note that, according to the Nyquist sampling theorem, the reference clock frequency needs to be at least twice the desired output analogue signal frequency, and in practice this multiple is usually higher than five. Thus, a very high-frequency clock signal is required when the DDS device is used in high-frequency applications.

Commercial DDS devices are available as ICs. Labelled complete-DDS, these include an integrated DAC function to provide analogue output signals. A typical example is the AD9854 (Analog Devices, Inc., Norwood, MA, USA). Based on the basic DDS architecture in Figure 3.12, this device contains additional digital blocks that perform various operations in the signal path, such as phase tuning, amplitude modulation, sine and cosine output, and frequency shift keying operation. However, such versatile devices must be packaged with high pin-counts and are thus not easy to implement in prototype circuitry. The AD9854 has 80 leads with 0.65 mm lead pitch, but can offer only four outputs ("CMOS 300MSPS Quadrature Complete-DDS AD9854", 2007). Hence the complexity and cost of circuitry will be hugely increased in multichannel implementations for Sonotweezer systems.

Apart from implementation of DDS with dedicated ICs, there are also DDS devices packaged as software IP cores. These are designed to include digital logic and functions, carefully packaged into forms similar to those of commercial ICs, with similar structures and complexity. Additional DACs are still needed to generate analogue waveforms. Typical examples of the DDS IP core are the ones offered by Xilinx, implemented as drop-in modules for various Xilinx FPGA families. The core offers quadrature output and

can be configured from a GUI-based core generator, and almost all the pins are reconfigurable for the adjustment of frequency or phase resolution, output dynamic range, channel information and various output noise shaping techniques. Figure 3.14 is a block diagram showing the primary architecture of a DDS IP core.

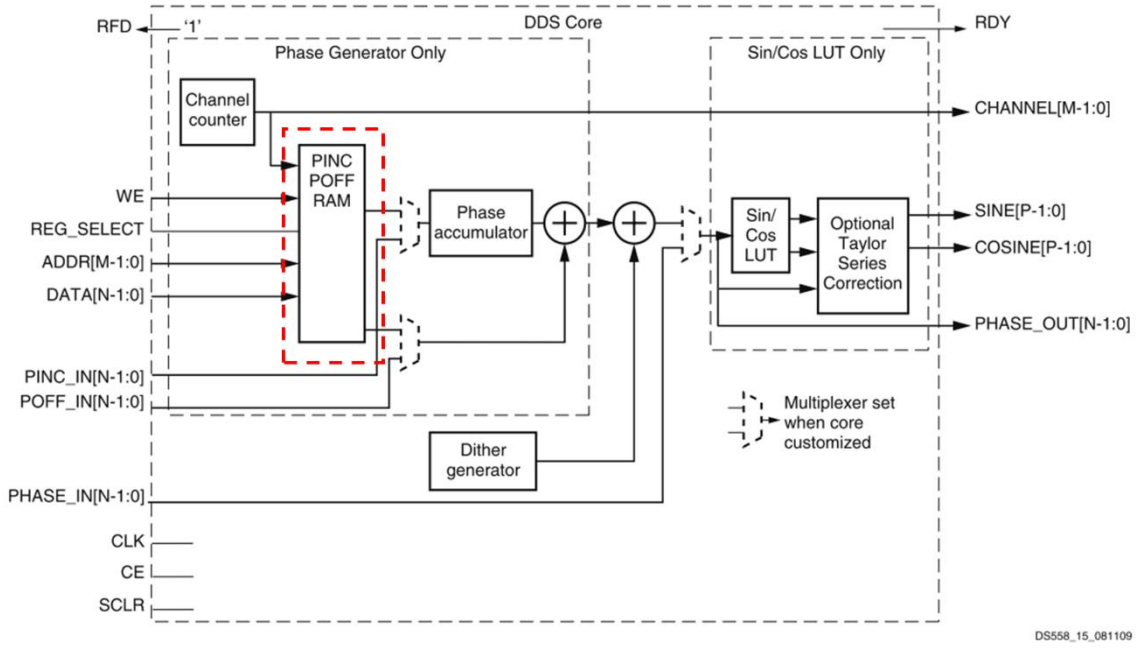

Figure 3.14 Core architecture from Xilinx DDS compiler (from "LogiCORE IP DDS Compiler v4.0", 2011). The frequency and phase modulation are controlled by the block *PINC POFF RAM* circled in red dashed-lines.

A software-based IP core was considered as a potential solution for Sonotweezer devices that require dynamic frequency and phase modulation functionalities. However, from detailed investigation of the Xilinx Spartan-3a FPGA development board at hand, some limiting issues were identified. The primary limitation is that only one channel is available per DDS core. Although the core can be implemented for multichannel applications with time-division multiplexing, additional multiplexing of the clock frequency and channel enable logic are needed.

Another limitation lies in the on-board DAC for generating MHz frequencies. The DAC provides on the FPGA development board is a LTC2624 quad DAC with 12-bit unsigned resolution (Linear Technology Corporation, Milpitas, CA, USA) which is representative of commercial devices. Data are transmitted to it through a Serial Peripheral Interface (SPI). Its maximum working frequency is 50 MHz, but with limitations such as serial communication and the Nyquist sampling theorem, the maximum frequency of the

analogue output that could be generated from the DAC was determined experimentally to be about 100 kHz, much lower than the required 1 ~ 10 MHz range. It is possible to use high speed DACs operating at hundreds of MHz to GHz but these fast devices are usually costly and have high pin-counts, as well as requiring high-frequency PCB design techniques for circuit implementation. Given the difficulties and limitations that have been highlighted, it was considered worthwhile to explore other more straightforward digital approaches that require less resources.

b. Algorithm-based Frequency Synthesizer

For digital electronics, as a typical example, the power-of-two or fractional-2N (N is an integer and N $\geqslant$ 1) clock divider is easy to implement with basic sequential logic components such as D-type flip-flops (DFFs). Programmable electronics such as FPGAs are very-effective for implementing such circuits, simply by providing the behavioural description of the circuit performance. In the following text, and as shown in Figure 3.15, a demonstration of how to generate half and quarter frequencies from a fundamental given clock signal, realized within the Xilinx EDA tool from a behavioural circuit model built with VHDL. The verified circuit could be readily implemented onto any FPGA platform, with the process discussed in Subsection 3.4.2.

Considering the efficiency of implementing frequency dividers with FPGAs, it is worthwhile to explore methods for versatile frequency synthesis based on HDL coding algorithms. Among the literature and industrial application notes can be found many approaches to realize arbitrary integer-N or fractional-N frequency dividers (Brennan et al., 2006; Gu et al., 2011; Hou et al., 2012; Kovacheva et al., 2014; SHEN et al., 2013; Tian et al., 2009; Wang et al., 2007; Zhang and Cheng, 2013). It is relatively easy to build an integer-N divider but to generate a frequency with high-order precision and tuning flexibility, it is better to consider an arbitrary fractional-N divider, with the form of ($N + K/M$), where N, K, M are all integers and $N \geqslant 2$, K, $M \geqslant 1$, with tunable values. Detailed information on the construction of a fractional-N frequency divider using HDL algorithms is further discussed in Chapter 5.

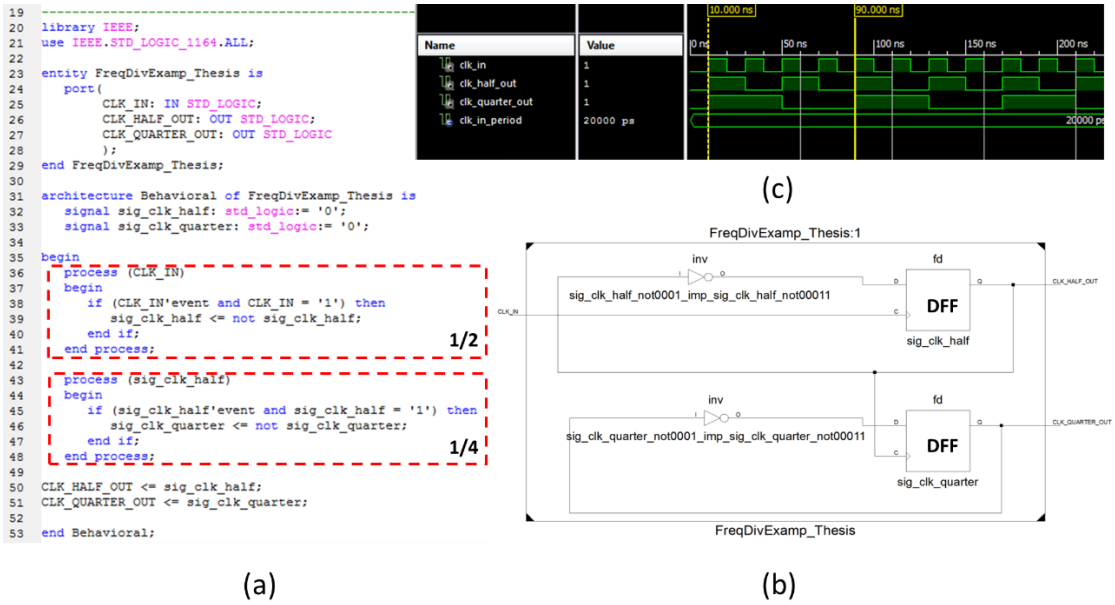

Figure 3.15 An example of a power-of-two frequency divider implementation with VHDL algorithms. The platform is Xilinx ISE Design Suite. (a) VHDL code for circuit behaviour description. The red dashed-line blocks are the descriptions for 1/2 and 1/4 frequency dividers. (b) Schematic circuitry generated from the VHDL codes. The circuit function is implemented with two cascaded DFFs. (c) The timing diagram of the 1/2 and 1/4 frequency outputs.

3.6 Conclusions

In conclusion, this chapter examined various electronic technologies that are useful for driving Sonotweezer devices. Conventional electronic beamforming technologies were outlined, and transmission beamformers were identified as particularly relevant. Depending on the Sonotweezer device and operational requirements, beamforming with different level of complexity should be considered.

For reconfigurable electronics, it is reasonable to conclude that an FPGA is a better option than an MCU because of its parallel execution and fast operation speed. However, considering the complexity and the cost of building customized FPGA implementation PCBs, it is necessary to source an FPGA development kit for research purpose.

For the analogue driver stage, amplifiers are essential components. Various ultrasound pulser designs were considered in Section 3.5. Conventional pulser designs with discrete transistors or pulser ICs can offer tens of volts peak-to-peak and pulses durations in nanoseconds, however these circuits become complex when containing multiple stages.

Sonotweezer devices mostly operate in CW mode to generate stable acoustic fields for trapping, and much less acoustic energy is required when handling biological cells. Thus, in this thesis, a simpler circuit topology is used, with operational amplifiers and current buffers forming the complete amplifier stage. Details of the circuit design and characterization are discussed further in Chapter 5.

Finally, investigation of methods for waveform generation and transformation in Subsection 3.5.3 drew the conclusion to use algorithm-based frequency dividers. Although DDS is an attractive technology with digitally-controlled precise frequency and phase tuning ability, its implementation is limited by the need for relatively high frequencies in Sonotweezers and the complexity of PCB layout. Instead, implementation of the frequency divider approach, which is much easier to realize and deemed sufficient for Sonotweezer applications, is also described in Chapter 6.

CHAPTER 4 METHODS FOR DESIGN, FABRICATION AND EXPERIMENTAL DEMONSTRATION

4.1 Introduction

This short chapter describes the methods for electronics design and development used in this thesis. First, EDA tools for designing the digital and analogue electronics are discussed, followed by the methods to develop electronic circuits. Later in the chapter, electronic testing methods are presented and the equipment for experimental characterization with Sonotweezers is outlined.

4.2 Electronic Design Methods

This section describes the EDA tools for digital and analogue circuit design. For programmable digital devices like FPGAs, the development tools are normally supplied by the device vendors. For analogue circuits, tools for circuit simulation are based on physical models of various electronic components. Specific software is also needed to design PCB layouts for manufacturing.

4.2.1 EDA Tools for FPGA Design and Implementation

For complex logical devices like FPGAs, specialized EDA tools are provided for digital circuit design and development. Currently different FPGA vendors have their own proprietary versions. The Xilinx ISE Design Suite WebPACK version (v14.7, Xilinx, Inc., San Jose, CA, USA) is used in this thesis. As shown in Figure 4.1 the software development environment provides a standalone top-down design flow to support the development from a top-level HDL circuit description to a bottom-level bit stream file

ready for FPGA configuration. Circuit behavioural simulation and post-route timing simulation are performed with the build-in ISIM simulators for circuit design and debugging (“ISE In-Depth Tutorial”, 2009). In this thesis, VHDL is used as the HDL development language.

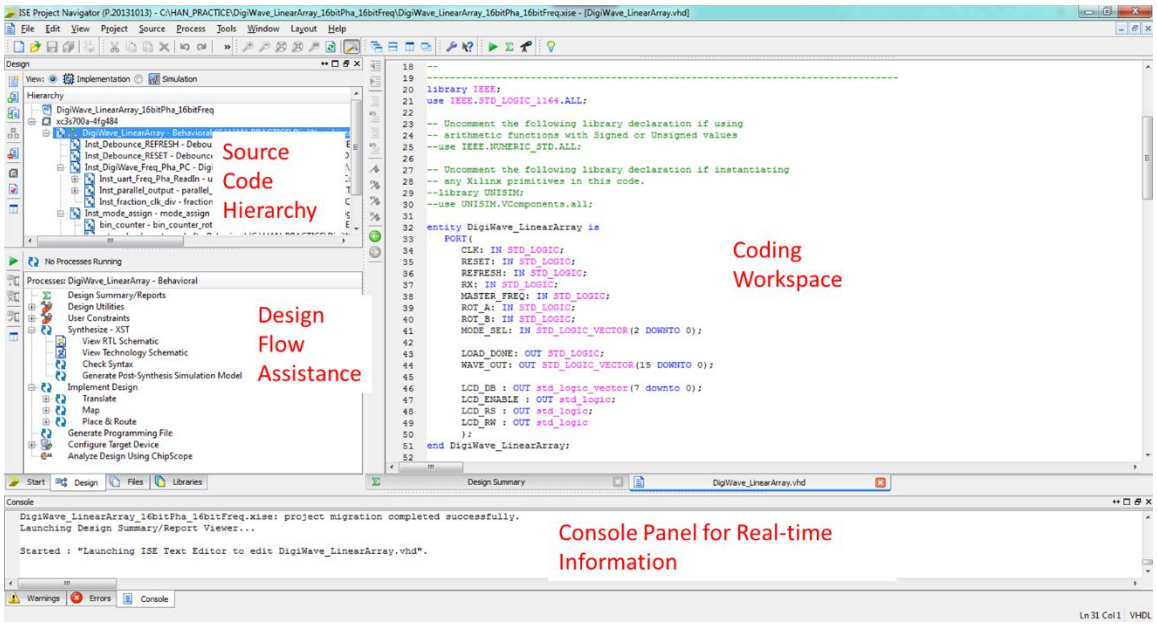

Figure 4.1 A screenshot of Xilinx ISE Design Suite project navigator.

4.2.2 EDA Tools for Analogue Circuit Design

A. SPICE Circuit Simulators

In the work described here circuit operation was first verified on a PC using the SPICE (Simulation Program with Integrated Circuit Emphasis) model-based circuit simulator. SPICE is a general purpose, open source electronic circuit simulator allowing both IC design and board-level circuit design for predicting the circuit behaviour at transistor level. Developed and released as SPICE2 in 1975 from University of California, Berkeley, SPICE was quickly adopted in academia and industry and many subsequent simulators were developed from it. For schematic-based circuit simulation in this thesis, the commercial software package, NI Multisim (v13.0, National Instruments, Austin, TX, USA), was used as it includes a sufficient component library and various analysis methods to examine circuit behaviour.

B. PCB Design Tools

For prototyping circuit design at board-level, the DesignSpark PCB (v5.1, RS Components, Corby, UK) free-of-charge schematic capture and PCB layout software package was used. A screenshot is shown in Figure 4.2. DesignSpark PCB has the same features as other EDA tools for schematic creation and translation into PCBs, based on the specific footprints of the electronic components used in the circuit. After completing the design a series of fabrication files can be generated for PCB manufacturers. Usually these files contain the PCB data in Gerber format and drilling information.

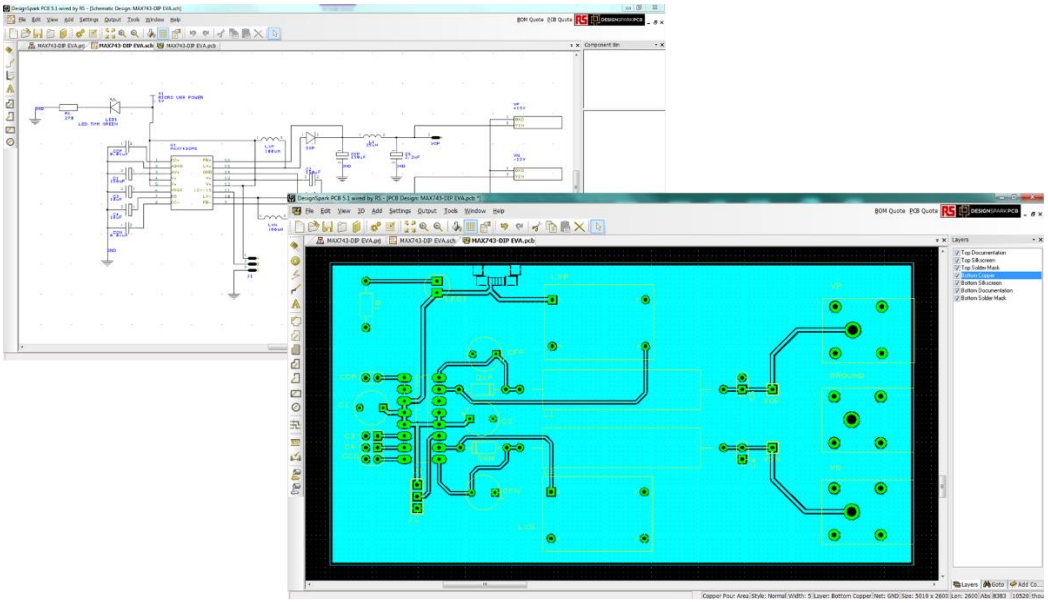

Figure 4.2 DesignSpark PCB software schematic capture and PCB layout design panels.

4.2.3 System Level Development Tools

For Sonotweezer devices implemented for particle manipulation, an intermediate layer is needed to translate the user operating commands, i.e. device operating conditions, particle positions, etc., into a series of configurations for electronics. MATLAB (R2012b, MathWorks, Natick, MA, USA) was chosen for this task as it provides a numerical computing environment in which is easy to implement computational acoustic models of various Sonotweezer devices. It can manage the required large amount of computational work with the CPU power in a conventional PC, to reduce the arithmetic work in the FPGA design. Hence the FPGA internal circuit space can be saved to provide larger output channel counts for the electronics. Moreover, it also provides a graphical user

interface (GUI) development kit to create intuitive control panels for the Sonotweezers-electronics combination. Finally, its data communication toolbox allows the PC on which MATLAB is running to link with customized electronic hardware.

4.3 Electronic Hardware Development Methods

4.3.1 FPGA Development Board

Although it has already been determined that the FPGA technology is best for Sonotweezers project, it is also necessary to consider carefully the most appropriate FPGA device. Normally, the limitation in an FPGA is the area, i.e. the number of logic gates contained in the device that can be used to implement the design. For multichannel Sonotweezers applications, devices with a large number of logic gates are preferred. However, larger devices usually come in packages with hundreds of pins which are difficult to manage in circuit prototyping. Instead, it is better to select an established, off-the-shelf development PCB that containing a specific FPGA. Such boards also usually contain useful dedicated electronic peripherals.

The Xilinx Spartan-3a FPGA starter kit (Xilinx, Inc., San Jose, CA, USA) was selected as it offers sufficient logic capacity, and on-board functionalities for a reasonable cost of approximately £200 per board. A photograph is shown in Figure 4.3 with key components for Sonotweezers highlighted. The on-board FPGA is an XC3S700A, with 484 pins, 13,248 equivalent logic cells and a maximum 372 user defined I/O lines. A range of resources on the development board can be configured with the FPGA. For clock signals, there are 50 MHz and 133.33 MHz on-board crystal oscillators, with an additional SMA input for an external clock source. For I/O, 40 programmable I/O lines can be configured for parallel outputs. On-board buttons, switches and the LCD panel can also be programed to provide simple user interfaces.

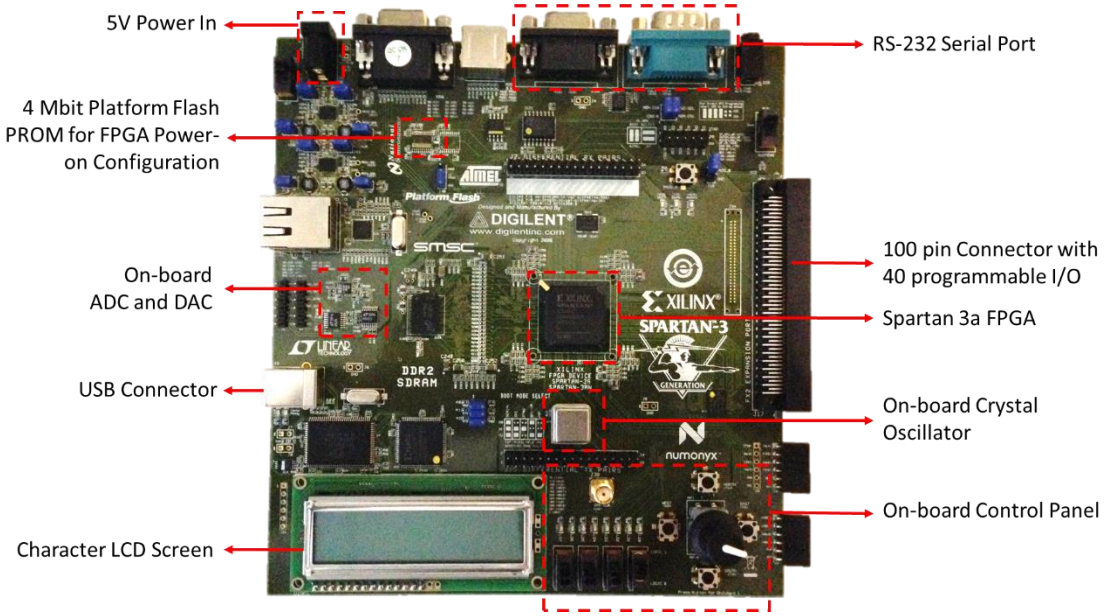

Figure 4.3 Spartan-3a FPGA development board. Highlighted are the key hardware components for Sonotweezers driving electronics development.

4.3.2 Electronics Prototyping and PCB Fabrication

After functional circuit design verification through SPICE simulation, the circuits were first physically constructed and tested on electrical breadboard with discrete alternatives for of the final intended components. For the PCB design, the electrical tracks were routed manually, and component placement and routing were performed according to generally accepted PCB design practices (Coombs, Jr., 2008). As noted previously, the operating frequency of the analogue electronics is within the range 1 – 10 MHz. Thus, to maintain signal integrity, cares was taken to place ground planes between signal tracks to reduce crosstalk wherever possible. In addition, wide power tracks were used to reduce the on-board impedance from the power supply to the active components (Jones, 2004).

Custom PCBs were either built in-house or supplied from an external vendor (PCB Train, Newbury Electronics Ltd, Berkshire, UK). The circuit designs were created with schematic capture and the transferred into a PCB layout with DesignSpark PCB. The PCBs created in this thesis had one, two or four metal layers depending on complexity. For PCBs that incorporating multiple copper layers, complete manufacturing files were generated for the PCB vendors, including the Gerber data and drill data files for the electrical copper layers, and non-electrical layers such as the solder mask and silkscreen.

In the PCB design, the signal tracks had two widths of 0.254 mm or 0.381 mm, and the power supply tracks two widths of 0.635 mm or 1.27 mm. The external fabricated PCBs had a finished cooper thickness of about 0.035 mm.

4.4 Electronics Characterization Methods

Electronics were characterised in the work reported here with standard tools: digital multimeters and oscilloscopes. A Fluke multimeter (Fluke 117, Fluke UK Ltd, Norfolk, UK) was used for quick measurements of instantaneous and root-mean-square (RMS) values of voltage, current, capacitance and resistance of circuit components and was also helpful for circuit troubleshooting with its built-in buzzer.

For more advanced circuit characterization, a 100-MHz-bandwidth, 4-channel digital oscilloscope (DSOX3014A, Keysight Technologies Inc., Santa Rosa, CA, USA) was used. The instrument has 16 digital channels and 4 analogue channels for mixed signal measurements including time-correlated triggering and acquisition, which is required for multichannel characterization of Sonotweezer systems.

Other important issues to consider in terms of electronics characterization include matching together the interconnections between the electronics during the design process and considerations for testability. To these ends, various electronic adaptors were fabricated for characterization purposes, and dedicated pins or pads were placed at critical positions on the PCBs to ease the electrical testing.

4.5 Instruments for Experimental Characterization of Sonotweezers

4.5.1 Electrical Impedance Spectroscopy

The most important instrument for Sonotweezers transducer characterization is an impedance / network / spectrum analyser (4395A, Keysight Technologies Inc., Santa

Rosa, CA, USA), connected with RF impedance test kit (43961A, Keysight Technologies Inc., Santa Rosa, CA, USA). These instruments can measure the impedance parameters of ultrasound transducers within the frequency range 100 kHz - 500 MHz. A probe fixture was also prepared with two testing leads for feeding the ground and RF signal to the transducers, as shown in Figure 4.4.

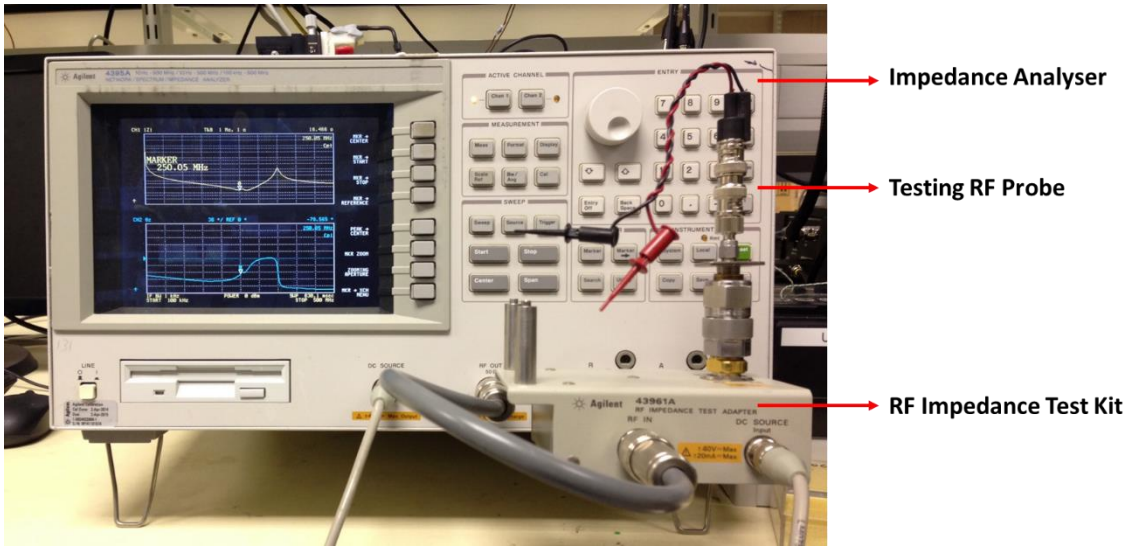

Figure 4.4 Equipment for transducer impedance spectrum measurement.

The impedance measurement is based on I-V method ("Agilent 4395A Network/Spectrum/Impedance Analyzer Operation Manual", 2008). As shown in Figure 4.5 (a), the unknown impedance Z of the device under test is calculated from direct measurement of the voltage and current across it using Ohm's law. With the impedance test kit connected, considering the input impedance of all ports, the actual test circuit is shown in Figure 4.5 (b). In the figure all R_0 represent 50 Ω resistance, voltmeter V_v measures the voltage of port *R* and voltmeter V_1 measures the voltage of port *A* to obtain a measurement of current.

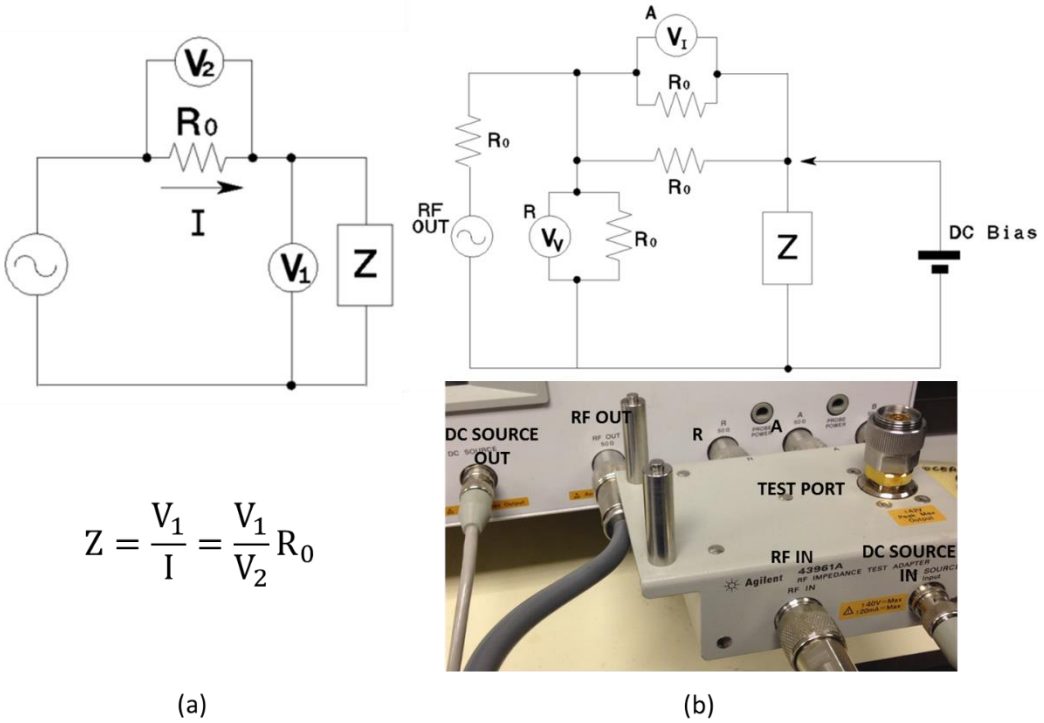

$$Z = \frac{V_1}{I} = \frac{V_1}{V_2} R_0$$

Figure 4.5 Electrical impedance spectroscopy (adapted from "Agilent 4395A Network/Spectrum/Impedance Analyzer Operation Manual", 2008). (a) I-V measurement method. (b) Schematic of the test circuit and image of equipment.

RF data from the impedance analyser are loaded into a PC over a general purpose instrumentation bus (GPIB) interface. Normally the test frequency range is selected as a few times of the fundamental transducer resonance frequency. A maximum of 801 points can be selected to plot the spectrum of transducer impedance magnitude and phase against frequency.

4.5.2 Laser Doppler Vibrometry (LDV)

As an alternative to direct electrical measurement, the functionality of complete Sonotweezer systems was also directly tested by measuring the surface displacement of transducer array elements using a commercial LDV. The core of the instrument is the heterodyne laser interferometer based vibrometer, which is a precision optical transducer used to determine vibration velocity and displacement at fixed points on the surface of the transducer under test. The technology is based on the Doppler-effect by which the frequency of light back-scattered from a moving surface is shifted, realised as shown in Figure 4.6 (a) ("Polytec: Basic Principles of Vibrometry", 2015).

The specific experimental setup for LDV measurement in the present work is shown in Figure 4.6 (b) (Xie, 2014). The transducer under test is mounted on an X-Y scanning stage (Motionpod, Motion Link, Ltd., Chaddleworth, Berkshire, UK) and the LDV components are a laser sensor head (OFV-534, Polytec GmbH, Waldbronn, Germany) and a vibrometer controller (OFV-2570, Polytec GmbH, Waldbronn, Germany). The laser head includes the optical components shown in Figure 4.6 (a), integrated with a microscope objective to adjust the laser focus to a microscale spot of about Ø400 µm. The OFV-2570 controller is designed for ultrasonic applications, measuring displacement in a 30 kHz – 24 MHz bandwidth up to a maximum peak value of ± 75 nm. The measurement data are recorded by a data acquisition system (PXIe-1071, National Instruments, Austin, TX, USA) controlled by a PC running a bespoke LabVIEW program (v2013, National Instruments, Austin, TX, USA). With the X-Y scanner, the complete system can perform 2-D scans for examination of transducer surface displacement profiles.

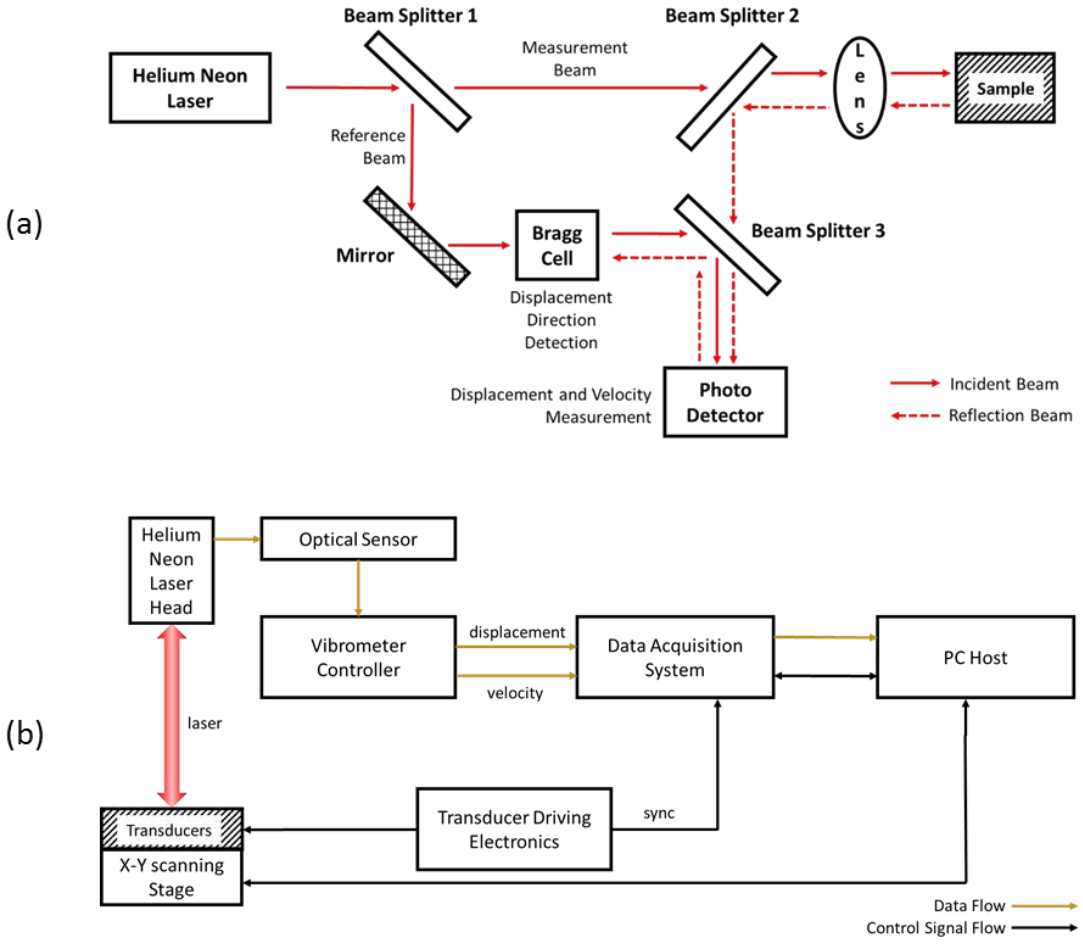

Figure 4.6 (a) Block diagram of the optical setup for LDV. (b) Block diagram of LDV experimental setup.

4.5.3 Fluorescence Optical Microscopy

Optical microscopy is another frequently used technique for experimental characterization of Sonotweezer devices. Microparticles such as polystyrene microspheres were used in the experiments to test the functionality of devices and systems investigated in the present work and fluorescence microscopy was adopted to enhance the optical contrast during observations.

The fluorescence microscope setup used in this thesis is shown as Figure 4.7. On a conventional trinocular microscope (ME.2665, Euromex Microscopen BV, Arnhem, The Netherlands), the halogen light source was replaced by a high luminance blue light emitting diode (LED) with 455 nm typical wavelength. The particles used in the experiments were Ø10 μm yellow-green fluorescent microspheres (Polysciences Inc., Eppelheim, Germany), with excitation wavelength 441 nm and the emission wavelength 486 nm. The reflected light from the particles passed through a 495 nm long-pass optical filter (FGL495, Thorlabs Inc., New Jersey, USA) to eliminate the ambient blue light so that only the green light emitted from the sample entered the microscope eyepieces. A CMOS camera (Moticam 2500, Motic, Wetzlar, Germany) was fixed onto the phototube of the microscope to record live videos of particle manipulation results.

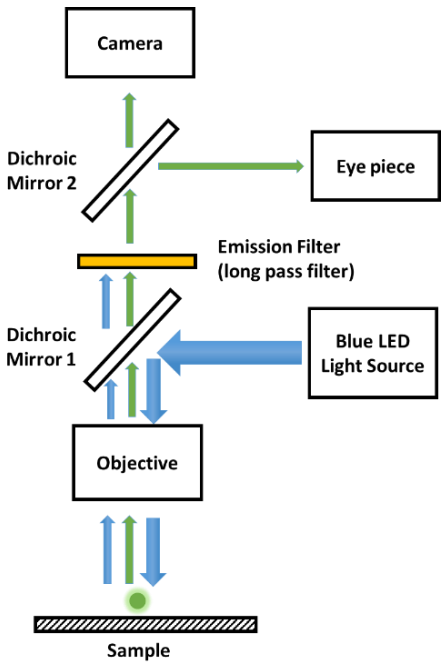

Figure 4.7 Experimental setup for epi-illumination fluorescent microscopy.

4.6 Post-processing Methods for Experimental Results

All the experimental images and videos were processed with the open source image processing software ImageJ (ver1.49o, Rasband, W.S., ImageJ, U. S. National Institutes of Health, Bethesda, Maryland, USA, http://imagej.nih.gov/ij/, 1997-2014). The captured micrographs were calibrated to different scales as listed in Table 4.1.

Table 4.1 Calibration table for post-process in ImageJ.

Microscope Objective	Pixel Calibration (μm/pixel)
4x	5.00
10x	1.40
20x	0.91
50x	0.35

In the experiments of using polystyrene particles for Sonotweezers characterization, during the process of particle agglomeration and manipulation in the viscous fluid, the acoustic lateral force exerted onto the individual particles and particle agglomerates because of the field kinetic energy gradient, $F_{lateral}$, was primarily balanced with the viscous drag force given by Stokes' law (Batchelor, 2000), F_d, i.e. a frictional force that exerted on spherical particles within a small Reynolds number viscous fluid. $F_{lateral}$ can be derived by measuring the velocity of the moving particle or particle agglomerate, which can be expressed as (Glynne-Jones, Démoré, et al., 2012):

$$F_{lateral} = F_d = 6\pi\mu r v, \tag{4.1}$$

In Equation (4.1), μ is the dynamic viscosity, and for water in 20°C, μ = 1.002 mPa·s ("Water - Absolute or Dynamic Viscosity"). r is the diameter of the particle of interest, which could be a single particle or a particle agglomerate. v is the velocity of the moving particle or particle agglomerate.

4.7 Conclusions

This chapter provided a summary of the techniques and equipment involved in the work described in this thesis for electronics design and fabrication, and Sonotweezers system characterization. The work of this thesis has an evident nature of multidisciplinary, ranging from choice of development resources for FPGA-based electronics to microparticles and equipment for fluorescence microscopy. As a summary, Table 4.2 and Table 4.3 listed the software packages and equipments respectively for electronics development and Sonotweezers system functional characterisation.

Table 4.2 Software packages used in the thesis.

Software	**Version**	**Supplier**	**Application**
Xilinx ISE Design Suite	v14.7, WebPACK	Xilinx Inc.	FPGA electronics prototyping
NI Multisim	v13.0, Student	National Instruments	SPICE circuit simulation
DesignSpark PCB	v5.1	RS Components	Circuit schematic and PCB design
MATLAB	R2012b	MathWorks	Modelling and PC interfacing
LabVIEW	2013	National Instruments	LDV scanning system control
ImageJ	V14.9o	U. S. National Institutes of Health	Image and video post-processing

Table 4.3 Equipment used in the thesis.

Equipment	**Model Number**	**Supplier**	**Application**
Digital multimeter	Fluke 117	Fluke UK Ltd	Electronics Characterisation
Digital oscilloscope	DSOX3014A	Keysight Technologies Inc.	Electronics Characterisation
Impedance/network/spectrum analyser	4395A	Keysight Technologies Inc.	Transducer Characterisation
RF impedance test kit	43961A	Keysight Technologies Inc.	Transducer Characterisation
LDV laser head	OFV-534	Polytec GmbH	Transducer Characterisation
LDV controller	OFV-2570	Polytec GmbH	Transducer Characterisation
Data acquisition system hardware	PXIe-1071	National Instruments	Transducer Characterisation
Trinocular microscope	ME.2665	Euromex Microscopen BV	Sonotweezers Functional Test
CMOS camera	Moticam 2500	Motic	Sonotweezers Functional Test

CHAPTER 5 DEXTEROUS MULTICHANNEL ELECTRONICS FOR SONOTWEEZERS

5.1 Introduction

This chapter describes the design, fabrication and characterisation of the electronics for complex acoustic field shaping with circular array for dexterous Sonotweezing. Firstly, an introduction is provided for the circular, 16-element ultrasound array that generates an acoustic field for purposes such as particle agglomeration and manipulation. Secondly, the design and development of the electronics that meet the demands for driving the array are described in detail. Lastly, characterisation of the electronics performance and demonstration of the system for particle trapping and manipulation are presented.

5.2 Electronics Design Consideration for Complex Acoustic Field Shaping with Sonotweezers

This section describes the advantages of a circular array for Sonotweezing over other counter-propagating standing wave acoustic tweezers, particularly in terms of particle manipulation dexterity. The circular arrays is as good example to which to apply the design of a dexterous electronic driving system, as the operation of such device requires modulation of transducer signals on a multichannel scale[1].

[1]Experiments published in the literature (Courtney et al., 2013, 2014) with circular array Sonotweezer device were performed with the electronic system developed by Kinneir Dufort (www.kinneirdufort.com/work/medical/sonotweezers-university-bristol, accessed on 5th March, 2015).

All the electronic design, system development, and experimental demonstration presented in this chapter are original, and completely independent of the electronic design by Kinneir Dufort involved in the previous publications.

5.2.1 Circular Array Sonotweezers

It has been demonstrated theoretically and experimentally that particles can be trapped and manipulated within an acoustic standing wave field created by opposing transducer pairs in one and two dimensions within multi-mm scale chambers. For these devices, counter-propagating acoustic waves create stable standing wave patterns with periodic pressure nodes and anti-nodes. The acoustic field can be manipulated by varying the driving signal frequency (Wood et al., 2009; Ding et al., 2012), or phase (Courtney et al., 2010, 2011). These devices can also be integrated with appropriate instrumentation for manipulation under programmable control (Meng et al., 2012). However, both frequency and phase control are limited because acoustic traps occur at pressure nodes or antinodes with $\lambda/2$ spacing and changes to the frequency or phase affect all the traps (Courtney et al., 2014).

Another approach for trapping and manipulation is using acoustic vortex (Hefner and Marston, 1999; Kang and Yeh, 2011). Acoustic vortices are beams having phases that rotates around their central axis with a dependence of $e^{im\theta}$, where m is the topological charge and θ is the azimuthal angle (Thomas and Marchiano, 2003). Within the vortex field the central pressure minima are surrounded by high pressure regions for particle trapping. Compare to propagating acoustic vortices with several wavelengths between nodal planes in the axial pressure distribution, stationary acoustic vortices can be more useful as they may provide larger potential gradients for trapping and manipulation of microparticles in a plane, with MPa acoustic pressures to generate moderate pN forces (Courtney et al., 2014). Such devices can be realized by a circular transducer array that produces Bessel-function field (Campbell, 1990; Hsu et al., 1989) without axial propagation. Whilst the operation of circular array devices is more difficult to fabricate than other counter-propagating USW devices (Wu, 2012), however it offers higher dexterity, overcoming the $\lambda/2$ pressure node spacing limit.

Courtney et al. have previously demonstrated dexterous particle trapping and manipulation with a 16-element circular transducer array (Courtney et al., 2013). The device was fabricated from a piezoceramic ring (PZ27, Meggitt Ferroperm, Denmark) of internal radius $R = 5.49$ mm, thickness $t = 0.87$ mm, and height $h = 1.60$ mm. The piezoceramic elements were mounted on a bespoke PCB and alumina-loaded epoxy was used as acoustic backing (Wu, 2012). The device is illustrated in Figure 5.1. The array

was operated at fundamental resonance frequency, f_r = 2.35 MHz, corresponding to λ = 630 µm in water, with speed of sound, c_{water} = 1481 m/s, at 20°C.

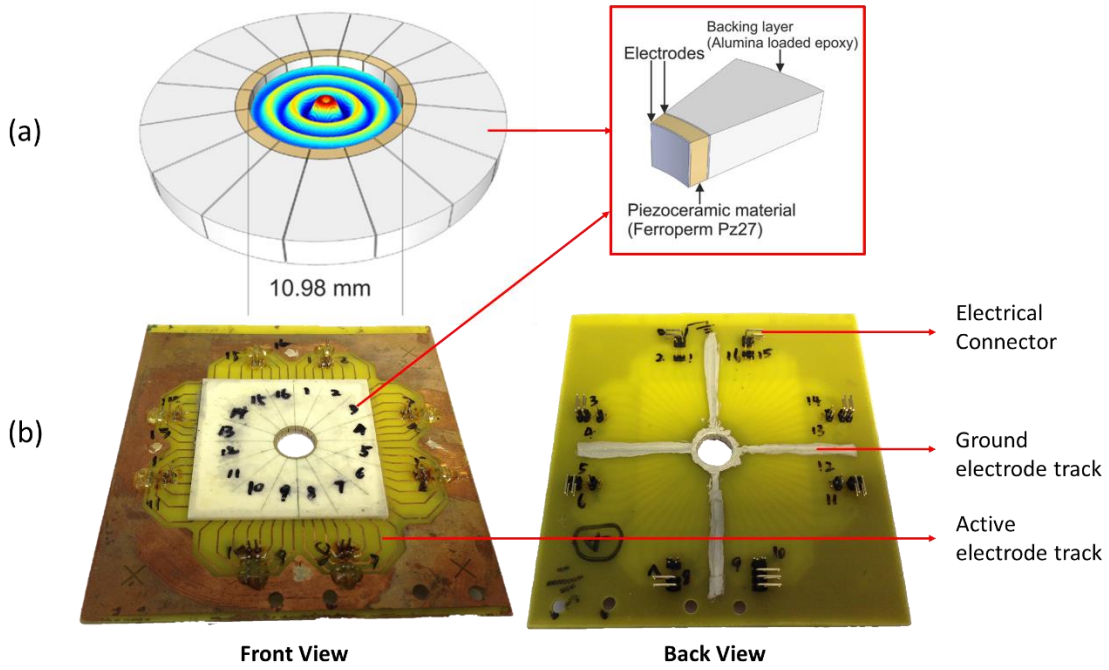

Figure 5.1 16-element circular array. (a) Illustrative diagram of the device fabricated from piezoceramic ring, and the shape of the 1st order Bessel-function acoustic field (from Courtney et al., 2013). (b) Photographs of the complete device with electrical connections.

Trapping and manipulation was demonstrated with a first order Bessel-function acoustic pressure field. An acoustic vortex with topological charge, m, will be generated if the sinusoidal drive signals are applied with a ramp of $2m\pi$ phase delay around the array. The relative phase of the driving signal for each of N elements, ϕ_{n0}, n = 1, 2, 3… N, is given by

$$\phi_{n0} = \left(\frac{2m\pi(n-1)}{N}\right) \quad \textbf{(5.1)}$$

The resulting pressure field in the chamber then approximates a Bessel function in pressure given by:

$$p(r,\theta) = P_0 J_m(kr) e^{im\theta} \quad \textbf{(5.2)}$$

In Equation (5.2), (r, θ) are polar coordinates with their origin at the centre of the Bessel function, coincident with the centre of the array for the phases given in Equation (5.1), and P_0 defines the peak pressure amplitude and $J_m(x)$ is an mth order Bessel function of the first kind. When $m = 1$, the central ($r = 0$) pressure node coincides with a velocity anti-node and a pressure node, ensuring that particles that are denser and stiffer than the fluid medium will experience a force toward the centre. Although the pressure nodes in the form of concentric rings further from the centre do not coincide with the velocity antinodes, the pressure contribution dominates for the polystyrene beads used in the present work, and the patterns of trapped particles match with the expected pressure distribution (Courtney et al., 2013).

The centre of the generated Bessel-function field can be manipulated into a target position (r_T, θ_T), with phase delay ϕ_n calculated from r_n as the relative distance between the field centre and each element n. For an mth order Bessel-function field generated from a circular array with N elements, the relative phase of element n can be represented by:

$$\phi_n = \left(\frac{2m\pi(n-1)}{N} - kr_n\right), \tag{5.3}$$

where k is the wave number.

Furthermore, Grinenko et al. have demonstrated analytically that the distortion-free distance of the Bessel-function field centre away from the circular array geometric centre, r_T, is limited by:

$$r_T < \frac{1}{2}\frac{(N-m)}{\pi e}\lambda, \tag{5.4}$$

where λ is the acoustic wavelength (Grinenko et al., 2012).

As a numerical example, for a 16-element circular array operating at 2.35 MHz with a 1st order Bessel-function field ($m = 1$), $r_T < 0.88\lambda$, the maximum manipulation distance of the field origin is 554 μm from the geometric centre of the array. Related aliasing of the Bessel-function field central trap is demonstrated in Figure 5.2.

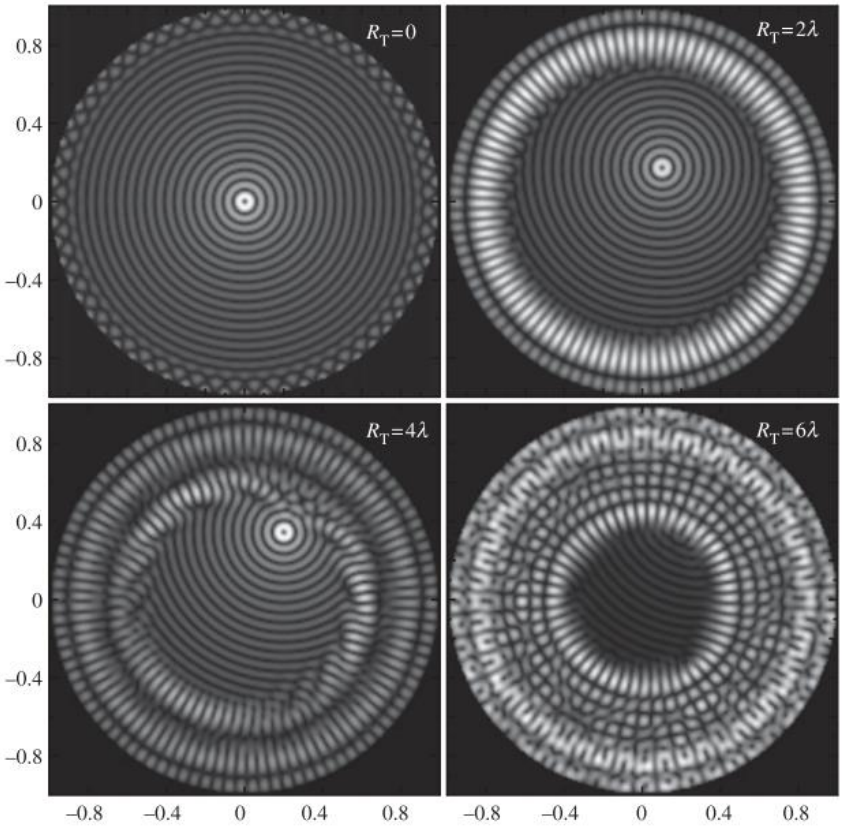

Figure 5.2 A J_1 Bessel trap generated by a 60-element circular array with radius $R = 10\lambda$ with the transducers modelled as point sources. The distortion free radius $R_T < 3.5\lambda$. In the modelling, the trap is aliased for conditions when R_T is larger than 4λ (from Grinenko et al., 2012).

5.2.2 Considerations for Circular Array Control

A. Background

According to Equation (5.3), each change in the position of the Bessel-function field centre requires an update of the driving signal phase for each array element. The signal phasing can be derived from the distance between the translated field centre to the position of each element. Consider the polar coordinate system shown as Figure 5.3. The coordinate pole $(r, \theta) = (0, 0)$ is coincide with the geometrical centre of the array circumference. Hence depending on the number of the array elements, the polar coordinate (r_n, θ_n) of each transducer can be determined by the fixed radius r_n = R = 5.49 mm, and azimuth θ_n, where $n = 1, 2, 3 \ldots$ N. The target Bessel-function field origin is represented as T (r_T, θ_T). The relative distance between each transducer and the target field centre, r_{nT}, can be determined by the following equations:

$$\begin{cases} r_{nT} = \sqrt{{r_T}^2 + R^2 - 2r_T R\cos|\theta_T - \theta_n|} & \textbf{(5.5)} \\ \theta_n = \dfrac{2\pi}{N}(n-1), & \textbf{(5.6)} \end{cases}$$

where n = 1, 2, 3, …, N.

From Equations (5.3), (5.5) and (5.6), the phases of driving signals, ϕ_n, for all elements of the circular array can then be easily derived.

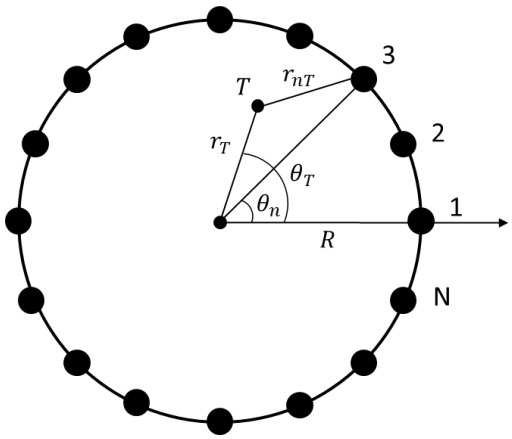

Figure 5.3 The polar coordinates used for calculating the phase profiles of driving signals for an N-element circular array when the Bessel-function field centre is under manipulation in order to move the particles trapped with it.

B. Electronics Design Considerations

According to Equation (5.4), the distortion free region for central trap manipulation can be extended with an increased number of elements. It has also been suggested that it is preferred to have more elements in an array to allow multiple separate Bessel-function field centre traps (Courtney et al., 2014). As a way to explore the trade-off between the electronic complexity and the number of channels, the construction of a scalable, mutually independent multichannel array driver specifically designed for Sonotweezers is described in this chapter. Based on initial theoretical and experimental results from complex devices including circular arrays and other counter-propagating USW arrays (Bernassau et al., 2012, 2013; Courtney et al., 2011, 2013, 2014; Ding et al., 2012; Ding et al., 2012; Grinenko et al., 2015, 2012), a technical specification of the electronics is summarised in Table 5.1.

Table 5.1 Technical specifications for the electronic array driving system suitable for complex Sonotweezers.

Parameters	**Specifications**
Number of Channels	Minimum 16, scalable
Drive Mode	CW sinusoidal (or near sinusoidal)
Output Signal Frequency	Adjustable, 1 - 10 MHz
Output Signal Phase	Adjustable, with resolution as low as to 22.5°
Output Signal Voltage (per Channel)	Adjustable, 0 – 30 V_{pp}
Load Impedance	10 – 30,00 Ω
Maximum Output RMS Power (per Channel)	37.5 mW – 2.25 W
Instrumentation	Direct PC control with GUI, MATLAB compatible

At the system level, the electronics architecture can be described as shown in Figure 5.4. The FPGA for digital control is programmed with appropriate logic as an embedded core to generate CW outputs as digital signals. The analogue multichannel driver is connected to the digital electronics to generate modulated signals with sufficient power. To allow more space in the FPGA architecture for potential scaling-up of the channel count, the computing complexity in the digital device is reduced to a minimum with the FPGA programmed as a core for phase generation and frequency synthesis. The core inputs are configured from a PC with a customized MATLAB GUI, based on acoustic models for various Sonotweezer devices. Because real-time amplitude modulation of the outputs was not necessary for driving most of the devices considered here, simple signal conditioning hardware built as a part of the analog stage to manually adjust the output amplitudes.

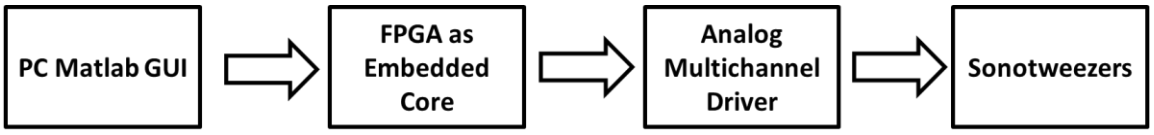

Figure 5.4 Electronic system architecture for circular array Sonotweezers.

5.3 Digital Electronics Development

Introduced in Chapter 3, the Spartan-3a FPGA development board has sufficient capacity for 16 output channels. This section will mainly discuss the development of an FPGA soft core for signal frequency and phase modulation, with the VHDL source code provided in supplemental CD in Appendix A.

5.3.1 Phase Generator

A digital signal consisting several bits "1" and the same number of bits "0" in the form "111…000…" can be recognized as a full cycle AC signal with 50% duty cycle. One cycle of such a signal can be digitized with a synchronous clock to represent a certain phase resolution. The total number of bits in one cycle is defined as the phase-resolution-in-bits, *PHA_RES_BIT*. Hence the phase-resolution-in-degrees, *PHA_RES_DEG*, is defined as:

$$PHA\_RES\_DEG = \frac{360^\circ}{PHA\_RES\_BIT} \tag{5.7}$$

Although the phase resolution is independent of the number of output channels, for a 16-element circular array, a *PHA_RES_DEG* with the value 22.5° is sufficient to perform the transportation of the Bessel-function field experimentally (Courtney et al., 2013). Hence in this thesis, 16 different phase levels were used in the design, equivalent to a 4-bit phase resolution. For more general cases, The *PHA_RES_BIT* can have more bits to represent a higher phase resolution. However, the *PHA_RES_BIT* cannot be unlimited as there are trade-off considerations relative to the maximum frequency generated in the current design. This will be further discussed in Subsection 5.3.2. Table 5.2 demonstrates the usage of 16-bit codes as the representation of phases from 0° to 337.5° with 22.5° intervals.

Table 5.2 16-bit binary codes as representations of 16 levels of phases.

Binary Code	Single-cycle Waveform Representation	Correlated Phase
1111111100000000		0°
0111111110000000		22.5°
0011111111000000		45°
0001111111100000		67.5°
0000111111110000		90°
0000011111111000		112.5°
0000001111111100		135°
0000000111111110		157.5°
0000000011111111		180°
1000000001111111		202.5°
1100000000111111		225°
1110000000011111		247.5°
1111000000001111		270°
1111100000000111		292.5°
1111110000000011		315°
1111111000000001		337.5°

A. Phase LUT

To represent a 16-level phase resolution for a one cycle signal, a 16-bit binary code, "1111111100000000", was created. All 16 possible phases were then generated with a universal circular shift register. The shift register can load parallel data and shift its content left or right with a synchronized clock signal and it can either "shift right" by adding the LSB (least significant bit) to the MSB (most significant bit), or "shift left" by moving the MSB to the LSB. The phase results from the shift register were stored in a FIFO (first in, first out) buffer and afterwards transferred into a 16-bit-by-16-bit register array. An illustration of the data flow for the resulting phase LUT is shown in Figure 5.5.

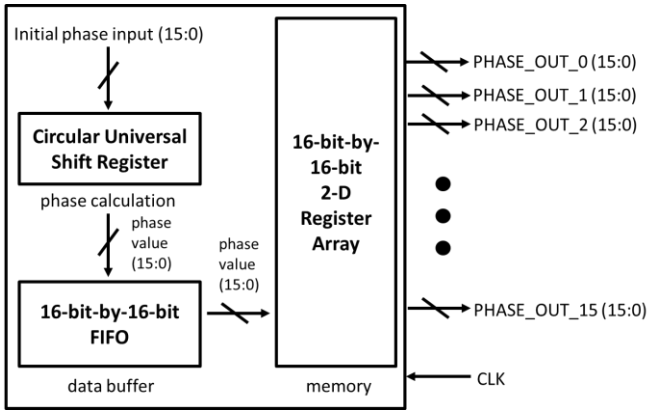

Figure 5.5 Diagram of the phase LUT module used to generate 16 different phases.

B. Phase Multiplexer

For each output channel, a 16-to-1 phase multiplexer (MUX) was connected with the phase LUT. In total, 16 MUXs were used for 16-channel configuration. The target phase value for each channel can be readily selected from 16 different phases, controlled by an input port, SELECT_MUX. An illustration of the phase multiplexer module is shown in Figure 5.6.

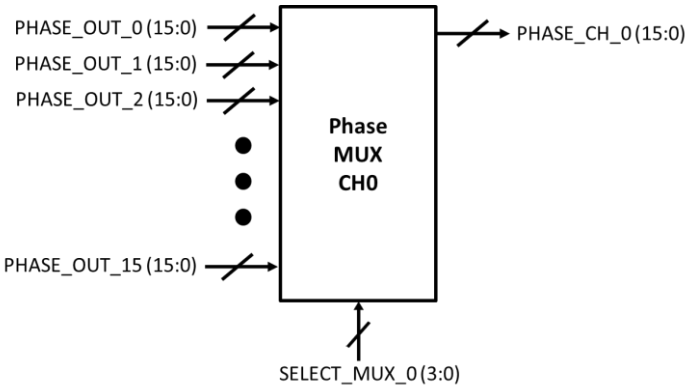

Figure 5.6 Diagram of the phase MUX for each channel.

C. Single-channel Waveform Generator

For each channel, the single-cycle phase value represented by a 16-bit binary code was selected from the phase multiplexer and transferred into a waveform generator, as shown in Figure 5.7. The phase data was read out bit-by-bit repeatedly, with a synchronous clock, WAVE_CLK, and a continuous waveform was generated, with the desired phase selected. A WAVE_EN input port was used as a channel enable / disable signal.

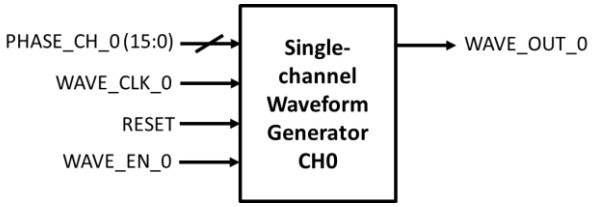

Figure 5.7 Diagram of the single-channel waveform generator module to transform a single-cycle signal into a continuous waveform.

D. Module Assembly and Verification

The complete 16-output phase generator was assembled with one phase LUT, 16 phase multiplexers and 16 single-channel waveform generators. After the phase generator was synthesized, the phase LUT was set up to represent 16 different phases from 0º to 337.5º. The target phases for each channel were designated through the multiplexer by an external phase select signal, and the corresponding continuous waveform was generated through a clock signal, WAVE_CLK, if the channel was enabled. The WAVE_CLK signal for each channel was generated from a customized frequency synthesizer module, discussed in detail in the following subsection. A simplified diagram of the phase generator module is shown in Figure 5.8.

The functionality of the phase generator module was verified through behavioural simulation, with output waveforms as shown in Figure 5.9. 16 channels of CW signals were generated, with 22.5° relative phase shift between each other.

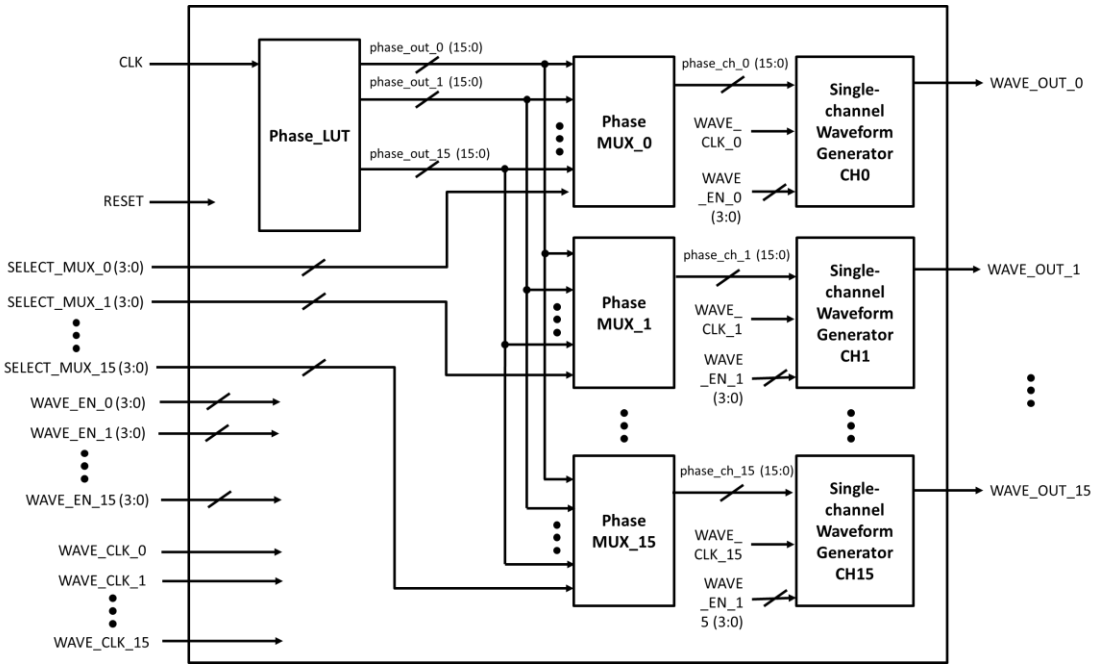

Figure 5.8 Simplified block diagram of the phase generator.

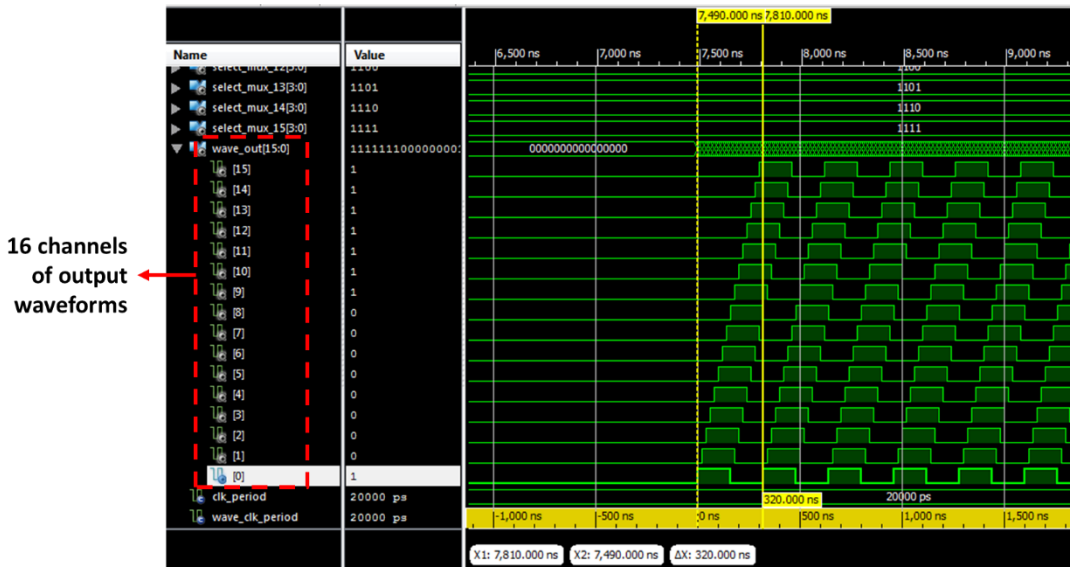

Figure 5.9 Behavioural simulation for functional verification of the phase generator. The phase resolution is 16-level. Phase values for each channel are selected from 0 to 337.5°.

5.3.2 Frequency Synthesizer

A. Fractional-N Frequency Divider

For each channel, the output signal frequency, *FREQ_OUT*, is determined by both parameter *PHA_RES_BIT* defined previously and the output of a customized digital frequency synthesizer module. The output of the frequency synthesizer, *FREQ_SYN* is used as the WAVE_CLK signal into the phase generator to clock out the single-cycle phase data. Hence, *FREQ_OUT* can be defined as:

$$FREQ\_OUT = \frac{FREQ\_SYN}{PHA\_RES\_BIT} \tag{5.8}$$

It is obvious that, for a higher phase resolution, the *PHA_RES_BIT* is larger and reduces the output frequency. Hence a trade-off must be considered in practical applications to achieve either a high phase resolution or a high output frequency.

The frequency synthesizer is built with an arbitrary fractional-N frequency divider. The synthesizer output, *FREQ_SYN*, can be calculated as the current FPGA reference

frequency, *FREQ_REF*, divided by a fractional factor ($N + K/M$) ($N \geqslant 2$, K, $M \geqslant 1$), which is represented as:

$$FREQ\_SYN = \frac{FREQ\_REF}{N\frac{K}{M}} \tag{5.9}$$

The denominator in Equation (5.9) is in the range $N < (N + K/M) < (N + 1)$, so the fractional frequency division can be achieved by performing a certain ratio of division by N and by (N + 1), respectively. Practically, for M cycles of the output signal, *FREQ_SYN*, there should be K cycles of (N + 1) division, and (M – K) cycles of N division. The resulting frequency division is a time-average of the two frequency division components.

It is also important to perform the N and (N + 1) division well-distributed over time to reduce spurious signals in the output (Barrett, 1999). For this purpose the division number should be varied dynamically between the two components. A modulus-M adder can be used here as an accumulator, with its contents accumulated repeatedly with the numerator, K, and its carry-out as a flag signal to control the division ratio between N and (N + 1) ("Basics of Dual Fractional-N Synthesizers / PLLs", 2005).

A block diagram of typical components in a fractional-N frequency divider is shown in Figure 5.10. N or (N + 1) division outputs from a dual-modulus-divider (DMD) are transferred into a MUX, controlled by an accumulator, to synthesize a time-averaged output. For a fractional factor of ($N + K/M$), the numerator accumulates the value of itself, K, within the modulus-M adder. The DMD performs N division when the carry-out of the accumulator remains "0", and performs (N + 1) division otherwise.

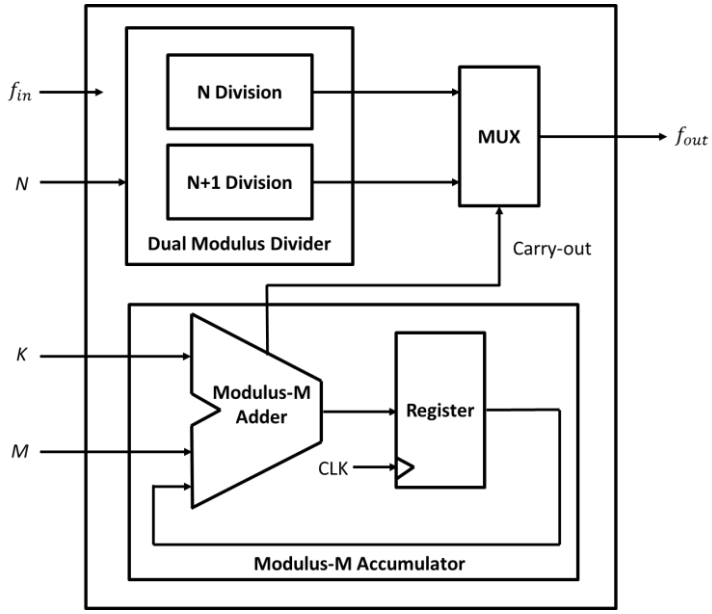

Figure 5.10 Block diagram of the fractional-N frequency divider.

For an integer-N frequency divider, it is easy to generate the output with 50% or tunable duty cycle. However, for the output of a fractional-N divider, the duty cycle of *FREQ_SYN* is not uniform over time. For CW output, the equivalent duty cycle of the synthesized signal can be calculated as a mathematically-weighted average of different sub-frequency components. Thus, for a fractional factor of ($N + K/M$), the equivalent duty cycle of the output can be expressed as:

$$Equivalent\ duty\ cycle = \begin{cases} \dfrac{\frac{N}{2} \times (M-K) + \frac{N}{2} \times K}{N \times M + K}, \\ (N\ is\ an\ even\ integer\ and\ N \geq 2;\ K, M \geq 1) \\ \dfrac{\frac{N-1}{2} \times (M-K) + \frac{N+1}{2} \times K}{N \times M + K}, \\ (N\ is\ an\ odd\ integer\ and\ N \geq 2;\ K, M \geq 1) \end{cases} \quad \textbf{(5.10)}$$

B. Frequency Range and Resolution

The maximum frequency tunability is determined by the resolution of the fractional factor, i.e., by the number of binary digits in *N*, *K*, and *M*. For an m-bit binary data resolution, $2 \leqslant N \leqslant (2^m - 1)$, $1 \leqslant K, M \leqslant (2^m - 1)$, the fractional factor will range from 2 to 2^m. Hence, theoretically, the minimum and maximum achievable frequency range can be

calculated, from Equation (5.8) and (5.9). This is further discussed with experimental results in Section 5.7.

C. Circuit Module Verification

Behavioural simulation was performed to verify the functionality of the frequency synthesizer. As an example, for the fractional factor ($N + K/M$), $N = 2$, $K = 3$, $M = 7$, the contents of the accumulator, and the DMD division factor distribution over a full fractional-dividing sequence can be represented as shown in Table 5.3.

Table 5.3 The DMD is controlled by a modulus-3 accumulator within a single fractional-dividing sequence, for a division factor of (2 + 3 /7).

Cycle Number	**1**	**2**	**3**	**4**	**5**	**6**	**7**
Accumulator Content	3	6	2	5	1	4	0
Carry-out	0	0	1	0	1	0	1
DMD Division Factor	2	2	3	2	3	2	3

Figure 5.11 shows the simulation waveforms of the I/O signals for a fractional factor of (2 + 3 /7). In the figure, the 50 MHz input reference frequency, *clk_in*, is divided into the output frequency, *clk_out*, of 20.588 MHz. Switching between division by two and division by three is controlled by the signal labelled as *ctrl2*. The patterns of the two frequency division factors matched the dividing sequence shown in Table 5.3. The equivalent duty cycle of *clk_out* is calculated to be 41.17 %.

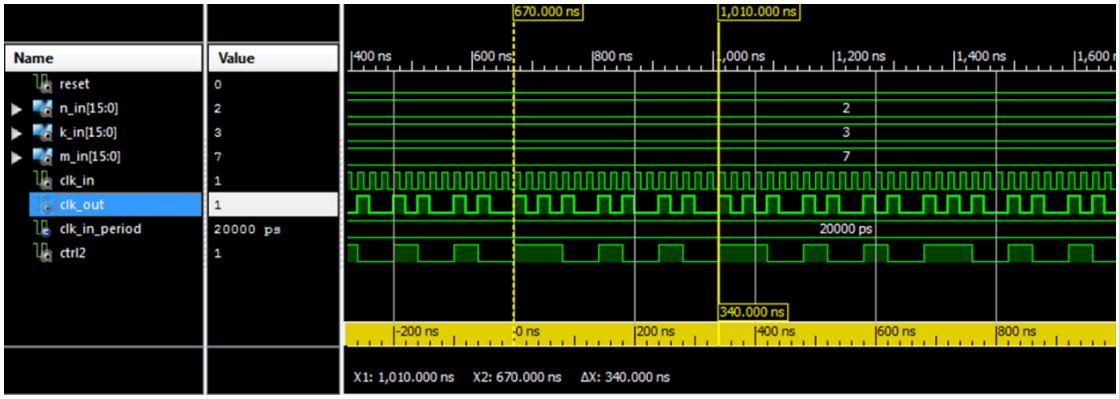

Figure 5.11 Behavioural simulation waveforms of the output frequency from a fractional factor of (2 + 3 /7). The output pulse is highlighted. A full division sequence of 7 cycles of *clk_out* equals 340 ns, matches with 17 cycles of the reference 50 MHz signal, where $N \times M + K = 17$.

5.3.3 Communication Interface to PC

As shown in Figure 5.8 and Figure 5.10, for the 16-channel array driving system, the phase and frequency information for each channel are configured by data array SELECT_MUX, and integers *N*, *K*, and *M*, respectively. At PC level, a programmable phase profile for all the channels is generated, based on the acoustic device models of different Sonotweezer devices, and SELECT_MUX is assigned accordingly. The integers *N*, *K*, and *M* can be calculated with Equation (5.8) and (5.9), with given *FREQ_REF*, *PHA_RES_BIT*, and target *FREQ_OUT*.

A serial-port was chosen as the communication interface between the FPGA core and the PC because of its simple but robust architecture of transceiving data bit-by-bit. For the Spartan-3a FPGA development board, an RS-232 DB9 (9 pin) serial port is available. In this chapter, a very simple RS-232 setup is adopted, which only needs three electrical wires, as provided by the FPGA development board hardware: data-transmission (TXD) and data-receiving (RXD), and ground (GND). The RS-232 serial port wiring with the FPGA is shown in Figure 5.12 (a). In Windows the serial ports are recognized and displayed as COM ports, and for PCs not having a serial port, a USB to RS-232 converter (US232R-100, FTDI Ltd., Glasgow, UK) is used to convert a USB port as a virtual COM port, as shown in Figure 5.12 (b).

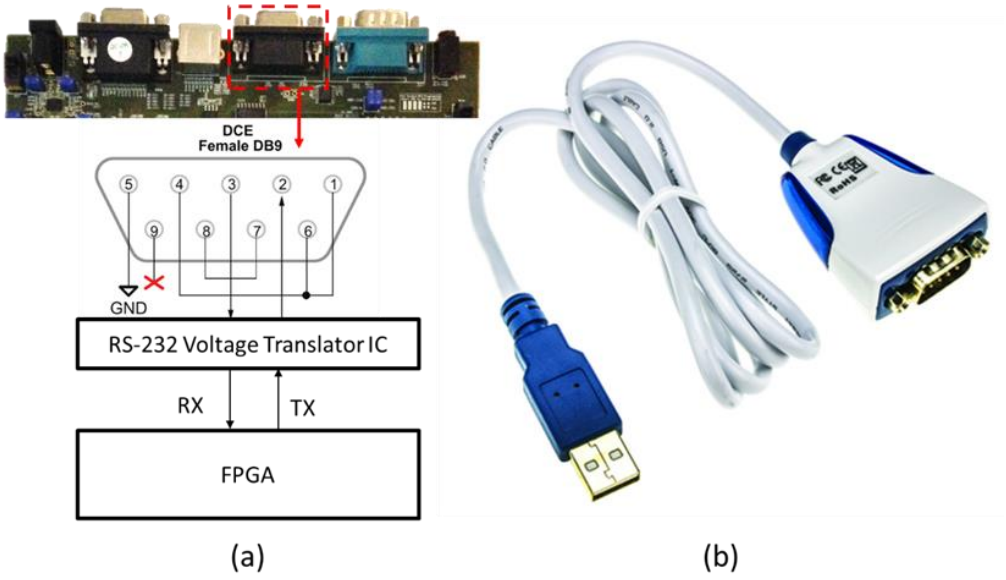

Figure 5.12 (a) Electrical interconnections of the on-board RS-232 DB9 female port (adapted from "Xilinx UG334 Spartan-3A/3AN FPGA Starter Kit Board User Guide", 2008). (b) A USB to RS-232 converter cable (US232R-100, FTDI Ltd., Glasgow, UK).

A communication interface is also needed as a customized VHDL module for the FPGA to transceive data from the PC. Usually universal asynchronous receiver and transmitter (UART) circuitry is associated with the RS-232 standard to send and receive parallel data through a serial line. The transmitter in a UART is a shift register that loads data in parallel and shifts out bit-by-bit whilst the receiver shifts the data in bit-by-bit and assembles them into parallel form. When idle, the data wires stay at logic "1". The data transmission starts with a *start bit*, 0, followed by *data bits*, which can be 6, 7, or 8, and an optional *parity bit*. The process ends with *stop bits*, which can be 1, 1.5, or 2. Since no clock signal is transmitted through the serial line, the PC and FPGA need to share parameters in advance, including baud rate, number of data bits and stop bits, and use of the parity bit. The baud rate can be from 110 bps to as high as 256,000 bps, depending on the operating systems and serial port devices ("DCB structure (Windows)", 2015). The UART design here is adapted from "Chapter 7 UART" in *FPGA Prototyping by VHDL Examples Xilinx Spartan-3 Version* (Chu, 2008). Figure 5.13 illustrates the protocol for the UART circuitry.

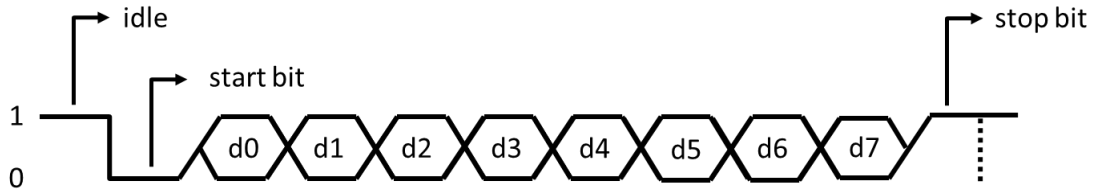

Figure 5.13 An example of UART communication for one byte data (adapted from Chu, 2008a). The LSB of the word is transmitted first.

The transmitter and receiver have similar structure. In this chapter, as a proof-of-concept study for system development, only the receiver was used to transfer the configurations from PC to the FPGA phase generator and frequency synthesizer. The complete UART architecture is shown in Figure 5.14, with the receiver highlighted by dashed lines. The receiver FIFO can provide some buffering space to prevent the received data being overwritten.

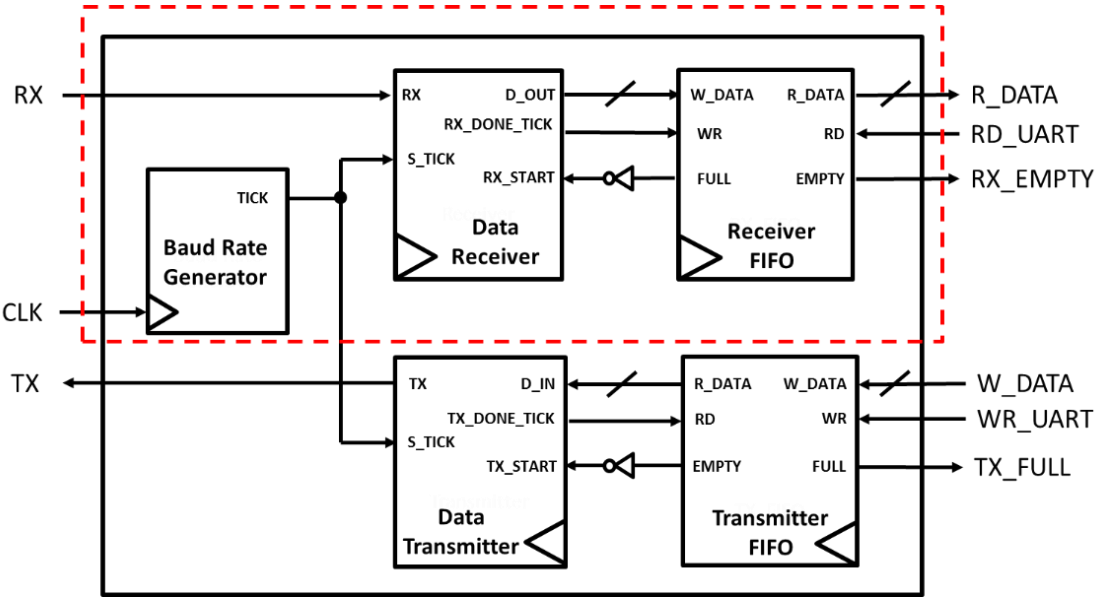

Figure 5.14 Block diagram of a complete FPGA UART module (adapted from Chu, 2008a).

The current UART design used a moderate baud rate of 19,200 bps, with 8 data bits, 1 stop bit, and no parity bit. Accordingly, a data transfer module was created in MATLAB with UART communication protocols at the beginning, followed by a multi-byte output memory, which stores the outputs generated from the Sonotweezer acoustic models.

The size of the FPGA receiver FIFO is scaled by the factor of 2, and can be adjusted in accordance with the MATLAB output memory. An illustration of the output memory

configuration is shown in Figure 5.15 (a). For the frequency fractional factors, 16-bit data is used to achieve a high frequency tuning resolution. Phase data of each channel is represented by a byte. A 16-bit data stores the enable commands for all 16 channels. Void data are assembled at the last, in order to make the data memory the same size as the UART FIFO. Particularly, for the circular array Sonotweezer all the elements are working at the same frequency, a 32-byte memory was prepared with simplified frequency data, as shown in Figure 5.15 (b).

For each output channel, the frequency and phase can be updated dynamically, simply by adding loops with adjustable time intervals in the MATLAB data transfer module. Hence output frequency and phase modulation can be achieved for specific applications, by modifying the current data transfer module.

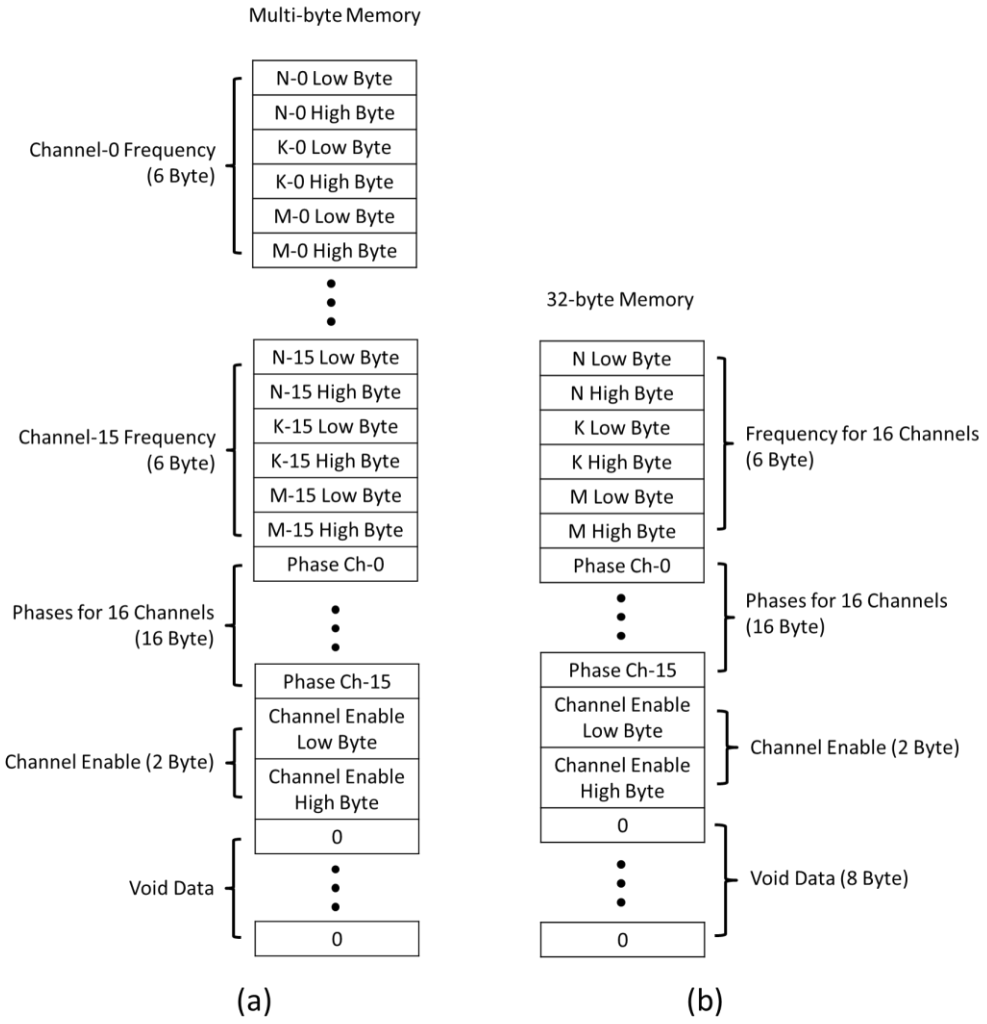

Figure 5.15 Configurations for MATLAB output memory. (a) Complete multi-byte memory for 16-channel electronics. (b) Simplified 32-byte memory used for 16-channel circular array device.

5.3.4 Complete architecture of the digital electronics

The complete digital electronics for multichannel digital waveform generation are constructed with the three submodules that have been discussed. A block diagram of the module assembly is shown in Figure 5.16.

In the FPGA core, all channels are controlled separately and are mutually independent. The core is scalable both in terms of channel count and frequency / phase resolution. However, some trade-offs should be considered. Firstly, more FPGA internal circuitry space is required for higher channel counts. Secondly, although a higher output frequency can be achieved with an increased reference frequency, to achieve a higher phase resolution, the reference frequency should be much higher still to avoid jeopardizing the maximum output frequency. Thirdly, an intrinsic drawback of the fractional-N frequency divider, is that there will be unavoidable phase error in the output signal. For applications that require high level of phase accuracy, technologies like PLL and DDS should be considered.

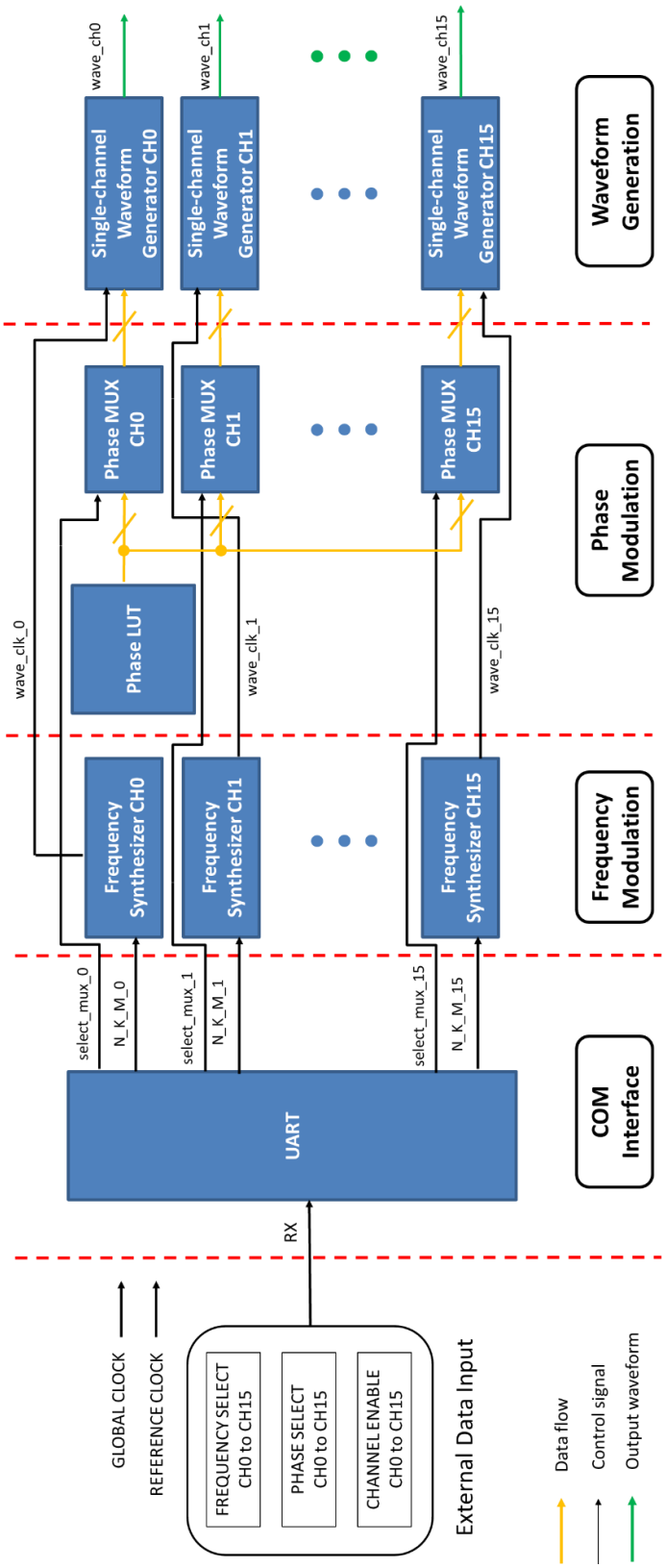

Figure 5.16 Block diagram of the complete FPGA core for a multi-channel signal generator.

5.4 User Interface Development for PC Control

The inputs to the digital electronics can be fully configured from MATLAB programs at PC level. For the current 16-channel FPGA core, two sets of MATLAB GUIs were created for different purposes. The GUIs interact with the FPGA core through different specific API layers created with MATLAB. The MATLAB source code can be found in the supplemental CD in Appendix A.

5.4.1 General-purpose MATLAB GUI

Figure 5.17 shows a general-purpose MATLAB GUI for the 16-channel array driving electronics. As the multichannel system was primarily designed for the circular array, all the channels were configured with the same frequency. Knowing the frequency and phase resolution, the associated frequency fractional parameters *N*, *K* and *M* are calculated and stored as a data matrix. Depending on the phase resolution, the phase value for each channel can be directly selected from possible minimum to maximum, and stored in a data matrix as a phase profile. Additionally, each channel can be independently selected or disabled. All the configuration data are stored in a data matrix with the size matched with the FPGA FIFO, and transferred through the UART interface into the FPGA for waveform generation.

5.4.2 Device Specific MATLAB GUI

A specific MATLAB GUI was created to control the multi-element circular array Sonotweezer, as shown in Figure 5.18. As discussed in Subsection 5.2.2, the phase profiles of the array elements can be calculated for each designated position of the centre of the Bessel-function field. For a desired PHA_RES_DEG, the exact phases are rounded-off into nearest phase values that can be represented by the FPGA outputs, based on a round-off resolution of $PHA\_RES\_DEG/2$. Although the calculation is based on the polar coordinate, it is more intuitive to assign the trapping positions within a Cartesian coordinate, hence a coordinate transformation is performed.

In the GUI, the inner diameter of the circular array is divided into N points, where N is the "Grid Points" that can be directly defined. Hence a Cartesian coordinate system can be created, as shown in Figure 5.19, with the axis length equal to the device inner diameter, R = 5.49 mm, to map the coordinates of the traps into real dimensions within the device. By default the array element No.1 is located at the coordinate of (250, 501), or (0, R) for the real dimension. The Bessel-function field centre can be manipulated to that position, with the coordinate directly configured from the GUI. A trajectory of multiple trapping positions can be designated with a set of coordinates, either by typing them into the GUI or by loading directly from an external data file. Particles can then be transported along the trajectory, either running continuously with a specific time interval between the steps, or being controlled step-by-step. For direct visual assistance, graphs are created to indicate the coordinates of the traps and the dimension of the overall manipulation trajectory. Once the output is defined, the output parameters for channel frequency and phase configurations are saved into a data matrix and transferred through the UART.

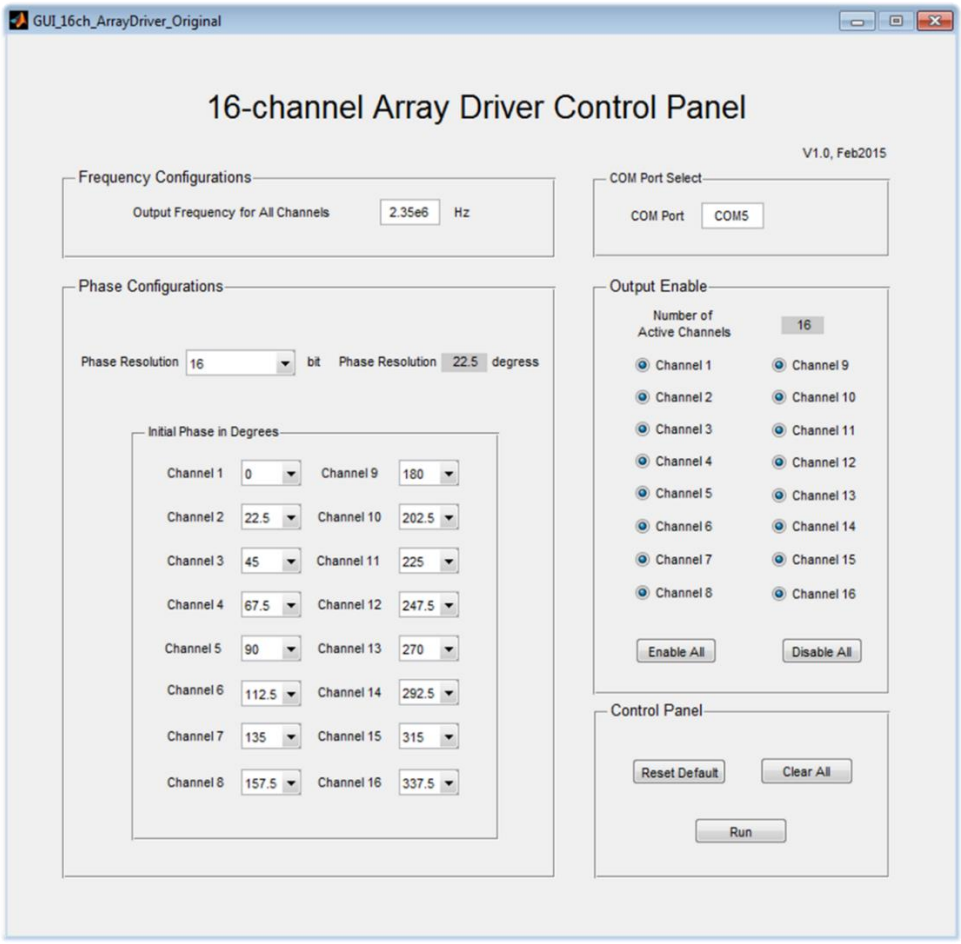

Figure 5.17 MATLAB GUI for a general-purpose 16-channel array driver control panel.

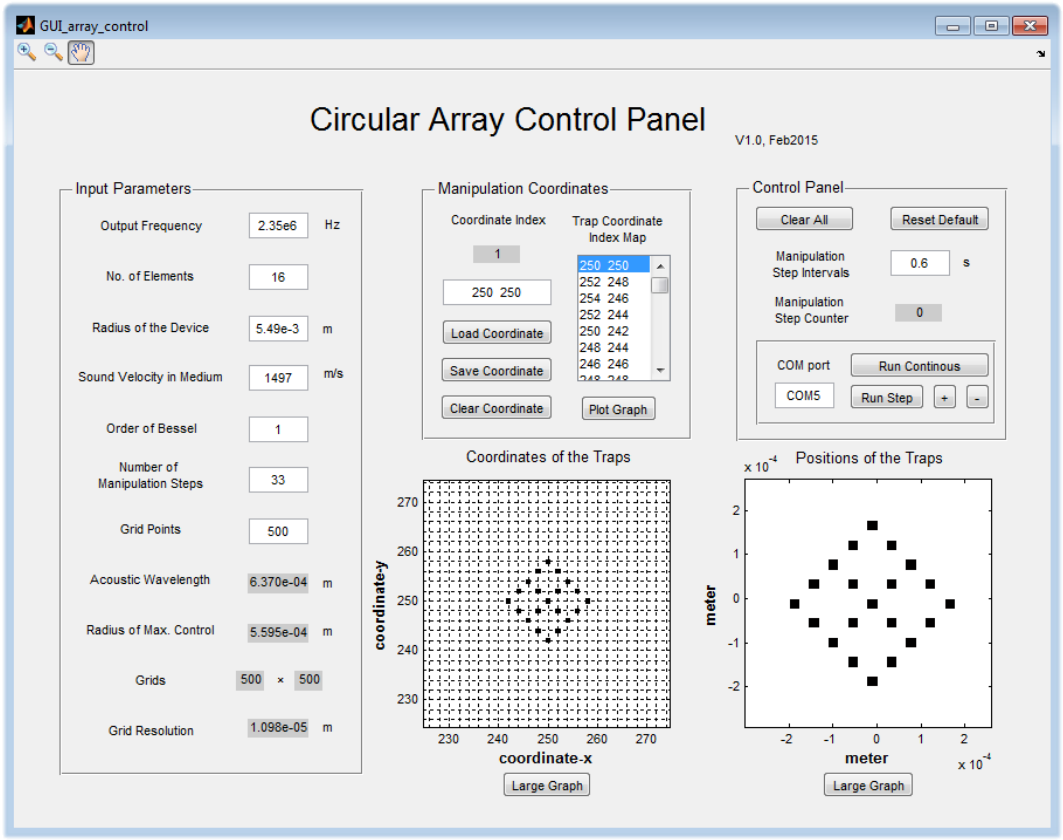

Figure 5.18 MATLAB GUI for the circular array Sonotweezer control panel.

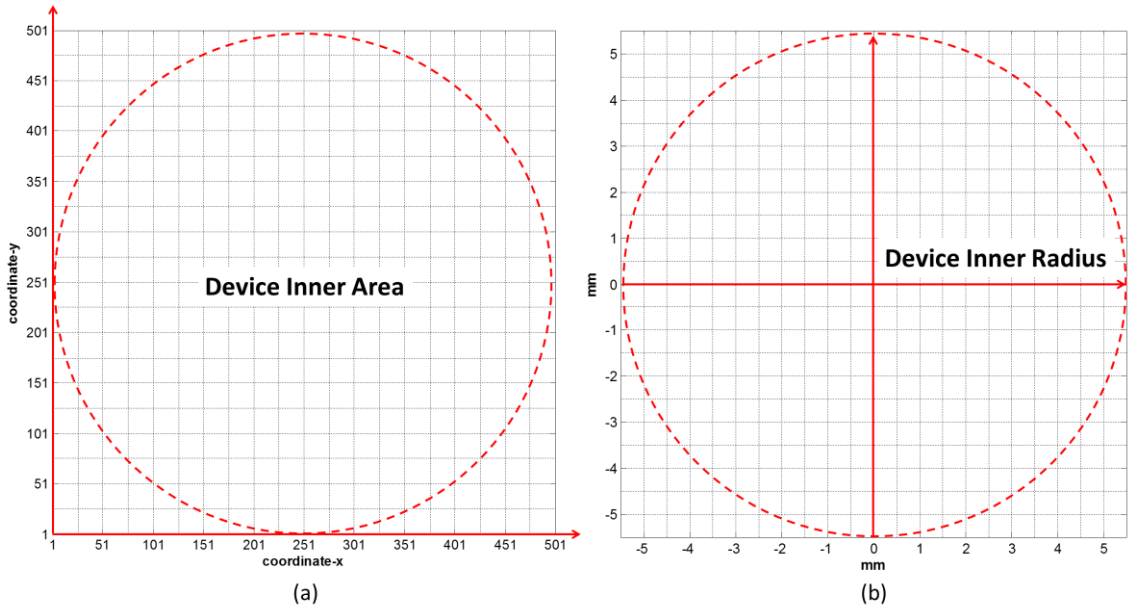

Figure 5.19 Cartesian coordinate system for the circular array Sonotweezer. The inner area of the device is mapped onto a matrix of 501 × 501 points.

5.5 Analogue Electronics Development

The outputs from the FPGA I/O lines all digital waveforms, represented by voltages of 0 or 3.3 V. To obtain both positive and negative voltages transducers and to provide sufficient drive amplitude, simple signal conditioning was connected to the FPGA outputs. The conditioning circuitry also serves as a signal amplitude modulation stage. A power amplifier array circuitry was cascaded with the conditioning circuit for generating parallel outputs with sufficient voltages. The amplifier circuit topology is identical for each channel, and the design is the same as discussed in Chapter 5. To realise the circuit, a schematic was first created and simulated with SPICE models. Then a single channel test circuit was constructed for debugging and practical functional verification. Finally complete circuitry with 16 channels was designed and constructed.

5.5.1 Signal Conditioning Circuitry

Figure 5.20 shows time domain data of a digital output directly from the FPGA and the fast Fourier transform (FFT) of the signal for spectra analysis. For a target frequency of 2.35 MHz, the FFT spectrum shows that the peak for the 3rd harmonics is only -9.6 dB below the fundamental peak, and there are significant ringing components in the high frequencies. These can be suppressed with a low-pass filter. The schematic design of the signal conditioning circuitry is shown in Figure 5.21 (a). The first part of the circuit is a simple passive low pass filter, which can reduce the overshoot at the transition edges of the digital voltages. The -3 dB cut-off frequency, f_c, can be calculated as $f_c = 1/(2\pi RC)$. With R_1 = 68 Ω and C_1 = 400 pF, f_c = 5.85 MHz. This passive RC filter may also be considered as an integrator circuit that can convert the square wave into a triangular, near sinusoidal waveform (Horowitz and Hill, 1989e).

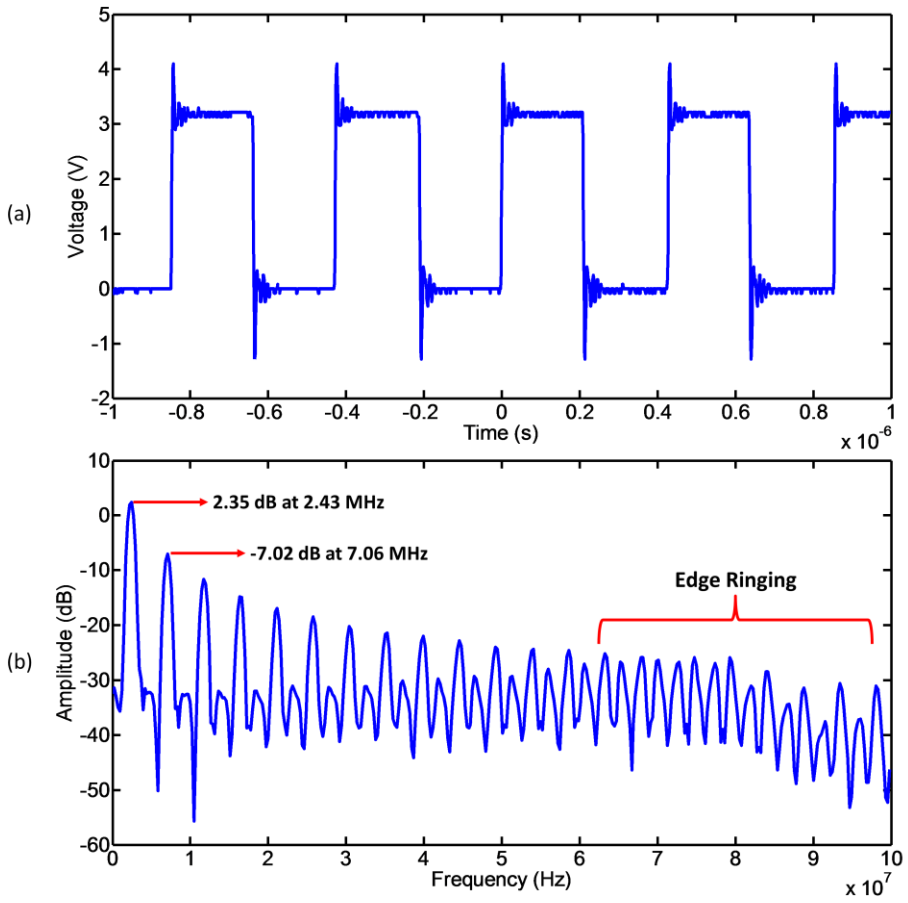

Figure 5.20 Time domain and FFT waveforms of the digital signal. (a) Time domain 2.35 MHz digital output from FPGA. (b) FFT output of the signal in (a). The frequency spectrum reveals the high-order harmonics, and the edge ringing frequency components.

The next part of the circuitry has two primary functions. First, the capacitor C_2 and resistor R_2 consist a differentiator circuit that converts the unipolar digital voltage into a bipolar voltage with both positive and negative swing (Horowitz and Hill, 1989e). Second, the resistance of R_2 can be adjusted with a potentiometer, and hence the output voltage amplitude can be linearly varied from zero to the maximum voltage. SPICE simulation is shown in Figure 5.21 (b) and (c). The values of the capacitor and the resistor were carefully chosen to obtain an appropriate RC time constant, short enough to allow a fast transition from unipolar state to bipolar state at the output, but not too short to regulate the output waveform into a pulse train. As shown in Figure 5.21 (c), for a 5 MHz test digital signal with a voltage of 3.3 V_{pp} at an unloaded output, the signal past C_2 is regulated into the range of ±1.65 V, and the output amplitude can be adjusted from 0 to 3.3 V_{pp} with the potentiometer. The output voltage settles into bipolar state within about 25 µs.

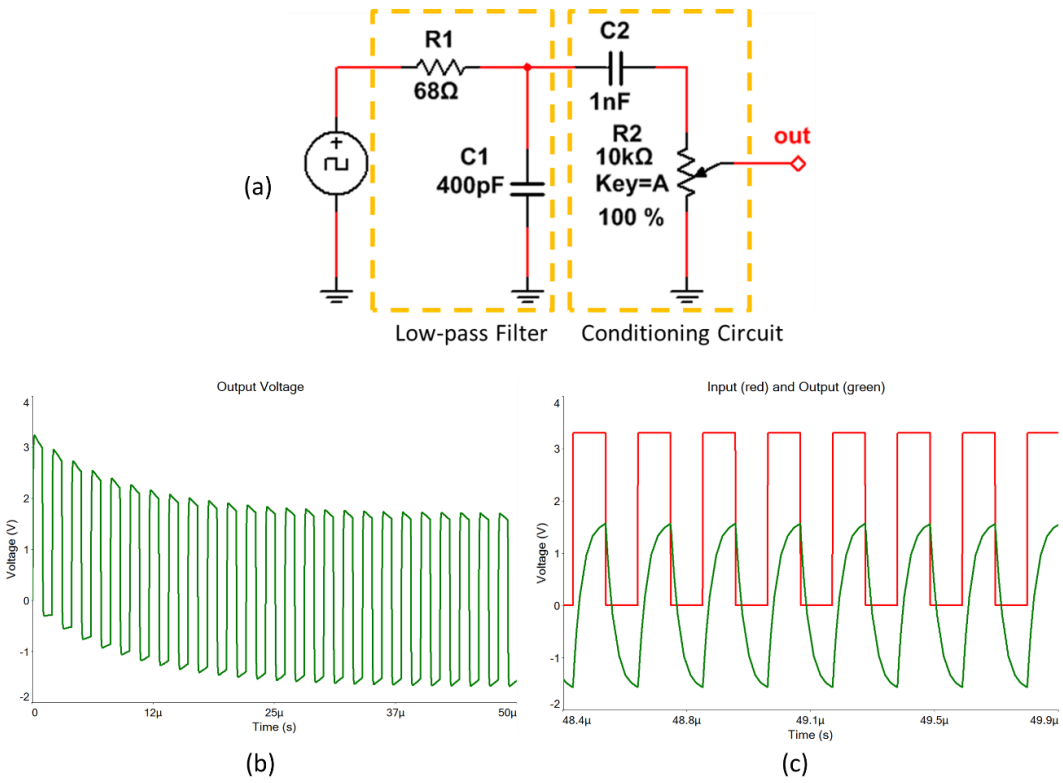

Figure 5.21 (a) Schematic design of the signal conditioning circuitry. A SPICE transient analysis of the signal conditioning circuitry is performed, with a digital input of 3.3 V_{pp}. (a) The output voltage settling time is about 25 µs. Frequency of the test signal is 500 kHz. (b) A comparison of the voltage polarity between the input (digital) and the output (near-sinusoidal). Frequency of the test signal is 5 MHz.

5.5.2 Amplifier Array

The circuit design of the amplifier for each channel is similar to the design in Chapter 5. An op-amp is connected to a current buffer and the circuit is configured as a non-inverting amplifier with a fixed voltage gain of 20 dB. Figure 5.22 (a) is the complete schematic of a single channel amplifier connected with a signal conditioning circuitry. At the non-inverting input of the op-amp, in contrast to the previous design, a voltage divider comprising two resistors, R_3 and R_4, is connected between the signal conditioning circuit and the amplifier. A pull-down resistor, R_4, serves to reduce noise at the non-inverting input. The value of R_4 is 100 times of R_3 to maintain the voltage level at the op-amp input at the level transferred from the previous stage. R_3 should have a large value, comparable to the maximum value of potentiometer, R_2, because when connected with the amplifier, R_3, R_4 and R_2 together with C_2 form a new differentiator circuit, and equivalent RC time constant will be maintained only if R_3 and R_4 are relatively large. In addition, a high resistance value of R_3 can be used as protection to prevent possible high surge currents

flowing back into the FPGA electronics. The SPICE simulation results are shown in Figure 5.22 (b) and (c). A 100 pF capacitor has been used as a load to mimic the Sonotweezer transducer.

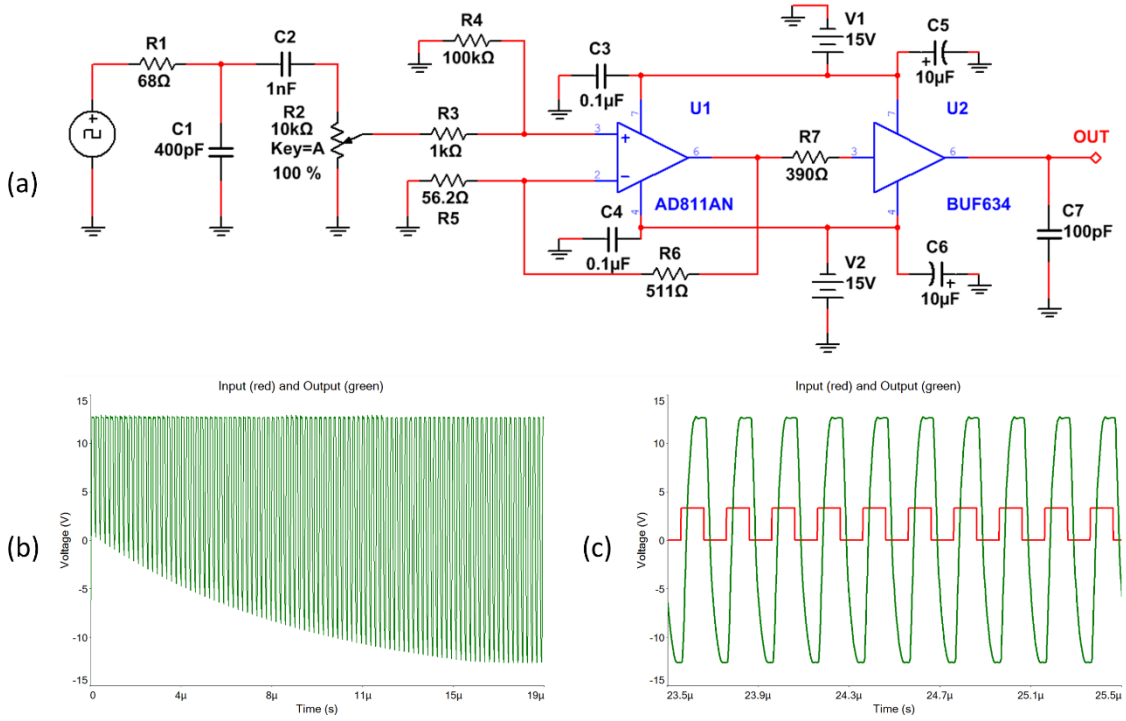

Figure 5.22 (a) Schematic for a single channel analogue circuitry. A SPICE transient analysis of the complete analog circuitry is performed with a digital input of 3.3 V_{pp} at 5 MHz. (a) The output voltage settling time is about 15 µs. (b) The output is bipolar signal with a maximum voltage of 26 V_{pp}.

5.6 Electronic Hardware Fabrication

A complete single-channel analogue circuit with a single conditioning circuit and an amplifier was firstly tested and verified with breadboard prototypes and in-house fabricated PCBs. The final version of PCB circuitry requires 16 identical analogue channels, with external power supply unit (PSU) and proper ventilation. This section will discuss the process for hardware fabrication and assembly of the final 16-channel system.

5.6.1 PCB Design and Fabrication

The signal conditioning PCB combines 16 identical channels and can be connected directly with Spartan-3a FPGA development board, as shown in Figure 5.23 (a). The

amplifier array PCB is shown in Figure 5.23 (b). Eight channels are combined together on a single PCB, and each 8-channel amplifier board is plugged into a backplane PCB, as shown in Figure 5.23 (c). The backplane provides electrical power for the amplifiers and buffers, and combines the output from all channels into two output sockets. The schematics and PCB layouts can be found in Appendix B.

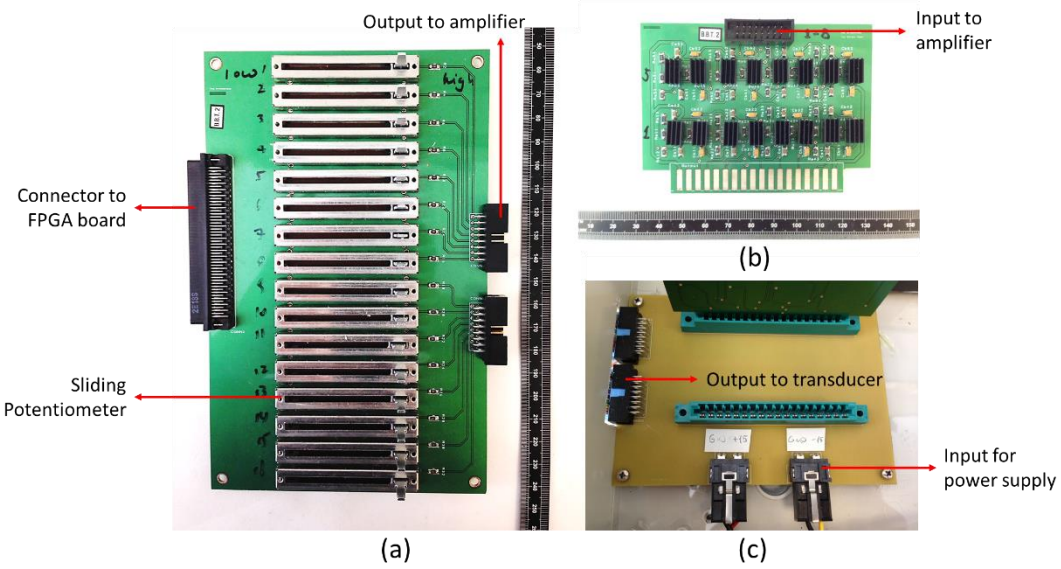

Figure 5.23 Fabricated PCBs for analogue electronics. (a) 16-channel signal conditioning circuitry PCB. (b) 8-channel amplifier PCB. (c) A backplane board for two 8-channel amplifiers.

5.6.2 PSU

The maximum electrical power needed for a 16-channel amplifier system can be assumed as an accumulation of the maximum output power and maximum quiescent power that will mostly be transformed into heat. Both op-amp and current buffer will consume quiescent power. For a single channel, the required power can be expressed as:

$$\begin{cases} P_{total} = P_{out} + P_{quiescent} \\ P_{quiescent} = 2I_{quiescent}V_{supply} \\ P_{out} = \frac{1}{2}V_{out}I_{out}\cos(\Delta\phi) \end{cases} \quad \textbf{(5.11)}$$

In the above equations, V_{out} and I_{out} are the peak output voltage and current respectively. The maximum output power will be achieved when there is no phase shift between the

output voltage and current and $\Delta\phi$ = 0. Referring to the data sheets ("250mA HIGH-SPEED BUFFER", 1996, "AD811 High Performance Video Op Amp", 1999), the maximum quiescent currents for the op-amp and buffer are ± 18 mA and ± 20 mA respectively, giving a total quiescent current $I_{quiescent}$ = ± 38 mA. For a ± 15 V voltage supply, the quiescent power, $P_{quiescent}$ can be calculated as 1.14 W for a single channel. At the output, the maximum possible output current from the buffer is ± 250 mA_{rms}, and the maximum possible output voltage is limited to 26 V_{pp}. The output power for a single channel can then be calculated as P_{out} = 1.56 W. Hence the maximum required power for each channel is P_{total} = 2.7 W. For a 16-channel system, the power needed are thus 43.2 W. Based on this calculation, a 60 W, ± 15 V switch mode modular PSU (TXL 060-0533TI, Farnell, UK) was selected.

5.6.3 Hardware assembly

All the electronics were assembled into a casing with a two-layer chassis. The PSU and the amplifier array were placed in the lower layer, and the FPGA development board and signal conditioning circuitry were fixed on top. A fan was attached to the back of the casing to provide ventilation. Each 8-channel amplifier board was directly plugged onto the backplane, and also connected with the signal conditioning PCB with flat ribbon cable. The outputs were connected to the transducer elements with a flat-to-twist ribbon cable. A photograph of the complete 16-channel array driving system is shown in Figure 5.24 and photographs of the hardware assembly can be found in the Appendix B.

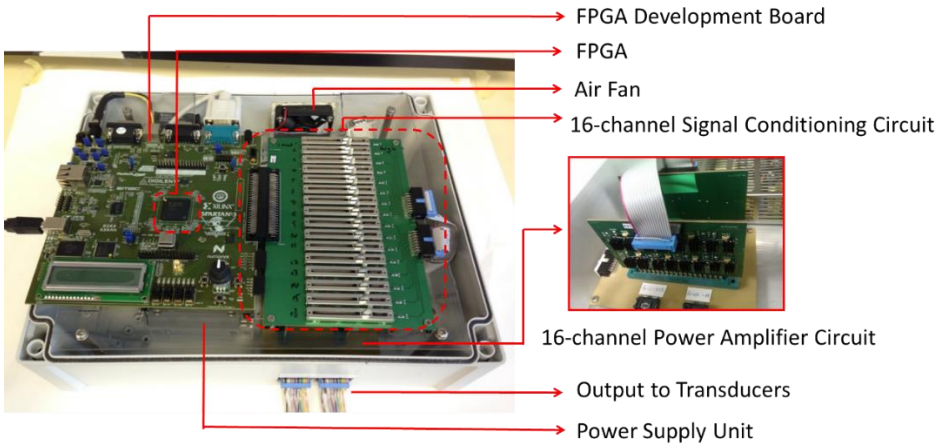

Figure 5.24 Photographs of the complete 16-channel array driving system assembly.

5.7 Functional Characterisation of Electronics

This section presents the electronics characterisation results. The digital and analog electronics were tested separately. Functional validation of the array driving system performed with direct measurement of the digital signals that transmitted from the FPGA development board. A bespoke pin-out extension PCB was attached to the FPGA 100-pin output connector, and signals from all 16 channels were measured with digital channels of the oscilloscope. The test signals were generated from the FPGA core under the control of the MATLAB GUI.

The analogue channels on the oscilloscope were also used for both digital and analog electronics characterisation. The signals were measured from the outputs of 1 m long flat to twist ribbon cables, with the ends split into multiple channels. The high voltage analogue outputs were measured directly by connecting a test probe on the outputs. Figure 5.25 is a photograph of the test fixture setup.

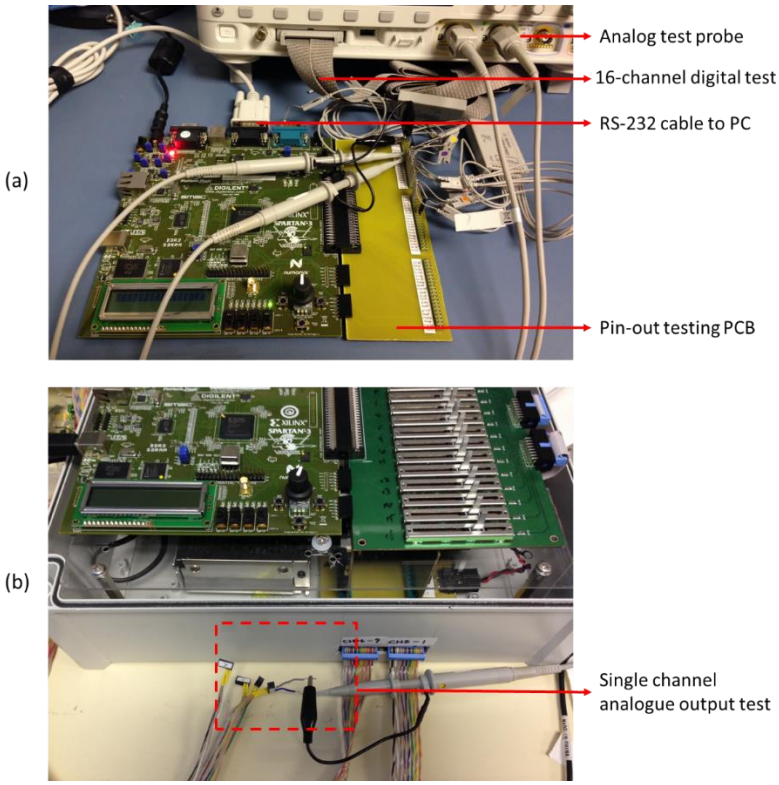

Figure 5.25 Test setup for electronic characterisation. (a) Setup for measuring the digital outputs from the FPGA. (b) Setup for measuring the analogue outputs from the whole system.

5.7.1 Digital Electronics Functional Validation

In the GUI, a test frequency of 2.35 MHz was used to configure all channels with various phase conditions. The phase resolution was set to be 16 levels, with 22.5° relative difference between channels. The measurements are shown in Figure 5.26. The waveforms displayed are digital with amplitudes of 0 and 3.3 V. For the frequency measurement, additional to the instantaneous signal frequency, in the oscilloscope an integrated hardware frequency counter counts the number of cycles that occur within a gate time (from twice the current time window up to 1 second) and gives an accurate measurement of the time-averaged signal frequency. The time-averaged minimum phase difference between two channel outputs was measured as 22.5°, which matches well with a theoretical 16-level phase resolution, and the instantaneous duty cycle of the signal was measured as 50 % ± 1 %, which is very close to the theoretical duty cycle of 50 % calculated from Equation (5.10) with N = 3, K = 2053 and M = 3760, for a fractional factor of (N + K/M).

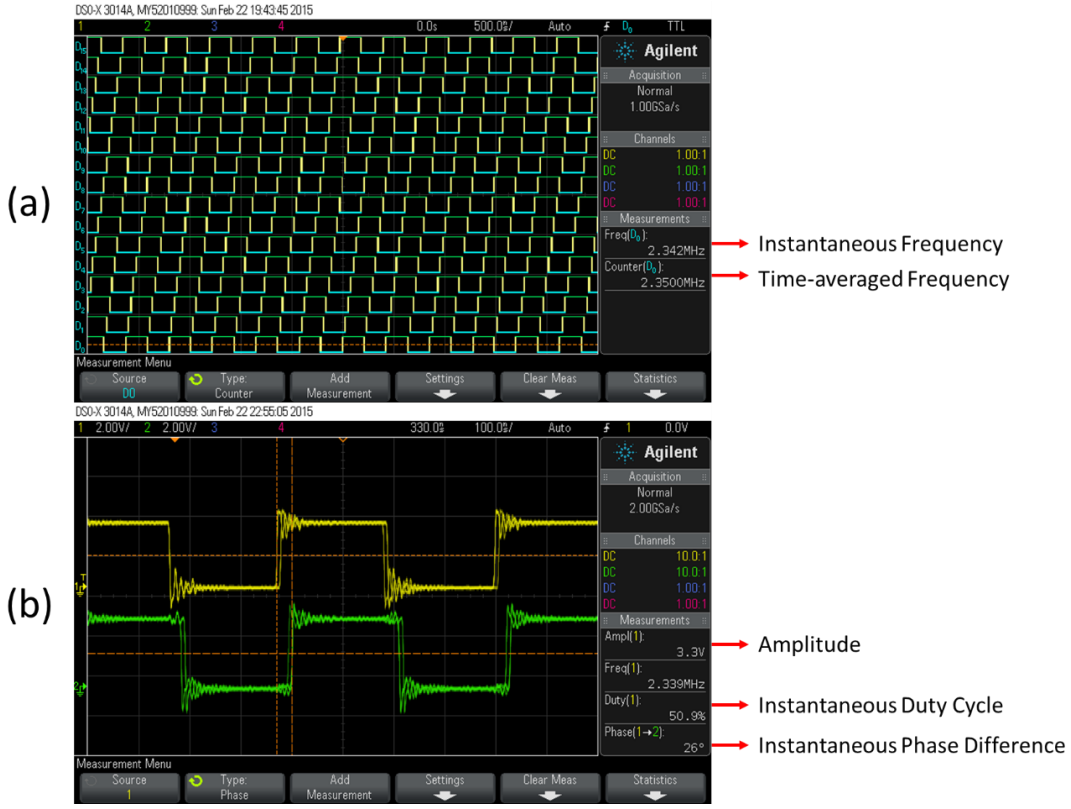

Figure 5.26 Oscilloscope measurement of frequencies and phases of digital outputs. The frequency was set as 2.35 MHz for all channels. (a) 16 output waveforms measured with oscilloscope digital channels. All outputs are enabled with a time-averaged relative phase difference of 22.5°. (b) Two output waveforms measured with oscilloscope analogue channels.

For 16-bit frequency resolution, theoretically the fractional factor ranges from 1 to 2^{16}. According to Equation (5.8), for the maximum clock frequency of 133.33 MHz by the FPGA development board, with 16-level phase resolution, the minimum and maximum achievable frequencies are 133.33 MHz / (2^{16} × 16) = 127.1534 Hz and 133.33 MHz / (2 × 16) = 4.1666 MHz, respectively. Additionally, higher output frequencies can be achieved, with a reduced *PHA_RES_BIT*. Theoretically with 2-bit phase resolution, the maximum output frequency for the existing setup is 133.33 MHz / (2 × 2) = 33.333 MHz. Hence the full range of frequency outputs for the current system is 127.15 Hz ~ 33.333 MHz.

Experimental measurements of the output frequency range are shown in Figure 5.27 (a). The generated minimum and maximum time-averaged frequencies are 127.15 Hz and 33.332 MHz respectively. Waveform jittering is visible, as shown in Figure 5.27 (b). This jittering can cause quantization phase error, which arises from quantized divisions with factors of N or (N + 1) in alternation to mimic an imaginary fractional factor of ($N + K/M$). The instantaneous quantization phase error, Φ, is time-integrated and relates to the real-time fractional factor of N_i, which is quantized as either N or (N + 1) ("Basics of Dual Fractional-N Synthesizers / PLLs", 2005):

$$\Phi = 360^\circ \cdot \sum i \left(\frac{N\frac{K}{M} - N_i}{N\frac{K}{M}} \right) \qquad \textbf{(5.12)}$$

The instantaneous quantization phase error appears less when the division factor is close to an integer value. Generally severe jittering can raise stability issue because of consequent errors in the instantaneous frequency and relative phase difference. Also such jittering at the outputs for driving transducers may potentially affect the positions of the pressure nodes / antinodes in the USW field, depending on the types of Sonotweezer devices under test.

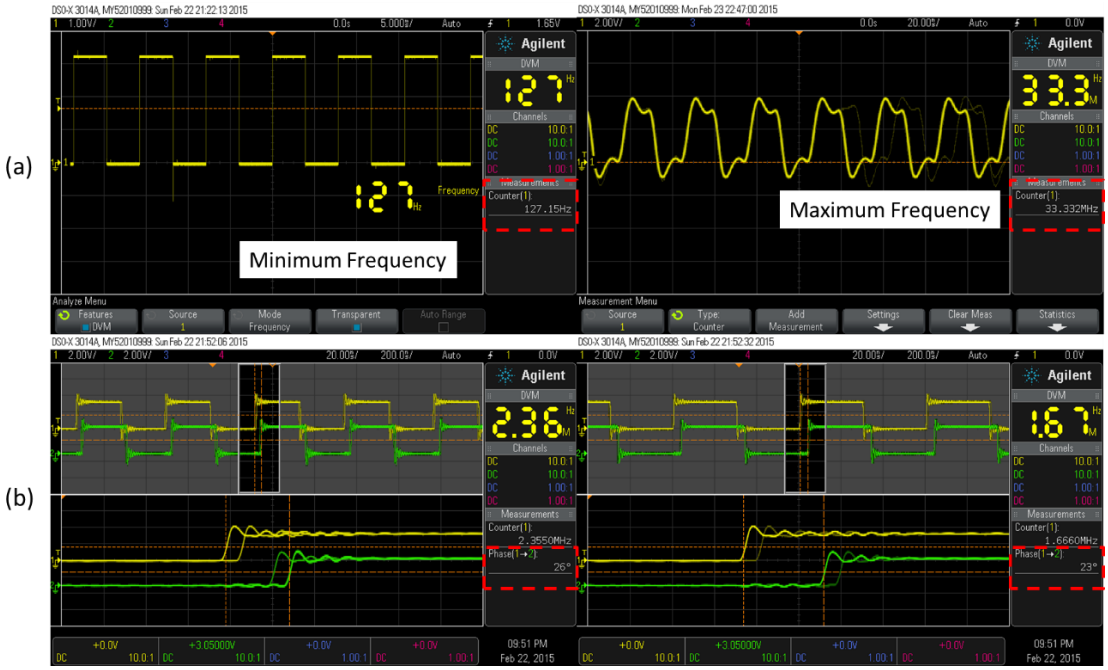

Figure 5.27 (a) Measured minimum and maximum frequency outputs. Red dashed lines indicate the measured minimum frequency of 127.15 Hz and maximum frequency of 33.332 MHz. (b) Zoom-in view for a comparison of the waveform jittering and instantaneous phase errors (red dashed line) for a 22.5° phase shift, with different fractional factors, reference to a source frequency of 133.33 MHz. A 1.666 MHz signal with a fractional factor of (5 + 25 / 13328) has less phase error than a 2.355 MHz signal with a fractional factor of (3 + 2029/3768).

For counter-propagating devices like circular arrays, although for a certain frequency fractional factor, the same scale of jittering appear at all output channels, however those channels are not exactly identical considering the variations of in the electrical interconnections. Measured from the output of the FPGA development board in Figure 5.27 (b), for a 16-level phase resolution with a reference frequency of 133.33 MHz, and a working frequency of 2.35 MHz, a fractional factor of (3 + 2029/3768) results in a jittering that cause instantaneous phase difference between two adjacent channels varies with a scale of ± 3.5° over the desired value. However since the 16-element array has a phase resolution of 22.5°, in the phase profile calculation algorithm the exact phase for each element are rounded-off into a certain phase from 0° to 337.5°, while the difference is within 11.25°. As a result the variation of ± 3.5° will not be influential as it is smaller than the round-off resolution of 11.25°. Further suppression of the jittering need to be considered for applications with high phase resolutions that are close to the instantaneous phase error. A consideration of the jittering when driving other kinds of Sonotweezer devices with be further discussed in Chapter 7.

Theoretically the frequency tuning resolution is increased with a higher binary resolution for the components *N*, *K*, *M* in the fractional factor. For a 16-bit data range, the frequency resolution was measured experimentally as shown in Table 5.4. For Sonotweezer devices working at the frequency range of 1 – 10 MHz, the tuning resolution is sufficient, and especially useful for the multilayer USW devices which have high demands for frequency tuning to match the device resonance accurately (Glynne-Jones et al., 2012).

Table 5.4 Measurement of frequency tuning resolution for different frequency range.

Frequency Range	Maximum Tuning Resolution
1 MHz – 33.332 MHz	0.001 MHz
1 kHz – 999.999 kHz	0.001 kHz
127.15 Hz –999.99 Hz	0.01 Hz

5.7.2 Analogue Electronics Characterisation

The analogue outputs from the multichannel electronics were measured to examine the characteristics of waveform shape, large signal response, bandwidth, output current and power, channel crosstalk, and output consistency across the channels. The characterization results demonstrated in the following text are based on the measurements from a single channel output.

A. Impedance Spectrum of Circular Array Sonotweezer

The circular array Sonotweezer was characterized specifically as the present target device to determine load conditions. Each transducer element was measured in air with an impedance analyser and the frequency spectrum was plotted. The piezoceramic ring has a thickness t = 0.87 mm, and height h = 1.60 mm. In Figure 5.28 (a) it can be found that the first thickness extensional resonance frequency measured in air is 2.35 MHz. Figure 5.28 (b) and (c) show the impedance magnitude and phase spectra for each element; at the operating frequency of 2.35 MHz the impedance amplitudes are relatively large in the range of 1.5 kΩ to 5 kΩ. A summary of the electrical impedance magnitude of each element at 2.35 MHz is shown in Table 5.5. The impedance magnitude inhomogeneity will introduce variations of the voltages over the array elements. This can be compensated

by carefully adjusting the amplitude control potentiometers at the output stage of the driving electronics.

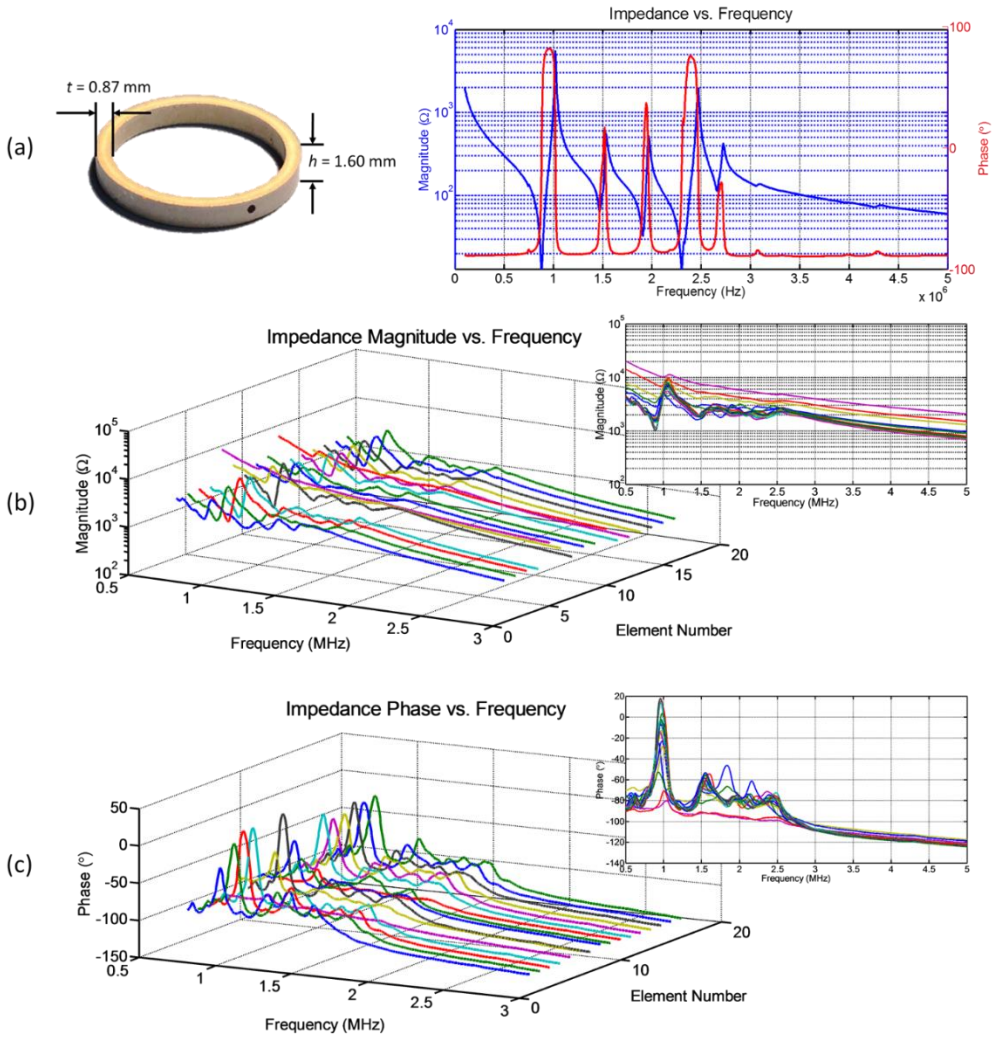

Figure 5.28 Impedance spectra of the 16-element circular array device. (a) The dimension of PZ-27 piezoelectric ring and its impedance characteristics. 1st thickness extensional resonance is 2.35 MHz. Impedance (b) magnitude and (c) phase for each transducer element after array fabrication.

Table 5.5 Summary of the electrical impedance magnitudes and phases of 16 transducer elements of the circular array at the working frequency of 2.3 MHz.

No.	Magnitude (kΩ)	Phase (°)	No.	Magnitude (kΩ)	Phase (°)
1	2.74	-83.13	**9**	2.51	-78.17
2	1.96	-82.60	**10**	3.62	-96.46
3	2.14	-83.94	**11**	1.87	-78.74
4	1.74	-80.12	**12**	1.82	-71.70
5	4.98	-99.13	**13**	1.85	-79.91
6	3.21	-84.17	**14**	2.09	-81.33
7	1.89	-77.46	**15**	1.98	-76.53
8	2.42	-80.42	**16**	1.99	-80.62

B. Waveform analysis

For each channel, the analogue output signal is a near-sinusoidal waveform, and the amplitude can be adjusted linearly with the potentiometers on the signal conditioning PCB. Figure 5.29 shows the time domain waveform and frequency spectrum of a 2.35 MHz signal with 20 V_{pp} amplitude. The high frequency components from the 3rd harmonics upwards have been suppressed to at least -20.5 dB compared to the fundamental frequency.

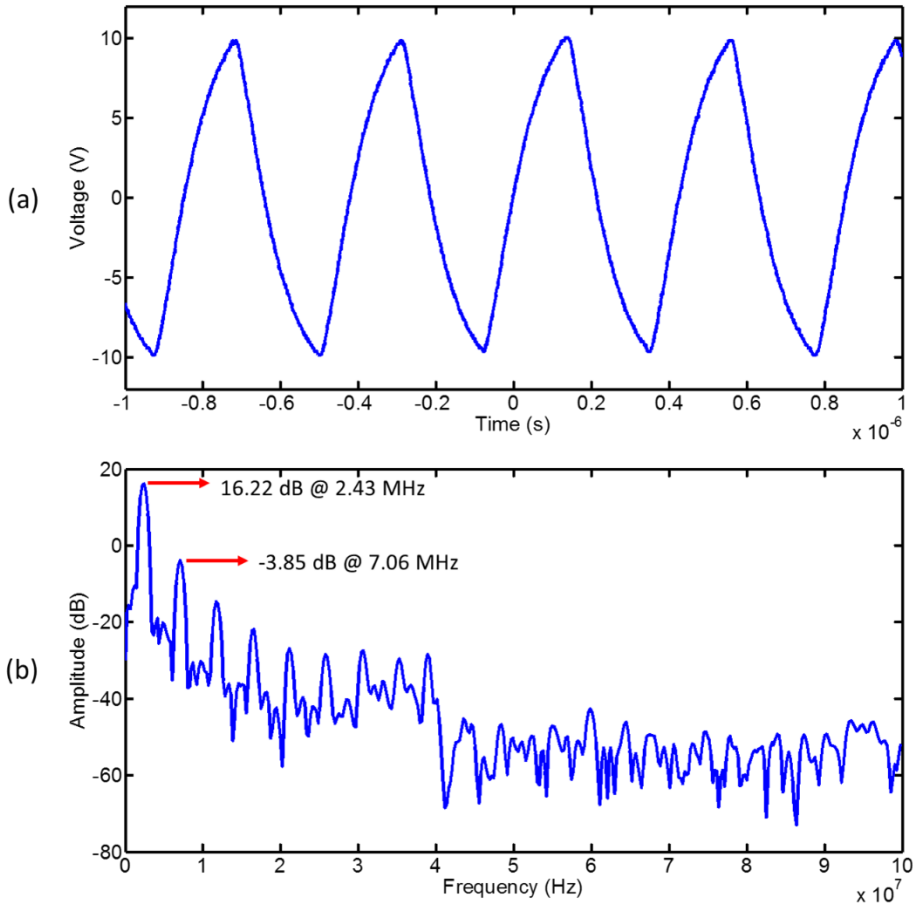

Figure 5.29 (a) 2.35 MHz, 20 V_{pp} near-sinusoidal signal output. (b) Frequency spectrum of the signal in (a) from FFT.

C. Large Signal Response

For the analogue circuitry, the large signal response was characterised by measuring the slew rate of the output signal with the waveforms shown in Figure 5.30. The square wave is the output from the FPGA (red dashed line). For a single-channel near sinusoidal output

with amplitude of 20 V_{pp} (blue line), the time for the amplitude transition from 10 % to 90 % is measured as 148 ns, corresponding to a slew rate of 108.6 V/µs. This slew rate is mainly affected by the passive RC filter in the first stage of the analogue circuitry.

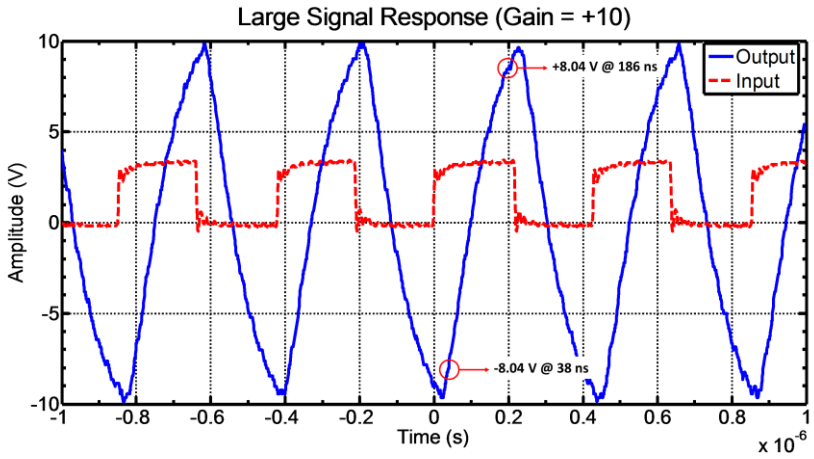

Figure 5.30 Larger signal response for Gain = +10.

D. Output Bandwidth

Theoretically, the large signal full power bandwidth (FPBW) of the amplifier array is 30 MHz. Experimentally, the output bandwidth was measured under different resistive load conditions, as shown in Figure 5.31. Resistive loads were chosen as the representatives for the ideal case of the electrical impedance magnitudes of the array elements. The test load ranges from 15 Ω to 3300 Ω. The amplifier has a fixed gain of 20 dB, and with open load, the output of the amplifier saturates and has a maximum amplitude of about 25 V_{pp}. For an input frequency over 11 MHz, the waveform becomes unstable and cannot be measured. For input frequency lower than 100 kHz, the resulted waveform resembles a pulse shape.

In Figure 5.31 it can be found that for all load conditions, the -3 dB bandwidth are between 5 MHz and 6 MHz, and -6 dB bandwidth are between 6 MHz to 8 MHz. For the circular array with impedance magnitude of 1.5 kΩ to 5 kΩ, the -3 dB and -6 dB bandwidth are around 6 MHz and 8 MHz, respectively. Also it can be noticed that the frequency response is poor for output loads under 30 Ω, as the output waveforms become unstable for frequencies higher than 6 MHz. A summary of the frequency responses for different resistive loads is given in Table 5.6. As the bandwidth measurement was taken at discrete

integer frequency values, the -3 dB and -6 dB cut-off frequencies are predicted by fitting the curve in the stop-band. The slopes of the bandwidth curves after -3 dB cut-off frequency are depicted by dB/octave.

The resultant bandwidth is a combined contribution of all the components in the analogue circuitry. As the FPBW of the op-amp and the current buffer are much higher, the main limitation is the bandwidth of the signal conditioning circuitry. At the low frequency end, the time constant, τ, is controlled by the differentiator circuit, $\tau = R \times C$, and the maximum value is τ = 1 nF × 10 kΩ = 10^{-5} s. Hence any signal with frequency lower than 100 kHz will have a shape close to a short pulse instead of a sinusoidal waveform. At the high frequency end, the low pass filter limits the -3 dB output frequency.

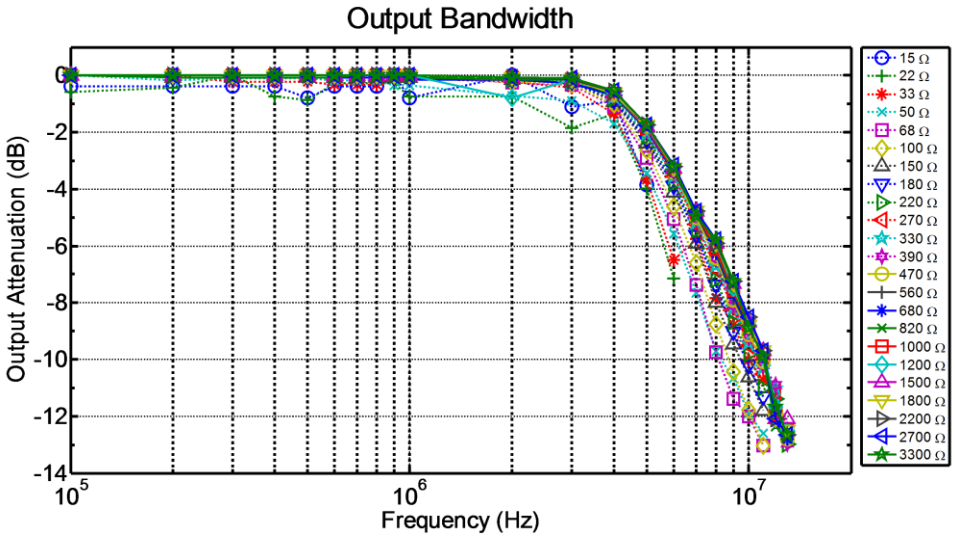

Figure 5.31 Output bandwidth measurement for different load conditions.

Table 5.6 Summary of the frequency response of the outputs for different resistive load conditions.

Load Resistance (Ω)	Cut-off Frequency (MHz)		Stop-band Slope (dB/octave)
	-3 dB	-6 dB	
15	4.71	5.72	N / A
22	4.63	5.76	N / A
33	4.46	6.82	6.35
50	4.74	6.51	8.48
68	5.06	6.70	9.10
100	5.20	6.83	9.14
150	5.37	7.19	8.23
180	5.46	7.35	7.94
220	5.55	7.50	7.67
270	5.68	7.67	7.52
330	5.63	7.66	7.36
390	5.72	7.78	7.29
470	5.79	7.83	7.23
560	5.81	7.92	7.08
680	5.78	7.93	6.97
820	5.82	7.98	6.92
1000	5.82	7.98	6.92
1200	5.85	8.04	6.86
1500	5.88	8.05	6.90
1800	5.89	8.02	7.05
2200	5.93	8.15	6.77
2700	5.93	8.15	6.77
3300	5.88	7.98	7.14

E. Output Peak-peak Voltage, RMS Current and RMS Power for Different Load Conditions

The output characteristics were examined by taking direct measurement of a single channel peak-peak voltages across different loads from 15 Ω to 3.3 kΩ, for the output frequencies from 100 kHz to 11 MHz. And for different loads, the output RMS current and RMS power were calculated. The results are shown in Figure 5.32, and it can be seen that the output voltage is low for small load resistance because of the limited maximum output current. Within a frequency range of 1 – 10 MHz, the maximum output RMS current can reach 216 mA for 15 Ω load, which is close to the 250 mA maximum rating of ADG5434. And maximum output RMS power can reach 1.0 W at 33 Ω load.

(a)

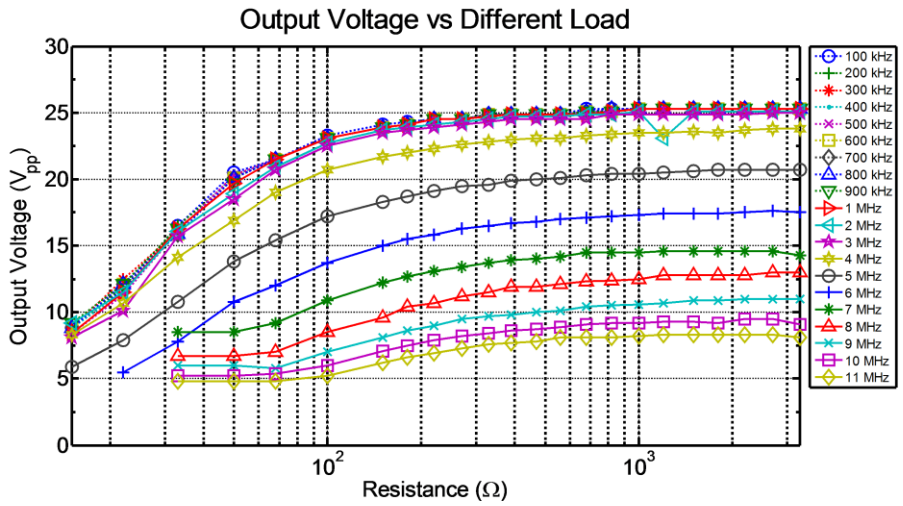

(b)

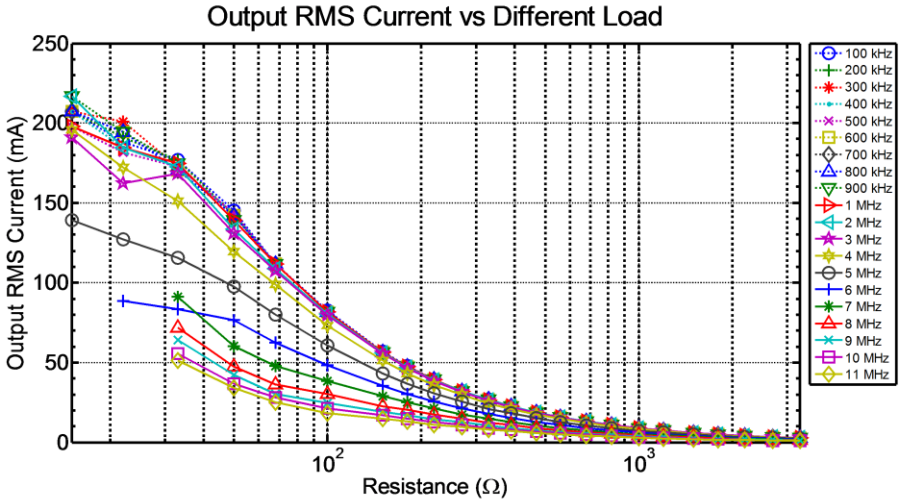

(c)

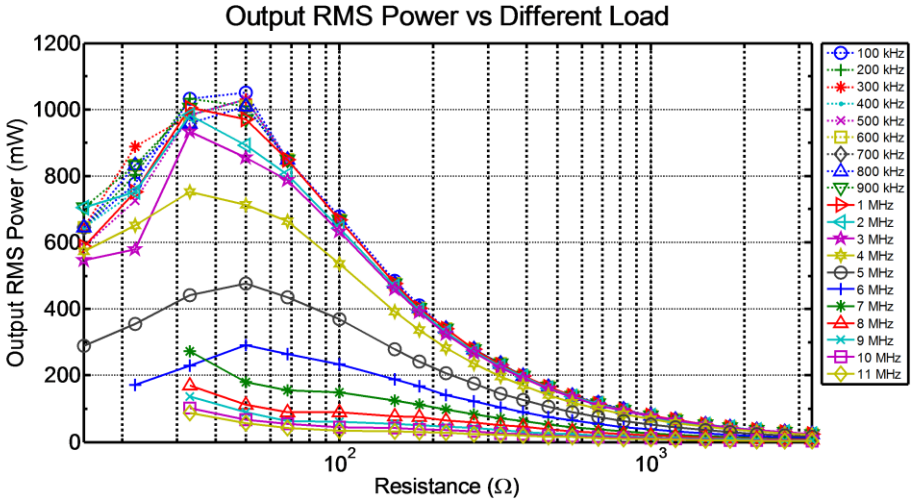

Figure 5.32 (a) Output peak-peak voltage vs. load resistance. (b) Output current vs. load resistance. (c) Output RMS power vs. load resistance.

F. Channel Crosstalk

The electrical crosstalk between channels can be defined as the ratio of the signal amplitude measured at the "ON" channel and the amplitude measured at the adjacent "OFF" channel, taking the form $crosstalk = 20\,log(V_{OFF}/V_{ON})$. Within -6 dB bandwidth for an output load of 50 Ω, the crosstalk was measured as -28 ± 2 dB.

G. Output Consistency across the Channels

The consistency across all the channels was examined by comparing the output amplitudes. For each channel, the output amplitude was set to be its maximum, by sliding the potentiometer to the maximum resistance position. Since the output of each channel can be varied linearly with the potentiometer, it is reasonable to infer the output consistency when the channels are working at other amplitudes. At the circular array working frequency of 2.35 MHz, with open load condition, the output voltages of all the channels were measured and summarized as shown in Table 5.7. There is a good output consistency across the channels, except for channel 4, with -0.57 dB attenuation compared with others. Repeated testing with different output amplitudes confirmed this inconsistency, mostly because of fabrication issue, which can be improved by circuit debugging.

Table 5.7 Maximum voltage output of each channel at 2.35 MHz.

Channel Number	1	2	3	4	5	6	7	8	9	10	11	12	13	14	15	16
Voltage (V_{pp})	25.33	25.13	25.33	23.71	25.33	25.33	25.33	25.33	25.33	25.33	25.33	25.33	25.33	25.33	25.33	25.33

5.8 Experimental Demonstrations with Circular Array Sonotweezer

5.8.1 Experimental Setup

In experiments with the circular array Sonotweezer, 10 μm diameter polystyrene fluorescent microspheres (Fluoresbrite, Polysciences, Inc., Warrington, PA, USA) were

used in a water-based suspension with a concentration of approximately 2.7×10^5 particles/ml. A fluid chamber was prepared as shown in Figure 5.33 (a). An agar (Fisher Scientific UK Ltd., Loughborough, UK) layer was applied to half-fill the chamber to reduce the thickness of the fluid, in order to minimize Eckart acoustic streaming caused by absorbing of the acoustic energy by the bulk fluid (Bernassau, Glynne-Jones, et al., 2013). The agar layer also serves as a good sealant to prevent the chamber from leaking at the bottom. A photograph of the complete experimental setup is shown in Figure 5.33 (b). The device was placed under an epi-illumination fluorescent microscope for observation, with a camera recording video. The 16-channel array driving system was connected to the transducer array with ribbon cables.

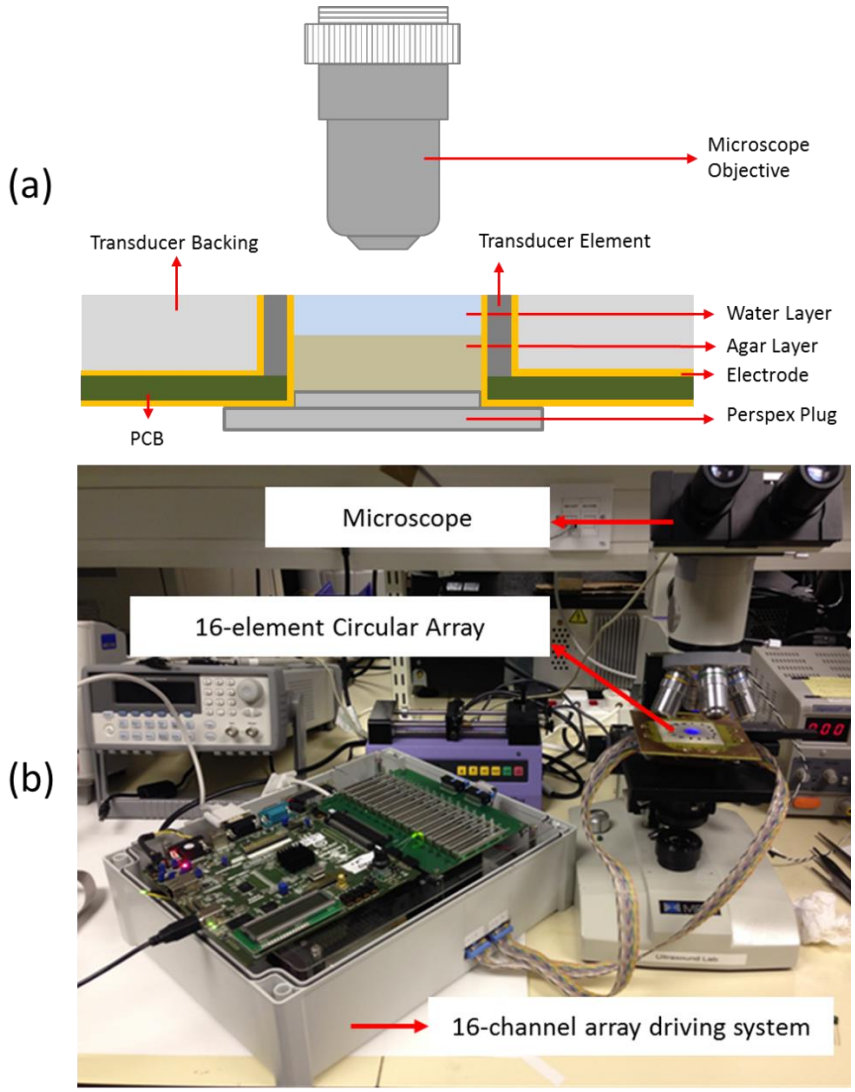

Figure 5.33 Experimental set-up for testing with the circular array Sonotweezer. (a) Cross-sectional view of the circular array device. The chamber is defined by a Perspex plug and the inner surface of the transducer elements. The cavity is half-filled with agar, and water suspension with polystyrene particles is introduced from the top. (b) A photograph of the complete experimental setup.

5.8.2 Experimental Results

A. Bessel-function Acoustic Field

When all the transducers were activated with relative phase shifts of 22.5°, a USW pressure field was formed, following a first-order Bessel function of the first kind given by $J_1(kr)e^{im\theta}$, with its centre coincident with the geometric centre of the array. k is the wave number and (r, θ) is the polar coordinate of each position in the acoustic field. The modelled acoustic field with normalized pressure amplitude is shown in Figure 5.34 (a). The boundary conditions were unrestricted and no acoustic attenuation and reflection were considered. The polystyrene microspheres were trapped at concentric circular-shape pressure nodes, with a central pressure node, as shown in Figure 5.34 (c). The diameter of the central trap was measured as about 30 μm. The diameter of each concentric circle in the field was derived from modelling, with the numbering shown in Figure 5.34 (b). In the experiment, the diameters of the same set of circles were measured from the image, and the results are compared in Figure 5.34 (d). The dimension of the measurements matches well with the theory, but with an increasing discrepancy towards the outer circles, attributed to the small trapping forces because of the lower pressure amplitudes.

B. Demonstration of Particle Manipulation

a. Trajectory Characterization

For the 16-element circular array Sonotweezer, a Cartesian coordinate system with 501 × 501 grids was projected onto the working volume as described previously. At PC level, a coordinate index map of 60 different intended acoustic trapping positions was imported into the GUI, as shown in Figure 5.35 (a), and a detailed zoom-in view is shown in Figure 5.35 (b). For the device internal diameter of 5.49 mm, the maximum coordinate resolution that can be defined by the grids as 5.49 mm × 2 / 500 = 21.96 μm. According to Equation (5.4), for a 16-element device with working frequency of 2.35 MHz, generating a 1st order Bessel-function field, the maximum manipulation area can thus be calculated to be within a circle of Ø1120 μm and theoretically, the overall manipulation dimension is 907.4 μm.

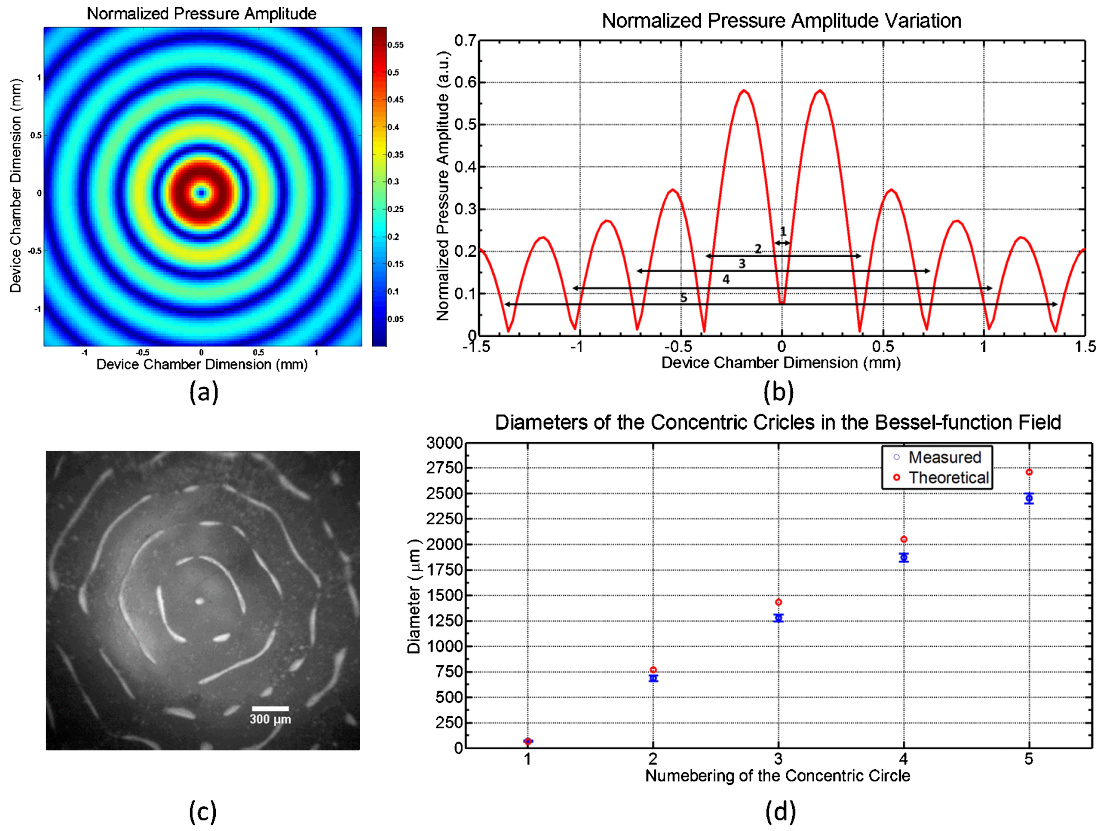

Figure 5.34 Bessel-function shape pressure field. (a) Calculated field of the 1st order Bessel-function of the first kind. (b) Polystyrene particles were trapped in the Bessel-function field pressure minimum positions. (c) A 1-D plot of the pressure amplitude variation across the device inner circle diameter. (d) Comparison between the calculations and measurements over the diameters of the concentric circles in the pressure field.

Based on the acoustic model, for each desired geometric position of the central pressure node, phase profiles for all 16 transducer elements were calculated and stored in a 16 × 60 2-D data matrix in MATLAB. Then these phase profiles were transmitted successively to the FPGA. After completion of data transmission, the FPGA core was then configured and output signals for all 16 channels were generated simultaneously to excite the transducers, with amplitudes of 22 V_{pp} at 2.35 MHz. Consequently, this allowed particles concentrated in the central pressure node, as well as those in surrounding circular pressure nodes, to be manipulated along the defined trajectory, either in real time with an update rate of 0.5 s, or manually step-by-step, under GUI control.

The central trap, together with other concentric traps were manipulated into 60 steps and the process was recorded into a video. The central trap movement trajectory was then manually tracked with ImageJ, as shown in Figure 5.35 (c). The shape of the trajectory was well maintained similar as depicted by the pre-assigned coordinates.

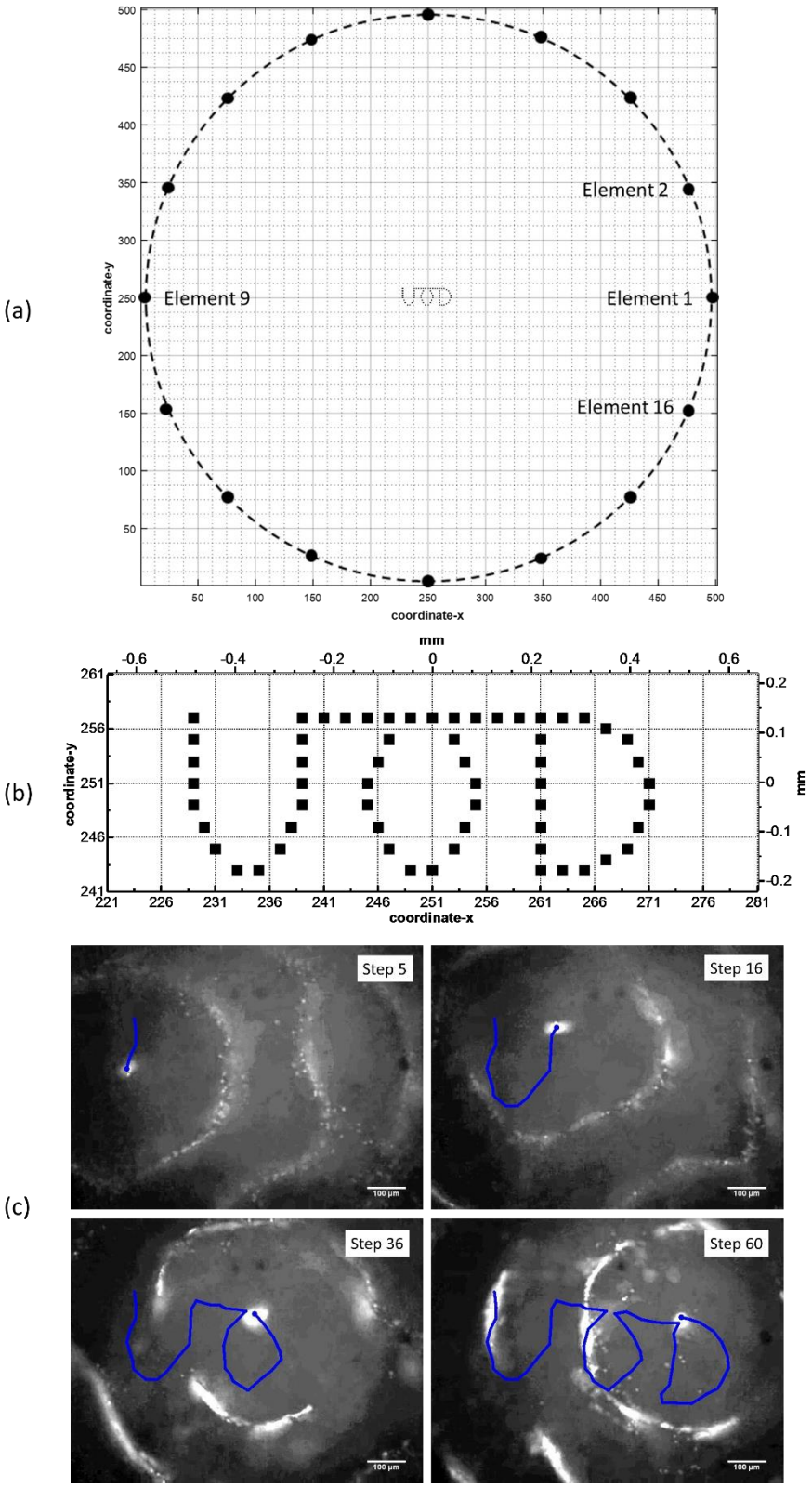

Figure 5.35 (a) A demonstration for the positions of the array elements and the overall orientation of the particle movement trajectory (b) The coordinate index map and corresponding real dimensions of 60 trapping positions. (c) Manual tracking of the central trap motion in the Bessel-function field to depict the trajectory. The slope appears in the overall trend of the trajectory was caused by the rotational misalignment of the camera viewing plane and the lateral plane of the circular array device.

b. Manipulation Step Distance

The distance between every two adjacent steps was characterised from the tracking results. Firstly, each manipulation step was measured to have a 0.72 s time interval, larger than the interval defined as 0.5 s in the MATLAB GUI. This delay can be variously combined contributions from the transmission delay in the USB-to-RS232 cable, the processing time in digital electronics, and the delay in analogue electronics output response. As the latter two factors are measured in nanoseconds and sub-microseconds respectively, the delay is mostly likely occurring during the transmission from the PC to electronics.

Considering the potential error involved in manual tracking, the measured distance for each two-step pair was derived from five different tracking results and they are presented as mean values with standard deviation. Figure 5.36 shows the measurements in comparison with the prediction directly calculated from the coordinates of each two traps. It can be found that the measured step sizes are smaller than the theoretical ones, mostly because for each trap coordinate, the calculation of the phase profiles for the transducer elements was based on ideal point sources and ignoring the reflections in the chamber. Also practically, frictional forces are caused by the viscosity of the fluid and the surface roughness of the agar substrate. Because the thickness of the fluid was about 0.5 mm, for a particle agglomerate with Ø30 μm, the central trap is in a pillar shape in 3-D, causing considerable friction between particles in different vertical layers during manipulation.

The manually-tracked positions of the central trap are demonstrated and compared with the theoretical pre-defined coordinates, as shown in Figure 5.37. The overall manipulation dimension is measured as 619.5 μm. Although there are discrepancies in the distances of manipulation steps caused by various factors as discussed, the shape of the trajectory is well maintained.

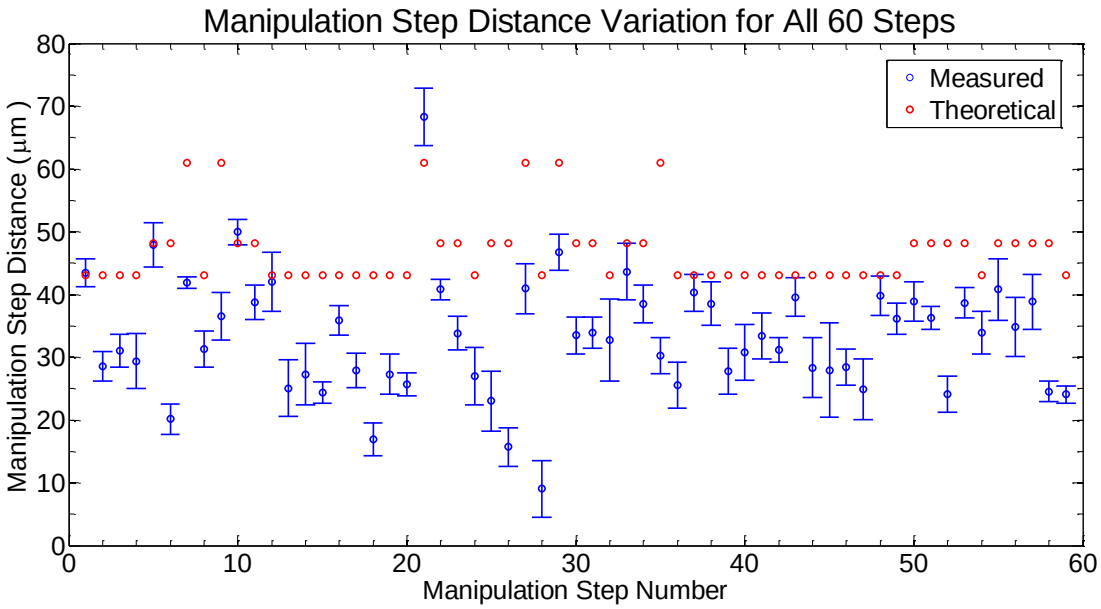

Figure 5.36 Comparison of the measurement and the direct calculation for the manipulation distance between each two adjacent steps over all 60 trapping positions.

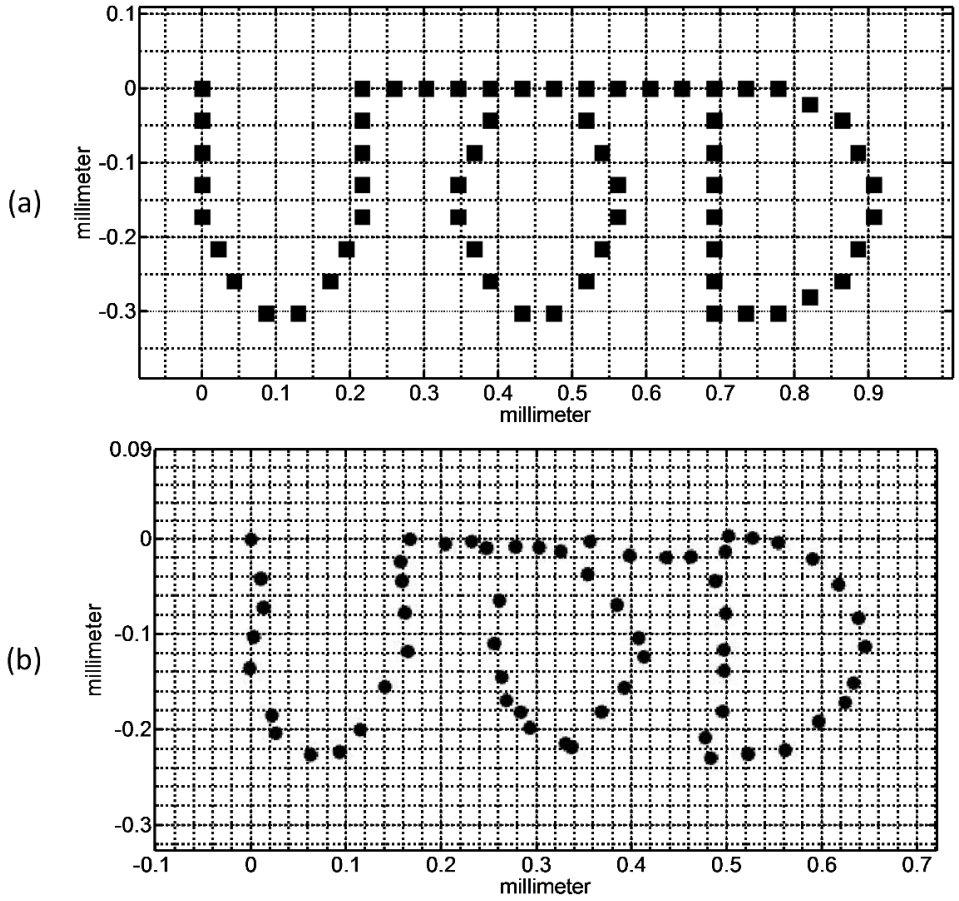

Figure 5.37 Comparison of the manual tracking results with the theoretical coordinates of 60 successive trapping positions.

c. Lateral Force Characterization

The original video was captured with a frame rate of 0.024 second/frame (41.7 fps). For the process of particle agglomeration, the measured average velocity of 8 single particles is 185.6 ± 26.5 μm/s. The agglomeration force for single particles, F_{agg}, balanced with the Stokes' drag force, can be calculated as 17.5 ± 2.5 pN. For the process of agglomeration manipulation, the time consumed for each manipulation step can be derived from the image sequence of the original video, and the average velocities for each step can also be calculated. The velocity of the manipulated agglomerate was calculated as 148.9 ± 50.7 μm/s, hence the agglomerate manipulation force, F_{manip}, which is responsible for moving the agglomerate balanced with the Stokes' drag, can be calculated to be 42.2 ± 14.4 pN.

5.9 Conclusions

This chapter provided a detailed description of the design and fabrication of an FPGA-based multichannel RF signal generator for Sonotweezers applications and a prototype of a 16-channel array driving system was developed. The FPGA plays the central role as reconfigurable hardware for frequency synthesis and phase generation, with an appropriate frequency and phase resolution for the desired application.

An analogue electronic is able to perform waveform amplitude regulation and amplification to generate a near sinusoidal signal with sufficient power to drive transducers with impedance of a few kΩ. Each output channel can provide a voltage up to of 25 V_{pp}, and a current up to 220 mA. For a wide range of resistive loads, the -3 dB and -6 dB output bandwidth can reach 6 MHz and 8 MHz, respectively, and the crosstalk between channels is about -28 dB. The system was demonstrated with a 16-element circular array Sonotweezer, by configuring the electronic hardware with a dedicated MATLAB GUI to perform programmable particle trapping and manipulation.

Apart from driving a specific Sonotweezer device, this multichannel signal generation system was designed to meet the demands of any single- or multi-element based acoustic tweezing device. Commercial signal generators normally have only a few output channels (usually a maximum of four), and although they can be synchronized, there may be

considerable delays between channels due to triggering between instruments via complex external communication protocols. However, with an FPGA based system, the FPGA itself can be configured as an embedded core for generating multi-channel signals, either for triggering the successive stage or for transducer excitation directly. The internal circuitry in the FPGA operates in parallel, and there are no synchronization issues between the channels. Also the channel count is not problematic as it is easily scalable, and there is an extensive range of devices to select for the demands of larger area in the FPGA circuitry. Real-time programming is another notable advantage for fast prototyping of circuits to test different acoustic tweezing devices.

At the PC end of the system, a compact software package such as MATLAB integrates the strength of computing and the convenience of a GUI, offering the ability to create a programmable platform to controlling the device in different applications. In this chapter, the general-purpose MATLAB GUI designed for the 16-channel array driver is an alternative to the GUI to control a specific Sonotweezer, and it offers flexibility for device characterisation under different electrical driving conditions.

The limitations of the current architecture of the electronics are firstly, the trade-off between the functionality and the channel count, and secondly, another trade-off between the maximum phase resolution and the maximum frequency of the outputs. Various approaches for optimizing the system, which can extend the realm of applications beyond the current electronics. This will be further discussed in the final chapter.

CHAPTER 6 CONTROL OF OUTPUT SWITCHING FOR PLANAR RESONATOR SONOTWEEZERS

6.1 Introduction

The dexterous multichannel electronic system discussed in Chapter 5 demonstrates the method for the control of counter-propagating ultrasonic arrays for acoustic tweezing, by dynamically shifting the relative phase of the driving CW signals for each transducer element. This chapter will explore another acoustic tweezing approach by introducing switching functions for the output channels with FPGA-based electronics, and demonstrate the functionality with 1-D and 2-D Sonotweezers based on planar resonators. The considerations for the electronics architecture are discussed at first, followed by the development process for both digital and analogue electronics. Characterization and experimental demonstration of the electronics are included as the final part of the chapter.

6.2 Electronics Design Considerations for Planar Array Sonotweezers

This section discusses considerations in designing electronics to drive planar array Sonotweezers. 1-D and 2-D planar ultrasonic arrays can be used to construct the acoustic tweezing devices, with individual transducer elements or groups of elements activated for particle trapping and manipulation within a resonator chamber coupled to the arrays. A novel 2-D ultrasonic array termed a “crossed-electrode” array will also be discussed. To complement these devices, the driving electronics need to be customized specifically for the desired functionality.

6.2.1 Conventional Arrays with Common Ground Electrode

The conventional piezoelectric transducer arrays are usually constructed with separated active electrodes and shared ground electrodes (Bernassau, García-Gancedo, et al., 2012). This design is common for kerf- or kerfless-ultrasonic arrays (Shung, 2009; Wu et al., 2009). As demonstrated in Figure 6.1, the transducer elements can be addressed individually by providing an AC driving signal to each active electrode, with reference to a shared ground electrode. Such a design is useful for making miniaturized ultrasonic arrays for acoustic tweezing applications.

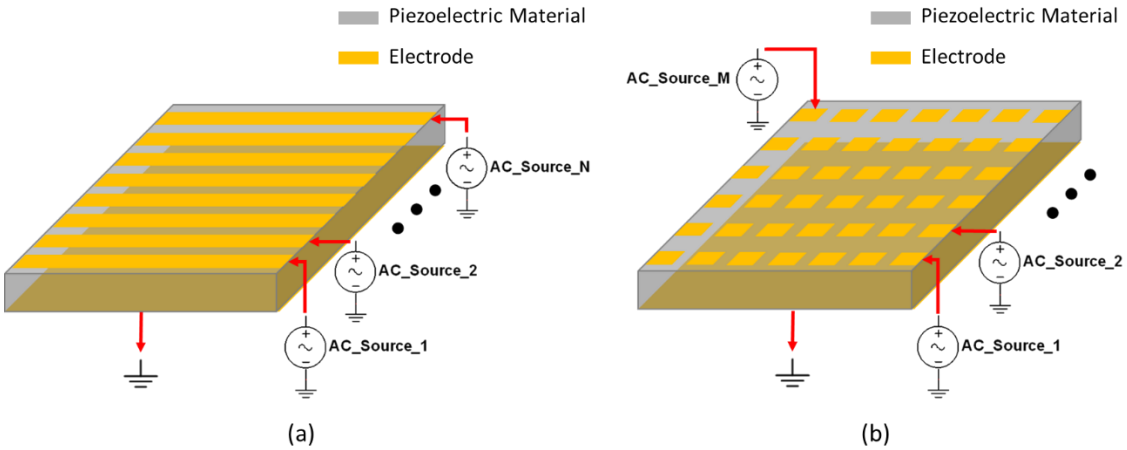

Figure 6.1 Demonstration of the electrode patterning for conventional ultrasound arrays. (a) Electrode configurations for an N-element 1-D linear array. (b) Electrode configuration for an M-element 2-D matrix array.

Acoustic resonators use USW fields to trap particles in pressure nodes / anti-nodes, depending on the relative density and compressibility of the particles compared with those of the fluid medium. As discussed in Chapter 2, the pressure distribution of the USW field can be defined by either the geometry of the fluid chamber (Petersson et al., 2004) or the limited dimensions of the ultrasound transducer itself. For the latter case, Glynne-Jones et al. demonstrated the possibility of using an ultrasound array coupled with a glass capillary to build a planar resonator for particle trapping and manipulation in 1-D (Glynne-Jones, Démoré, et al., 2012).

The operation of this device is based on two key components, as shown in Figure 6.2 (a). One is the multilayer resonator, which is experimentally constructed by coupling a glass capillary on top of an ultrasound transducer. The thickness of the fluid layer is defined by

the top and bottom walls of the capillary. Normally this thickness is small, and preferably 1/2 the acoustic wavelength in the fluid at the transducer operating frequency. Minimizing the fluid thickness in this way maximizes the pressure gradient in the direction of ultrasound wave propagation, i.e. the axial direction, and hence the particles in the fluid will experience a maximum gradient force towards the pressure node (Qiu, 2014).

The other important component is the ultrasonic array. As shown in Figure 6.2 (b), the USW field is limited by the dimension of the transducer. Thus, as well as the pressure gradient in the axial direction, an acoustic kinetic energy gradient is also established in the lateral direction. Particles with higher densities than the surrounding fluid will experience a component of force towards the position of E_{kin} maximum, centred above the transducer. Consequently, it is possible to use an ultrasound array to trap and manipulate a particle agglomerate in the lateral dimension, simply by selecting appropriate elements to be active to move the position of the kinetic energy maximum.

A 12-element, 500-µm pitch piezoceramic (PZ26, Meggitt Ferroperm, Denmark) transducer array was fabricated, and integrated into a Sonotweezing device, as shown in Figure 6.2 (c). For experimental use, a water suspension with Ø10 µm polystyrene particles was pumped into the capillary, and each two adjacent transducers were paired together for activation by an external signal source. The driving signal was manually switched along the electrical connections of the array. The experimental results shown in Figure 6.2 (d) demonstrated a good conformance with the design, with a particle agglomerate of approximate 500-µm in length created and manipulated freely along the length of the array in the lateral direction.

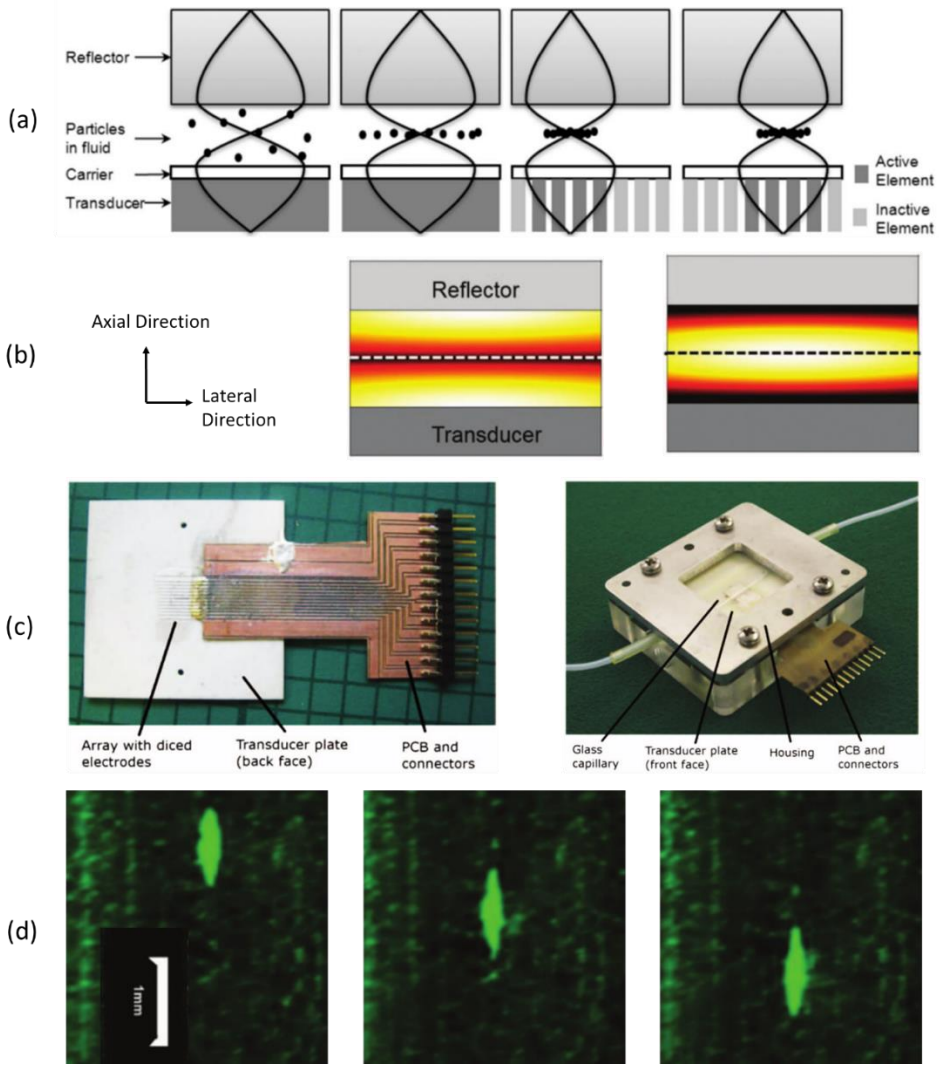

Figure 6.2 Planar array Sonotweezer constructed with the 1-D ultrasonic array (adapted from Glynne-Jones et al., 2012). (a) An illustration of the operating principle for particle manipulation with an array-controlled multilayer resonator. (b) Example of acoustic pressure field distribution in axial and lateral directions. The colour map is in arbitrary units – light: 1, dark: 0. (c) Photographs of the fabricated ultrasonic array and acoustic tweezing device assembly. The transducers in the array operate around 2.5 MHz, a 300-µm-thick glass capillary is coupled on top of the array, and both are secured in a housing. (d) A 500-µm long particle agglomerate is manipulated along the length of the transducer array (axis shown vertical).

Inspired by this previous work of using a 1-D linear array resonator for particle manipulation, in this thesis, a new version of a 30-element, 200-µm pitch 1-D linear array was fabricated by collaborative researchers (Qiu, 2014a) as the target device for electronics development. As shown in Figure 6.3 (a), the array was fabricated with a smaller pitch than for the published work, in order to explore the possibility for particle manipulation at a higher spatial resolution. The impedance spectra of the array elements were measured in air with the results shown in Figure 6.3 (b) and (c). The first thickness extensional resonance frequency for each element can be found around 2.55 MHz, with an impedance magnitude around 2 – 3 kΩ. A variation of the impedance magnitudes of

the array can be observed from the results, which is caused mostly in the fabrication of the electrical interconnections, by the uneven removal of Ag epoxy during the scratch-dicing process reported by Qiu (Qiu, 2014a)

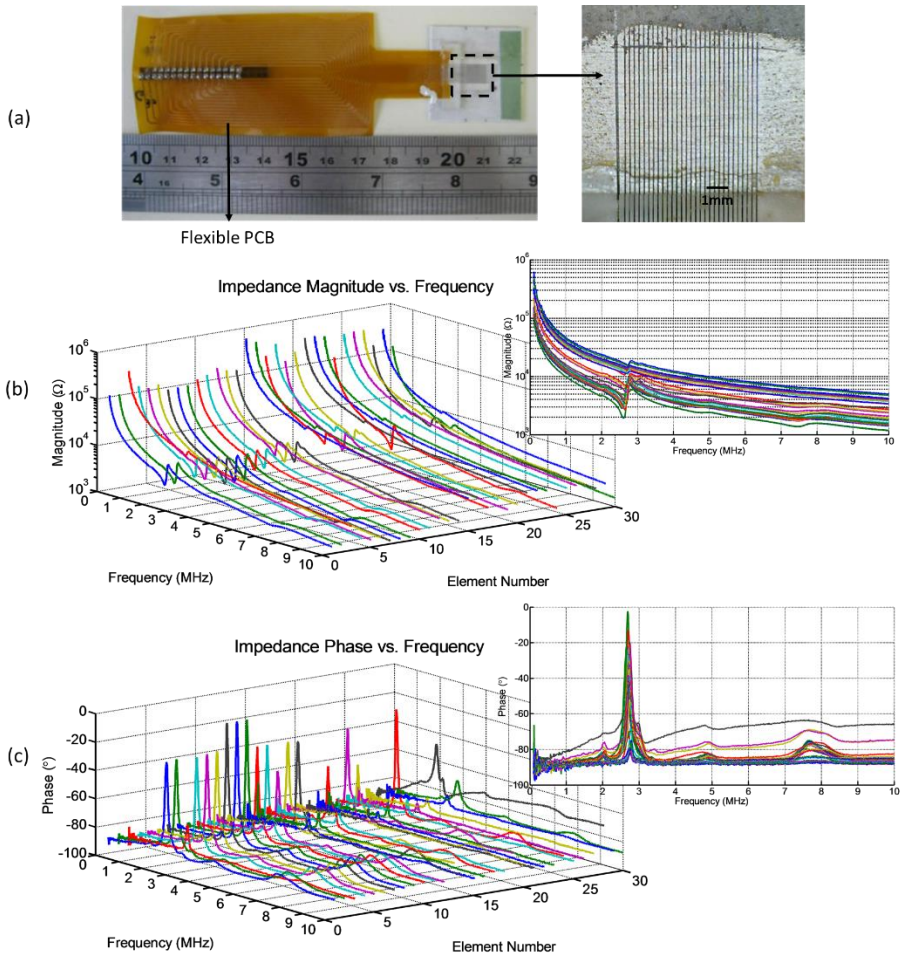

Figure 6.3 30-element 1-D linear array device and impedance spectra of the transducer elements. (a) 30-element array made from 1-3 piezocomposite and flexible PCB. (b) and (c) Electrical impedance spectra for the elements in the array (adapted from Qiu, 2014a).

The same principle can also be extended from 1-D into 2-D, by extending the dimensionality of the transducer array. An exploration of using a 2-D matrix array in a planar resonator arrangement for particle trapping and manipulation is outlined in Appendix D.

6.2.2 2-D Crossed-electrode Array

Apart from the conventional transducer arrays with common-ground electrodes, a crossed-electrode configuration is a novel design for creating 2-D arrays, previously

proposed as a new modality for ultrasound imaging (Démoré et al., 2009). As shown in Figure 6.4, a kerfless crossed-electrode transducer array can be created with the top and bottom electrodes placed orthogonally on each major surface of the piezoelectric material. The transducer elements are then defined by the cross-points of the top and bottom electrodes. The clear advantage of this setup is that it is possible to design a 2-D transducer array with a very large number of elements but using a minimal number of electrical interconnections. Considering a crossed-electrode configuration with N top electrodes and N bottom electrodes respectively, a 2-D transducer array with N^2 elements can be defined with $2N$ electrodes in total, while for a conventional matrix array, N^2 active electrodes are needed with one common-ground electrode. As N increases the electrical interconnection thus becomes rapidly more difficult for the matrix array (Qiu, 2014b).

In this chapter, a multi-layer thick-film PZT crossed-electrode 2-D transducer array developed by collaborative researchers [2] is used as a typical device for electronics development. As shown in Figure 6.5, the crossed-electrode array has 30 top electrodes (row electrodes) and 30 bottom electrodes (column electrodes), which can be considered equivalent to 900 cross-point transducer elements. Each electrode track is 440 µm wide, and the pitch between the electrodes is 500 µm with a 60 µm kerf. Thus, the element pitch of the 2-D array is 500 µm.

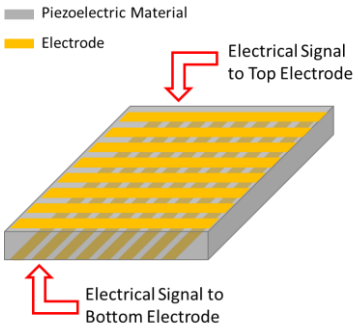

Figure 6.4 Demonstration of the crossed-electrode configuration for creating an equivalent 2-D array.

[2] This research, involving transducer design and fabrication, is a collaboration between IMSaT, University of Dundee, UK, and Frauhofer IKTS, Germany.

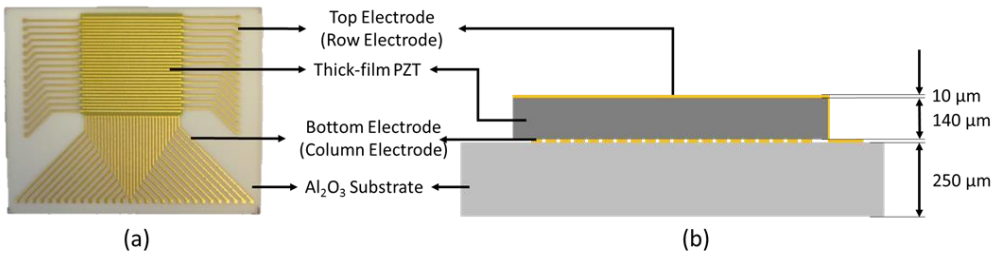

Figure 6.5 (a) Photograph of top view of crossed-electrode array. The pitch of the electrode fan-outs is 1.27 mm. (b) Diagram of the cross-section view of the layers in the device and the thickness of each layer.

An electrical testing / driving platform was developed with a wire-bonded PCB frame and a PCB adaptor, as shown in Figure 6.6. The 2-D array was glued onto a PCB frame exposing the transducer working area, and the electrode fan-outs were bonded onto PCB tracks with conductive wires. Then the device was mounted on top of a substrate PCB with ribbon cables. As a proof-of-concept study, considering there were in total 40 output channels provided by the available signal switching electronics, the substrate PCB was designed to drive the transducer array defined by 20 × 20 electrodes.

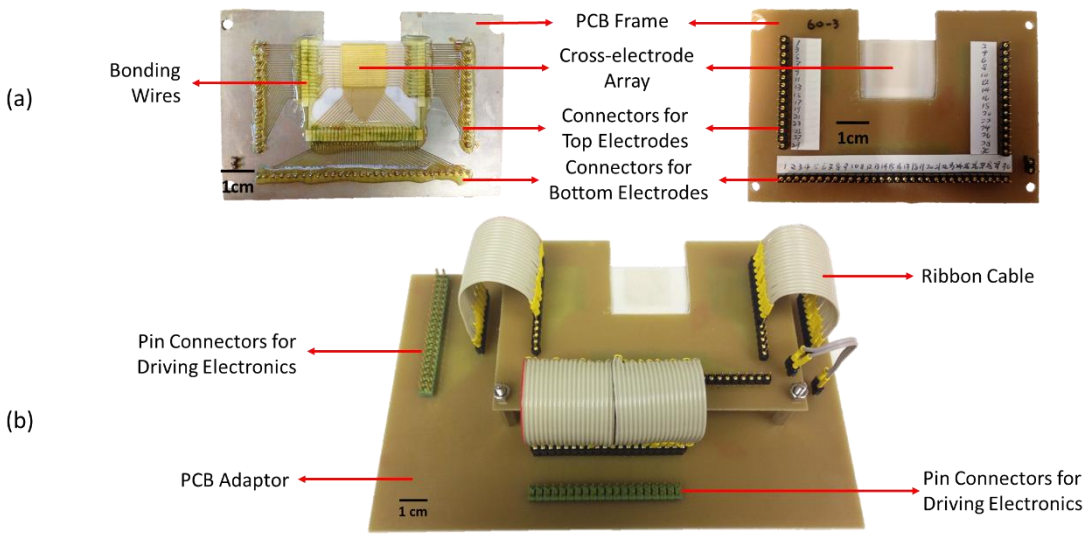

Figure 6.6 Electrical testing / driving platform for the 2-D crossed-electrode array. (a) The PCB frame for securing the crossed-electrode array device. (b) Complete platform assembled with the PCB frame and the adaptor, with connectors for the driving electronics.

As an experimental study, as shown in Figure 6.7 (a), an area of 8 × 8 transducer elements was examined by activating the first eight electrodes of the top and the bottom layers. Each transducer element defined by a top-bottom orthogonal pair was characterized in terms of its impedance spectrum. The results measured in air for the total 64 elements are shown in Figure 6.7 (b) and (c). The electrical impedance characteristics across all the

elements have good consistency and, for each element, the 1st thickness extensional resonance frequency of the PZT and the Al_2O_3 layer together can be found around 7.25 MHz, with an electrical impedance magnitude of 40 – 50 Ω.

As discussed previously, for ultrasound arrays with a common ground electrode, manual switching demonstrated the principle of array-controlled particle manipulation. Additionally the functionality of both such 1-D and 2-D arrays can be greatly extended with some sort of electronic control. Moreover for 2-D arrays with the crossed-electrode configuration, it is impractical to use manual control in Sonotweezer applications. Proper electronic control will greatly improve the functionalities of the transducer arrays and provide novel possibilities of using planar resonator Sonotweezers for diverse applications. The contents of the rest of this chapter concern the development of control electronics with a switching function for element multiplexing in planar resonator Sonotweezers.

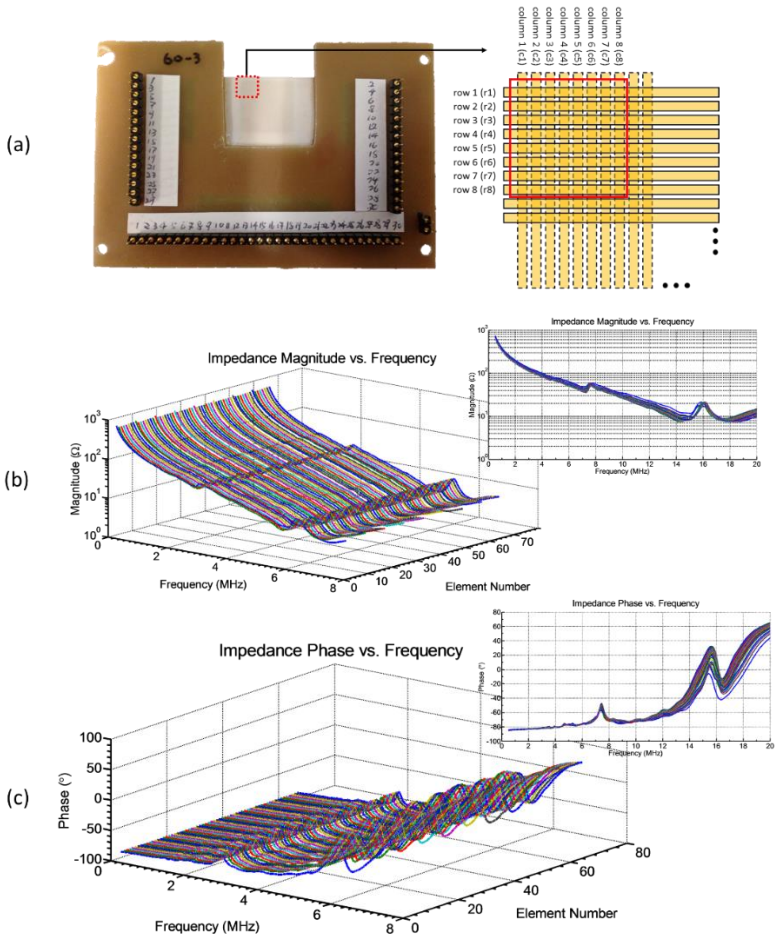

Figure 6.7 Impedance spectrum characterization of 64 elements of the crossed-electrode array. (a) The position of the active transducer elements. (b) and (c) Impedance magnitude and phase for each transducer element in the array.

6.2.3 Architectures for Switching Electronics

A diagram illustrating the operational principle of the electronics is shown in Figure 6.8 (a). As an analogy to the manual control by alternately applying the excitation signal along the array elements, for electronic control, the transducer excitation signals all come from a single signal source, and the output signal is electronically switched along the transducer elements, through bespoke analogue signal switching circuitry, as shown in Figure 6.8 (b). The FPGA was programmed as a specific core for controlling the analogue circuits. A physical user interface can be built from resources on the Spartan-3a FPGA board, such as slide switches, buttons and rotary knobs (Wang et al., 2012).

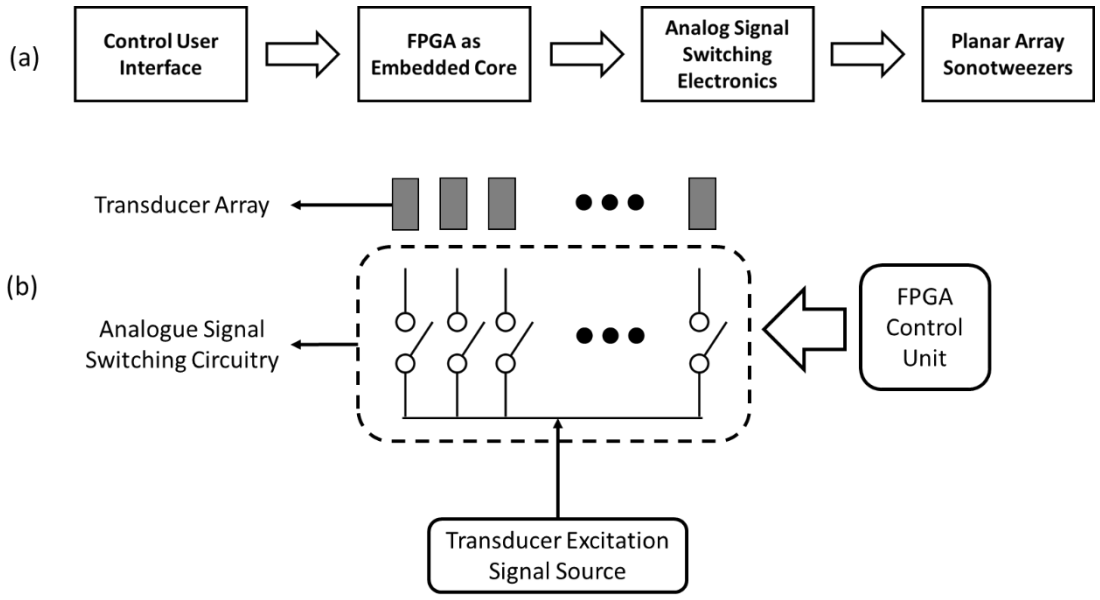

Figure 6.8 Illustration of the electronics system for planar array Sonotweezers. (a) Block diagram of the electronics architecture. (b) Block diagram showing the basic functionality of the signal switching electronics.

The electronics architecture was based on the characteristics of the planar array resonator devices. This type of Sonotweezer requires highly accurate frequency tuning each time a device is assembled. For all the transducer elements, the signals then have the same frequency, amplitude, and phase. Thus, for driving such devices, it is reasonable to pursuit a straightforward analogue signal multiplexing approach. The signal switching circuitry was constructed with an array of analogue switch ICs. The “ON” and “OFF” status of the switches are controlled by digital signals which can be generated from the FPGA. This circuitry provides a wide bandwidth for the excitation signal and is able to maintain high

signal integrity across all the active elements while the excitation signal is switched along the array.

In an array the element “ON” and “OFF” status are determined by the voltage potential applied to the top and bottom electrodes of each element. For the “ON” status, an AC voltage potential is applied to the transducer element, and for the “OFF” status, the applied voltage potential is close to zero. Hence an SPDT (single-pole-double-throw) electronic switch (ADG5434, Analog Devices, Inc., Norwood, MA, USA) is an appropriate choice. The footprint and truth table of the IC are shown in Figure 6.9. Each ADG5434 IC can offer four SPDT channels with very low on-resistance of 13.5 Ω typically and 15 Ω maximum at 25°C. According its specification, the IC is compatible with 3.3 V FPGA logic, and can tolerate voltage output up to 48 V_{pp} from V_{DD} to V_{SS}, with rail-to-rail operation for dual-supply voltages. Its -3 dB bandwidth is 145 MHz, and channel-to-channel crosstalk is -60 dB. At 25°C with ±15 V supplies, the continuous output current is 70 mA maximum per channel. (“ADG5434 Datasheet”, 2013).

(a)

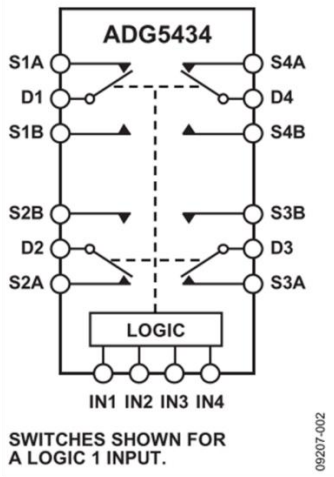

(b)

INx	SxA	SxB
0	OFF	ON
1	ON	OFF

Figure 6.9 (a) Functional block diagram of quad-channel analogue switch IC. (b) Truth table for controlling the signal path.

A. Electronics Architecture for Common-ground Arrays

For each SPDT switch, a digital input port, INx, controls the analogue signal path from inputs SxA or SxB to the output Dx, according to the logic control truth table. Figure 6.10 (a) shows the electrical connections to drive the 1-D linear array Sonotweezer. The common electrode of the transducer array is connected to analogue ground and each separate active electrode is connected to an output Dx. The FPGA output signals are connected to INx ports which control the AC signal path, either by connecting the transducer to the signal source through SxA ("ON"), or to a 1 MΩ high resistance terminal through SxB ("OFF"). The "OFF" circuitry can be effectively considered as an open circuit, as the current flowing through the transducer is greatly limited. The equivalent circuits are shown in Figure 6.10 (b). R_{on} represents the on-resistance between SxA and Dx for each channel of the analogue switch.

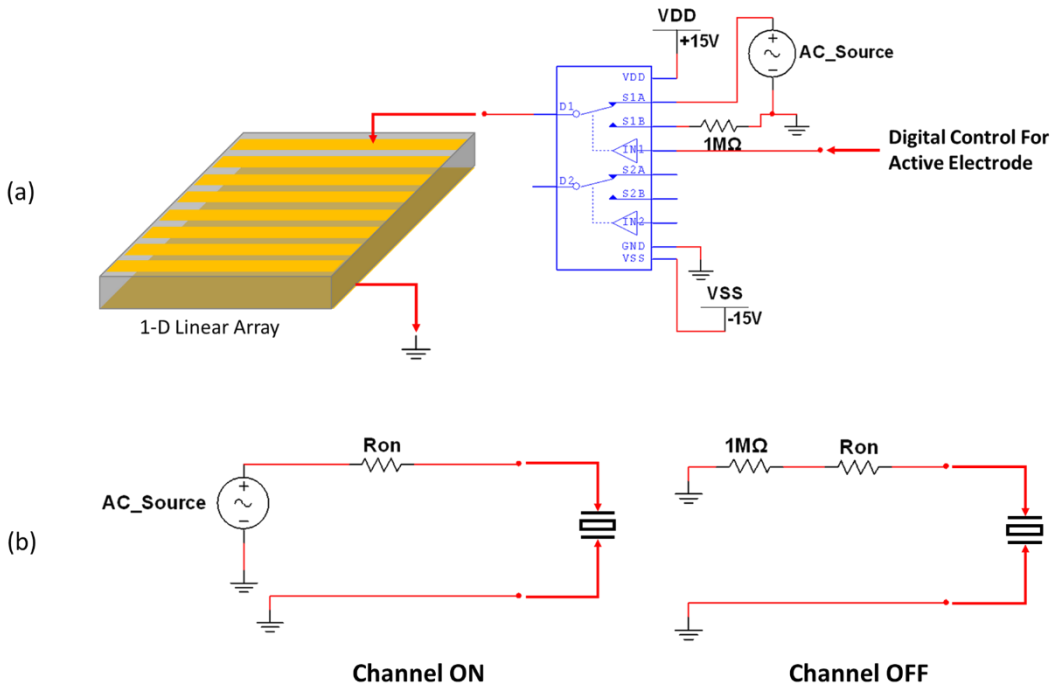

Figure 6.10 Design for the signal switching circuitry. (a) Functional block diagram and the truth table of the analogue switch IC ADG5434, from ("ADG5434 Datasheet", 2013). (b) A demonstration diagram of the signal interconnections. (c) Equivalent circuit for channel "ON" status. (d) Equivalent circuit for channel "OFF" status.

B. Electronics Architecture for Crossed-electrode Arrays

Both conventional 1-D linear and 2-D matrix arrays have similar topology defining transducer elements, using a common ground electrode and separated active electrodes. For such a transducer configuration, a binary signal switching method is sufficient, by connecting the active electrodes to either AC signal source or ground to define the "ON" and "OFF" status of the transducer elements, respectively. However defining a single transducer element within the 2-D crossed-electrode array is more difficult, as there is no common ground electrode. Instead, a ternary electrical switching method is needed.

The ternary switching is realized by using "signal", "ground" and "high impedance" to control the top and bottom electrodes. Based on the analogue switch IC ADG5434 already implemented, Figure 6.11 shows the circuit diagram for controlling the crossed-electrode array. The top electrode can be switched between the signal state and the high-impedance state, and the bottom electrode can be switched between the ground state and high-impedance state.

Figure 6.12 shows an impedance analysis for the ternary configuration. According to the truth table in Figure 6.11 (b), for each element defined by the intersection area of the top and bottom electrodes, in total there are 2 × 2 combinations, and these four types of electrical connection represent one "ON" status and three "OFF" statuses. Shown in Figure 6.12 (a), the "ON" status has the same configuration as for a linear array with common ground. The "OFF" status-1 and status-2 are simply realized by supplying no AC source signal to either electrode. For the "OFF" status-3, a very high impedance component (1 MΩ resistor) is connected in the electrical path to limit the AC current flowing through the transducer, in turn to reduce the voltage potential difference across the transducer electrodes close to zero.

(a)

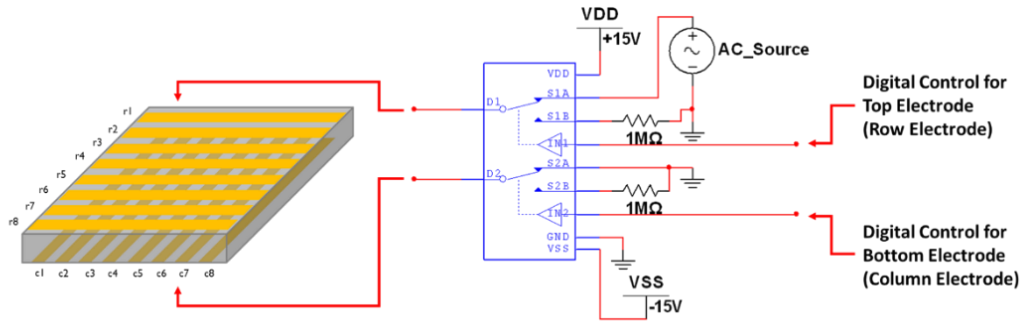

(b)

Top Electrode			Bottom Electrode		
INx	SxA (AC Source)	SxB (High Impedance)	INx	SxA (Ground)	SxB (High Impedance)
0	OFF	ON	0	OFF	ON
1	ON	OFF	1	ON	OFF

Figure 6.11 Demonstration of driving the crossed-electrode array with an analogue switch IC. (a) Schematic diagram of the electrical interconnections. (b) Truth tables of the digital control signal for top and bottom electrodes.

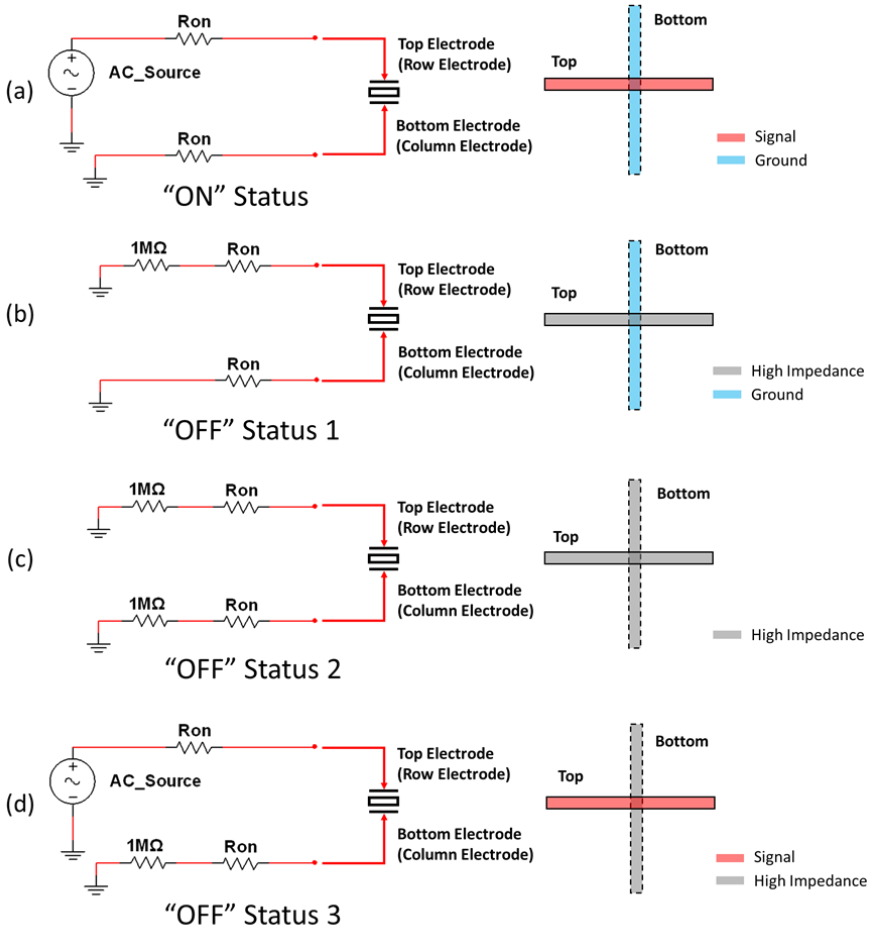

Figure 6.12 Demonstration of the ternary configuration for driving a crossed-electrode array with equivalent circuits and electrode arrangements for the "ON" and "OFF" statuses. (a) "ON" status for the active element. (b) – (d) "OFF" statuses for the inactive element.

6.3 Digital Electronics Development

6.3.1 FPGA Core for Linear Array

Digital control circuitry was designed to work with FPGA electronics, based on the truth table of the analogue switch IC. Considering the target 30-element linear array, the outputs were configured for 30 channels, and the same principle can be applied for larger numbers of channels. Digital bits "1" and "0" represent switch "ON" and "OFF" statuses, respectively. The transducer elements can be activated with different patterns under the control of the FPGA development board slide switches, and element switching can also be controlled via an on-board rotary knob.

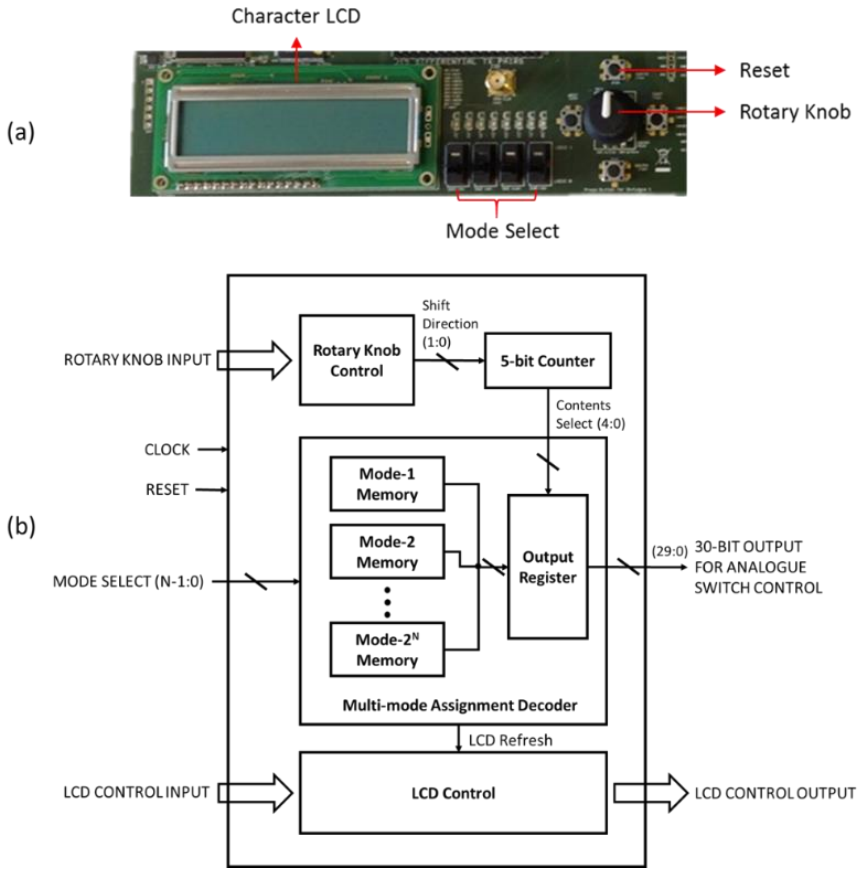

Figure 6.13 FPGA control for linear array. (a) Control hardware interface on the FPGA development board. (b) Functional block diagram of the FPGA core for the control of 1-D linear array Sonotweezer. The patterns for the active transducer elements are configured with "Mode Select" input signal. The multiplexing of the elements is controlled by the on-board rotary knob. The output from the FPGA is a 30-bit parallel signal for configuring the analogue switches.

The block diagram in Figure 6.13 shows the FPGA core configuration. Each pattern for the transducer element activation is defined with a 30-bit code, and the representations

for all variations of a single activation pattern are stored in a specific memory element. Hence it is possible to store different patterns within various memory elements, which can be selected by input signals as “mode1”, “mode2”, etc., through a decoder controlled by on-board slide switches. For a 30-element configuration, a 5-bit counter is controlled by the on-board rotary knob, to read through the contents of the selected memory bi-directionally. For mechanical components such as the rotary knob and slide switches, debouncing circuitry was applied in the VHDL coding to prevent the faults from glitches. The functionality of the FPGA core was verified through behavioural simulation (Wang et al., 2012). The VHDL source code is provided in supplemental CD in Appendix A.

6.3.2 FPGA Core for Crossed-electrode Array

The architecture of the FPGA core for the crossed-electrode array is similar to that for the 1-D linear array, using two separate memory elements to control the top and bottom electrodes respectively. The input hardware interface and the functional block diagram of the FPGA core are shown in Figure 6.14. In the experimental study, an 8 × 8 transducer element matrix will be activated, hence two ROMs with 20-bit width and 8-bit depth were prepared. Similarly to the configuration for the 1-D linear array, the patterns for electrode activation are stored in the “top electrode ROM” and “bottom electrode ROM”, respectively. A control logic block interprets the commands provided from push-button inputs and triggers successive logic to generate required top-bottom electrode combinations at the output. The functionality of the FPGA core was verified through behavioural simulation. VHDL source code is provided in supplemental CD in Appendix A.

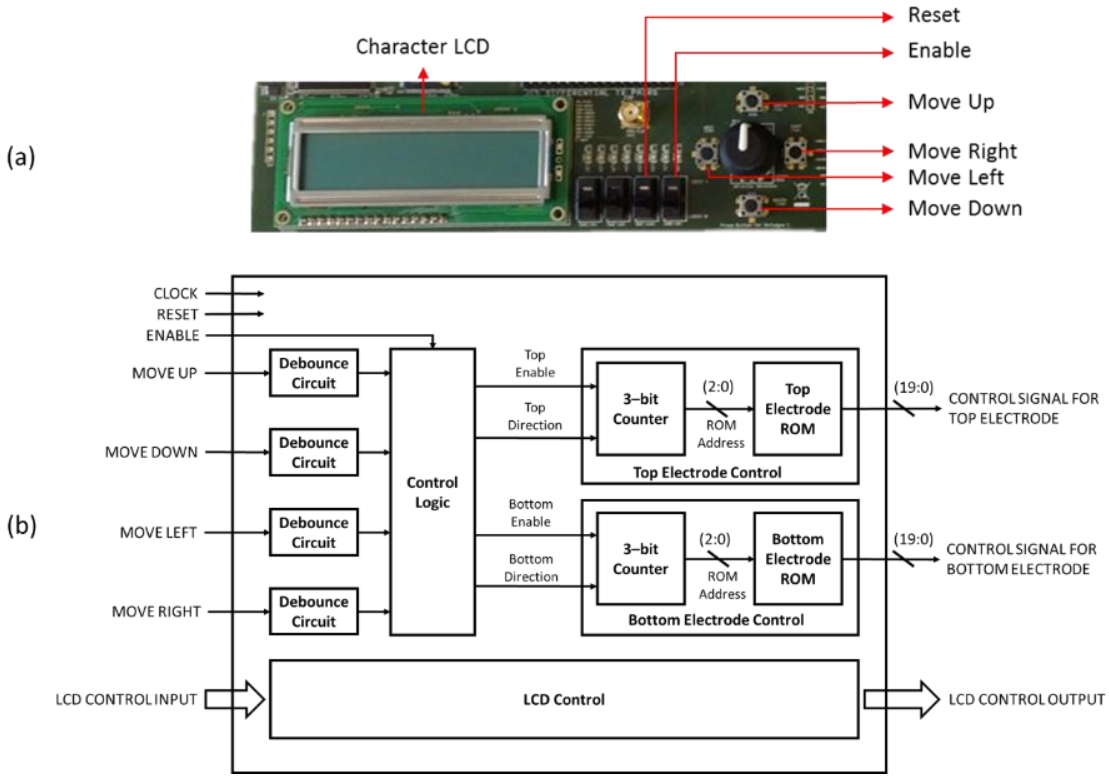

Figure 6.14 FPGA control for crossed-electrode array. (a) Control hardware interface on the FPGA development board. (b) Functional block diagram of the FPGA core. This core can be configured to control single-elements, row-of-elements, column-of-elements and symmetric-multiple-element patterns by editing the contents stored in the ROMs for the top and bottom electrodes.

6.4 Analogue Electronics Development

This section describes the development of analogue switching circuitry built with the ADG5434 IC, for realizing signal multiplexing to drive the transducer arrays under FPGA control.

6.4.1 Signal Switching PCB

The signal switching circuitry was created on a four-layer PCB, as shown in Figure 6.15. Given the availability of I/O ports from the FPGA development board, the signal switching circuitry was designed with 40 output channels in total, and 10 analogue switch ICs were used. The ICs are powered with ±15 V voltage supplies, and a switch-mode DC-DC voltage converter IC (MAX743, Maxim Integrated, San Jose, CA, USA) was used to convert a +5 V DC voltage into ±15 V voltages (“MAX743 Data Sheet”, 1990). The

transducer actuation AC signals were provided from a single external source through a BNC connector. A function-select switch was constructed on the PCB to change the functionality of the electronics for either controlling the arrays with common ground electrodes, or arrays with crossed-electrodes.

In conclusion, the switching electronics can drive common-ground 1-D or 2-D arrays with 40 elements, or crossed-electrode 2-D arrays with 20 × 20 elements. The 40-channel FPGA control signals were bypassed into an output to connect with bespoke LED indicators for different transducer arrays, as a visual feedback for the array operation conditions. The schematics and PCB layouts of the circuitry can be found in Appendix C.

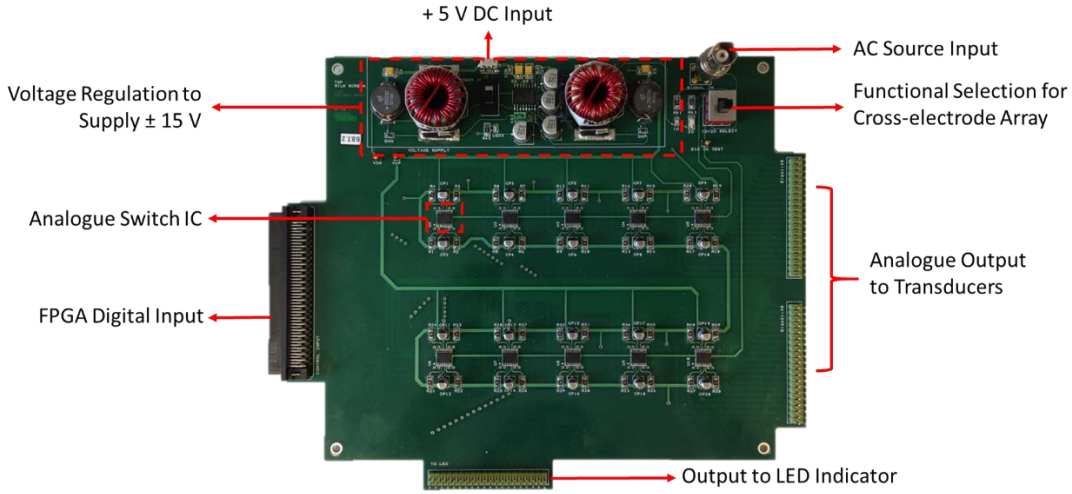

Figure 6.15 Complete signal switching circuitry to control planar-array based Sonotweezers.

6.4.2 LED Indicators

A. LED Indicator for Linear Array

An LED array was connected with the signal switching PCB to provide a visual assistance for different element activation conditions of the linear transducer array. As shown in Figure 6.16, the element “ON” and “OFF” status can be directly represented by the illuminance of the LEDs.

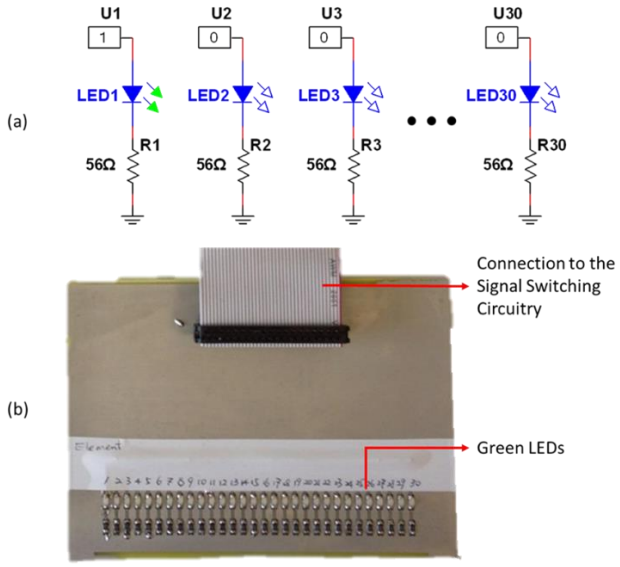

Figure 6.16 LED array indicator for the linear array. (a) Circuit schematic for driving a single LED with digital signals generated from the FPGA. (c) Photograph of the LED indicator circuitry.

B. LED Indicator for Crossed-electrode Array

The actuation of the crossed-electrode array transducer elements can be realized by controlling top and bottom electrodes separately. The fundamental mechanism for FPGA control is similar to that designed for the 1-D linear array, by using a memory element to store the electrode activation patterns, and reading the memory contents bi-directionally. Two separate ROMs are implemented for the top and bottom electrode sets. For debugging and visual assistance, an 8 × 8 LED matrix was developed as a representation of the 64 transducer elements defined by the first eight top and first eight bottom electrodes. Because the LEDs represent the activation of the top and bottom electrodes of the transducer array, the circuit schematic for controlling the LED matrix is exactly the same as the one designed for the signal switching circuitry, as shown in Figure 6.17, using analogue switch ICs from the same device family with similar characteristics (ADG333A, Analogue Devices, Inc., Norwood, MA, USA). For each LED the anode and cathode are controlled by two electronic SPDT switch channels. The LED anodes are driven from a DC voltage, V_{DD} = 3.3 V. The schematics and PCB layouts for the complete LED indicator circuitry can be found in Appendix C.

(a)

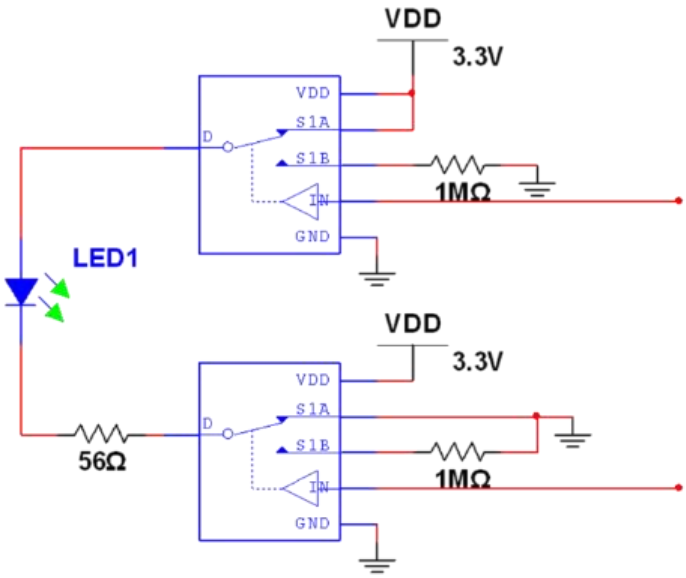

(b)

Top Electrode

INx	SxA (V_{DD})	SxB (High Impedance)
0	OFF	ON
1	ON	OFF

Bottom Electrode

INx	SxA (Ground)	SxB (High Impedance)
0	OFF	ON
1	ON	OFF

(c)

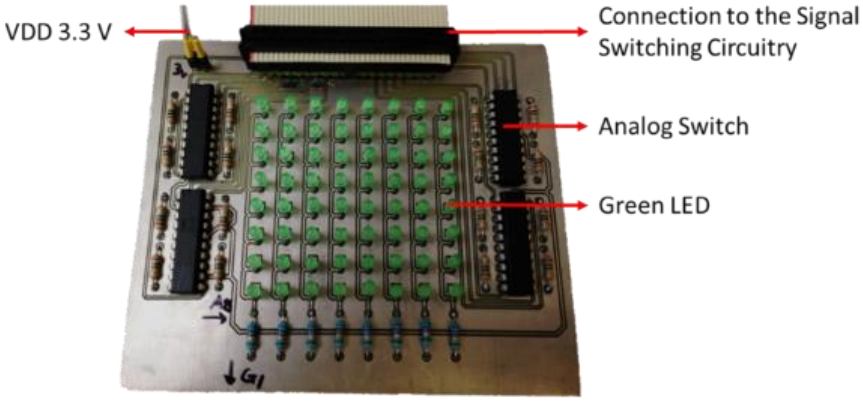

Figure 6.17 LED matrix indicator for the crossed-electrode array. (a) Circuit schematic for driving a single LED with analogue switches. (b) Truth tables of the digital control signal for top and bottom electrodes. (c) A photograph of the LED indicator circuitry.

6.5 Electronics Characterisation

The outputs of the signal switching electronics were measured with an oscilloscope for functional validation. For each channel, the output bandwidth, on-resistance frequency response, and channel crosstalk were determined.

6.5.1 Functional Validation

The CW sinusoidal input was provided from an arbitrary function generator (33250A, Keysight Technologies Inc., Santa Rosa, CA, USA) with frequency and amplitude of 2.5 MHz and 17.7 V_{pp} respectively. As shown in Figure 6.18, at first Channel 1 (yellow), Channel 2 (green), and Channel 3 (violet) were all active, and Channel 4 (pink) was switched off. Then the three-element group was shifted along the array by one element step. It can be seen from the voltage value that for the "ON" channel, the signal amplitude remained approximately the same as the input signal, whereas for the "OFF" channel, the signal amplitude is around 0.8 to 1.2 V_{pp}. The voltages were measured under open load conditions.

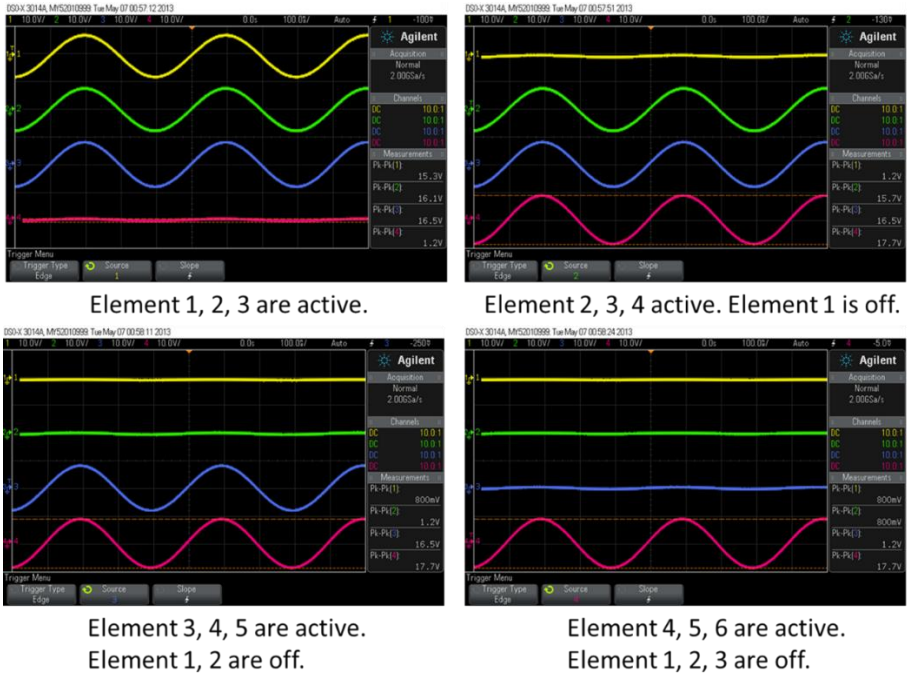

Figure 6.18 Screenshots of the waveforms displayed on the oscilloscope. Elements 1, 2, 3 were firstly activated as a 3-element-group and shifted along by one-element-step towards elements 4, 5, 6.

6.5.2 Output Bandwidth

The single channel output bandwidth was tested in the frequency range from 100 kHz to 50 MHz with an input signal provided from a function generator (33250A, Keysight Technologies Inc., Santa Rosa, CA, USA). The output was loaded with resistors from 15 Ω to 3.3 kΩ. The output was tested directly from the pin header outputs of the signal switching PCB. The test results are plotted in Figure 6.19. For different loads, the output

frequency responses were measured at discrete frequencies, and the -3 dB and -6 dB bandwidth and stop-band slopes are summarized in Table 6.1. For the Sonotweezer devices under test, the switching electronics offers sufficient bandwidth at the outputs. However according to the data sheet, for ±15 V supplies, the typical -3 dB bandwidth of the analogue switch IC is 200 MHz (“ADG5434 Datasheet”, 2013). The reduction of bandwidth in the present circuitry is assumed to come from several sources, and it can be further improved (Ardizzoni, 2005). One possible reason is the parasitic inductance introduced from the long PCB electrical tracks at the inputs and outputs of the analogue switch ICs. For RF circuits working in MHz range, controlled-impedance technique can be implemented, by maintaining the tracing impedance to a characteristic value, such as 50 ohms. Additionally, routing and shielding in the PCB should be further considered. For example, long parallel tracks with close proximity need to be further avoided to reduce inductive coupling. Ground shielding techniques such as microstrip or stripline that also used for impedance control can be beneficial to improve the output signal integrity for a higher bandwidth that close to the specification of the IC in use.

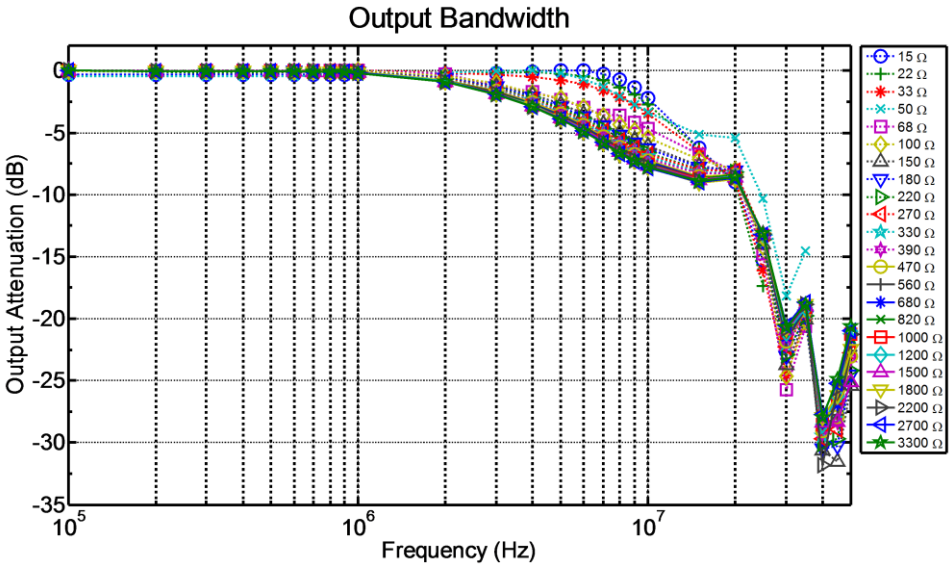

Figure 6.19 Output bandwidth measurement for different resistive loads.

Table 6.1 Summary of the frequency response of the outputs for different resistive load conditions.

Load Resistance (Ω)	Cut-off Frequency (MHz)		Stop-band Slope from -3 dB frequency to 20 MHz (dB/octave)	Stop-band Slope after 20 MHz (dB/octave)
	-3 dB	-6 dB		
15	11.17	15.58	6.81	10.06
22	10.46	15.14	6.40	13.17
33	9.17	14.71	5.41	20.99
50	9.45	20.47	3.13	17.04
68	5.51	13.08	3.17	17.53
100	5.56	12.41	3.50	22.18
150	5.46	9.91	3.37	20.87
180	5.18	9.55	3.43	19.94
220	4.95	9.14	3.58	19.70
270	4.76	8.95	3.57	18.95
330	4.58	8.70	3.64	18.34
390	4.43	8.52	3.67	18.40
470	4.35	8.31	3.79	17.91
560	4.19	8.23	3.71	17.61
680	4.14	8.14	3.75	17.28
820	4.09	8.06	3.79	17.22
1000	4.03	7.97	3.80	16.64
1200	3.95	7.89	3.81	16.79
1500	3.92	7.84	3.83	16.46
1800	3.89	7.71	3.93	15.99
2200	3.84	7.75	3.83	16.21
2700	3.86	7.67	3.94	15.87
3300	3.80	7.68	3.87	16.12

6.5.3 Channel Crosstalk

The electrical crosstalk between output channels can be defined as the ratio of the signal amplitude measured at the "ON" channel and at the adjacent "OFF" channel, taking the form $crosstalk = 20\ log(V_{OFF}/V_{ON})\ (dB)$. For the test, both "ON" and "OFF" channels were loaded with 50 Ω resistors at the outputs. Also the output crosstalk was characterised from 100 kHz to 30 MHz, as shown in Figure 6.20. The crosstalk is as low as -53 dB at frequencies below 1 MHz, and the highest crosstalk of -19 dB appears at 14 MHz. For Sonotweezer transducers working at 1 to 10 MHz, the crosstalk is within the range of -53 to -23 dB.

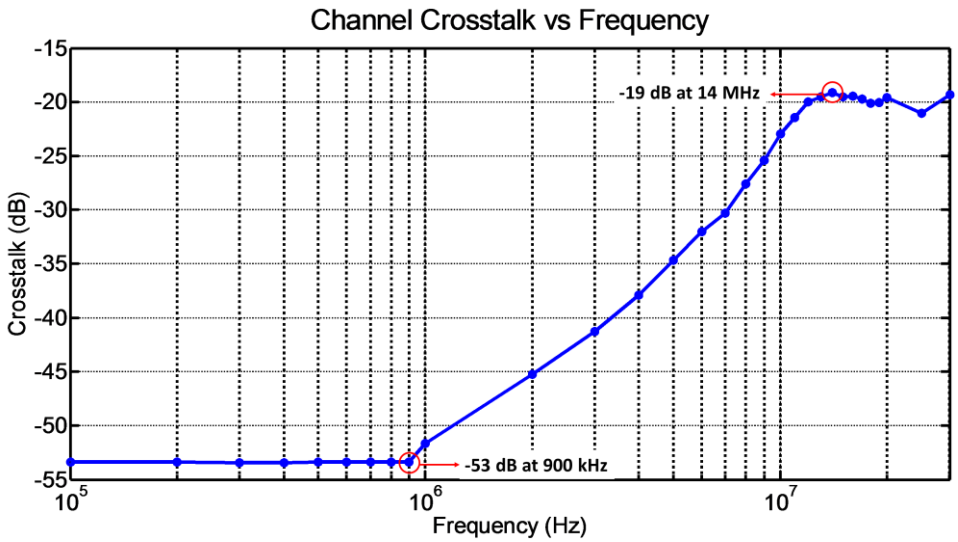

Figure 6.20 Output channel crosstalk frequency response within -3 dB bandwidth.

6.5.4 On-resistance Frequency Response

During the characterisation it was noted that R_{on} varies with the output frequency. According to the analogue switch IC specification, at 25°C the R_{on} is typically 13.5 Ω, with a variation in value of ±0.9 Ω. For Sonotweezer devices such as the 30-element linear array, with an element impedance of 2.8 kΩ at the working frequency, this variation will not influence the output voltage swing over the load. However for Sonotweezer devices such as the crossed-electrode array with low element impedance that is close to $R_{on,}$ it is useful to measure the R_{on} frequency response of the analogue ICs built within the PCB. R_{on} was measured between signal ports SxA/SxB and Dx of the analogue switch IC with a digital multimeter. The R_{on} value within the -6 dB bandwidth was calculated from the measurements as 12.8 ± 1.1 Ω, as shown in Figure 6.21. The R_{on} value is significantly higher than the average in the frequency range 5 - 9 MHz.

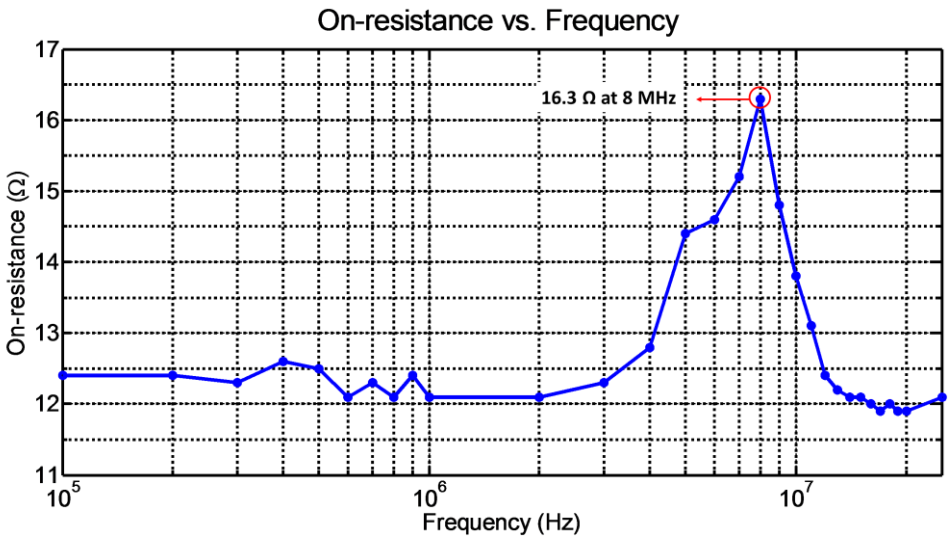

Figure 6.21 The on-resistance of a single analogue switch channel with -3 dB bandwidth.

6.5.5 Output Peak-peak Voltage, RMS Current and RMS Power for Different Load Conditions

The output characteristics were recorded by measuring a single channel voltage swing across different loads from 15 Ω to 3.3 kΩ, for output frequencies from 100 kHz to 50 MHz. The input signal was set to 30.0 V_{pp} for open load condition. The output RMS current and RMS power was calculated for different loads as well. The results are shown in Figure 6.22. Within the Sonotweezers transducers frequency range of 1 – 10 MHz, the output can generate a maximum RMS current of about 144 mA at 6 MHz, and the maximum output power can reach about 500 mW for 50 Ω load at 4 MHz.

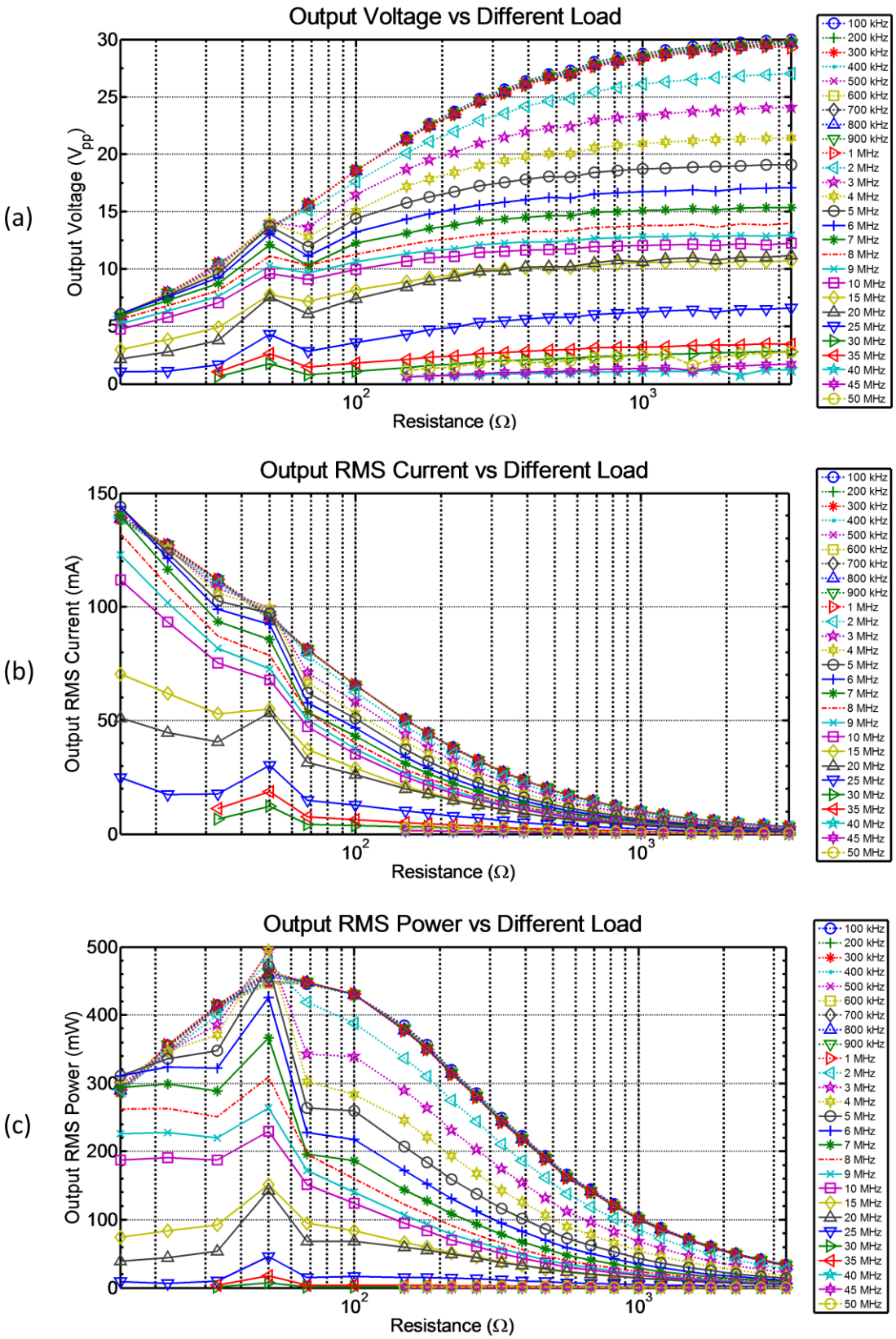

Figure 6.22 (a) Output peak-peak voltage vs. load resistance. (b) Output current vs. load resistance. (c) Output RMS power vs. load resistance.

6.6 Experimental Demonstration

6.6.1 Transducer Surface Displacement Measurement

A. Surface Displacement Measurement of Linear Array

The functionality of the driving electronics and the 1-D array Sonotweezer were characterised directly by measuring the transducer surface displacement. The driving signal was a CW sinusoid of 11.7 V_{pp} at 2.55 MHz. As shown in Figure 6.23 (a)-(c), because the lateral width and length of the piezocrystal pillars in the piezocomposite material are about 100 µm, and the pitch between each two adjacent linear array elements is 200 µm, the scanning step size was selected as 30 µm, which is less than half of the composite pillar pitch, for high resolution mapping. The LDV scanning stage setup is shown in Figure 6.23 (d).

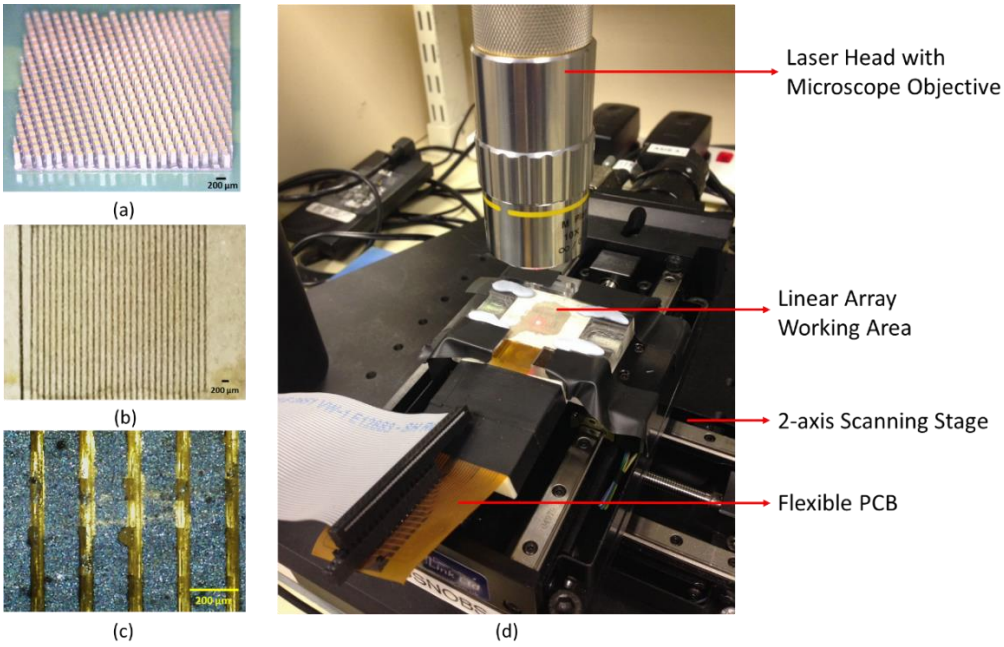

Figure 6.23 LDV for surface displacement measurement of the array transducer elements under the control of the driving electronics. (a) An example of piezo-crystal pillars for a 1-3 piezocomposite (adapted from Qiu, 2014a). The lateral pillar dimensions are 100 × 100 µm^2, with a 200-µm pitch. (b) The electrodes applied onto the piezocomposite material, with a 200-µm electrode pitch. (c) A micrograph showing the full-coverage of the electrode and composite piezoelectric pillars. (d) Experimental setup for LDV scanning.

Three elements were activated and manipulated in single element steps. Figure 6.24 shows the displacement mapping when elements 6 – 8, 7 – 9, 8 – 10 and 9 – 11 were

activated in turn. Since the effective area of the transducer array is 6 × 6 mm^2, the scanning area was also selected to have the same dimensions. Although signal crosstalk can be recognized between the active and non-active transducer elements, it is clear that the positions of the vibration maximum have been manipulated with the active elements. A non-uniformity of the transducer element displacement can be seen from the mapping results. At 2.55 MHz, the electrical impedance magnitudes and output electrical power for element 6 to 11 are listed in Table 6.2. Because of the variation in the impedance magnitudes, with a single driving input of 11.7 V_{pp}, the actual power delivered to each element appears differently during the output multiplexing, which leads to the transducer displacement variation in the LDV results.

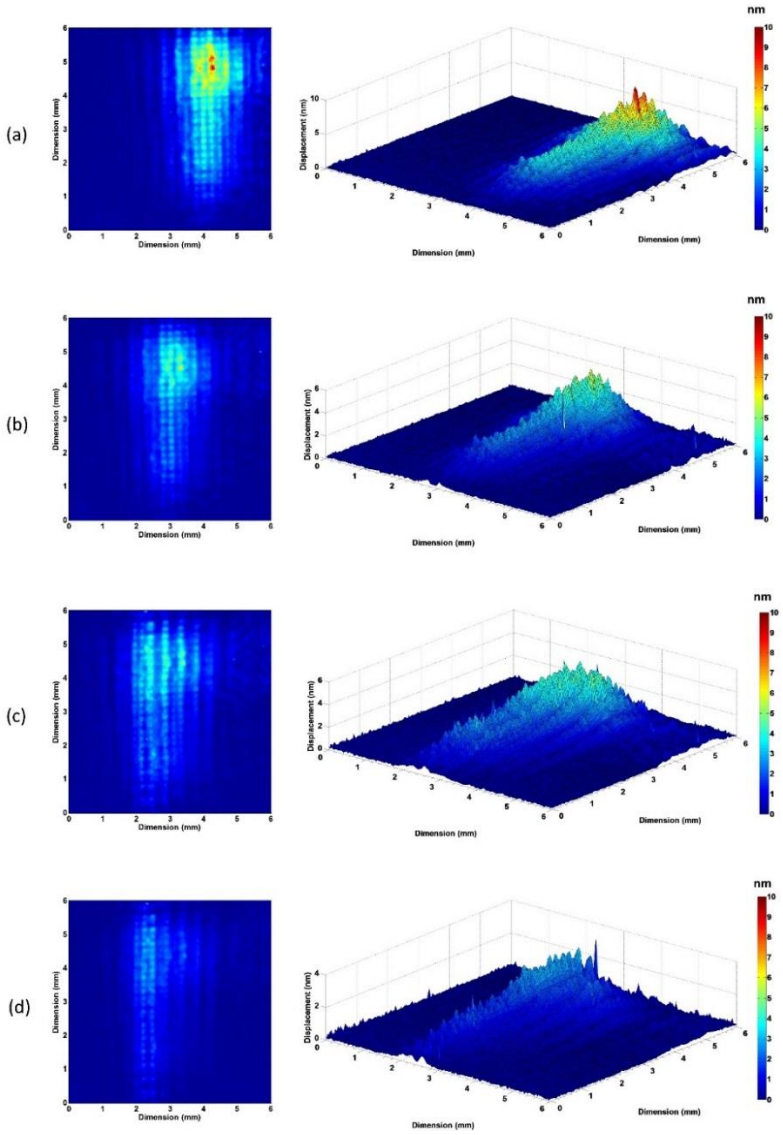

Figure 6.24 LDV mapping results for manipulating of an activation of 3-element group. The displacement was measured with SI units in nm. (a) – (d) The transducer elements are activated in a sequence of element 6 – 8, 7 – 9, 8 – 10 and 9 – 11.

Table 6.2 Electrical impedance magnitudes and corresponding output power for element 6 to 11, at the driving voltage input of 11.7 V_{pp}.

Element Number	Impedance Magnitude (Ω)	Output Power (mW)
6	3005	5.69
7	2179	7.85
8	2184	7.83
9	2177	7.86
10	3677	4.65
11	3689	4.64

B. Surface Displacement Measurement of Crossed-electrode Array

The patterns for element activation of the 8 × 8 crossed-electrode array are based on the ternary signal switching configurations, and the transducer elements can be activated in different patterns as single elements, row-of-elements, column-of-elements and symmetric-multiple-elements, depending on the control information stored in the ROMs. The surface displacement of the transducer array was measured with 2-D LDV scans to verify the functionality of the electronics. The experimental setup is demonstrated in Figure 6.25.

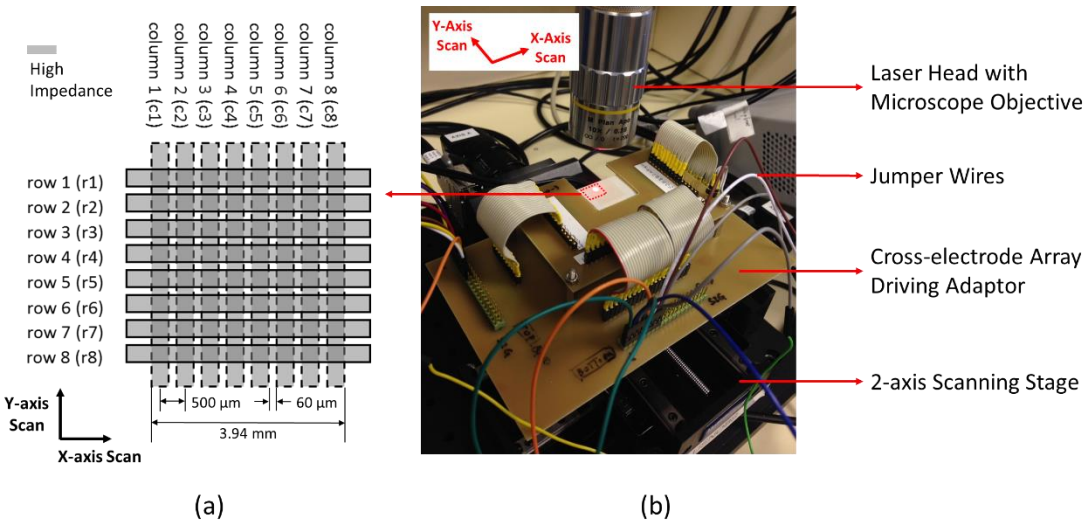

Figure 6.25 LDV scans for surface displacement measurement of the crossed-array transducer elements under electronic control. (a) Demonstration of the 64-element working area of the transducer array. By default all top and bottom electrodes are connected to "high impedance" states for "OFF" status. (b) Experimental setup for LDV 2-D scan.

In Figure 6.25 (a), top electrodes are represented by “rows” and bottom electrodes are represented by “columns”. With the element width, kerf and pitch previously stated, 8 × 8 elements cover an area of 3.94 × 3.94 mm^2. Hence the LDV scan area was selected as 6 × 6 mm^2, with 0.1 mm and 0.03 mm step resolution. Shown in Figure 6.25 (b), eight top electrodes and eight bottom electrodes were connected to the signal switching electronics with jumper wires. The AC signal source was provided, as before, by a signal generator (33250A, Keysight Technologies Inc., Santa Rosa, CA, USA) and the manipulation of the active transducer elements was controlled by the hardware interface on the FPGA development board.

The transducer surface displacements were measured for different element activation patterns. At all times during the scans, the transducers were driven with CW sinusoidal signals at a frequency of 7.25 MHz. Firstly the array was activated in rows and columns respectively to confirm the dimensions of the working area with results shown in Figure 6.26. Measured from the mapping results of the row- and column-activation, the 64-element active area is located in a square with the dimension of approximately 3.4 × 3.4 mm^2. This result corresponds well with the dimension defined by the 8 × 8 electrodes, which is 3.5 × 3.5 mm^2 when measured to the centre of the electrodes at the edges of the rows and columns.

Next, the array was activated in single element patterns and the surface displacement was measured as shown in Figure 6.27 and Figure 6.28. The active elements were altered with the FPGA electronics from the element defined by electrodes row-1 and column-1 (r1c1), to the element defined by electrodes row-8 and column-8 (r8c8). The active elements can be identified from the LDV scanning results, and the locations of the active elements matches with the dimensions measured from the displacement mapping graphs. However apart from the primary activations shown in Figure 6.27 and Figure 6.28, there are subsidiary activations over the elements with high impedance and ground signals connected on top and bottom electrodes, respectively. This indicates that there are possible cross-talk of the active signals onto the adjacent high impedance top electrodes. Additionally, Figure 6.27 shows activation over undesired element area that supposed to be turned “OFF”, again this can be the crosstalk of driving voltages over the elements with signal and high impedance connected to the top and bottom electrodes, respectively. Further examination of the actual voltages across the transducer elements over the “ON” and “OFF” elements is needed for the characterisation of the array.

Multiple transducer elements were also activated in different symmetrical patterns. Figure 6.29 demonstrates the displacement mapping of the activation patterns for four elements. The active elements of different electrode patterns can be clearly identified. In conclusion, as a preliminary study, the results of the displacement mapping of the array transducers have a good correlation with the localization of the active elements. Four symmetrically located transducers are activated, beginning from the four rear corners of the 8 × 8 element matrix, as shown in Figure 6.29 (a). Then the elements are successively activated along the diagonals in the matrix. For the array of 500 μm pitch, the elements are activated at a step size of 707 μm, which correlates with the dimension shown in Figure 6.29 (a) – (d). However, subsidiary activations are also visible from the scanning results due to element crosstalk, and this will be further examined by measuring the driving voltages over the array elements.

Further improvement can also be made to the LDV scanning system. Currently the laser beam is focused with a 10× microscope objective for a spot size of Ø400, which is relatively large compared to the 500 μm array pitch, and active elements are hard to be differentiated from the displacement mapping results, as shown in Figure 6.29 (d). This laser spot size can be further reduced, ideally smaller than half of the array pitch, with an objective of higher magnification.

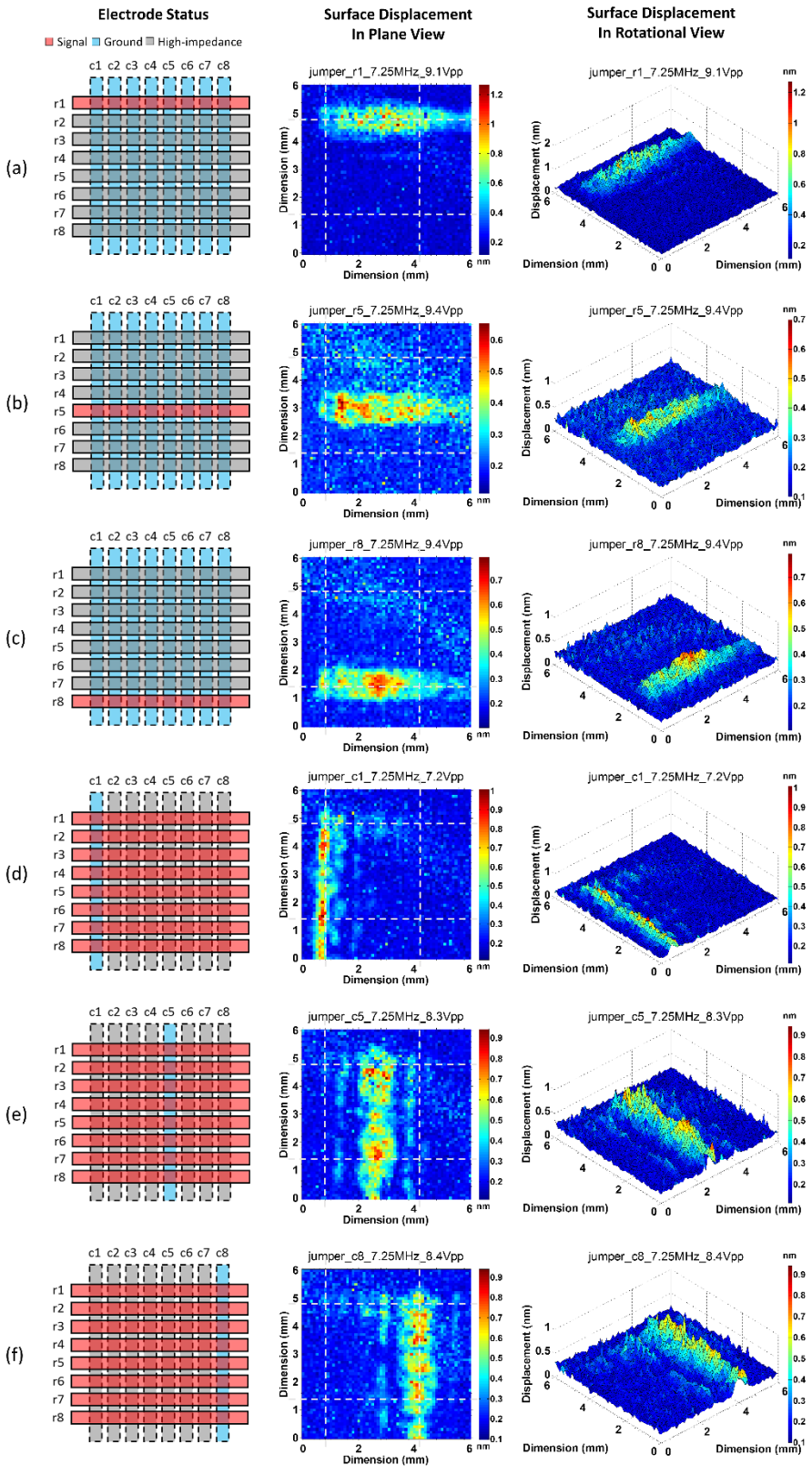

Figure 6.26 Crossed-electrode array activation by rows and columns. All displacements are measured in nm. (a) – (c) row-1 (r1), row-5 (r5) and row-8 (r8) are activated. (d) – (f) column-1 (c1), column-5 (c5) and column-8 (c8) are activated.

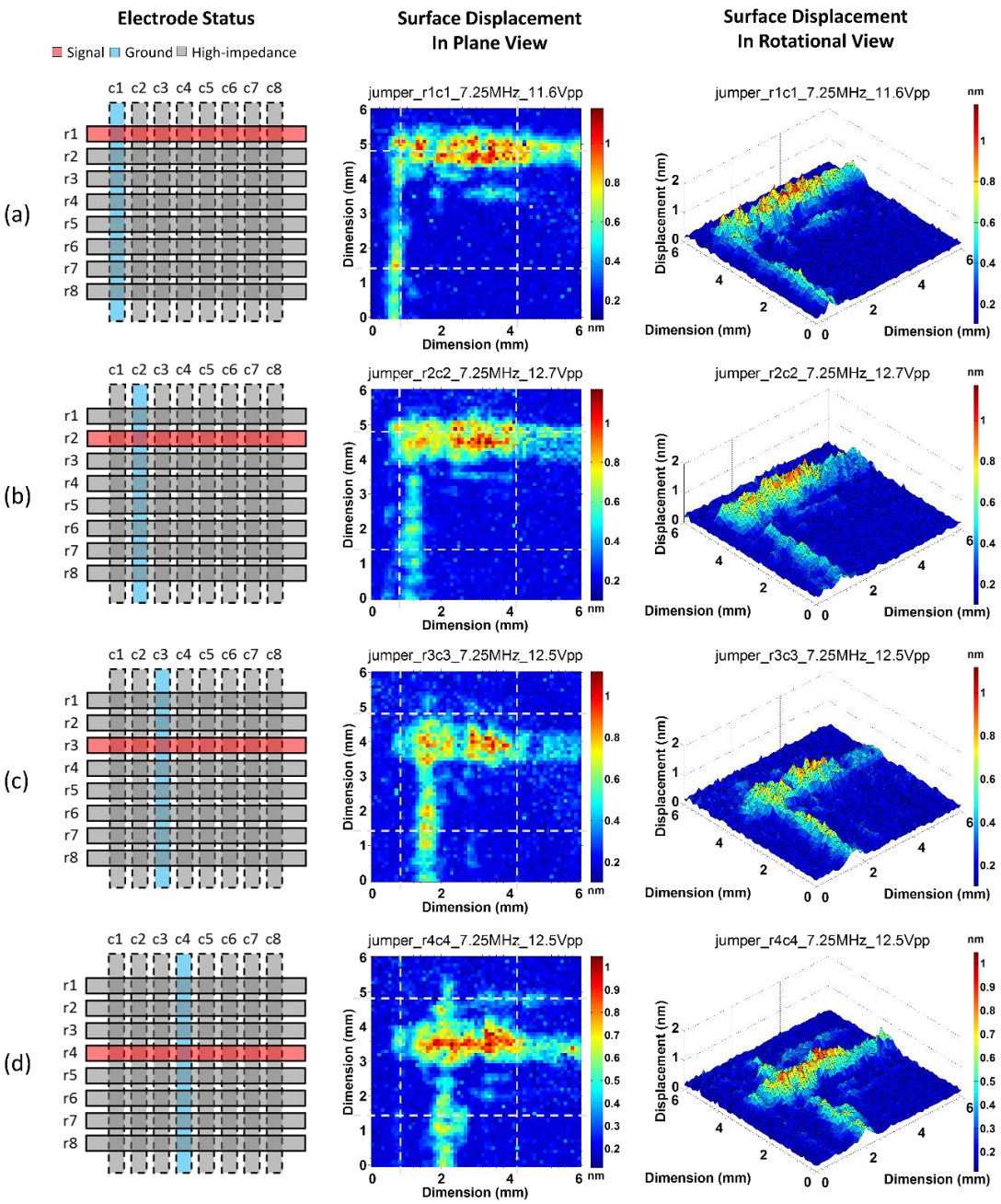

Figure 6.27 Crossed-electrode array activation by a single element. All displacements are measured in nm. (a) – (d) The active transducer element is altered from r1c1 to r4c4.

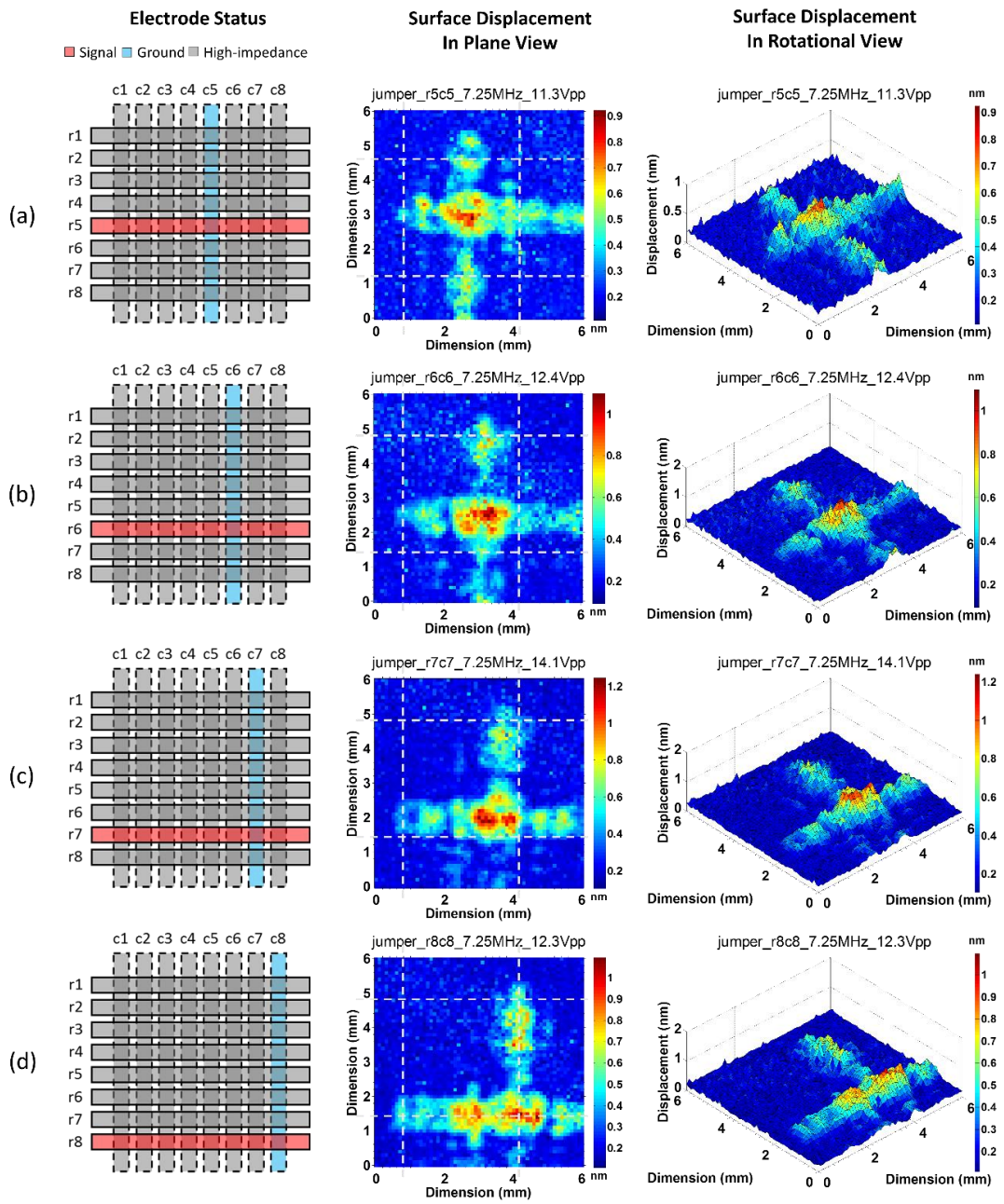

Figure 6.28 Crossed-electrode array activation by a single element. All displacements are measured in nm. (a) – (d) The active transducer element is altered from r5c5to r8c8.

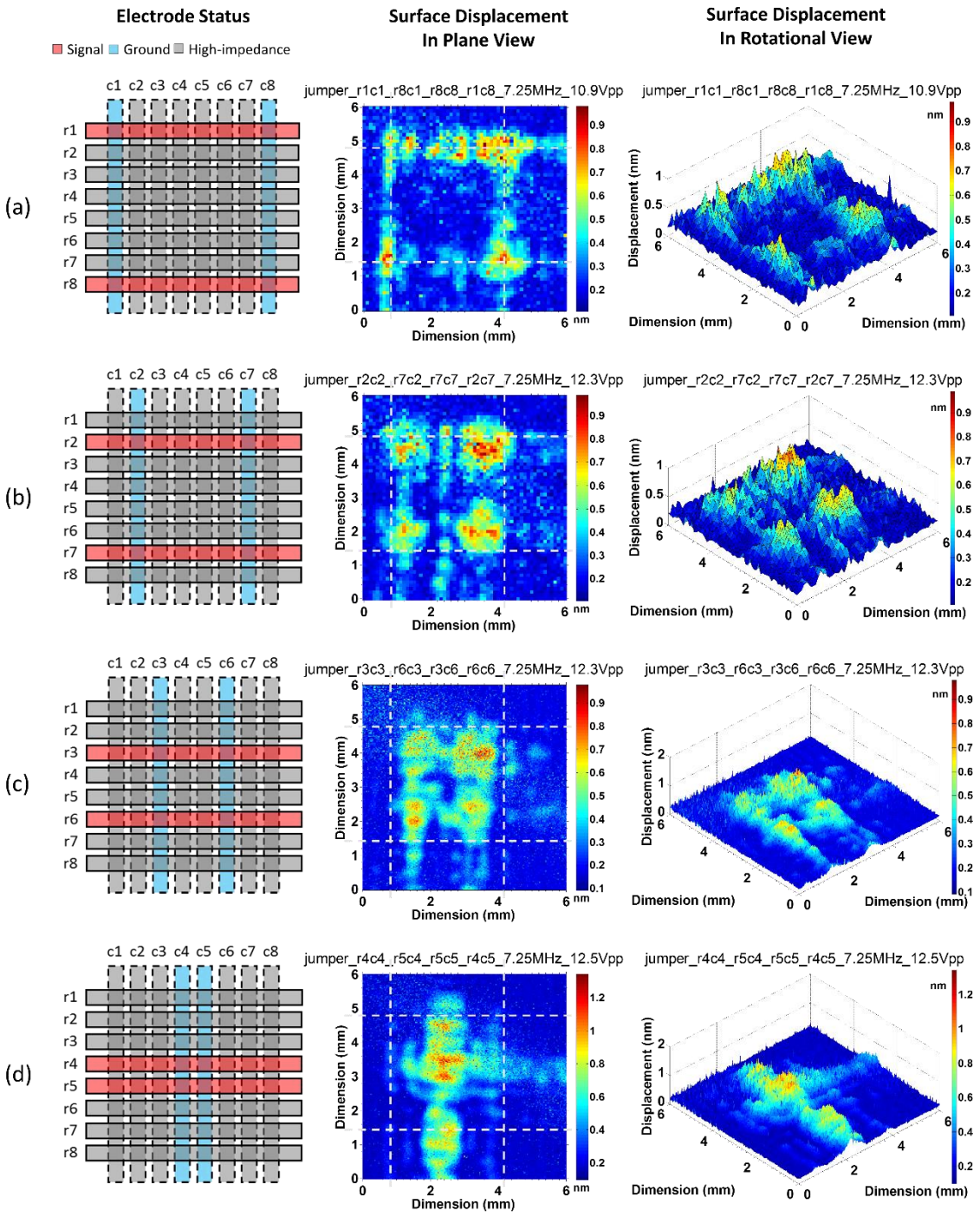

Figure 6.29 Crossed-electrode array activation by four elements simultaneously. All displacements are measured in nm. (a) The active elements are r1c1, r8c1, r8c8 and r1c8. (b) The active elements are r2c2, r7c2, r7c7 and r2c7. (c) The active elements are r3c3, r6c3, r6c6 and r3c6. (d) The active elements are r4c4, r5c4, r5c5 and r4c5. In (c) and (d) the scans were performed with 0.03 mm step size to give a better resolution for element differentiation, as they were manipulated closer to each other.

6.6.2 Experimental Demonstration with 1-D Linear Array

A. Experimental Setup

Figure 6.30, illustrates the experimental setup for particle manipulation. The 1-D linear array Sonotweezer was placed under a fluorescence microscope and Ø10 µm fluorescent microspheres were prepared in a water-based suspension. The suspension was first introduced into a glass capillary with 300-µm fluid thickness and 6 mm width (VitroCom, Mountain Lakes, NJ, USA) through plastic tubing, and then maintained there by sealing both ends of the tubing. The signal switching electronic system was connected to the flexible array PCB through a 0.5 m long flat-to-twist ribbon cable.

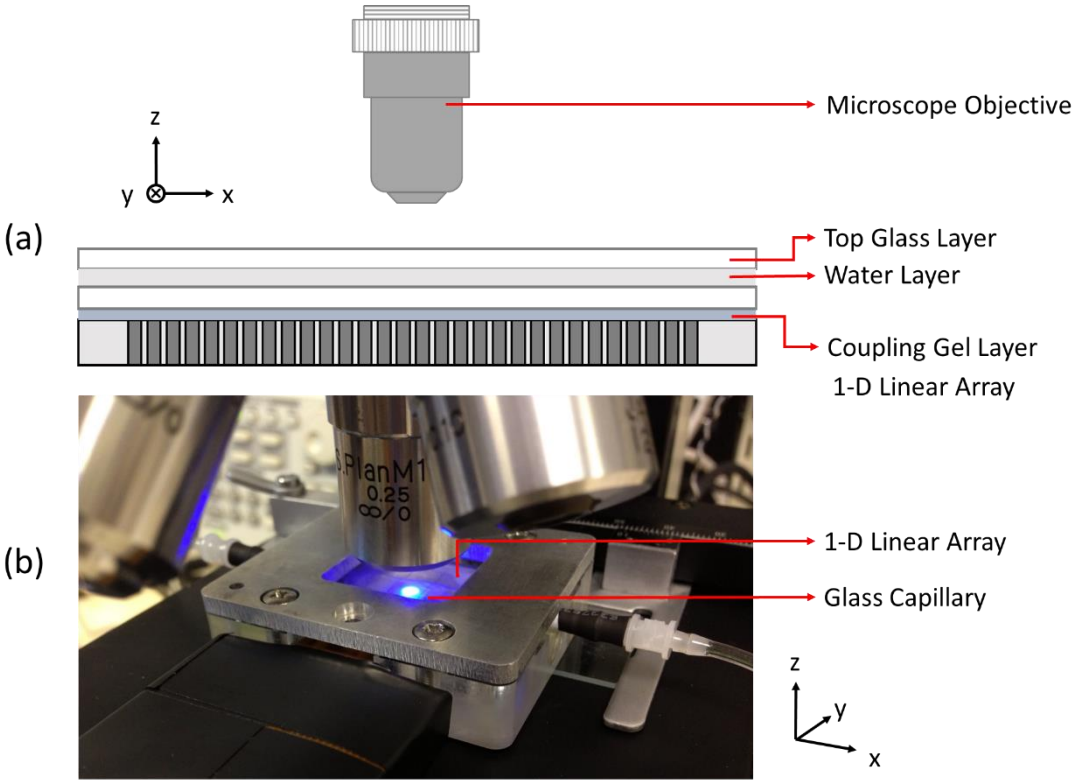

Figure 6.30 Experimental setup for particle manipulation with 1-D linear array Sonotweezer. (a) Diagram illustrates the multilayer resonator setup in cross-section. (b) A photograph of the setup.

B. Experimental Results

a. Manually Controlled Particle Manipulation

An experiment for demonstrating the particle manipulation with linear array Sonotweezer was performed using the FPGA core described in Subsection 6.3.1. A water-based particle suspension with a concentration of approximately 2.7×10^5 particles/ml was introduced into the glass capillary. Three transducer elements were activated with a 16 V_{pp} CW sinusoidal signal at 2.55 MHz. The combined electrical impedance magnitude for the active elements was approximately 600 Ω. A USW field was created in the capillary and particles concentrated together, forming an agglomerate with dimensions 202×450 μm^2. During the agglomeration process, video was captured with a frame rate of 0.021 second/frame (47.6 fps), so the average concentration velocity of 10 single particles can be measured as 18.9 ± 6.2 μm/s. The lateral agglomerating force is balanced with the Stokes' drag force, calculated as 1.8 ± 0.6 pN.

The active transducer elements were shifted across the array in one element steps, and the agglomerate was manipulated according to the updated positions of the E_{kin} maximum "hot spots", as shown in Figure 6.31. The agglomerate was firstly created at active elements 4 – 6, and was manipulated forward to elements 9 – 10 in four steps, and then moved back to the original position. The manipulation was controlled with the rotary knob on the FPGA development board. The video was captured at 0.023 second/frame (43.5 fps), and the average agglomerate lateral manipulation velocity is thus measured as 27.5 ± 0.7 μm/s from 10 manual tracking results, equivalent to a lateral manipulation force of 117 ± 3.0 pN.

The distance of each manipulation step is measured and compared with the transducer array element pitch, as shown in Figure 6.32. The actual distances are 80 ~ 180 μm, smaller than the designed element pitch of 200 μm. The most likely reason is misalignment of the array and the capillary, i.e. the capillary placed at an angle relative to the x-axis of the array, as shown in Figure 6.33. Another reason can be the variance of the driving power delivered to the array elements.

Table 6.3 shows a summary of the electrical impedance magnitude of elements 4 to 10 at 2.55 MHz, and output power for 16 V_{pp} driving voltage. The variation of the impedance

magnitude leads to the inhomogeneity of the element vibration displacement, which is also demonstrated as LDV scanning results shown in Figure 6.24. As a result, the positions of E_{kin} maxima and the E_{kin} gradient distribution will vary, which will affect the localization of the particle agglomerate for each step of manipulation. Other possible reasons are the variation of the thicknesses of the fluid layer, the glass layer and the coupling gel layer along the x-axis, which can lead to inhomogeneity in the resonance structure that affects the USW field.

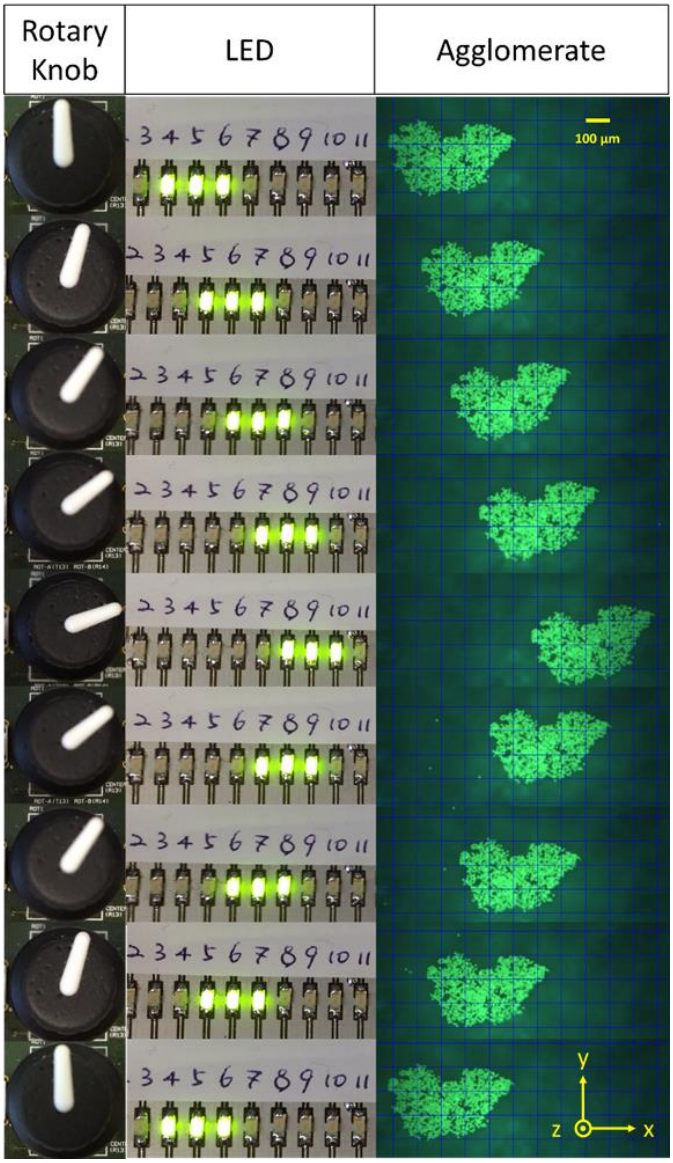

Figure 6.31 A composite graph demonstrating the experimental results of manipulating a particle agglomerate with signal switching electronics. LED indicator denotes the numbering of the active elements, under the control of the rotary knob. An agglomerate formed with Ø10 µm polystyrene particles was manipulated in several steps forward and backward along the fluid channel.

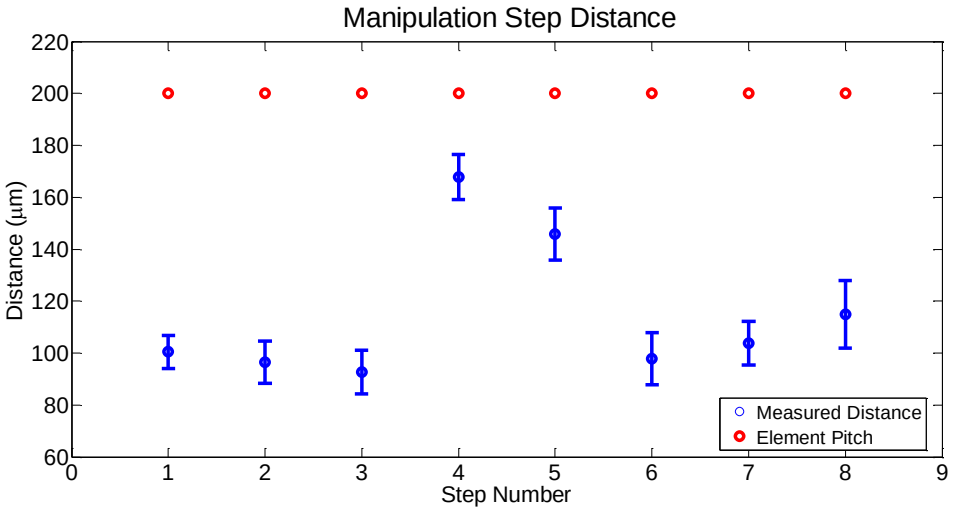

Figure 6.32 Comparison between the array element pitch and the manipulation steps.

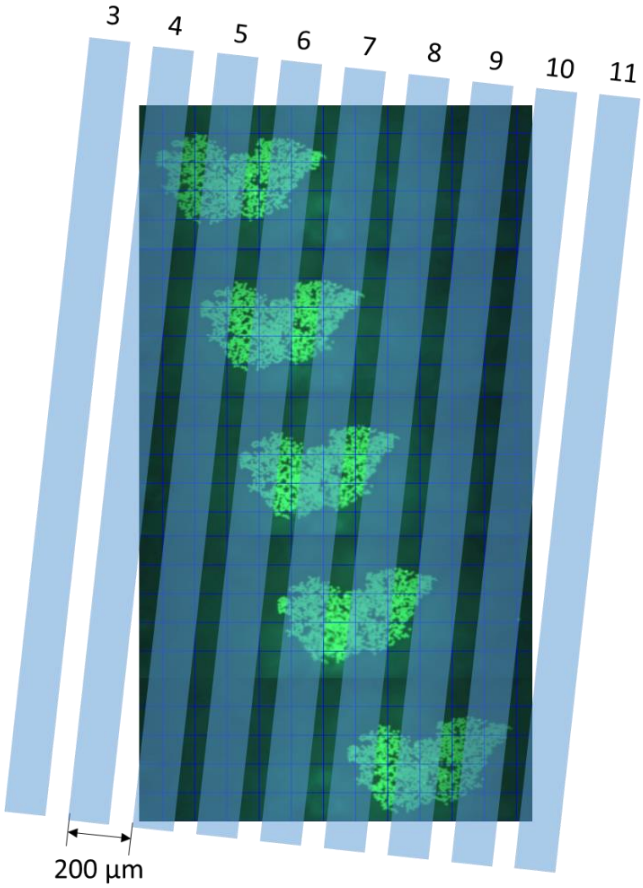

Figure 6.33 Demonstration of possible misalignment of the transducer array and the glass capillary used as the fluid channel. The light blue rectangulars demonstrate the array elements, and the dark blue grid represents 100 µm in length. In the picture, the capillary fluid channel and the array are positioned with an angle of 7.0°.

Table 6.3 Electrical impedance magnitudes and corresponding output power for element 4 to 10, at the driving voltage input of 16 V_{pp}.

Element Number	Impedance Magnitude (Ω)	Output Power (mW)
4	3427	9.34
5	2980	10.74
6	3005	10.65
7	2177	14.70
8	2179	14.69
9	2184	14.65
10	3677	8.70

b. Automatically Controlled Particle Manipulation (Element Hopping)

During the experiment of manipulating the agglomerate with manually controlled rotary shaft on the FPGA development board, the particle concentrate was migrated slowly (~ 4 s in average) from one lateral trapping site to another. In order to find the limit of the linear array device for lateral manipulation, i.e., the maximum manipulation forces for shifting the particle agglomerate between the trapping sites, an experiment was designed with modified linear array FPGA logic for switching the activation of two transducer elements with precisely controlled frequencies (element hopping). Hence the trapping sites can be dynamically alternated between the positions of the active elements. Figure 6.34 gives a demonstration of the element hopping control, and the FPGA source codes is given in Appendix A.

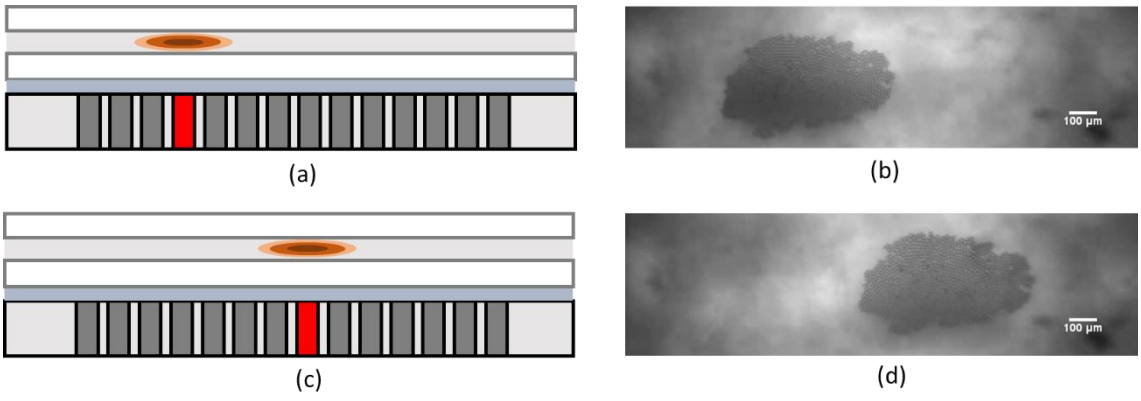

Figure 6.34 Element hopping control for dynamically changing the position of the particle agglomerate between two trapping sites. (a) and (c): Array element 4 and 8 are activated respectively, with illustrative energy gradient created above the active transducers. (b) and (d): A particle agglomerate is created by the active array element, and positioned over element 4 and element 8 respectively.

Ø10 μm polystyrene particle water-based suspension with a concentration of 4.3×10^6 particles/ml was introduced into the glass capillary. The particle concentration was increased in this experiment to enhance the agglomeration process. The agglomerate created by activating one transducer element at 2.574 MHz, is demonstrated in Figure 6.34, with the dimension of 323×608 μm^2. The trapping sites were switched dynamically between element No.4 and No.8, with various frequencies, controlled precisely from a signal generator (33220A, Keysight Technologies Inc., Santa Rosa, CA, USA). For a certain transducer driving voltage, the range of the switching frequency was determined, with the lowest one mimic the process of manual control, and the highest one at which the trapped agglomerate fail to follow the transition of the trapping positions.

For the conditions of different driving voltage and different shift frequencies, the migration of the particle agglomerate was recorded as a series of videos with 16.7 fps (0.06 second/frame), and the lateral velocities of the agglomerate under manipulation were calculated from manual tracking results processed with ImageJ. For all the videos, the pixels were calibrated with a scale of 2.8 μm/pixel. Figure 6.35 gives a demonstration of the agglomerate positions under different element hopping frequencies. With an increased frequency, the agglomerate displacement reduces and tends to oscillate at the middle position of the active elements 4 and 8.

The agglomerate migration distances and the lateral forces for manipulating the agglomerate between two trapping sites were calibrated against different transducer driving voltages and element hopping frequencies, as shown in Figure 6.36. In Figure 6.36 (a), for a certain hopping frequency, the lateral manipulation distance decreases with the reduced driving voltage. For a given voltage, the manipulation distance decreases with increased hopping frequency, and at certain frequencies, when the displacement reduces to 5 ± 1 μm, the pixel differences for each movement step reach the aliasing limit of the recorded video resolution, and the agglomerate appears still from the live videos. Such frequencies were recorded as the maximum hopping frequency for a given voltage for manipulating the agglomerate.

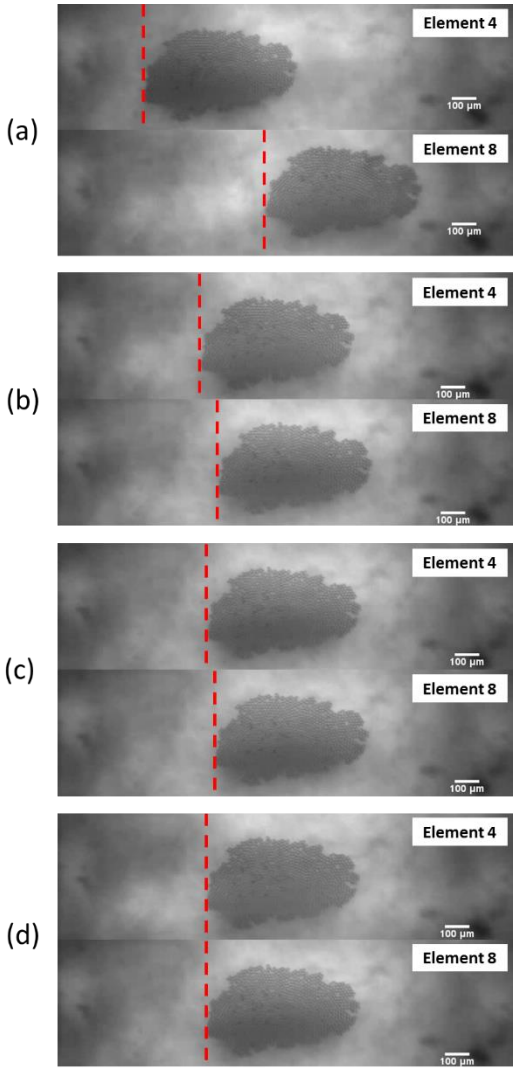

Figure 6.35 Positions of the particle agglomerate when the active elements switching between No.4 and No.8 with a hopping frequency of (a) 0.05 Hz. (b) 0.5 Hz. (c) 1 Hz. (d) 4 Hz. The transducers were driven with 28 V_{pp}, CW sinusoidal signals.

The lateral forces were balanced with Stokes drag forces, and calculated as shown in Figure 6.36 (b), and the force measurements at the maximum hopping frequencies for different driving voltages are further summarized in Figure 6.36 (c) and Table 6.4. For each given voltage, the lateral forces for the maximum hopping frequency are listed. The forces increase with the driving voltage and the shifting frequency. This trend appears more significant for higher driving voltages due to stronger force gradients created in the lateral dimension in the capillary (Glynne-Jones, Démoré, et al., 2012).

(a)

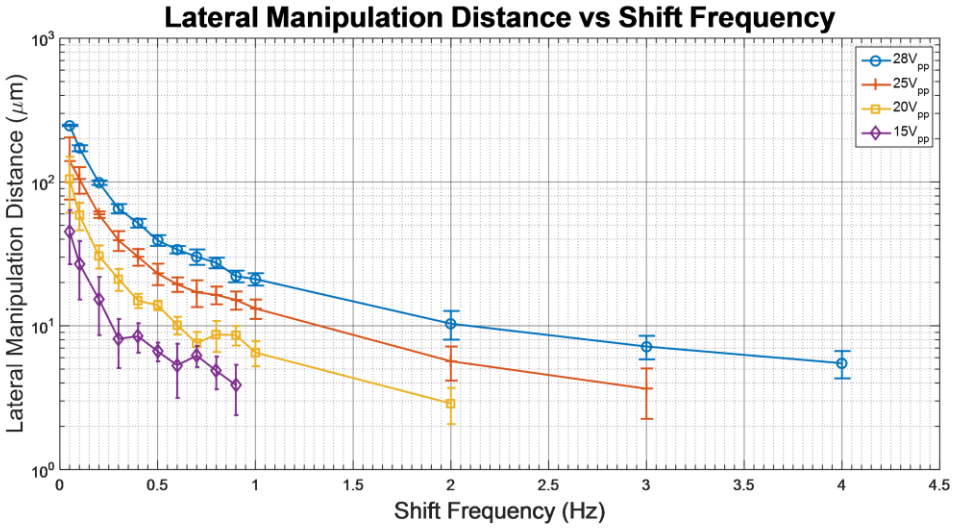

(b)

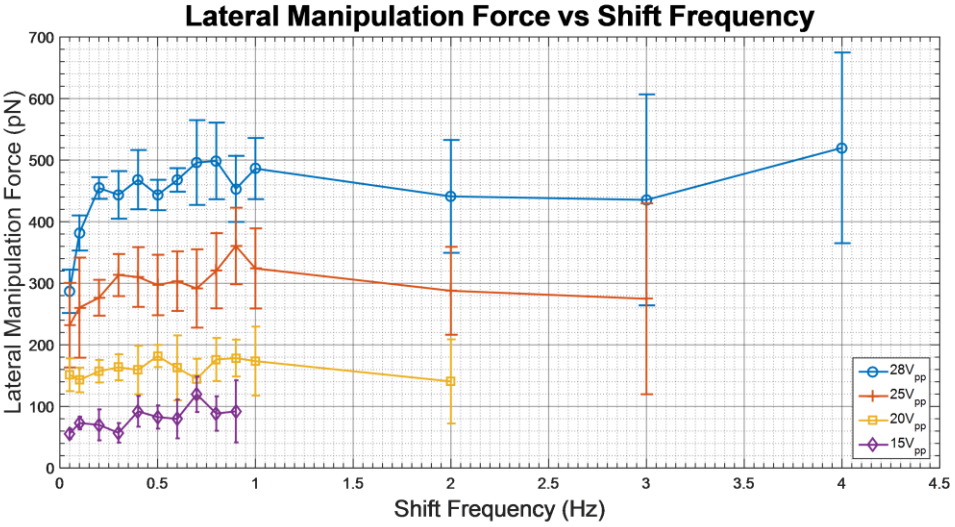

(c)

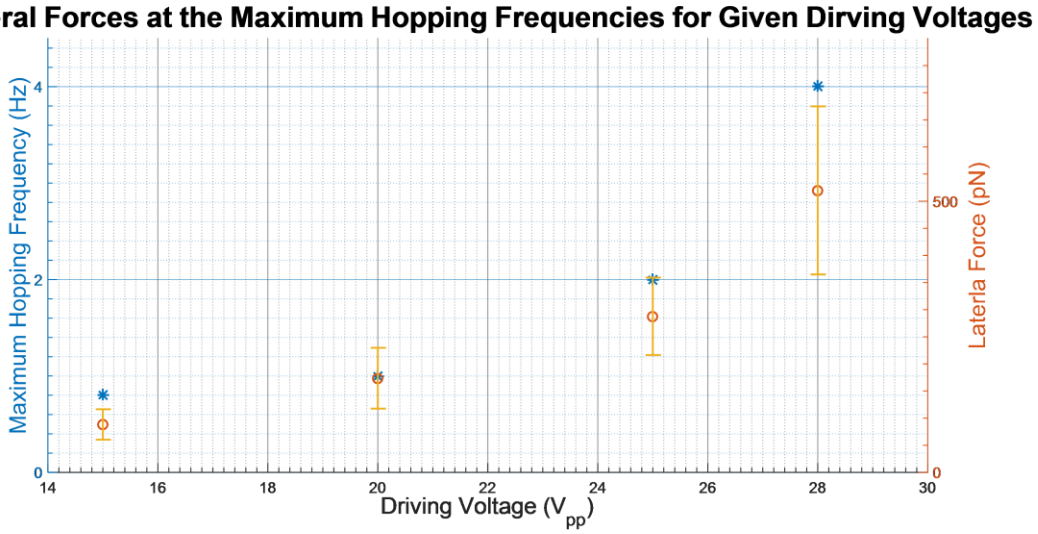

Figure 6.36 Particle agglomerate lateral displacement magnitude and force magnitude measured against different hopping frequencies between the active elements No.4 and No.8. (a) Lateral displacement magnitude. (b) Lateral force magnitude. (c) A summary of the maximum hopping frequencies and the correlated lateral forces at different driving voltages.

Table 6.4 Lateral force measurements at the maximum hopping frequencies for given driving voltages.

Driving Voltage (V_{pp})	Maximum Hopping Frequency (Hz)	Lateral Force (pN)
28	4	519.9 ± 154.9
25	2	287.8 ± 71.4
20	1	173.6 ± 56.1
15	0.8	88.4 ± 28.0

6.7 Conclusions

This chapter focused on the electronics development for control of planar resonator based Sonotweezers. Conventional ultrasonic arrays are normally constructed with separated active electrodes and a shared ground electrode to define transducer elements. Ultrasonic arrays can be used for acoustic tweezing applications, and the experimental demonstration of such devices was reported by Glynne-Jones et al. with a manually-controlled 1-D linear array. The crossed-electrode configuration provides a possibility of creating a 2-D transducer array with a large number of elements with simplified electrical interconnections, compared to the electrode design for conventional 2-D arrays. However, the mechanism for element activation of the crossed-electrode array becomes more complex.

This chapter explored the possibility of using an electronically-controlled switching mechanism to control both arrays with common ground electrodes and arrays with crossed-electrodes, towards planar resonator based acoustic tweezing applications. Because of the need for accurate frequency tuning of such Sonotweezers, as a proof of concept study, the signal source was simplified as a single input provided from a contemporary commercial signal generator. The FPGA-controlled electronics that were developed were able to successfully perform multiplexing of the external input signal along the output channels. For each channel the analogue signal switching circuitry can provide output voltages up to 30 V_{pp}. The -6 dB bandwidth of the output can reach 20 MHz, with channel crosstalk of -53 to -23 dB for Sonotweezers working frequencies

of 1 to 10 MHz. The electronics provides a straightforward user interface, as well as LED indicators for direct visual feedback.

The switching functionality of electronics has been successfully demonstrated with the linear array Sonotweezer for particle trapping and manipulation. The experimental results have fulfilled the aim of this chapter to explore the possibility of using electronically controlled ultrasound arrays for precise particle manipulation, and for acoustic force calibration. The functionality of the electronics for controlling crossed-electrode arrays was also verified with LDV measurements. It is possible to address single or multiple transducer elements of a crossed-electrode 2-D array with a ternary switching method. Currently it is difficult to examine the 7 MHz crossed-electrode array with particle manipulation experiments in planar resonators, as it is difficult construct resonator chambers for the thick-film PZT crossed-electrode array discussed here. The transducers are working at 7 MHz, which corresponds to a $\lambda/2$ fluid thickness of 100 μm for an optimum condition for particle trapping and manipulation (Glynne-Jones, Boltryk, et al., 2012; Qiu, 2014a). More discussion on this point will be given in Chapter 7.

The main limitation of the electronics described here is that the output current per channel is reduced as the number of outputs is increased, since the output AC signals for all active channels have a single external source. The fan-out capacity of the circuitry is thus greatly limited as more transducer elements are connected. However, in Chapter 5 it has been demonstrated that the multichannel electronics can generate independent outputs, thus there is an obvious advantage to be gained in combining the signal switching functionality with the multichannel electronics system. Again, further discussion will be given in Chapter 7.

Another possibility is to control the array dynamically with the FPGA, e.g. by synchronizing the channel "ON" or "OFF" status with the FPGA clock signal. The frequency of this signal can be as high as tens of MHz. However the maximum switching frequency is primarily limited by the dynamic characteristics of the analogue switch IC. For a ±15 V power supply at 25°C, the maximum transition time of the ADG5434 is 207 ns ("ADG5434 Datasheet", 2013). Hence the maximum switching frequency between each two channels is less than 4.83 MHz. With electronically controlled switching, the present electronics can be configured to control relatively more complex

array devices. The possibility to dynamically control a crossed-electrode array for activating elements in arbitrary 2-D patterns will be discussed in Chapter 7.

Element multiplexing with 1-D or 2-D transducer array based planar resonator Sonotweezers indicates potential uses in life sciences applications. Biological cells can be concentrated and suspended in the medium, and manipulated manually or electronically. This may provide a useful mechanism for applications such as cell medium exchange, micro-centrifugation, and studies of interactions between different cell groups.

CHAPTER 7 CONCLUSIONS AND FUTURE WORK

7.1 Conclusions

This thesis has presented an exploration of the development of driving electronics for different Sonotweezer devices.

Firstly, in Chapter 2, different particle manipulation technologies were compared, and the uniqueness of the technique of acoustic tweezing was demonstrated, particularly its straightforward potential to integrate with life sciences applications. Chapter 3 discussed the basic theory and technologies for electronics design and fabrication involved in this thesis, and Chapter 4 gave a brief introduction to the electronic development methods, as well as the equipment for electronic characterisation and experimental demonstration with Sonotweezers.

Chapters 5 and 6 demonstrated two types of electronics that were developed. Chapter 5 discussed the development of dexterous multichannel electronics that can generate independent outputs with the flexibility for computer-controlled frequency and phase modulation, and manually-controlled amplitude modulation. The functionality of the electronics was demonstrated with typical counter-propagating Sonotweezer devices, principally circular arrays, to create dynamic Bessel-function shaped acoustic fields for particle trapping and manipulation. Chapter 6 particularly focused on providing a solution for controlling planar resonator based Sonotweezers with prototype signal switching electronics. The developed electronics can control conventional transducer arrays with common ground electrodes, or arrays with crossed-electrodes. The functionality of the electronics was characterised with LDV displacement mapping and particle manipulation experiments.

7.1.1 Multichannel Electronics for Complex Acoustic Field Modulation

Acoustic particle trapping and manipulation with Bessel-function shaped acoustic fields has gained great interest in recent 10 years (Démoré et al., 2012; Marston, 2006; Silva et al., 2013). Experimental studies focused on creating propagating acoustic Bessel beams for particle trapping with a few transducers (Kang and Yeh, 2011) or with acoustic lenses (Choe et al., 2011). Grinenko et al. (2012) and Courtney et al. (2013, 2014) demonstrated theoretically and experimentally how to generate stationary Bessel-function acoustic fields with 16-element counter-propagating wave circular transducer array. Microparticles can then be trapped into pressure nodes in the shape of multiple concentric circles. The particles trapped at the centre of the Bessel-function field can be manipulated by changing the relative phases of the driving electrical signals for each array element.

Using a circular array as a typical Sonotweezer device, multichannel electronics were developed with 16 separate channels that can be configured individually, giving them great flexibility for configuring ultrasonic arrays for complex acoustic field shaping. Each output channel can generate a near-sinusoidal CW signal with maximum voltage 26 V_{pp}. For each channel, the output phase and frequency can be modulated with computer control. The output phase resolution is tunable and selected in 22.5° steps for the 16-element circular array. The -3 dB and -6 dB frequency bandwidths are 6 MHz and 9 MHz respectively, with a tuning resolution of 0.001 MHz in the MHz range. The output amplitude can be manually changed in a linear manner from 0 to 26 V_{pp} maximum. With customized PC-based GUI control, the electronics were successfully demonstrated with the circular array Sonotweezer to generate pN-level acoustic forces for dynamic dexterous particle trapping and manipulation. The current configurations for both digital and analogue electronics are all scalable and the GUI that has been developed with the multichannel electronics system may find uses as a highly-customized research platform for characterizing array-based Sonotweezer devices for many potential applications.

7.1.2 Signal Switching Electronics for Planar Resonator Sonotweezers

It has been demonstrated that microparticles can be focused and manually manipulated with ultrasonic transducer array-controlled planar resonators constructed with glass capillaries (Glynne-Jones, Démoré, et al., 2012; Qiu et al., 2014). This principle can be extended to manipulate particles in 2-D with 2-D transducer arrays (Appendix D).

These transducer arrays have similar characteristics with separated active electrodes and a common ground electrode to define the elements. In order to address individual elements or element-groups in arbitrary patterns, prototype signal switching electronics were developed. The electronics can switch an AC input signal through multiple output channels, and each channel is able to provide an output up to 30 V_{pp}. The output channels have satisfactory -3 dB and -6 dB bandwidth of 14 MHz and 20 MHz respectively, with the channel crosstalk as low as -53 to -23 dB within the 1 to 10 MHz range of current Sonotweezer working frequencies. The functionality of the electronics was successfully demonstrated with a 2.55 MHz linear array Sonotweezer device to generate pN-level acoustic forces for particle trapping and manipulation.

The crossed-electrode transducer array configuration opens up the possibility to define elements with multiple orthogonally arranged top and bottom electrodes (Démoré et al., 2009). For acoustic tweezing applications with planar resonators, it is possible to create a 2-D array with a large number of elements with simplified electrical interconnections, at a cost of increased complexity for electronic control (Qiu, 2014a). Individual elements or element groups in symmetrical patterns can be addressed with the switching electronics that have been developed, with a ternary switching mechanism. The basic functionality of the electronics was successfully demonstrated with a 7 MHz thick-film crossed-electrode array with LDV surface displacement mapping.

The experimental characterisation results suggest that electronically-controlled ultrasound array-based planar resonators may be useful in life sciences studies for applications such as precise cell positioning, cell medium exchange, and force measurement between cell groups.

7.1.3 Electronics Development at System Level for Sonotweezer Applications

The multichannel electronics and signal switching electronics were designed with either simple or more complex user interfaces. The multichannel electronics were designed with a PC-level GUI interface. Each channel can be configured independently for signal frequency and phase, and the GUI can be easily adapted to incorporate acoustic models of different Sonotweezer devices. The FPGA core was developed as a generic embedded core to generate CW signals with arbitrary frequencies and quantized phases within the range of design limitations. A data communication interface was successfully configured for the multichannel electronics, to allow dynamic transducer control for particle trapping and manipulation under control of a PC-level interface.

User interface hardware on the FPGA development board, such as rotary knobs and slide switches, was configured as a straightforward user interface for the signal switching electronics. The LED indicators integrated with the electronics give intuitive feedback of the transducer element operating conditions. The FPGA core can be easily tailored to adapt different switching functions for 1-D and 2-D arrays. Fully automatic operation with a PC-based GUI interface would also be possible.

7.2 Future Work

The possibility to use signal switching electronics to control crossed-electrode arrays has been demonstrated in Chapter 6. Additionally, as a key indication of future work, it is possible to control a crossed-electrode array dynamically, with an analogy to holographic optical tweezers (Grier, 2003), to create multiple independently controlled acoustic traps with planar resonators. A proposed mechanism of time-shared multiplexing with the present signal switching electronics will be discussed here.

The dexterous multichannel electronics can be further configured to incorporate the function of the signal switching electronics, with the advantage of generating independent CW outputs. A case study using adapted multichannel electronics for driving the 1-D linear array Sonotweezer will be demonstrated later in this section. Additionally, further

improvements can be considered for the multichannel electronic system outputs to provide higher power and higher bandwidth, by using “push-and-pull” amplifier design. At last, an outlook will be given for packaging the developed electronics as a versatile toolkit, and integrating with future technologies in piezoelectric transducers as dexterous acoustic tweezers.

7.2.1 Outlook for Crossed-electrode Array Control

A. Dexterous Control of Crossed-electrode Array Sonotweezer with Switching Electronics

As previously shown in Chapter 6, Figure 6.30, the key feature of the present configuration for multi-element activation is that it requires common active electrodes, either the top electrodes connected to the AC signal, or the bottom electrodes connected to the ground. However, in another approach, the elements in a crossed-electrode array can be activated in arbitrary patterns, by introducing time-shared electrode control. The modified FPGA core functional block diagram is shown in Figure 7.1.

For dynamic control, the bottom electrodes (column electrodes) are connected to signal ground one-by-one alternately and the top electrodes (row electrodes) are connected to the driving signal, in synchronization with the bottom electrode. Hence the transducer array is activated in a single column for each time instant, and a time-shared 2-D activation pattern can be realized when the column activation patterns are switched rapidly. In the FPGA core, a swept clock signal is used to control the electrode sweeping frequency and the column patterns can be activated manually by pressing a push-button for debugging.

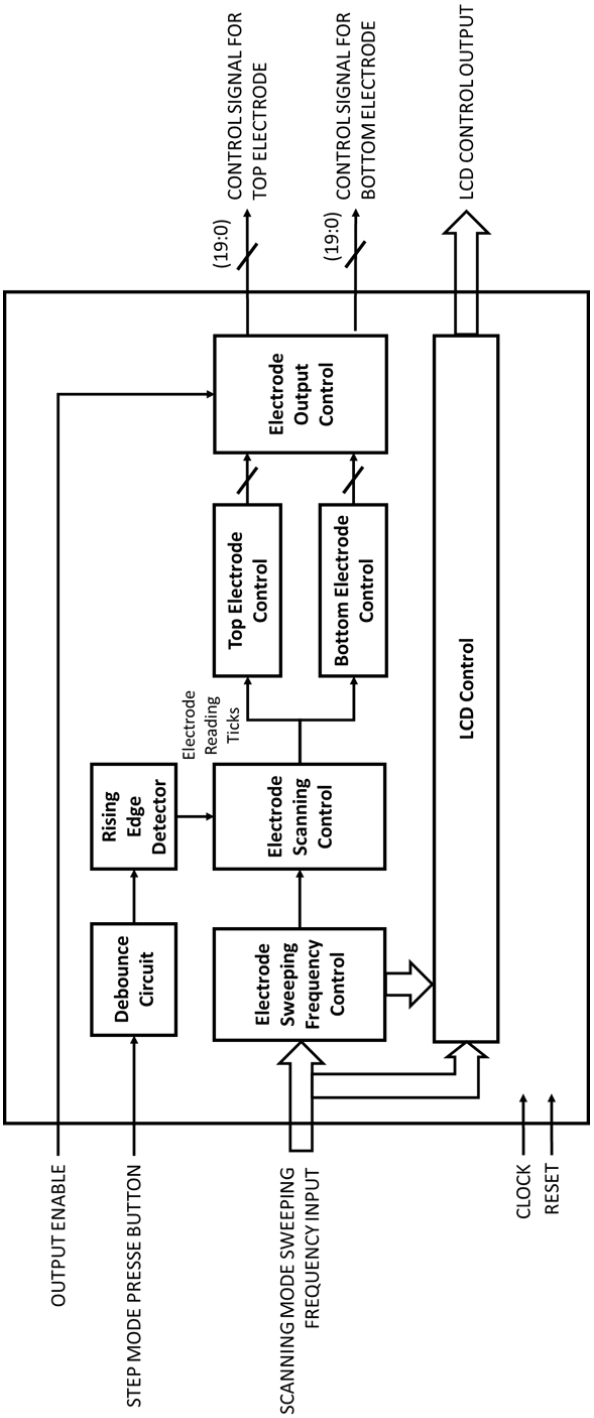

Figure 7.1 Functional block diagram of the FPGA core for activating crossed-electrode array in arbitrary patterns.

The functionality of the FPGA core in this mode was demonstrated with the LED matrix indicator with the results shown in Figure 7.2, when the electrode sweeping frequency was 500 Hz. For each activated column, the element switching frequency was 500 / 8 = 62.5 Hz.

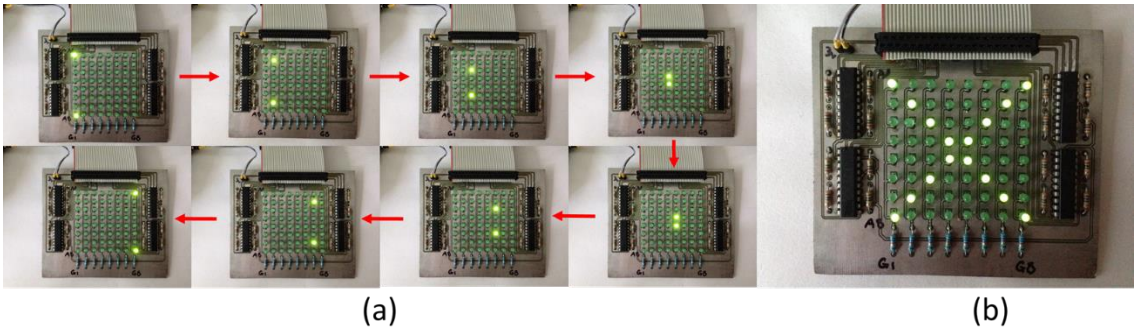

Figure 7.2 Demonstration of FPGA control of time-shared activation of transducer elements in 2-D patterns using the LED matrix indicator. (a) The transducer element activation sequence. (b) A stable 2-D pattern is formed with a sweep frequency of 500 Hz.

It is also possible to manipulate an arbitrary number of transducer elements without shared electrodes. Similarly to the mechanism in holographic optical tweezers that use an SLM to create multiple optical traps from a time-shared laser beam (Grier, 2003; Padgett and Di Leonardo, 2011; Spalding, 2008), an arbitrary multi-element pattern can be created with the crossed-electrode array, by switching a time-shared CW drive signal amongst multiple transducer elements defined by the cross-points of each top-bottom electrode pair.

As a preliminary study, an FPGA core was developed to control four transducer elements individually with the signal switching electronics. Each selected element can be manipulated to an arbitrary position within the area defined by the 8 × 8 electrodes. Four elements were activated in sequence following a certain switching frequency. For the analogue switch IC, ADG5434, the maximum switching frequency between two elements is 4.83 MHz. A functional block diagram of the FPGA core to control four elements is shown in Figure 7.3.

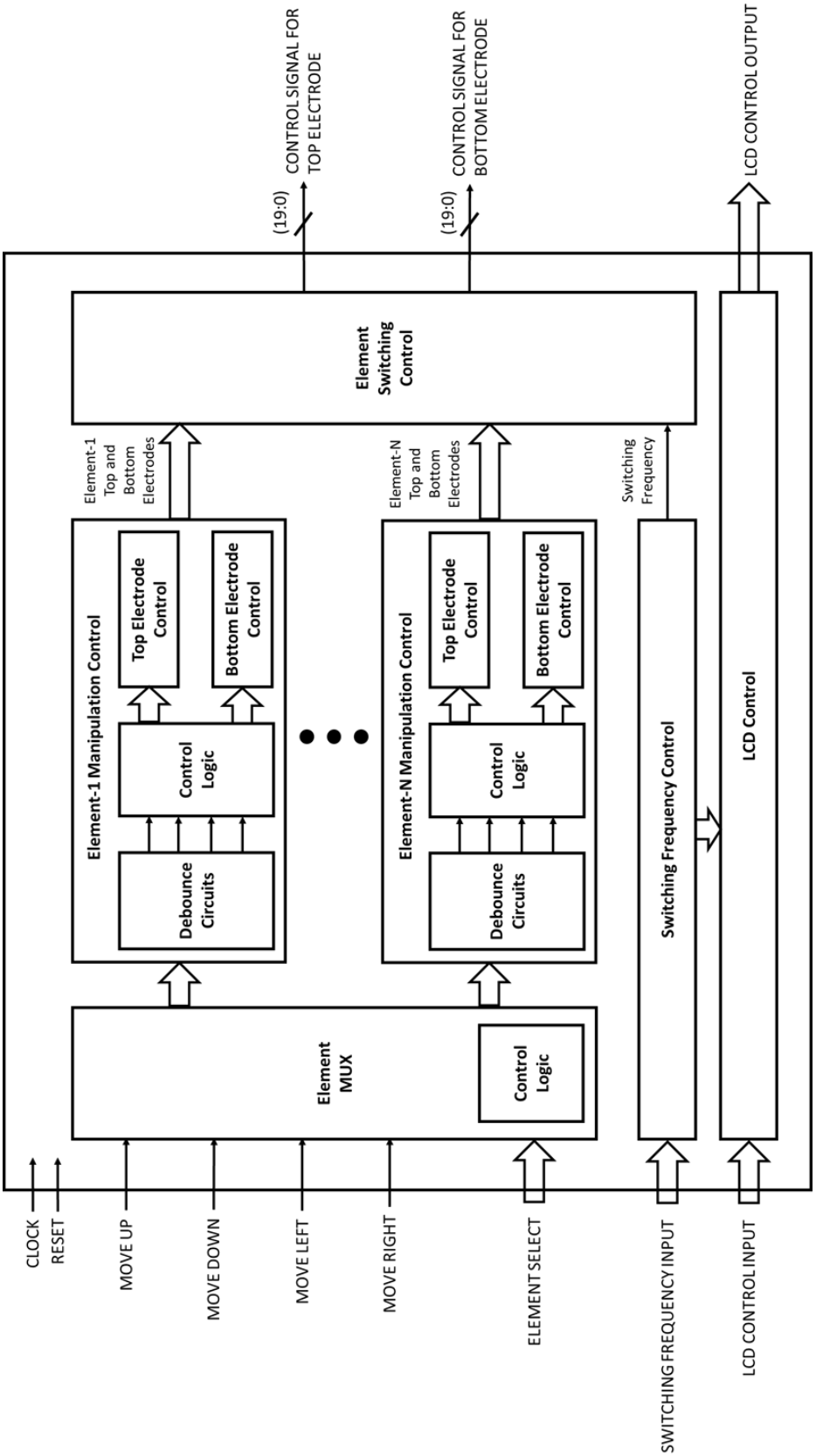

Figure 7.3 Functional block diagram of the FPGA core for individual control of multiple elements for the crossed-electrode array.

Again, the functionality of the FPGA core was demonstrated with the LED matrix indicator. Four transducer elements were activated, as indicated by LEDs, with each element able to be manipulated independently. A switching frequency of 250 Hz was chosen to alternatively enable four transducer elements, with each element switching on and off at a frequency of 250 / 4 = 62.5 Hz. The active elements were manipulated individually into various positions, and the LED matrix gave straightforward real-time feedback of the positions of all the elements. The transducer activation patterns were further explored with LDV characterisation. The driving signal was a CW sinusoid with frequency 7.25 MHz and amplitude 12.3 V_{pp}. Figure 7.4 shows preliminary results of activating multiple independent transducer elements with switching electronics.

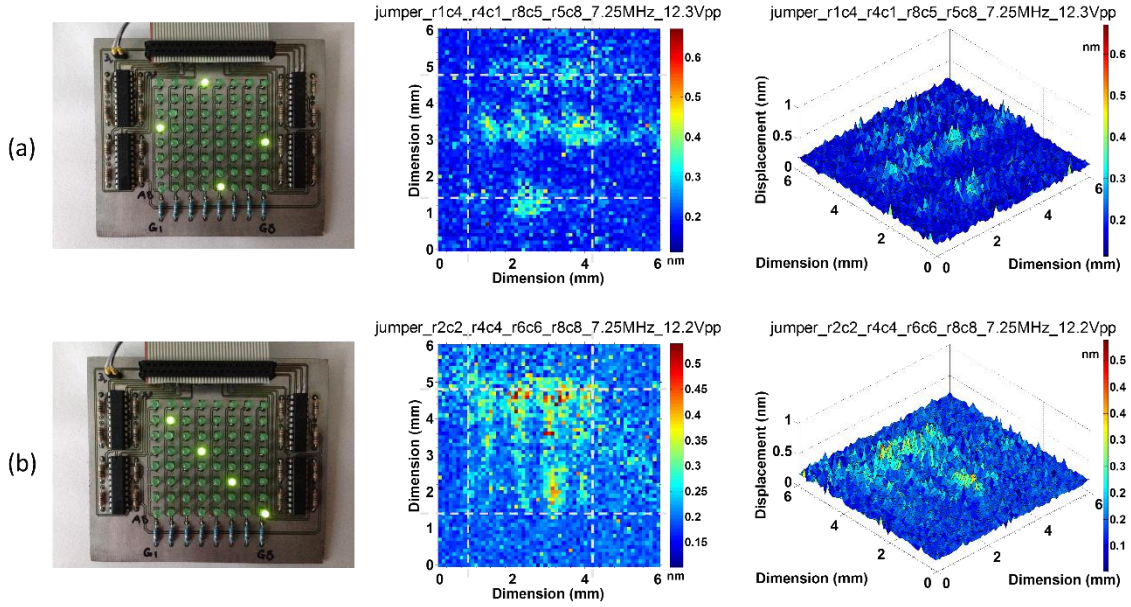

Figure 7.4 Four transducer elements activated and individually manipulated to form different patterns.

It can be seen that the results are less than optimum, since the activation patterns are not obvious, and the maximum displacements of the active elements are about half of those for common-electrode conditions. This is mostly because of a mismatch between the scanning speed and the signal switching frequency. Additionally, the number of averages for the displacement measurements can be further increased during the scanning process. Nevertheless, it is possible to conclude that, with the crossed-electrode transducer array, the time-sharing mechanism that has been realized with signal switching electronics can be used to activate multiple transducer elements simultaneously.

Further investigation is needed to calibrate the electronic control of the crossed-electrode array. The voltage potentials across all the transducer elements for different activation patterns should be directly measured and correlated with LDV scanning results. In addition, particle manipulation experiments with a multilayer resonator integrated with the array will be useful to assist the device calibration process.

B. Particle Manipulation Experiments with a High-frequency Transducer based Multilayer Resonator Sonotweezers

It has been demonstrated that multilayer resonators can be used for particle trapping and manipulation. Glynne-Jones et al. presented a study of the optimized design of $\lambda/2$ resonance chambers to generate relatively large acoustic trapping forces, without a carrier layer and with a reflector layer with thickness of ~ $\lambda/4$ (Glynne-Jones, Boltryk, et al., 2012). For devices with transducers working at relatively low frequencies, such as the 2.5 MHz linear array discussed in Chapter 5, the resonant chamber can be easily constructed with off-the-shelf glass capillaries. However, for the current thick-film transducer working at around 7 MHz, the challenge for the particle trapping experiment lies in the development of a resonator chamber covering a relatively large area, with a much thinner fluid layer about 100 μm for a half-wavelength configuration. Such a chamber was designed as shown in Appendix D for the thick-film 2-D matrix array as a preliminary prototype, but it needs further improvement to maintain the homogeneity of the fluid layer thickness across the whole manipulation lateral plane, in order to maintain the integrity of the USW field. Considering all the requirements to construct a resonant fluid chamber integrated with a high frequency transducer, a carefully designed fabrication process with microfabrication technology will be necessary.

7.2.2 Combining the Functionality of Multichannel Electronics and Signal Switching Electronics

The functionalities of the two versions of electronics that have been developed can be easily combined. For the FPGA core for the multichannel electronics, the channel output enable signals can be controlled by the FPGA cores developed for the signal switching

electronics. The combination of the two electronics systems will further extend the usefulness of each configuration for more diverse applications.

An example is to use the multichannel electronics to control planar resonator Sonotweezers, with the principal advantage that the multichannel driver can offer a higher load driving capacity with mutually independent output channels. A proof-of-concept study was performed with the 30-element 1-D linear array to demonstrate this. In total 16 output channels were connected to the first 16 elements of the linear array, with a 23 V_{pp} CW sinusoidal driving signal at 2.55 MHz for each channel. The outputs from the multichannel electronics were configured with a minimum PHA_RES_BIT with the value of 2, as there is no requirement for the signal phasing in the current resonator setup. 3 elements were activated, and Ø10 µm polystyrene particles were concentrated into an agglomerate which was manipulated manually with the multichannel electronics. Similarly as the experiment presented in Chapter 6, the array were activated alternatively by one element step forward. For measuring the agglomeration force, 10 single particles were manually tracked from the video captured at a rate of 0.04 s/frame (25 fps).

Figure 7.5 illustrates the results for lateral manipulation. The measured average velocity for the particle agglomerate was 44.9 ± 10.6 µm/s, corresponding to an acoustic concentration force of 4.2 ± 1.0 pN. The particles formed an agglomerate with the dimensions of 574 × 943 μm^2. The average distance for each manipulation step was measured as 120.5 ± 6.3 µm. The average agglomerate lateral manipulation velocity can be calculated as 126.9 ± 6.6 µm/s, corresponding to a lateral manipulation force of 1.1 ± 0.058 nN, which is ~ 10 times larger than the force generated with signal switching electronics, for which the driving signal was provided from a general-purpose signal generator (33250A, Keysight Technologies Inc., Santa Rosa, CA, USA). With a higher driving voltage provided with the multichannel electronics, higher acoustic manipulation forces can be generated for particle tweezing applications with planar resonator Sonotweezers.

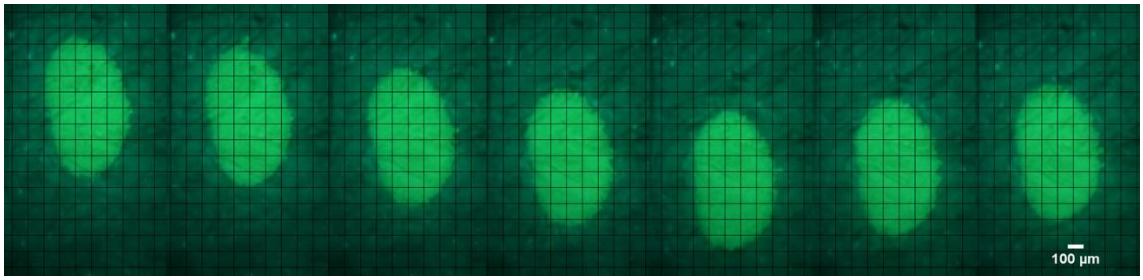

Figure 7.5 The particle agglomerate formed from Ø10 µm polystyrene particles manipulated forward and backward (down and up as shown in the micrographs) by one element step.

Additionally, while using multichannel electronics to drive resonator based Sonotweezers, the effects of waveform jittering as discussed in Chapter 5 should be considered. The instantaneous frequencies from the output channels will vary as results of division factors of N or (N + 1), causing small variations of the pressure nodal plane in the axial position, as indicated in Subsection 6.2.1. The instantaneous nodal plane variation, D, can be quantized as $D = \frac{1}{2} \cdot \left(\frac{c}{f(N+1)} - \frac{c}{f(N)} \right)$, where c is the sound speed in the fluid, $f(N + 1)$ and $f(N)$ are the frequencies derived from the reference frequency with different division factors. These frequencies, $f(N_i)$, where N_i is either (N + 1) or N, can be expressed as $\frac{FREQ\_REF}{N_i \cdot PHA\_RES\_BIT}$. So the pressure node variation is $D = \frac{c}{2} \cdot \frac{PHA\_RES\_BIT}{FREQ\_REF}$, and it is proportional to the phase resolution being used. For the present linear array under test working at 2.55 MHz, with a reference frequency of 133.33 MHz, and $PHA\_RES\_BIT = 2$, the resultant D = 11.2 µm. As shown in Figure 7.5, from the experimental results this variation of the pressure nodes in the axial dimension didn't affect the positioning of the particle agglomerate in the lateral dimension.

The multichannel electronics could also be configured as a transmitting beamformer for driving 1-D and 2-D ultrasonic arrays, with an analogy to conventional electronic beamformer in ultrasound imaging. Instead of generating short pulses, the electronics can generate CW signals to create focused beams for particle trapping, and manipulation can be realized with electronic steering. Moreover, the functionality of the electronics could be further extended to drive devices like crossed-electrode 2-D arrays. Instead of driving all the transducer elements with signals of common frequency, phase and amplitude, each channel could be configured independently with multichannel electronics. Apart from using such an array in planar resonators for acoustic tweezing, the device could also be adapted for complex beam shaping with CW driving signals. This offers the possibility to create miniaturized acoustic beam modulators with 2-D ultrasound arrays, with an

analogy to SLMs in optics. Potential applications are similar to the experiments designed for creating helical beams (Démoré et al., 2012) and self-bending beams (Zhang et al., 2014) acoustically, as discussed in Chapter 2.

7.2.3 Improvements for Signal Output

The electronics that have been developed are sufficient for Sonotweezer applications that requires driving voltages up to 30 V_{pp}. However acoustic tweezing applications with high frequency (> 10 MHz) ultrasound have been demonstrated in various publications, either with bulk transducers (Lam et al., 2013; Lee et al., 2009; Qiu et al., 2014) or SAW transducers (Ding, Shi, et al., 2012). HF devices can provide higher resolution for manipulating particles between nodal planes, and also to generate higher acoustic forces (Qiu et al., 2014). Additionally with reduced piezoelectric element dimensions in the ultrasonic array, the electrical impedance of each transducer element increases, hence requiring high voltage drive, either for CW or pulsed applications. HV drive may also be useful for SAW tweezing devices with PDMS channels, as these additional PDMS polymer features introduce significant attenuation with increased frequencies of the acoustic waves (Tsou et al., 2008).

Ideally, high power MOSFETs should be used for applications requiring high frequency and high voltage driving signals. Modern power MOSFETs can switch output voltages up to ± 200 V_{pp}, with switching time less than 10 ns, corresponding to an output frequency over 100 MHz. There are also specifically designed ultrasound pulser ICs supplied by various commercial vendors such as Microchip Technology, Inc. (Chu, 2009) and Maxim Integrated Products Inc. (“MAX4940 High-Voltage Digital Pulsers”). However these pulser chips requires more complex digital circuit design to provide various trigger signals.

A classic push-and-pull bipolar configuration can be adopted for the design of driving electronics with power MOSFETs. The slew rate for the signal pulser is relatively large for HF and HV outputs, so line drivers are required as current sources in a stage to drive the MOSFETs effectively. Normally these pulsers are designed to generate single or a few cycle pulses for ultrasound imaging (Brown and Lockwood, 2002; Lay, 2011; Park et al., 2010), while in Sonotweezer applications they would need be modified or

redesigned for CW outputs. In such conditions extra care should be given to temperature management for dealing with excessive heat generation from continuous drive (Lewis and Olbricht, 2009).

The present multichannel electronics can provide PC-controlled frequency and phase modulated outputs, while the amplitudes are still changed manually. Improvements could be made for PC-controlled amplitude modulation. Possible solutions could be using digitally controlled potentiometers ("MCP4021/2/3/4", 2006) to replace the mechanical potentiometers from the current circuitry for quantized amplitude modulation, but additionally digital I/O lines would be required. Additionally, Smith et al. proposed a method for amplitude modulation by generating width-modulated square-wave pulse sequences to trigger MOSFET-based ultrasound pulsers (Smith et al., 2013).

Additionally, the quantization phase error arises from the jittering at the FPGA outputs need to be further suppressed, in order to prevent the potential influences over the variations of USW pressure nodes / antinodes. There are existing technologies can be adapted, such as current injection-based fractional compensation or ΔΣ nosing shaping techniques ("Basics of Dual Fractional-N Synthesizers / PLLs", 2005).

7.2.4 Potential for Miniature, Integrated Sonotweezers

At present, optical tweezers have demonstrated unique advantages in the field of single particle / biological cell manipulation with high dexterity (O'Neil et al., 2002) and measurements of delicate cell-level or molecule-level forces (Stevenson et al., 2014). Highly dexterous optical tweezers are now commercially available, and such systems can be adapted for diverse research applications (Bowman et al., 2011). However current optical tweezing technologies lack integration with microelectronics.

The research work presented in this thesis provides a potential solution by developing programmable FPGA-based electronics as embedded soft-cores for driving array-based Sonotweezers for acoustic tweezing applications. Both digital and analogue electronics developed can be potentially miniaturized and integrated into ASICs with microelectronics technologies. Micromachined ultrasound transducers (MUTs), i.e. capacitive MUTs (CMUTs) and piezoelectric MUTs (PMUTs) can generate ultrasonic

waves with frequencies of a few MHz to 10s of MHz (Qiu et al., 2015; Zhuang et al., 2005), which is potentially useful for HF acoustic manipulation of single particles or biological cells (Ding, Lin, et al., 2012; Lee et al., 2009; Zheng et al., 2012) with relatively larger trapping forces than using lower frequencies (Qiu, 2014a).

Research has also been published on electronics integration with miniature piezoelectric transducer arrays (Cochran et al., 2010; Triger et al., 2010) and CMUTs (Gurun et al., 2014; Zhuang et al., 2005) for ultrasound imaging applications. Bernassau et al. has reported a pioneering study using a single photon avalanche diode (SPAD) array for imaging of fluorescent particles patterned in an octagonal acoustic manipulator (Bernassau, Al-Rawhani, et al., 2013). It may thus be possible to merge microelectronic technologies such as ASICs or embedded electronics with microfabrication technologies such as HF transducer arrays development to create low-cost, miniature Sonotweezer devices, for applications including single cell immobilization, single- / multi-cell 2-D and 3-D manipulation, and the creation of micro-assays by cell patterning for high throughput analysis.

REFRENCES

"250mA HIGH-SPEED BUFFER." (1996), , BURR - BROWN.

"A Technical Tutorial on Digital Signal Synthesis." (1999), , Analog Devices.

"AD811 High Performance Video Op Amp." (1999), , Analog Devices.

"ADG5434 Datasheet." (2013), , Analog Devices.

Afrin, R., Watanabe-Nakayama, T., Machida, S., Saito, M., Ikai, a., Zohora, U.S., Uehara, H., et al. (2012), "Exploring Atomic Force Microscopy For Single Cell Manipulations", *Microsc. Microanal.*, Vol. 18 No. S2, pp. 260–261.

Afrin, R., Zohora, U.S., Uehara, H., Watanabe-Nakayama, T. and Ikai, A. (2009), "Atomic force microscopy for cellular level manipulation: imaging intracellular structures and DNA delivery through a membrane hole.", *J. Mol. Recognit.*, Vol. 22 No. 5, pp. 363–72.

"Agilent 4395A Network/Spectrum/Impedance Analyzer Operation Manual." (2008), , Agilent Technologies, Inc.

Andersson, H. and van den Berg, A. (2003), "Microfluidic devices for cellomics: a review", *Sensors Actuators B Chem.*, Vol. 92 No. 3, pp. 315–325.

Anis, Y., Holl, M. and Meldrum, D. (2010), "Automated selection and placement of single cells using vision-based feedback control", *IEEE Trans. Autom. Sci. Eng.*, Vol. 7 No. 3, pp. 598–606.

Ardizzoni, J. (2005), "Practical Guide to High-Speed Printed-Circuit-Board Layout", *Analog Dialogue*, Vol. 39 No. 09, pp. 1–6.

Ashkin, A. (1970), "Accelertion and Trapping of Particles by Radiation Pressure", *Phys. Rev. Lett.*, Vol. 26 No. 4, pp. 24–27.

Ashkin, A. (1978), "Trapping of atoms by resonance radiation pressure", *Phys. Rev. Lett.*, Vol. 40 No. 12, pp. 729–732.

Ashkin, A. (1992), "Forces of a single-beam gradient laser trap on a dielectric sphere in the ray optics regime", *Biophys. J.*, Vol. 61 No. 2, pp. 569–582.

Ashkin, A. (1997), "Optical trapping and manipulation of neutral particles", *Proc. Natl. Acad. Sci. U. S. A.*, Vol. 94 No. 10, pp. 4853–4860.

Ashkin, A., Dziedzic, J. and Yamane, T. (1987), "Optical trapping and manipulation of single cells using infrared laser beams", *Nature*, Vol. 330 No. 24, pp. 769 – 771.

Ashkin, A., Dziedzic, J.M., Bjorkholm, J.E. and Chu, S. (1986), "Observation of a single-beam gradient force optical trap for dielectric particles", *Opt. Lett.*, Vol. 11 No. 5, p. 288.

Ashkin, A., Schütze, K., Dziedzic, J.M., Euteneuer, U. and Schliwa, M. (1990), "Force generation of organelle transport measured in vivo by an infrared laser trap.", *Nature*, Vol. 348 No. 6299, pp. 346–348.

Augustsson, P., Barnkob, R., Wereley, S.T., Bruus, H. and Laurell, T. (2011), "Automated and temperature-controlled micro-PIV measurements enabling long-term-stable microchannel acoustophoresis characterization", *Lab Chip*, Vol. 11 No. 24, p. 4152.

Bang, H., Chung, C., Kim, J.K., Kim, S.H., Chung, S., Park, J., Lee, W.G., et al. (2006), "Microfabricated fluorescence-activated cell sorter through hydrodynamic flow manipulation", *Microsyst. Technol.*, Vol. 12 No. 8, pp. 746–753.

Barrett, C. (1999), "Fractional/integer-N PLL basics", *Texas Instruments Tech. Br. SWRA029*, Texas Instruments.

Bashkin, J., Bartosiewicz, M., Roach, D., Leong, J., Barker, D. and Johnston, R. (1996), "Implementation of a capillary array electrophoresis instrument.", *J. Capillary Electrophor.*, Vol. 3 No. 2, pp. 61–8.

"Basics of Dual Fractional-N Synthesizers / PLLs." (2005), *Skyworks White Pap.*, Skyworks Solutions, Inc.

Batchelor, G.K. (2000), *An Introduction to Fluid Dynamics*, Cambridge University Press, available at: https://books.google.com/books?hl=en&lr=&id=Rla7OihRvUgC&pgis=1 (accessed 26 April 2015).

Bazou, D., Coakley, W.T., Hayes, A.J. and Jackson, S.K. (2008), "Long-term viability and proliferation of alginate-encapsulated 3-D HepG2 aggregates formed in an ultrasound trap", *Toxicol. In Vitro*, Vol. 22 No. 5, pp. 1321–31.

Bernassau, A.L., Al-Rawhani, M., Beeley, J. and Cumming, D.R.S. (2013), "Integrated ultrasonic particle positioning and low excitation light fluorescence imaging", *Appl. Phys. Lett.*, AIP Publishing, Vol. 103 No. 24, p. 244103.

Bernassau, A.L., Courtney, C.R.P., Beeley, J., Drinkwater, B.W. and Cumming, D.R.S. (2013), "Interactive manipulation of microparticles in an octagonal sonotweezer", *Appl. Phys. Lett.*, Vol. 102 No. 16, p. 164101.

Bernassau, A.L., García-Gancedo, L., Hutson, D., Démoré, C.E.M., McAneny, J.J., Button, T.W. and Cochran, S. (2012), "Microfabrication of electrode patterns for high-frequency ultrasound transducer arrays.", *IEEE Trans. Ultrason. Ferroelectr. Freq. Control*, Vol. 59 No. 8, pp. 1820–9.

Bernassau, A.L., Gesellchen, F., Macpherson, P.G.A., Riehle, M. and Cumming, D.R.S. (2012), "Direct patterning of mammalian cells in an ultrasonic heptagon stencil.", *Biomed. Microdevices*, Vol. 14 No. 3, pp. 559–64.

Bernassau, A.L., Glynne-Jones, P., Gesellchen, F., Riehle, M., Hill, M. and Cumming, D.R.S. (2013), "Controlling acoustic streaming in an ultrasonic heptagonal tweezers with application to cell manipulation", *Ultrasonics*, Elsevier B.V., doi:10.1016/j.ultras.2013.04.019.

Beyeler, F., Member, S., Neild, A., Oberti, S., Bell, D.J., Sun, Y., Dual, J., et al. (2007), "Monolithically Fabricated Microgripper With Integrated Force Sensor for Manipulating Microobjects and Biological Cells Aligned in an Ultrasonic Field", *J. Microelectromechanical Syst.*, Vol. 16 No. 1, pp. 7–15.

Binnig, G., Quate, C. and Gerber, C. (1986), "Atomic force microscope", *Phys. Rev. Lett.*, Vol. 56 No. 9, pp. 930–933.

Bishop, P. (2009), "A tradeoff between microcontroller, DSP, FPGA and ASIC technologies", *EE Times*, available at: http://www.eetimes.com/document.asp?doc_id=1275272 (accessed 31 December 2014).

Bjerknes, V.F.K. (1906), *Bjerknes, Fields of Force*, The Columbia University Press.

Bolopion, A. and Régnier, S. (2013), "A Review of Haptic Feedback Teleoperation Systems for Micromanipulation and Microassembly", *IEEE Trans. Autom. Sci. Eng.*, Vol. 10 No. 3, pp. 496–502.

Bowman, R.W., Gibson, G., Carberry, D., Picco, L., Miles, M. and Padgett, M.J. (2011), "iTweezers: optical micromanipulation controlled by an Apple iPad", *J. Opt.*, Vol. 13 No. 4, p. 044002.

Brennan, P.V., Jiang, D. and Wang, H. (2006), "Memory-controlled frequency divider for fractional-N synthesisers", *Electron. Lett.*, Vol. 42 No. 21, p. 1202.

Brillouët, M., Arden, W., Brillouët, M., Cogez, P., Graef, M., Huizing, B., Mahnkopf, R., et al. (2011), *Towards a "More-than-Moore" roadmap*, available at: http://www2.imec.be/content/user/File/MtM WG report.pdf (accessed 6 July 2015).

Brown, J. a and Lockwood, G.R. (2002), "A low-cost, high-performance pulse generator for ultrasound imaging.", *IEEE Trans. Ultrason. Ferroelectr. Freq. Control*, Vol. 49 No. 6, pp. 848–851.

Burkhardt, J.K., McIlvain, J.M., Sheetz, M.P. and Argon, Y. (1993), "Lytic granules from cytotoxic T cells exhibit kinesin-dependent motility on microtubules in vitro.", *J. Cell Sci.*, Vol. 104 (Pt 1, pp. 151–162.

Cabrera, C.R. (2001), "Continuous concentration of bacteria in a microfluidic flow cell using electrokinetic techniques Miniaturization", *Electrophoresis*, Vol. 22 No. 2, pp. 355–362.

Campbell, J.A. (1990), "Generation of a nondiffracting beam with frequency- independent beamwidth", *J. Acoust. Soc. Am.*

Carlson, R., Gabel, C., Chan, S., Austin, R., Brody, J. and Winkelman, J. (1997), "Self-Sorting of White Blood Cells in a Lattice", *Phys. Rev. Lett.*, Vol. 79 No. 11, pp. 2149–2152.

Carugo, D., Ankrett, D.N., Glynne-Jones, P., Capretto, L., Boltryk, R.J., Zhang, X., Townsend, P. a, et al. (2011), "Contrast agent-free sonoporation: The use of an ultrasonic standing wave microfluidic system for the delivery of pharmaceutical agents.", *Biomicrofluidics*, Vol. 5 No. 4, pp. 44108–4410815.

Chen, P., Luo, Z., Güven, S., Tasoglu, S., Ganesan, A.V., Weng, A. and Demirci, U. (2014), "Microscale Assembly Directed by Liquid-Based Template", *Adv. Mater.*, pp. 1–6.

Chen, Y.-F., Serey, X., Sarkar, R., Chen, P. and Erickson, D. (2012), "Controlled photonic manipulation of proteins and other nanomaterials.", *Nano Lett.*, Vol. 12 No. 3, pp. 1633–7.

Choe, Y., Kim, J.W., Shung, K.K. and Kim, E.S. (2011), "Microparticle trapping in an ultrasonic Bessel beam", *Appl. Phys. Lett.*, Vol. 99 No. 2011, pp. 2009–2012.

Choi, J.-W., Oh, K.W., Thomas, J.H., Heineman, W.R., Halsall, H.B., Nevin, J.H., Helmicki, A.J., et al. (2002), "An integrated microfluidic biochemical detection system for protein analysis with magnetic bead-based sampling capabilities.", *Lab Chip*, Vol. 2 No. 1, pp. 27–30.

Chu, C. (2009), "Designing An Ultrasound Pulser with MD1812/MD1813 Composite Drivers", Supertex, Inc., available at: http://appnote.avrportal.com/appnotes/Ultrasonic-sensor/Designing-An-Ultrasound-Pulser-with-MD1812-MD1813-Composite-Drivers.pdf (accessed 1 October 2014).

Chu, P.P. (2008), "Chapter 7 UART", *FPGA Prototyp. by VHDL Examples Xilinx Spartan-3 Version*, John Wiley & Sons. Inc., New Jersey, pp. 163–182.

"CMOS 300MSPS Quadrature Complete-DDS AD9854." (2007), , Analog Devices, available at: http://www.analog.com/static/imported-files/data_sheets/AD9854.pdf (accessed 10 December 2014).

Cobbold, R.S.C. (2007a), "Chapter 6 Ultrasound Transducers", *Found. Biomed. Ultrasound*, Oxford University Press, Inc, pp. 329–412.

Cobbold, R.S.C. (2007b), “Chapter 7 Ultrasound Imaging Arrays”, *Found. Biomed. Ultrasound*, Oxford University Press, Inc, pp. 413–490.

Cochran, S., Bernassau, A., Cumming, D., Démoré, C., Desmulliez, M. and Sweet, J. (2010), “Future Integration of Silicon Electronics with Miniature Piezoelectric Ultrasonic Transducers and Arrays”, pp. 1108–1116.

Coombs, Jr., C.F. (2008), *Printed Circuits Handbook*, McGraw-Hill, New York, Sixth Edit., doi:10.1036/0071467343.

Cosgrove, J. a., Buick, J.M., Pye, S.D. and Greated, C. a. (2001), “PIV applied to Eckart streaming produced by a medical ultrasound transducer”, *Ultrasonics*, Vol. 39 No. 6, pp. 461–464.

Coulter, C. (1921), “The equilibrium between hemolytic sensitizer and red blood cells in relation to the hydrogen ion concentration”, *J. Gen. Physiol.*, Vol. 3 No. 4, pp. 513–521.

Courtney, C.R.P., Demore, C.E.M., Wu, H., Grinenko, A., Wilcox, P.D., Cochran, S. and Drinkwater, B.W. (2014), “Independent trapping and manipulation of microparticles using dexterous acoustic tweezers”, *Appl. Phys. Lett.*, Vol. 104 No. 15, p. 154103.

Courtney, C.R.P., Drinkwater, B.W., Demore, C.E.M., Cochran, S., Grinenko, A. and Wilcox, P.D. (2013), “Dexterous manipulation of microparticles using Bessel-function acoustic pressure fields”, *Appl. Phys. Lett.*, Vol. 102 No. 12, p. 123508.

Courtney, C.R.P., Ong, C.-K., Drinkwater, B.W., Bernassau, a. L., Wilcox, P.D. and Cumming, D.R.S. (2011), “Manipulation of particles in two dimensions using phase controllable ultrasonic standing waves”, *Proc. R. Soc. A Math. Phys. Eng. Sci.*, Vol. 468 No. 2138, pp. 337–360.

Courtney, C.R.P., Ong, C.K., Drinkwater, B.W., Wilcox, P.D., Demore, C., Cochran, S., Glynne-Jones, P., et al. (2010), “Manipulation of microparticles using phase-controllable ultrasonic standing waves.”, *J. Acoust. Soc. Am.*, Vol. 128 No. 4, pp. EL195–L199.

Cousins, C.M., Holownia, P., Hawkes, J.J., Limaye, M.S., Price, C.P., Keay, P.J. and Coakley, W.T. (2000), “Plasma preparation from whole blood using ultrasound”, *Ultrasound Med. Biol.*, Elsevier Science Ltd, Vol. 26 No. 5, pp. 881–888.

Curtis, J., Koss, B. and Grier, D. (2002), “Dynamic holographic optical tweezers”, *Opt. Commun.*, Vol. 207, pp. 169–175.

Curtis, J.E. and Grier, D.G. (2003), “Modulated optical vortices”, *Opt. Lett.*, Vol. 28 No. 11, p. 872.

Dai, J. and Sheetz, M.P. (1995), “Mechanical properties of neuronal growth cone membranes studied by tether formation with laser optical tweezers.”, *Biophys. J.*, Vol. 68 No. 3, pp. 988–996.

Daily, B., Elson, E. and Zahalak, G. (1984), “Cell poking: Determination of the elastic area compressibility modulus of the erythrocyte membrane”, *Biophys. J.*, Vol. 45 No. 4, pp. 671–82.

“DCB structure (Windows).” (2015), *Microsoft Dev. Netw.*, available at: https://msdn.microsoft.com/en-us/library/aa363214(VS.85).aspx (accessed 5 February 2015).

Démoré, C., Yang, Z., Volovick, A., Wang, H., Cochran, S., MacDonald, M. and Spalding, G. (2011), “A sonic screwdriver: Acoustic angular momentum transfer for ultrasonic manipulation”, *2011 IEEE Int. Ultrason. Symp.*, IEEE, pp. 180–183.

Démoré, C.E.M. (2010), “Sonotweezer Device Taxonomy”, Private Communication.

Démoré, C.E.M., Joyce, A.W., Wall, K. and Lockwood, G.R. (2009), “Real-time volume imaging using a crossed electrode array.”, *IEEE Trans. Ultrason. Ferroelectr. Freq. Control*, Vol. 56 No. 6, pp. 1252–61.

Démoré, C.E.M., Yang, Z., Volovick, A., Cochran, S., MacDonald, M.P. and Spalding, G.C. (2012), "Mechanical Evidence of the Orbital Angular Momentum to Energy Ratio of Vortex Beams", *Phys. Rev. Lett.*, Vol. 108 No. 19, p. 194301.

Ding, X., Lin, S.-C.S., Kiraly, B., Yue, H., Li, S., Chiang, I.-K., Shi, J., et al. (2012), "On-chip manipulation of single microparticles, cells, and organisms using surface acoustic waves.", *Proc. Natl. Acad. Sci. U. S. A.*, Vol. 109 No. 28, pp. 11105–9.

Ding, X., Lin, S.-C.S., Lapsley, M.I., Li, S., Guo, X., Chan, C.Y., Chiang, I.-K., et al. (2012), "Standing surface acoustic wave (SSAW) based multichannel cell sorting.", *Lab Chip*, Vol. 12 No. 21, pp. 4228–31.

Ding, X., Shi, J., Lin, S.-C.S., Yazdi, S., Kiraly, B. and Huang, T.J. (2012), "Tunable patterning of microparticles and cells using standing surface acoustic waves.", *Lab Chip*, Vol. 12 No. 14, pp. 2491–7.

Dual, J. and Möller, D. (2012), "Acoustofluidics 4: Piezoelectricity and application in the excitation of acoustic fields for ultrasonic particle manipulation.", *Lab Chip*, Vol. 12 No. 3, pp. 506–14.

Dziubinski, M. (2012), "Hydrodynamic Focusing in Microfluidic Devices", in Kelly, R. (Ed.),*Adv. Microfluid.*, InTech, pp. 29–54.

Eckart, C. (1948), "Vortices and streams caused by sound waves", *Phys. Rev.*, Vol. 73 No. 1, pp. 68–76.

Evans, E., Ritchie, K. and Merkel, R. (1995), "Sensitive force technique to probe molecular adhesion and structural linkages at biological interfaces", *Biophys. J.*, Vol. 68 No. June, pp. 2580–2587.

Fan, Z.H., Mangru, S., Granzow, R., Heaney, P., Ho, W., Dong, Q. and Kumar, R. (1999), "Dynamic DNA Hybridization on a Chip Using Paramagnetic Beads", *Anal. Chem.*, Vol. 71 No. 21, pp. 4851–4859.

Ferreira, H.A., Feliciano, N., Graham, D.L. and Freitas, P.P. (2005), "Effect of spin-valve sensor magnetostatic fields on nanobead detection for biochip applications", *J. Appl. Phys.*, Vol. 97 No. 10.

Finer, J.T., Simmons, R.M. and Spudich, J.A. (1994), "Single myosin molecule mechanics: piconewton forces and nanometre steps.", *Nature*, Vol. 368 No. 6467, pp. 113–119.

"Four-Channel, High Speed, ±65V 750mA Ultrasound Pulser." (2011), , Supertex, Inc.

Frampton, K.D., Martin, S.E. and Minor, K. (2003), "The scaling of acoustic streaming for application in micro-fluidic devices", *Appl. Acoust.*, Vol. 64 No. 7, pp. 681–692.

Gahagan, K.T. and Swartzlander, Jr., G. a. (1996), "Optical vortex trapping of particles", *Opt. Lett.*, Vol. 21 No. 11, p. 827.

Gesellchen, F., Bernassau, A.L., Déjardin, T., Cumming, D.R.S. and Riehle, M.O. (2014), "Cell patterning with a heptagon acoustic tweezer - application in neurite guidance", *Lab Chip*, Vol. 14 No. 13, pp. 2266–2275.

Givan, A.L. (2011), "Flow cytometry: an introduction.", *Methods Mol. Biol.*, Vol. 699, pp. 1–29.

Glynne-Jones, P., Boltryk, R.J., Harris, N.R., Cranny, A.W.J. and Hill, M. (2010), "Mode-switching: a new technique for electronically varying the agglomeration position in an acoustic particle manipulator.", *Ultrasonics*, Elsevier B.V., Vol. 50 No. 1, pp. 68–75.

Glynne-Jones, P., Boltryk, R.J. and Hill, M. (2012), "Acoustofluidics 9: Modelling and applications of planar resonant devices for acoustic particle manipulation.", *Lab Chip*, Vol. 12 No. 8, pp. 1417–26.

Glynne-Jones, P., Boltryk, R.J., Hill, M., Zhang, F., Dong, L., Wilkinson, J.S., Brown, T., et al. (2010), "Multi-modal particle manipulator to enhance bead-based bioassays", *Phys. Procedia*, Elsevier, Vol. 3 No. 1, pp. 269–275.

Glynne-Jones, P., Démoré, C.E.M., Ye, C., Qiu, Y., Cochran, S. and Hill, M. (2012), "Array-controlled ultrasonic manipulation of particles in planar acoustic resonator.", *IEEE Trans. Ultrason. Ferroelectr. Freq. Control*, Vol. 59 No. 6, pp. 1258–66.

Glynne-Jones, P. and Hill, M. (2013), "Acoustofluidics 23: acoustic manipulation combined with other force fields", *Lab Chip*, Vol. 13 No. 6, pp. 1003–10.

González, I., Fernández, L.J., Gómez, T.E., Berganzo, J., Soto, J.L. and Carrato, A. (2010), "A polymeric chip for micromanipulation and particle sorting by ultrasounds based on a multilayer configuration", *Sensors Actuators B Chem.*, Vol. 144 No. 1, pp. 310–317.

Gor'kov, L.P. (1962), "On the forces acting on a small particle in an acoustic field in an ideal fluid", *Sov. Phys. - Dokl.*, Soviet Physics - Doklady, Vol. 6 No. 9, pp. 773–775.

Grier, D.G. (2003), "A revolution in optical manipulation.", *Nature*, Vol. 424 No. 6950, pp. 810–6.

Grinenko, a., MacDonald, M.P., Courtney, C.R.P., Wilcox, P.D., Demore, C.E.M., Cochran, S. and Drinkwater, B.W. (2015), "Tunable beam shaping with a phased array acousto-optic modulator", *Opt. Express*, Vol. 23 No. 1, p. 26.

Grinenko, A., Wilcox, P.D., Courtney, C.R.P. and Drinkwater, B.W. (2012a), "Proof of principle study of ultrasonic particle manipulation by a circular array device", *Proc. R. Soc. A Math. Phys. Eng. Sci.*, Vol. 468 No. 2147, pp. 3571–3586.

Grinenko, A., Wilcox, P.D., Courtney, C.R.P. and Drinkwater, B.W. (2012b), "Proof of principle study of ultrasonic particle manipulation by a circular array device.", *Proc. R. Soc. A Math. Phys. Eng. Sci.*, Vol. 468 No. 2147, pp. 3571–3586.

Gröschl, M. (1998), "Ultrasonic separation of suspended particles-Part I: Fundamentals", *Acta Acust. united with Acust.*, Vol. 84, pp. 432–447.

Gu, L., Zhou, N. and Li, H. (2011), "Research of Frequency Divider Based on Programmable Logic Device", *2011 3rd Int. Conf. Environ. Sci. Inf. Appl. Technol. (ESIAT 2011)*, Vol. 10, pp. 820–824.

Guillaume-Gentil, O., Potthoff, E., Ossola, D., Franz, C.M., Zambelli, T. and Vorholt, J. a. (2014), "Force-controlled manipulation of single cells: from AFM to FluidFM.", *Trends Biotechnol.*, Elsevier Ltd, Vol. 32 No. 7, pp. 381–8.

Guo, F., French, J.B., Li, P., Zhao, H., Chan, C.Y., Fick, J.R., Benkovic, S.J., et al. (2013), "Probing cell-cell communication with microfluidic devices.", *Lab Chip*, Vol. 13 No. 16, pp. 3152–62.

Gurun, G., Tekes, C., Zahorian, J., Xu, T., Satir, S., Karaman, M., Hasler, J., et al. (2014), "Single-chip CMUT-on-CMOS front-end system for real-time volumetric IVUS and ICE imaging", *IEEE Trans. Ultrason. Ferroelectr. Freq. Control*, Vol. 61 No. 2, pp. 239–50.

Haake, A., Neild, A., Radziwill, G. and Dual, J. (2005), "Positioning, displacement, and localization of cells using ultrasonic forces", *Biotechnol. Bioeng.*, Vol. 92 No. 1, pp. 8–14.

Hansma, P., Elings, V., Marti, O. and Bracker, C. (1988), "Scanning tunneling microscopy and atomic force microscopy: application to biology and technology", *Science (80-.).*, Vol. 242 No. 4876, pp. 209–216.

Harris, N.R., Hill, M., Beeby, S., Shen, Y., White, N.M., Hawkes, J.J. and Coakley, W.T. (2003), "A silicon microfluidic ultrasonic separator", *Sensors Actuators B Chem.*, Vol. 95 No. 1-3, pp. 425–434.

Hatch, A. and Kamholz, A. (2001), "A ferrofluidic magnetic micropump", *J. Microelectromechanical Syst.*, Vol. 10 No. 2, pp. 215–221.

Hawkes, J.J., Barber, R.W., Emerson, D.R. and Coakley, W.T. (2004), "Continuous cell washing and mixing driven by an ultrasound standing wave within a microfluidic channel", *Lab Chip*, Vol. 4 No. 5, pp. 446–52.

Hawkes, J.J., Long, M.J., Coakley, W.T. and McDonnell, M.B. (2004), "Ultrasonic deposition of cells on a surface.", *Biosens. Bioelectron.*, Vol. 19 No. 9, pp. 1021–8.

Hawkes, J.J. and Radel, S. (2013), "Acoustofluidics 22: Multi-wavelength resonators, applications and considerations.", *Lab Chip*, Vol. 13 No. 4, pp. 610–27.

Hayt Jr., W.H., Kemmerly, J.E. and Durbin, S.M. (2002), "Chapter 6 The Operational Amplifier", *Eng. Circuit Anal.*, The McGraw-Hill Companies, Inc., 6thed., pp. 147–171.

He, H. and Friese, M. (1995), "Direct observation of transfer of angular momentum to absorptive particles from a laser beam with a phase singularity", *Phys. Rev. Lett.*, Vol. 75 No. 5, pp. 826–829.

He, H., Heckenberg, N.R. and Rubinsztein-Dunlop, H. (1995), "Optical Particle Trapping with Higher-order Doughnut Beams Produced Using High Efficiency Computer Generated Holograms", *J. Mod. Opt.*, Vol. 42 No. 1, pp. 217–223.

Hefner, B. and Marston, P. (1999), "An acoustical helicoidal wave transducer with applications for the alignment of ultrasonic and underwater systems", *J. Acoust. Soc. Am.*, Vol. 106 No. August 1999, pp. 3313–3316.

Henderson, E., Haydon, P. and Sakaguchi, D. (1992), "Actin filament dynamics in living glial cells imaged by atomic force microscopy", *Science (80-.).*, Vol. 257 No. 5078, pp. 1944–1946.

Hill, M. (2003), "The selection of layer thicknesses to control acoustic radiation force profiles in layered resonators", *J. Acoust. Soc. Am.*, Vol. 114 No. 5, p. 2654.

Hill, M. and Harris, N.R. (2007), "Chapter 9 Ultrasonic Particle Manipulation", in Hardt, S. and Schönfeld, F. (Eds.),*Microfluid. Technol. Miniaturized Anal. Syst.*, Springer US, pp. 357–392.

"History of FPGAs." (n.d.). *Wayback Mach.*, available at: https://web.archive.org/web/20070412183416/http://filebox.vt.edu/users/tmagin/history.htm (accessed 26 April 2015).

"History of Xilinx, Inc." (n.d.). , available at: http://www.fundinguniverse.com/company-histories/xilinx-inc-history/ (accessed 26 April 2015).

Hochmuth, R.M. (2000), "Micropipette aspiration of living cells", *J. Biomech.*, Vol. 33 No. 1, pp. 15–22.

Horowitz, P. and Hill, W. (1989a), "Chapter 10 Microcomputers", *Art Electron.*, Cambridge University Press, Second Edi., p. 673.

Horowitz, P. and Hill, W. (1989b), "Chapter 11 MICROPROCESSORS", *Art Electron.*, Cambridge University Press, Second Edi., pp. 743–825.

Horowitz, P. and Hill, W. (1989c), "Chapter 4 Feedback and Operational Amplifiers", *Art Electron.*, Cambridge University Press, Second Edi., pp. 175–251.

Horowitz, P. and Hill, W. (1989d), "Chapter 5 Active Filters and Oscillators", *Art Electron.*, Cambridge University Press, Second Edi., pp. 263–306.

Horowitz, P. and Hill, W. (1989e), "Chapter 1 Foundations", *Art Electron.*, Cambridge University Press, Second Edi., pp. 1–58.

Hou, L., Zhang, T., Wang, J. and Li, Y. (2012), “A High-Accuracy Design of Frequency Divider with FPGA and ASIC Implementation”, *2012 Int. Conf. Ind. Control Electron. Eng.*, IEEE, Vol. 8, pp. 1653–1656.

Hsu, D.K., Margetan, F.J. and Thompson, D.O. (1989), “Bessel beam ultrasonic transducer: Fabrication method and experimental results”, *Appl. Phys. Lett.*, AIP Publishing, Vol. 55 No. 20, p. 2066.

Hu, X. and Lin, Y. (2011), “Realization on decimal frequency divider based on FPGA and Quartus II”, *Inf. Manag. Eng.*, pp. 350–356.

Huang, Y., Joo, S., Duhon, M., Heller, M., Wallace, B. and Xu, X. (2002), “Dielectrophoretic cell separation and gene expression profiling on microelectronic chip arrays”, *Anal. Chem.*, Vol. 74 No. 14, pp. 3362–3371.

Huber, R., Burggraf, S., Mayer, T., Barns, S.M., Rossnagel, P. and Stetter, K.O. (1995), “Isolation of a hyperthermophilic archaeum predicted by in situ RNA analysis.”, *Nature*, Vol. 376 No. 6535, pp. 57–58.

Hughes, D. a., Weijer, C.J., Demore, C. and Cochran, S. (2012), “Investigating the motility of Dictyostelium discodeum using high frequency ultrasound as a method of manipulation”, *2012 IEEE Int. Ultrason. Symp.*, IEEE, pp. 2002–2005.

Hultström, J., Manneberg, O., Dopf, K., Hertz, H.M., Brismar, H. and Wiklund, M. (2007), “Proliferation and viability of adherent cells manipulated by standing-wave ultrasound in a microfluidic chip.”, *Ultrasound Med. Biol.*, Vol. 33 No. 1, pp. 145–51.

“Introduction to FPGA Design with Vivado High-Level Synthesis.” (2013), , Xilinx, Inc.

“ISE In-Depth Tutorial.” (2009), , Xilinx, Inc.

Jia, Y. and Xu, Q. (2013), “MEMS Microgripper Actuators and Sensors: The State-of-the-Art Survey”, *Recent Patents Mech. Eng.*, Vol. 6 No. 2, pp. 132–142.

Jones, D.L. (2004), *PCB Design Tutorial*, available at: http://pdf.aminer.org/000/286/160/fine_line_printed_circuit_board_for_high_performance_computer_design.pdf.

Junno, T. and Deppert, K. (1995), “Controlled manipulation of nanoparticles with an atomic force microscope”, *Appl. Phys. Lett.*, Vol. 66, pp. 3627–3629.

Kang, S.-T. and Yeh, C.-K. (2011), “Potential-well model in acoustic tweezers”, *IEEE Trans. Ultrason. Ferroelectr. Freq. Control*, Vol. 58 No. 3, pp. 662–5.

Khanna, S., Hudson, B., Pepper, C.J., Amso, N.N. and Coakley, W.T. (2006), “Fluorescein isothiocynate-dextran uptake by Chinese hamster ovary cells in a 1.5 MHz ultrasonic standing wave in the presence of contrast agent”, *Ultrasound Med. Biol.*, Vol. 32 No. 2, pp. 289–295.

King, L. V. (1934), “On the Acoustic Radiation Pressure on Spheres”, *Proc. R. Soc. A Math. Phys. Eng. Sci.*, Vol. 147 No. 861, pp. 212–240.

Kinoshita, M. and Hynynen, K. (2007), “Key factors that affect sonoporation efficiency in in vitro settings: the importance of standing wave in sonoporation.”, *Biochem. Biophys. Res. Commun.*, Vol. 359 No. 4, pp. 860–5.

Kovacheva, M., Stoimenov, E. and Milanov, I. (2014), “FPGA–based Arbitrary Integer Frequency Divider with 50% Duty Cycle of the Output Signal”, *Annu. J. Electron.*, pp. 104–107.

Kuznetsova, T.G., Starodubtseva, M.N., Yegorenkov, N.I., Chizhik, S. a and Zhdanov, R.I. (2007), “Atomic force microscopy probing of cell elasticity.”, *Micron*, Vol. 38 No. 8, pp. 824–33.

Lam, K.H., Hsu, H.-S., Li, Y., Lee, C., Lin, A., Zhou, Q., Kim, E.S., et al. (2013), "Ultrahigh frequency lensless ultrasonic transducers for acoustic tweezers application.", *Biotechnol. Bioeng.*, Vol. 110 No. 3, pp. 881–6.

Laurell, T., Petersson, F. and Nilsson, A. (2007), "Chip integrated strategies for acoustic separation and manipulation of cells and particles.", *Chem. Soc. Rev.*, Vol. 36 No. 3, pp. 492–506.

Lay, H. (2011), *Design and manufacture of a high-frequency annular array ultrasound system for medical imaging*, Queen's University Kingston, Ontario, Canada, available at: http://qspace.library.queensu.ca/handle/1974/6506 (accessed 5 June 2014).

"LED lamp BG-490-515." (2006), , Multicomp.

Lee, H., Purdon, a. M. and Westervelt, R.M. (2004), "Manipulation of biological cells using a microelectromagnet matrix", *Appl. Phys. Lett.*, Vol. 85 No. 6, p. 1063.

Lee, J., Lee, C., Kim, H.H., Jakob, A., Lemor, R., Teh, S.-Y., Lee, A., et al. (2011), "Targeted cell immobilization by ultrasound microbeam.", *Biotechnol. Bioeng.*, Vol. 108 No. 7, pp. 1643–50.

Lee, J., Teh, S.-Y., Lee, A., Kim, H.H., Lee, C. and Shung, K.K. (2009), "Single beam acoustic trapping.", *Appl. Phys. Lett.*, Vol. 95 No. 7, p. 73701.

Lenshof, A., Magnusson, C. and Laurell, T. (2012), "Acoustofluidics 8: applications of acoustophoresis in continuous flow microsystems.", *Lab Chip*, Vol. 12 No. 7, pp. 1210–23.

Lewis, G.K. and Olbricht, W.L. (2009), "Design and characterization of a high-power ultrasound driver with ultralow-output impedance.", *Rev. Sci. Instrum.*, Vol. 80 No. 11, p. 114704.

Li, F., Cai, F., Liu, Z., Meng, L., Qian, M., Wang, C., Cheng, Q., et al. (2014), "Phononic-Crystal-Based Acoustic Sieve for Tunable Manipulations of Particles by a Highly Localized Radiation Force", *Phys. Rev. Appl.*, Vol. 1 No. 5, p. 051001.

Li, P.C.H. and Harrison, D.J. (1997), "Transport, Manipulation, and Reaction of Biological Cells On-Chip Using Electrokinetic Effects", *Anal. Chem.*, Vol. 69 No. 8, pp. 1564–1568.

Liu, R.H., Yang, J., Lenigk, R., Bonanno, J. and Grodzinski, P. (2004), "Self-contained, fully integrated biochip for sample preparation, polymerase chain reaction amplification, and DNA microarray detection.", *Anal. Chem.*, Vol. 76 No. 7, pp. 1824–31.

"LM741 Operational Amplifier." (2013), , Texas Instruments.

"LogiCORE IP DDS Compiler v4.0." (2011), , Xilinx, Inc.

Lord Rayleigh, F.R.. (1902), "On the pressure of vibrations", *Philos. Mag. Ser. 6*, Vol. 3 No. 15, pp. 338–346.

Lu, X., Huang, W.-H., Wang, Z.-L. and Cheng, J.-K. (2004), "Recent developments in single-cell analysis", *Anal. Chim. Acta*, Vol. 510 No. 2, pp. 127–138.

MacDonald, M., Dholakia, K., Rhodes, D. and Milne, G. (2010), "Acousto-Optic Sorting."

Manaresi, N., Romani, a., Medoro, G., Altomare, L., Leonardi, a., Tartagni, M. and Guerrieri, R. (2003), "A cmos chip for individual cell manipulation and detection", *IEEE J. Solid-State Circuits*, Vol. 38 No. 12, pp. 2297–2305.

Markx, G.H. (1994), "Separation of viable and non-viable yeast using dielectrophoresis", *J. Biotechnol.*, Vol. 32 No. 1, pp. 29–37.

Markx, G.H., Huang, Y., Zhou, X.F. and Pethig, R. (1994), “Dielectrophoretic characterization and separation of micro-organisms”, Vol. 140 No. 3, pp. 585–591.

Marmottant, P. and Hilgenfeldt, S. (2003), “Controlled vesicle deformation and lysis by single oscillating bubbles.”, *Nature*, Vol. 423 No. 6936, pp. 153–156.

Marston, P.L. (2006), “Axial radiation force of a bessel beam on a sphere and direction reversal of the force.”, *J. Acoust. Soc. Am.*, Vol. 120 No. September 2006, pp. 3518–3524.

Martin, S.P., Townsend, R.J., Kuznetsova, L. a, Borthwick, K. a J., Hill, M., McDonnell, M.B. and Coakley, W.T. (2005), “Spore and micro-particle capture on an immunosensor surface in an ultrasound standing wave system.”, *Biosens. Bioelectron.*, Vol. 21 No. 5, pp. 758–67.

Matthews, J.N.A. (2009), “Commercial optical traps emerge from biophysics labs”, *Phys. Today*, Vol. 62 No. 2, p. 26.

“MAX4940 High-Voltage Digital Pulsers.” (n.d.). , Maxim Integrated.

“MAX743 Data Sheet.” (1990), , Maxim Integrated.

Maxfield, C. (2008), “Chapter 17 Application-Specific Integrated Circuits (ASICs)”, *Bebop to Boolean Boogie – An Unconv. Guid. to Electron.*, pp. 235–249.

Maxfield, M. (2014), “ASIC, ASSP, SoC, FPGA - What’s the Difference? | EE Times”, *EE Times*, available at: http://www.eetimes.com/author.asp?section_id=36&doc_id=1322856 (accessed 6 May 2015).

“MCP4021/2/3/4.” (2006), , Microchip Technology, Inc.

Mehrishi, J.N. and Bauer, J. (2002), “Review Electrophoresis of cells and the biological relevance of surface charge”, *Electrophoresis*, Vol. 23 No. 13, pp. 1984–1994.

Menciassi, A., Eisinberg, A., Carrozza, M.C., Dario, P. and Member, S. (2003), “Force Sensing Microinstrument for Measuring Tissue Properties and Pulse in Microsurgery”, *IEEE/ASME Trans. Mechatronics*, Vol. 8 No. 1, pp. 10–17.

Meng, L., Cai, F., Chen, J., Niu, L., Li, Y., Wu, J. and Zheng, H. (2012), “Precise and programmable manipulation of microbubbles by two-dimensional standing surface acoustic waves”, *Appl. Phys. Lett.*, Vol. 100 No. 2012, doi:10.1063/1.4704922.

Milne, G., Rhodes, D., MacDonald, M. and Dholakia, K. (2007), “Fractionation of polydisperse colloid with acousto-optically generated potential energy landscapes”, *Opt. Lett.*, Vol. 32 No. 9, p. 1144.

Mitchison, J. and Swann, M. (1954), “The mechanical properties of the cell surface II. The unfertilized sea-urchin egg”, *J. Exp. Biol.*, Vol. 31 No. 3, pp. 461–472.

Molloy, J.E., Burns, J.E., Sparrow, J.C., Tregear, R.T., Kendrick-Jones, J. and White, D.C. (1995), “Single-molecule mechanics of heavy meromyosin and S1 interacting with rabbit or Drosophila actins using optical tweezers.”, *Biophys. J.*, Vol. 68 No. 4 Suppl, p. 298S–303S; 303S–305S.

Nawaz, A.A., Zhang, X., Mao, X., Rufo, J., Lin, S.-C.S., Guo, F., Zhao, Y., et al. (2014), “Sub-micrometer-precision, three-dimensional (3D) hydrodynamic focusing via ‘microfluidic drifting’.”, *Lab Chip*, Vol. 14 No. 2, pp. 415–23.

Neuman, K.C. and Block, S.M. (2004), “Optical Trapping”, *Rev. Sci. Instrum.*, Vol. 75 No. 9, pp. 2787–809.

Nishizaka, T., Miyata, H., Yoshikawa, H., Ishiwata, S. and Kinosita, K. (1995), “Unbinding force of a single motor molecule of muscle measured using optical tweezers.”, *Nature*, Vol. 377 No. 6546, pp. 251–254.

Nyborg, W.L. (1958), “Acoustic Streaming Near A Boundary”, *J. Acoust. Soc. Am.*, Vol. 30 No. 4, pp. 329–339.

O’Neil, a., MacVicar, I., Allen, L. and Padgett, M. (2002), “Intrinsic and Extrinsic Nature of the Orbital Angular Momentum of a Light Beam”, *Phys. Rev. Lett.*, Vol. 88 No. 5, p. 053601.

Ochiai, Y., Hoshi, T. and Rekimoto, J. (2013), “Three-dimensional Mid-air Acoustic Manipulation by Ultrasonic Phased Arrays”, *PloS one 9*, Vol. 9 No. 5, p. e97590.

Ochiai, Y., Rekimoto, J. and Hoshi, T. (2014), “Pixie Dust : Graphics Generated by Levitated and Animated Objects in”, *ACM Trans. Graph. - Proc. ACM SIGGRAPH 2014*, Vol. 33, pp. 85:1–13.

Oh, M.-J., Kuhr, F., Byfield, F. and Levitan, I. (2012), “Micropipette aspiration of substrate-attached cells to estimate cell stiffness.”, *J. Vis. Exp.*, No. 67, pp. 1–7.

Ohta, A., Chiou, P., Phan, H.L., Sherwood, S.W., Yang, J.M., Lau, A.N.K., Hsu, H.-Y., et al. (2007), “Optically controlled cell discrimination and trapping using optoelectronic tweezers”, *IEEE J. Sel. Top. Quantum Electron.*, Vol. 13 No. 2, pp. 235–243.

Or-Bach, Z. (2014), “FPGAs as ASIC Alternatives: Past & Future”, *EE Times*, available at: http://www.eetimes.com/author.asp?doc_id=1322021 (accessed 6 May 2015).

Padgett, M. and Di Leonardo, R. (2011), “Holographic optical tweezers and their relevance to lab on chip devices.”, *Lab Chip*, Vol. 11 No. 7, pp. 1196–205.

Pamme, N. (2006), “Magnetism and microfluidics.”, *Lab Chip*, Vol. 6 No. 1, pp. 24–38.

Pamme, N. and Manz, A. (2004), “On-chip free-flow magnetophoresis: continuous flow separation of magnetic particles and agglomerates.”, *Anal. Chem.*, Vol. 76 No. 24, pp. 7250–6.

Pankhurst, Q. a, Connolly, J., Jones, S.K. and Dobson, J. (2003), “Applications of magnetic nanoparticles in biomedicine”, *J. Phys. D. Appl. Phys.*, Vol. 36 No. 13, pp. R167–R181.

Park, J., Hu, C. and Shung, K.K. (2010), “Linear power amplifier for high frequency ultrasound coded excitation imaging”, *2010 IEEE Int. Ultrason. Symp.*, IEEE, pp. 1809–1812.

Parkin, S.J., Knöner, G., Nieminen, T.A., Heckenberg, N.R. and Rubinsztein-Dunlop, H. (2007), “Picoliter viscometry using optically rotated particles”, *Phys. Rev. E - Stat. Nonlinear, Soft Matter Phys.*, Vol. 76 No. 4.

Parkin, S.J., Vogel, R., Persson, M., Funk, M., Loke, V.L.Y., Nieminen, T.A., Heckenberg, N.R., et al. (2009), “Highly birefringent vaterite microspheres: production, characterization and applications for optical micromanipulation.”, *Opt. Express*, Vol. 17 No. 24, pp. 21944–21955.

Petersson, F., Nilsson, A., Holm, C., Jonsson, H. and Laurell, T. (2004), “Separation of lipids from blood utilizing ultrasonic standing waves in microfluidic channels.”, *Analyst*, Vol. 129 No. 10, pp. 938–43.

Petersson, F., Nilsson, A., Holm, C., Jonsson, H. and Laurell, T. (2005), “Continuous separation of lipid particles from erythrocytes by means of laminar flow and acoustic standing wave forces.”, *Lab Chip*, Vol. 5 No. 1, pp. 20–2.

“Polytec: Basic Principles of Vibrometry.” (2015), , Polytec GmbH, available at: http://www.polytec-ltd.co.uk/uk/solutions/vibration-measurement/basic-principles-of-vibrometry/ (accessed 9 January 2015).

Preece, D., Keen, S., Botvinick, E., Bowman, R., Padgett, M. and Leach, J. (2008), "Independent polarisation control of multiple optical traps", *Opt. Express*, Vol. 16 No. 20, p. 15897.

Qiu, Y. (2014a), *Development of Ultrasonic Devices for Microparticle and Cell Manipulation*, University of Dundee, Dundee, UK.

Qiu, Y., Wang, H., Demore, C., Hughes, D., Glynne-Jones, P., Gebhardt, S., Bolhovitins, A., et al. (2014), "Acoustic Devices for Particle and Cell Manipulation and Sensing", *Sensors*, Vol. 14 No. 8, pp. 14806–14838.

Qiu, Y., Wang, H., Gebhardt, S., Bolhovitins, A., Démoré, C.E.M., Schönecker, A. and Cochran, S. (2015), "Screen-printed Ultrasonic 2-D Matrix Array Transducers for Microparticle Manipulation", *Ultrasonics*, Elsevier B.V., doi:10.1016/j.ultras.2015.05.010.

Qiu, Z. (2014b), *Development of MRI-compatible Transducer Array for Focused Ultrasound Surgery: The Use of Relaxor-based Piezocrystals*, University of Dundee, Dundee, UK.

Raiton, B., McLaughlan, J.R., Harput, S., Smith, P.R., Cowell, D.M.J. and Freear, S. (2012), "The capture of flowing microbubbles with an ultrasonic tap using acoustic radiation force", *Appl. Phys. Lett.*, Vol. 101 No. 4, p. 044102.

Riley, N. (2001), "Steady Streaming", *Annu. Rev. Fluid Mech.*, Vol. 33, pp. 43–65.

Russell, D. (2012), "Standing Sound Waves (Longitudinal Standing Waves)", *Pennsylvania State Univ.*, available at: http://www.acs.psu.edu/drussell/Demos/StandingWaves/StandingWaves.html (accessed 28 January 2015).

Ryu, K.S., Shaikh, K., Goluch, E., Fan, Z. and Liu, C. (2004), "Micro magnetic stir-bar mixer integrated with parylene microfluidic channels.", *Lab Chip*, Vol. 4 No. 6, pp. 608–613.

Šafařík, I. and Šafaříková, M. (1999), "Use of magnetic techniques for the isolation of cells", *J. Chromatogr. B Biomed. Sci. …*, Vol. 722, pp. 33–53.

Sarwar, A. (2012), "FPGAs vs Microcontrollers", available at: http://electrodesigns.net/blog/fpgas-microcontrollers/ (accessed 1 January 2015).

SHEN, J., TAO, T., MEI, X., XU, M. and LIU, S. (2013), "An improved Line-Drawing Algorithm for Arbitrary Fractional Frequency Divider/Multiplier Based on FPGA", *J. Eng. Sci. Technol. Rev.*, Vol. 6 No. 5, pp. 90–94.

Shojaei-Baghini, E., Zheng, Y. and Sun, Y. (2013), "Automated micropipette aspiration of single cells.", *Ann. Biomed. Eng.*, Vol. 41 No. 6, pp. 1208–16.

Shuler, M., Aris, R. and Tsuchiya, H. (1972), "Hydrodynamic focusing and electronic cell-sizing techniques", *Appl. Microbiol.*, Vol. 24 No. 3, pp. 384–388.

Silva, G.T., Lopes, J.H. and Mitri, F.G. (2013), "Off-axial acoustic radiation force of repulsor and tractor bessel beams on a sphere", *IEEE Trans. Ultrason. Ferroelectr. Freq. Control*, Vol. 60 No. 6, pp. 1207–1212.

Simpson, N.B., Dholakia, K., Allen, L. and Padgett, M.J. (1997), "Mechanical equivalence of spin and orbital angular momentum of light: an optical spanner.", *Opt. Lett.*, Vol. 22 No. 1, pp. 52–4.

"SMD Chip LED 703-0109." (2012), , Multicomp.

Smith, P.R., Cowell, D.M.J. and Freear, S. (2013), "Width-modulated square-wave pulses for ultrasound applications", *IEEE Trans. Ultrason. Ferroelectr. Freq. Control*, Vol. 60 No. 11, pp. 2244–2256.

Smith, Q. and Gerecht, S. (2014), “Going with the flow: Microfluidic platforms in vascular tissue engineering”, *Curr. Opin. Chem. Eng.*, Elsevier Ltd, Vol. 3 No. c, pp. 42–50.

Smith, S.P. (1999), “Inexpensive optical tweezers for undergraduate laboratories”, *Am. J. Phys.*, Vol. 67 No. 1, p. 26.

Spalding, G. (2008), “Holographic optical tweezers”, *Struct. Light Its Appl.*, available at: http://books.google.com/books?hl=en&lr=&id=BNdCkCXOXX4C&oi=fnd&pg=PA139&dq=Holographic+optical+tweezers&ots=28yjwUSeQo&sig=zFMt1gRaAw31aa-rpBHsxFmYFAU (accessed 23 May 2014).

“Spartan-3A FPGA Family: Data Sheet.” (2010), , Xilinx, Inc.

Stevenson, D.J., Gunn-Moore, F. and Dholakia, K. (2014), “Light forces the pace: optical manipulation for biophotonics.”, *J. Biomed. Opt.*, Vol. 15 No. 4, p. 041503.

Suehiro, J. and Pethig, R. (1998), “The dielectrophoretic movement and positioning of a biological cell using a three-dimensional grid electrode system”, *J. Phys. D. Appl. Phys.*, Vol. 31 No. 22, pp. 3298–3305.

Svoboda, K., Schmidt, C.F., Schnapp, B.J. and Block, S.M. (1993), “Direct observation of kinesin stepping by optical trapping interferometry.”, *Nature*, Vol. 365 No. 6448, pp. 721–727.

Thomas, J.-L. and Marchiano, R. (2003), “Pseudo Angular Momentum and Topological Charge Conservation for Nonlinear Acoustical Vortices”, *Phys. Rev. Lett.*, Vol. 91 No. 24, p. 244302.

Tian, H., Shi, S., Zhang, J. and Zhao, H. (2009), “Controllable Arbitrary Integer Frequency Divider Based on VHDL”, *2009 Int. Jt. Conf. Artif. Intell.*, pp. 691–694.

Tong, L., Zhu, T. and Liu, Z. (2008), “Atomic force microscope manipulation of gold nanoparticles for controlled Raman enhancement”, *Appl. Phys. Lett.*, Vol. 92, p. 023109.

Triger, S., Saillant, J.F., Demore, C.E.M., Cochran, S. and Cumming, D.R.S. (2010), “Low-voltage coded excitation utilizing a miniaturized integrated ultrasound system employing piezoelectric 2-D arrays”, *IEEE Trans. Ultrason. Ferroelectr. Freq. Control*, Vol. 57 No. 2, pp. 353–362.

Trumbull, J.D., Glasgow, I.K., Beebe, D.J. and Magin, R.L. (2000), “Integrating microfabricated fluidic systems and NMR spectroscopy”, *IEEE Trans. Biomed. Eng.*, Vol. 47 No. 1, pp. 3–7.

Tsou, J.K., Liu, J., Barakat, A.I. and Insana, M.F. (2008), “Role of ultrasonic shear rate estimation errors in assessing inflammatory response and vascular risk”, *Ultrasound Med. Biol.*, Vol. 34 No. 6, pp. 963–72.

“Understanding Direct Digital Synthesis (DDS).” (2013), , National Instruments.

Vanherberghen, B., Manneberg, O., Christakou, A., Frisk, T., Ohlin, M., Hertz, H.M., Önfelt, B., et al. (2010), “Ultrasound-controlled cell aggregation in a multi-well chip.”, *Lab Chip*, Vol. 10 No. 20, pp. 2727–32.

Verle, M. (2014), “Chatper 1 Introduction to Microcontrollers”, *Archit. Program. 8051 Microcontrollers*, mikroElektronika, available at: http://www.mikroe.com/chapters/view/64/chapter-1-introduction-to-microcontrollers/.

Voldman, J. (2006), “Electrical forces for microscale cell manipulation.”, *Annu. Rev. Bomedical Eng.*, Vol. 8, pp. 425–54.

Wang, H., Brennan, P. and Jiang, D. (2007), “A Generic Multi-Modulus Divider Architecture for Fractional-N Frequency Synthesisers”, *2007 IEEE Int. Freq. Control Symp. Jt. with 21st Eur. Freq. Time Forum*, IEEE, pp. 261–265.

Wang, H., Qiu, Y., Démoré, C. and Cochran, S. (2014), "FPGA embedded system for ultrasound particle manipulation with Sonotweezers", *2014 IEEE Int. Ultrason. Symp.*, IEEE, pp. 1440–1443.

Wang, H., Qiu, Y., Demore, C., Cochran, S., Glynne-jones, P. and Hill, M. (2012), "Particle Manipulation in a Microfluidic Channel with an Electronically Controlled Linear Piezoelectric Array", *2012 IEEE Int. Ultrason. Symp.*, IEEE, pp. 1998–2001.

Watarai, H. and Namba, M. (2002), "Capillary magnetophoresis of human blood cells and their magnetophoretic trapping in a flow system", *J. Chromatogr. A*, Vol. 961 No. 1, pp. 3–8.

"Water - Absolute or Dynamic Viscosity." (n.d.). , available at: http://www.engineeringtoolbox.com/absolute-dynamic-viscosity-water-d_575.html (accessed 26 April 2015).

Weiser, M.A.H., Apfel, R.E. and Neppiras, E.A. (1984), "Interparticle Forces on Red Cells in a Standing Wave Field", *Acta Acust. united with Acust.*, Vol. 56 No. 2, pp. 114–119.

Wester, B. a., Rajaraman, S., Ross, J.D., LaPlaca, M.C. and Allen, M.G. (2011), "Development and characterization of a packaged mechanically actuated microtweezer system", *Sensors Actuators A Phys.*, Elsevier B.V., Vol. 167 No. 2, pp. 502–511.

Wheeler, A.R., Throndset, W.R., Whelan, R.J., Leach, A.M., Zare, R.N., Liao, Y.H., Farrell, K., et al. (2003), "Microfluidic Device for Single-Cell Analysis", *Anal. Chem.*, Vol. 75 No. 14, pp. 3581–3586.

Whittingham, T. and Martin, K. (2010), "Chapter 3 Transducers and beam-forming", *Diagnostic Ultrasound Phys. Equip.*, Cambridge University Press, pp. 23–45.

Wiklund, M., Green, R. and Ohlin, M. (2012), "Acoustofluidics 14: Applications of acoustic streaming in microfluidic devices.", *Lab Chip*, Vol. 12 No. 14, pp. 2438–51.

Wiklund, M. and Önfelt, B. (2012), "Ultrasonic manipulation of single cells", in Lindström, S. and Andersson-Svahn, H. (Eds.),*Single-Cell Anal. Methods Protoc.*, Springer Protocols, Vol. 853, pp. 177–196.

Wiklund, M., Radel, S. and Hawkes, J.J. (2013), "Acoustofluidics 21: ultrasound-enhanced immunoassays and particle sensors.", *Lab Chip*, Vol. 13 No. 1, pp. 25–39.

Wood, C.D., Cunningham, J.E., O'Rorke, R., Wälti, C., Linfield, E.H., Davies, a. G. and Evans, S.D. (2009), "Formation and manipulation of two-dimensional arrays of micron-scale particles in microfluidic systems by surface acoustic waves", *Appl. Phys. Lett.*, Vol. 94 No. 2009, pp. 1–4.

Wu, D.W., Zhou, Q., Geng, X., Liu, C.G., Djuth, F. and Shung, K.K. (2009), "Very high frequency (beyond 100 MHz) PZT kerfless linear arrays", *IEEE Trans. Ultrason. Ferroelectr. Freq. Control*, Vol. 56 No. 10, pp. 2304–2310.

Wu, H. (2012), *Transducer Arrays For Manipulating Cells With Ultrasound*, University of Dundee, Dundee, UK.

Wu, J. (1991), "Acoustical Tweezers", *J. Acoust. Soc. Am.*, Vol. 89 No. 5, pp. 2140–2143.

Xie, X. (2014), *A Novel High Power Characterization System for Piezoelectric Materials*, University of Dundee, Dundee, UK.

"Xilinx Synthesis and Simulation Design Guide." (2010), , Xilinx, Inc.

"Xilinx UG334 Spartan-3A/3AN FPGA Starter Kit Board User Guide." (2008), , Xilinx, Inc.

Yang, J., Huang, Y., Wang, X.B., Becker, F.F. and Gascoyne, P.R. (2000), “Differential analysis of human leukocytes by dielectrophoretic field-flow-fractionation.”, *Biophys. J.*, Vol. 78 No. 5, pp. 2680–9.

Yin, H., Wang, M.D., Svoboda, K., Landick, R., Block, S.M. and Gelles, J. (1995), “Transcription against an applied force.”, *Science (80-.).*, Vol. 270 No. 5242, pp. 1653–1657.

Yosioka, K. and Kawasima, Y. (1955), “Acoustic radiation pressure on a compressible sphere”, *Acta Acust. united with Acust.*, Vol. 5 No. 3, pp. 167–173.

Zhang, P., Li, T., Zhu, J., Zhu, X., Yang, S., Wang, Y., Yin, X., et al. (2014), “Generation of acoustic self-bending and bottle beams by phase engineering.”, *Nat. Commun.*, Nature Publishing Group, Vol. 5, p. 4316.

Zhang, R., Chu, J., Wang, H. and Chen, Z. (2012), “A multipurpose electrothermal microgripper for biological micro-manipulation”, *Microsyst. Technol.*, Vol. 19 No. 1, pp. 89–97.

Zhang, S. and Zhao, C. (2013), “Design for realizing arbitrary fractional divider based on FPGA which duty cycle is up to 50 %”, *Proc. 2nd Int. Symp. Comput. Commun. Control Autom.*, pp. 58–61.

Zhang, X.P., Leung, C., Lu, Z., Esfandiari, N., Casper, R.F. and Sun, Y. (2012), “Controlled aspiration and positioning of biological cells in a micropipette”, *IEEE Trans. Biomed. Eng.*, Vol. 59 No. 4, pp. 1032–1040.

Zheng, F., Li, Y., Hsu, H.-S., Liu, C., Tat Chiu, C., Lee, C., Ham Kim, H., et al. (2012), “Acoustic trapping with a high frequency linear phased array.”, *Appl. Phys. Lett.*, Vol. 101 No. 21, p. 214104.

Zheng, X. and Apfel, R. (1995), “Acoustic interaction forces between two fluid spheres in an acoustic field”, *J. Acoust. Soc. Am.*, Vol. 97 No. 4, pp. 2218–2226.

Zhong, J., Yi, M. and Bau, H.H. (2002), “Magneto hydrodynamic (MHD) pump fabricated with ceramic tapes”, *Sensors Actuators A Phys.*, Vol. 96 No. 1, pp. 59–66.

Zhuang, X., Wygant, I.O., Yeh, D.T., Nikoozadeh, A., Oralkan, O., Ergun, A.S., Cheng, C.-H., et al. (2005), “Two-Dimensional Capacitive Micromachined Ultrasonic Transducer (CMUT) Arrays for a Miniature Integrated Volumetric Ultrasonic Imaging System”, (Walker, W.F. and Emelianov, S.Y.,Eds.), Vol. 5750, pp. 37–46.

Appendix A Source Code in Supplemental CD

A-1 VHDL Source Code for FPGA Cores

A-1-1 Linear Array Manual Control

A-1-2 Linear Array Element Hopping Control

A-1-3 Cross-electrode Array Static Control

A-1-4 Cross-electrode Array Dynamic Control

A-1-5 Multichannel Transmitter FPGA Core

A-2 MATLAB Source Code for GUI Development and Specific API

A-2-1 GUI for General-purpose 16-channel Array Driver

A-2-1-1 GUI Creation

A-2-1-2 API for 16-channel Array Driver

A-2-2 GUI for Circular Array Sonotweezer

A-2-2-1 GUI Creation

A-2-2-2 API for Circular Array Sonotweezer

Appendix B Supplementary Materials for Multichannel Electronics

B-1 PCB Layouts

B-1-1 Signal Conditioning Circuitry

Figure B.1: Stack-up PCB layout of the 16-channel signal conditioning circuitry.

B-1-2 Power Amplifier Array

Figure B.2: stack-up PCB layout of an 8-channel power amplifier array. Each channel is constructed with an op-amp (AD811) and a current buffer (BUF634). Figure B.3: single layer PCB layout of the backplane for the power amplifiers.

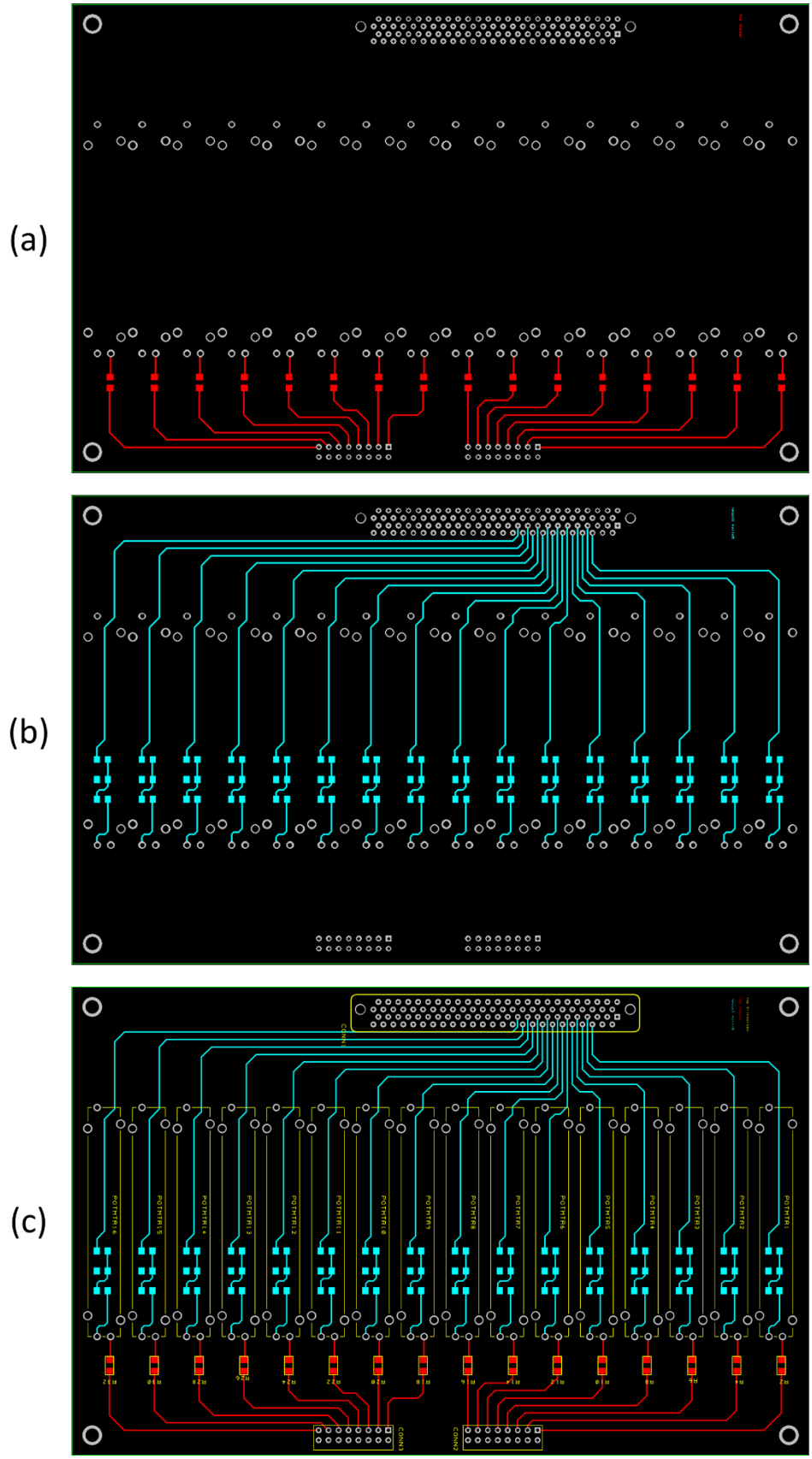

Figure B.1 2-layer PCB layouts of the signal conditioning circuitry. (a) Top layer. (b) Bottom layer. (c) Stack-up layout.

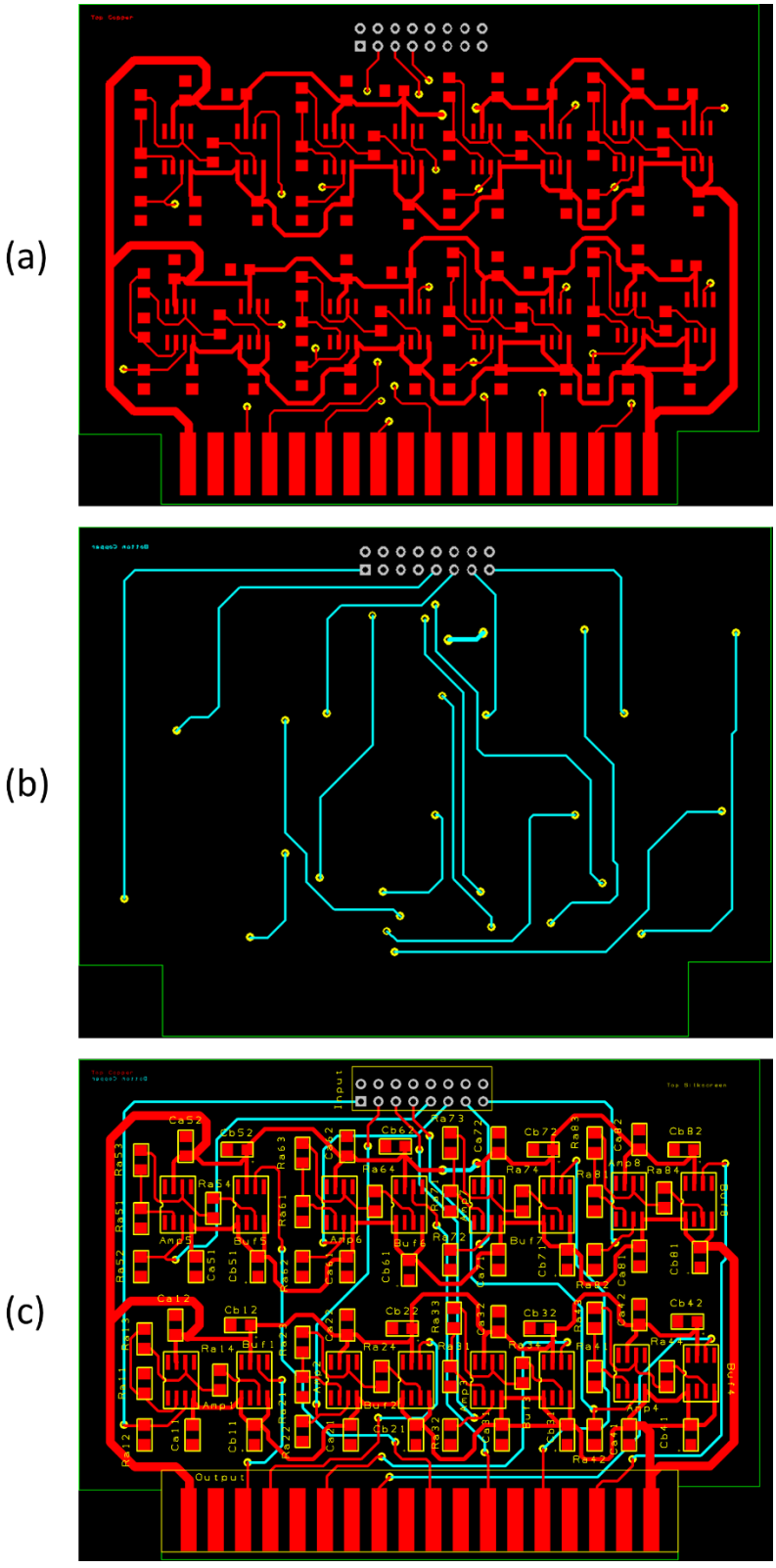

Figure B.2 2-layer PCB layouts of an 8-channel power amplifier array. (a) Top layer. (b) Bottom layer. (c) Stack-up layout.

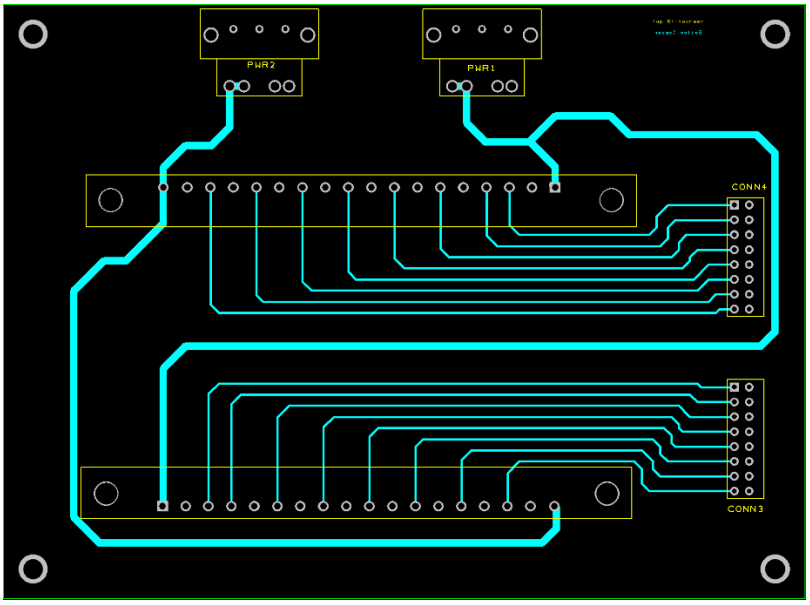

Figure B.3 Single layer PCB layout of the backplane for the power amplifiers.

B-2 Component Inventory

Table B.1 lists all the electric and mechanical components used for constructing the multichannel electronics. Unit costs are listed as well, including the cost for the PCB fabrication. The total cost (May 2015) is £773.91.

Table B.1 Inventory for all the components in the multichannel electronics.

Category	Component	Part Number	Unit Cost	Unit	Total Cost
PCB Fabrication	PCB Train 1 layer PCB 138mm*102mm	N/A	£34.18	1	£34.18
PCB Fabrication	PCB Train 2 layer PCB 99mm*73mm	N/A	£15.51	2	£31.02
PCB Fabrication	PCB Train 4 layer PCB 120mm*188mm	N/A	£50.31	1	£50.31
FPGA Electronics	XILINX SPARTAN-3A, LCD, VGA, STARTER KIT	HW-SPAR3A-SK-UNI-G	£206.11	1	£206.11
IC	TEXAS INSTRUMENTS BUFFER AMP, HIGH SPEED, 180MHZ, SOIC	BUF634U	£6.06	16	£96.96
IC	AD811JRZ, Video Amplifier 2500V/µs, 8-Pin SOIC N	AD811JRZ	£5.33	16	£85.28
USB to RS232	USB to RS232 Adapter cable, 1m	US232R-100-BLK	£18.87	1	£18.87
Resistor	MULTICOMP RESISTOR, 56R2, 0.125W, 1%, 1206	MC0125W1206156R2	£0.05	16	£0.80
Resistor	VISHAY DRALORIC RESISTOR, 1206, 511R, 1%	CRCW1206511RFKEA	£0.02	16	£0.34
Resistor	MULTICOMP RESISTOR, 68R, 0.125W, 1%, 1206	MC0125W1206168R	£0.03	16	£0.46
Resistor	MULTICOMP RESISTOR, 100K, 0.125W, 1%, 1206	MC0125W12061100K	£0.03	16	£0.43
Resistor	MULTICOMP RESISTOR, 1K, 0.125W, 1%, 1206	MC0125W120611K	£0.03	16	£0.45
Resistor	MULTICOMP RESISTOR, 390R, 0.125W, 1%, 1206	MC0125W12061390R	£0.03	16	£0.43
Potentiometer	BOURNS POTENTIOMETER, SLIDE, 10K, 45MM	PTA4543-2015DPB103	£3.09	16	£49.44
Capacitor	KEMET CAP, TANT, 10UF, 20V, CASE A	T491A106M020AT	£0.58	32	£18.50
Capacitor	MURATA CAP, MLCC, X7R, 100NF, 50V, 1206	GRM319R71H104KA01D	£0.05	32	£1.44
Capacitor	MULTICOMP CAP, MLCC, X7R, 390PF, 50V, 1206	MC1206B391K500CT	£0.02	16	£0.35
Capacitor	MULTICOMP CAP, MLCC, X7R, 1NF, 100V, 1206	MC1206B102K101CT	£0.04	16	£0.65
PSU	TRACOPOWER PSU, METAL, 60W, 15V/3A	TXL 060-0533TI	£60.08	1	£60.08
Connector	ITW MCMURDO EDGE CONNECTOR, 18WAY	307-018-525-102	£4.37	2	£8.74
Connector	TE CONNECTIVITY / AMP HEADER, BOX, RIGHT ANGLE, 16WAY	1-1634689-6	£0.70	6	£4.22
Connector	TE CONNECTIVITY / AMP SOCKET, IDC, 16WAY	1-1658526-1	£3.38	6	£20.28
Connector	TE CONNECTIVITY PLUG, CABLE TYPE, TWO CODING, 2WAY	1982299-3	£1.89	2	£3.78
Connector	TE CONNECTIVITY / AMP CONTACT, SOCKET, 17 TO 13 AWG, CRIMP	927837-1	£0.39	2	£0.78
Connector	TE CONNECTIVITY HEADER, R/A, 2 WAY, CODING CONTACTS, PCB	1982295-1	£1.46	2	£2.92
Connector	SCHURTER INLET, IEC, 2P SWITCH, W/OUT FUSE DRAWER	DD11.0111.1111	£6.91	1	£6.91
Connector	SCHURTER FUSE HOLDER, DRAWER, SNAP IN	4301.1405	£1.38	1	£1.38
Fan	SEPA FAN, 60MM, 5VDC	MFB60D05	£16.27	1	£16.27
Casing	TEMPO ABS Enclosure, IP65, 344 x 289 x 117.4mm	TA342912	£29.54	1	£29.54
Cable	RS SNYD Series Insulated Crimp Spade Connector, 22 → 16 AWG, M3 (#4), Red Nylon	SNYD1-3.2	£0.08	20	£1.62
Cable	Harting 40 Way Unscreened Flat Ribbon Cable, 51.73 mm Width (5 m)	6618297001105	£13.12	0.1	£1.31
Cable	AMPHENOL SPECTRA-STRIP 132-2801-040 RIBBON CABLE, 40WAY (1 m)	132-2801-040	£6.60	1	£6.60
Spacer	35mm High Brass Threaded Hex Spacer 7mm Wide for M4 Thread	HTSB-M4-35-7-1	£0.39	8	£3.12
Heat Sink	FISCHER ELEKTRONIK HEAT SINK, FOR SMD, 75°C/W	ICK SMD A 10 SA	£0.32	32	£10.34

B-3 Electronics Assembly

Figure B.4 – Figure B.7 demonstrate the electronics assembly on a two-layer chassis within an ABS casing with dimensions of 334 × 289 × 117 mm^3.

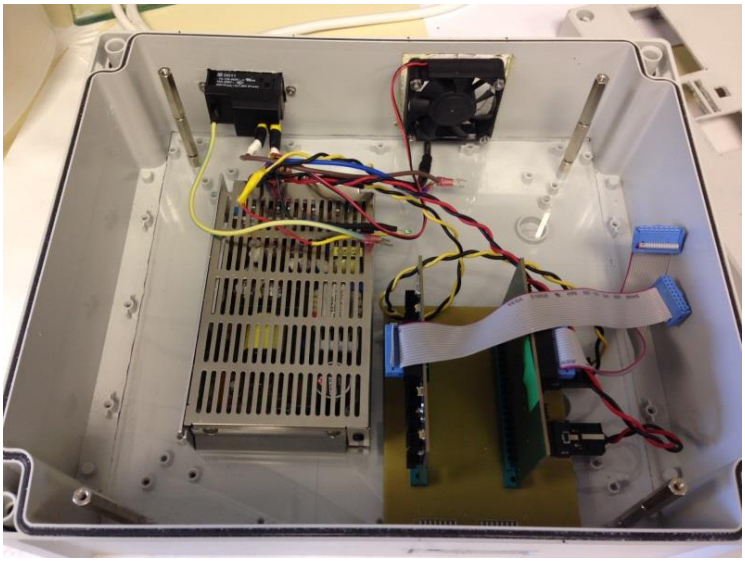

Figure B.4 Bottom chassis for PSU and the amplifier PCBs.

Figure B.5 Top chassis for the FPGA development board and the signal conditioning circuitry.

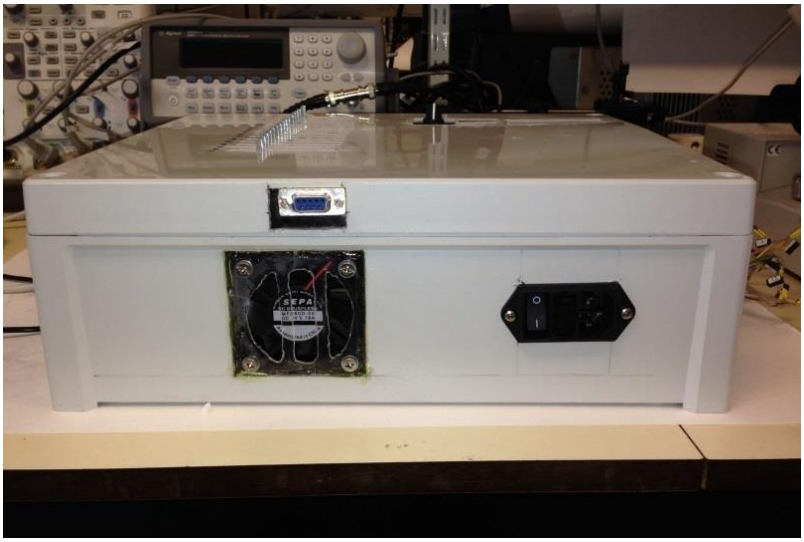

Figure B.6 Back view of the casing showing the fan, power supply input and the COM port.

Figure B.7 Top view of the casing showing the FPGA hardware user interface and the panel for channel output amplitude control.

Appendix C Supplemental Materials for Signal Switching Electronics

C-1 Schematics and PCB Layouts

All schematics and PCB layouts for the circuitry were created with DesignSpark PCB v5.0.

C-1-1 Signal Switching Electronics

C-1-1-1 Schematics of Key Circuits

Figure C.1: ADG5434 IC controls the driving signal connected to the active electrode of arrays with common-ground electrode. Outputs of channels 1 – 40 can be switched between AC signal source and 1 MΩ resistor.

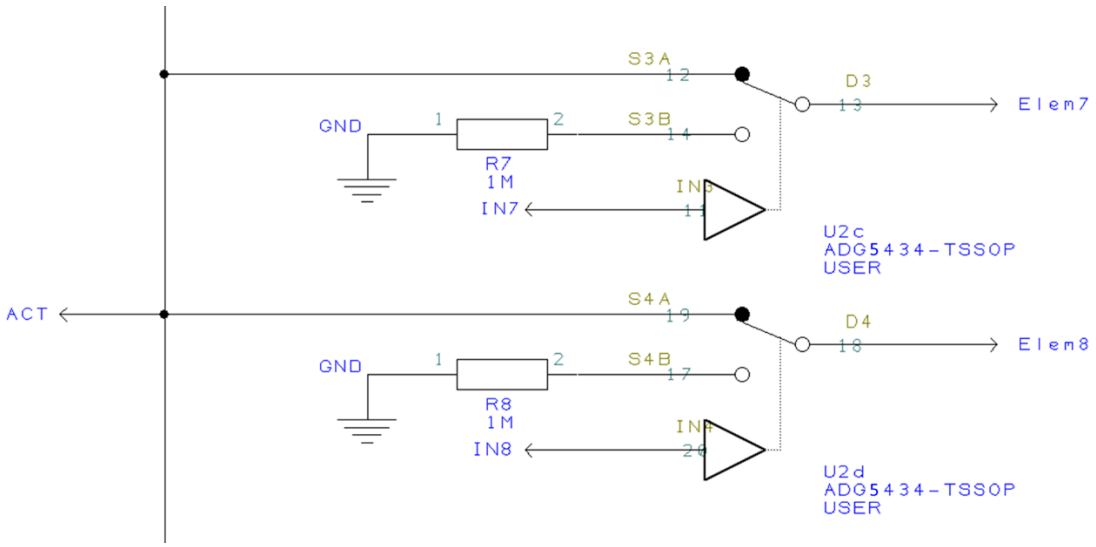

Figure C.1 Part of the schematic with ADG5434 for switching the transducer driving signal between AC source and 1 MΩ resistor.

Figure C.2: A mechanical switch can change the output of channel 21 – 40 to an alternation between ground and 1 MΩ resistor. This configuration can be used for controlling cross-electrode array.

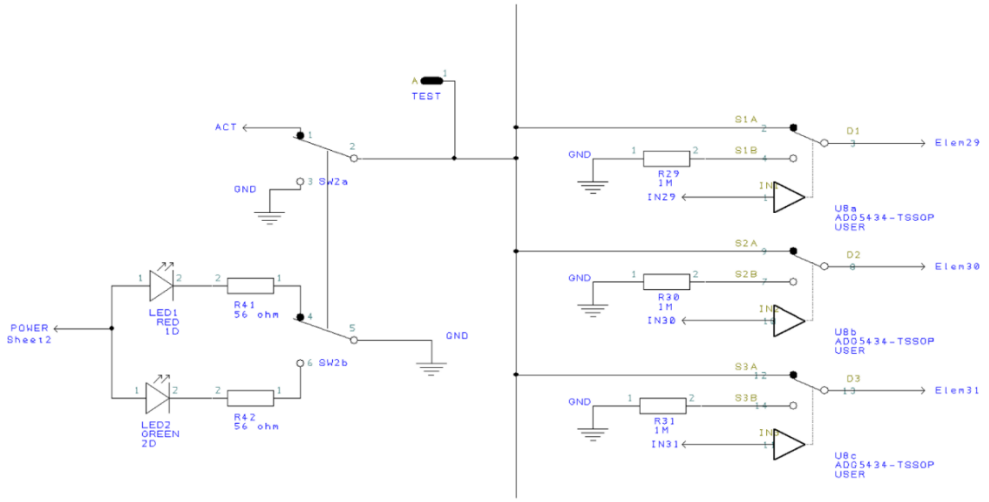

Figure C.2 Part of the schematics with a mechanical switch for controlling the functionality of driving common-ground electrode array and cross-electrode array.

Figure C.3: Schematic of DC-DC voltage regulation circuit adapted from suggested application circuit from the MAX743 datasheet (“MAX743 Data Sheet”, 1990).

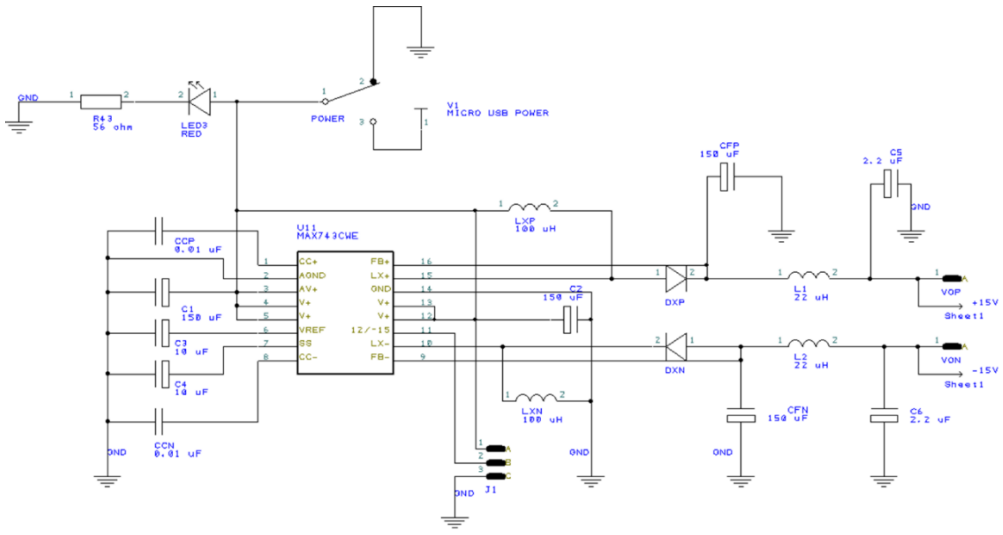

Figure C.3 Schematics of the voltage regulation circuitry for converting +5 V DC voltage to ±15 V DC voltages.

C-1-1-2 PCBs

The PCBs were designed with four electrical layers, with the middle layers as ground planes. The tracks of analogue AC signals and digital signals working in the MHz range were also placed in the middle layers with the ground planes to reduce channel crosstalk.

PCB fabrication was provided by PCB Train (Newbury Electronics Ltd, Newbury Berkshire, UK). Figure C.4 shows the layer stack-up for manufacture. The finished PCB is fabricated on a 1.6 mm FR4 laminate with immersion silver finish. The overall dimension is 17.5 mm × 19.5 mm.

No blind or buried vias were used in the design. Figure C.6 to Figure C.5 show the PCB layouts of the signal switching circuitry.

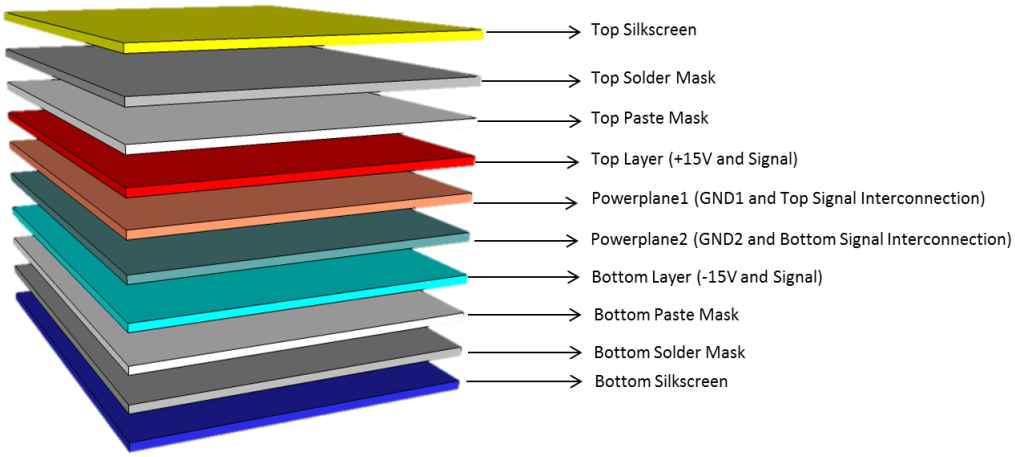

Figure C.4 Demonstration of PCB layer specification for manufacturing.

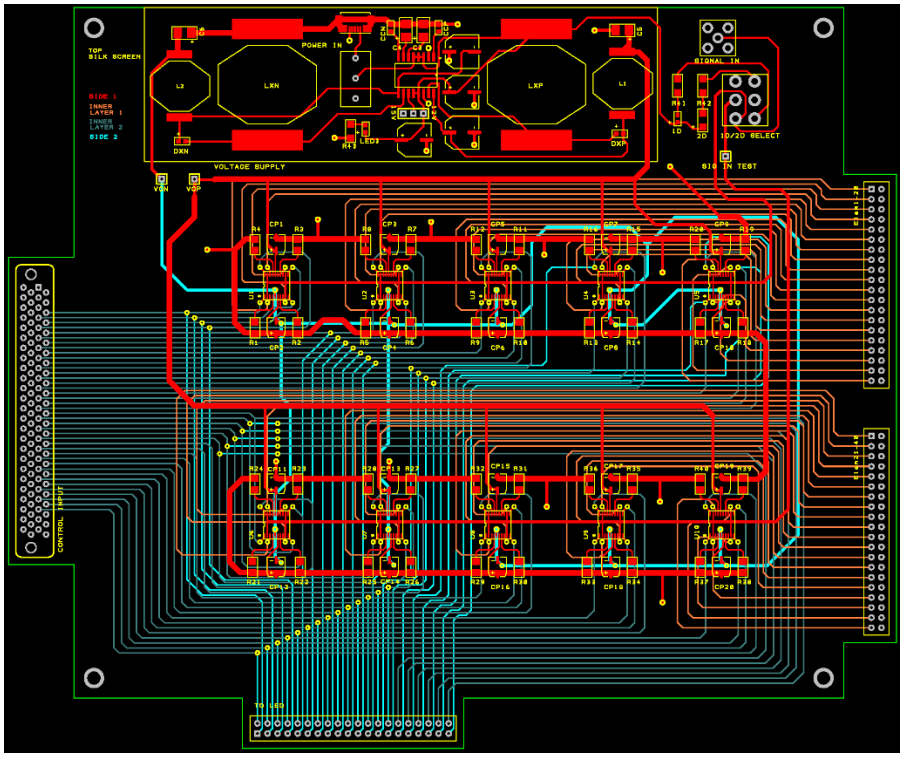

Figure C.5 4-layer PCB stack-up layout demonstration of multiple PCB layers.

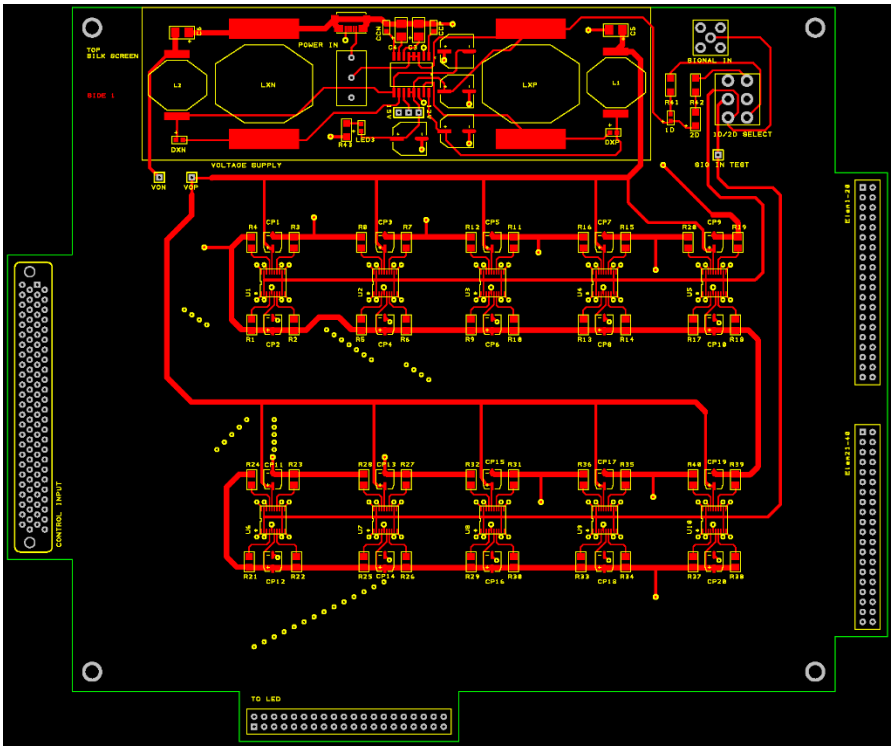

Figure C.6 Top layer PCB layout with tracks for + 15 V DC voltage and AC source signal.

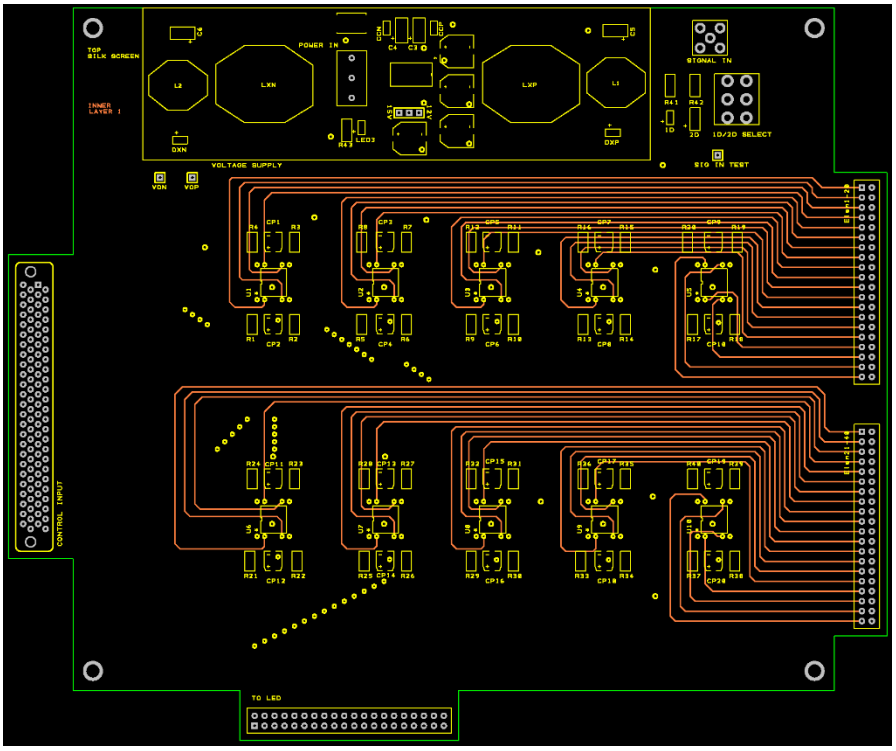

Figure C.7 First middle layer PCB layout with ground plane and tracks for output analogue signals.

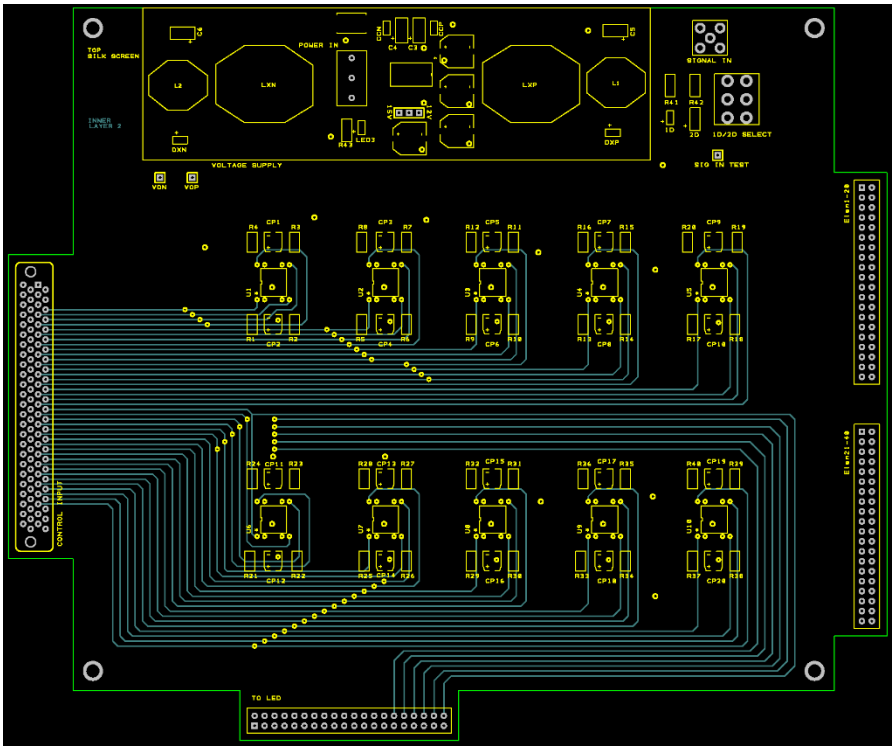

Figure C.8 Second middle layer PCB layout with ground plane and tracks for digital control signals.

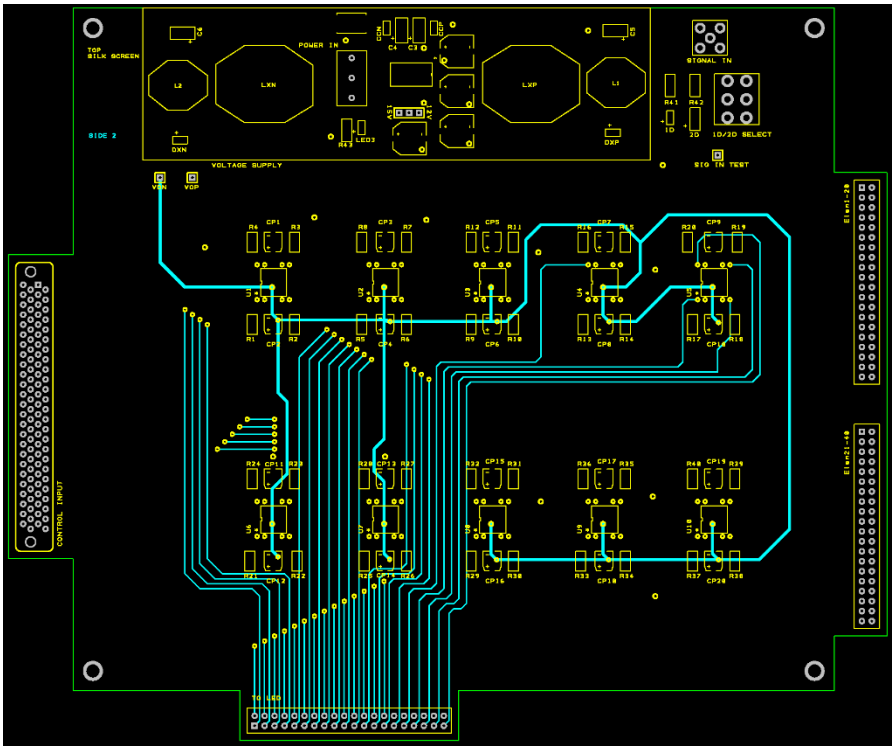

Figure C.9 Bottom layer PCB layout with tracks for - 15 V DC voltage and a bypass of digital control signals to the LED indicator.

C-1-2 LED Indicator for Linear Array

C-1-2-1 Schematic

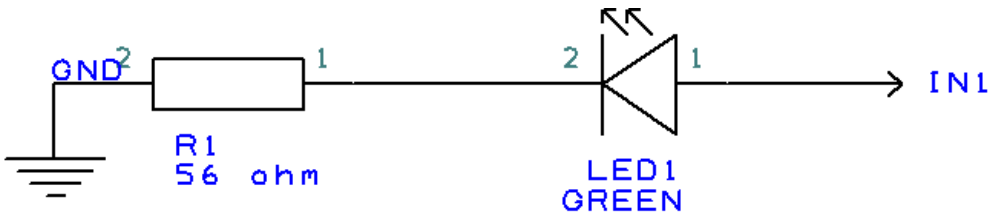

Figure C.10 Part of the schematic for LED array as indicator. The LED ("SMD Chip LED 703-0109", 2012) is actuated with FPGA output signal. A 56 Ω resistor is used for current limiting purposes.

C-1-2-2 PCB

(a)

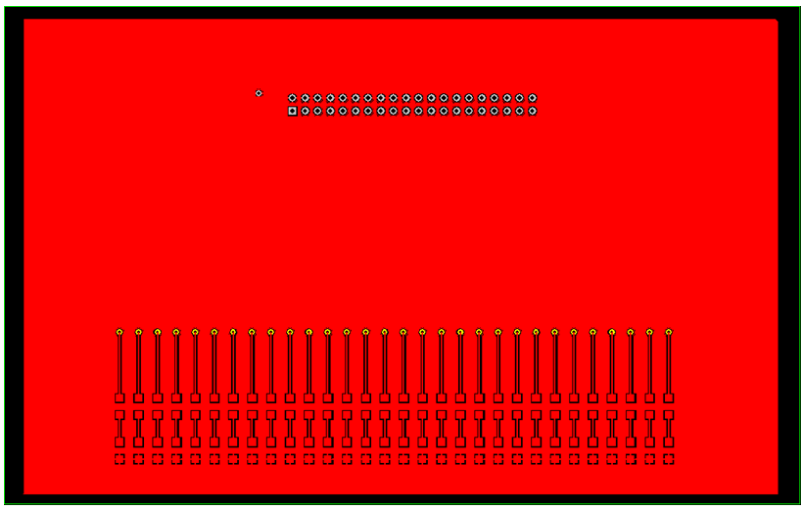

(b)

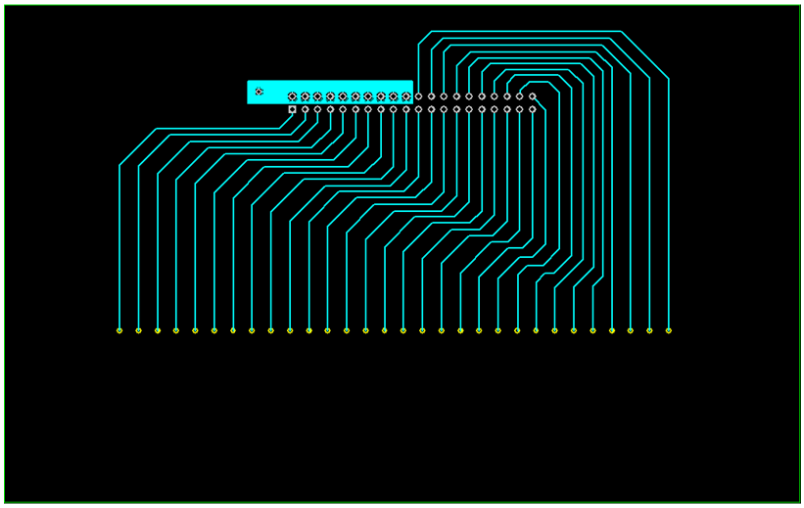

(c)

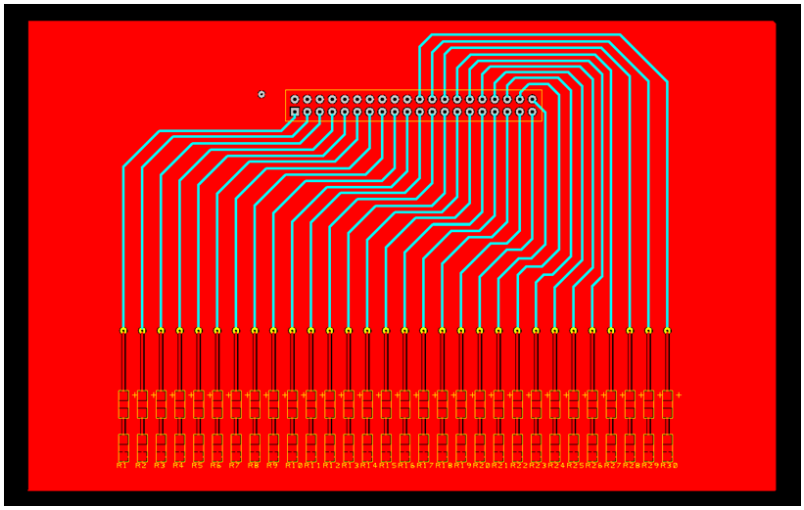

Figure C.11 2-layer PCB layouts of LED indicator for linear array. (a) Top layer. (b) Bottom layer. (c) Stack-up layout.

C-1-3 LED Indicator for Crossed-electrode Array

C-1-3-1 Schematics

In total 64 green LEDs (“LED lamp BG-490-515”, 2006) were arranged into a matrix and controlled by 8 anode electrodes and 8 cathode electrodes. Each electrode is controlled with a SPDT switch channel of the analogue switch IC ADG333.

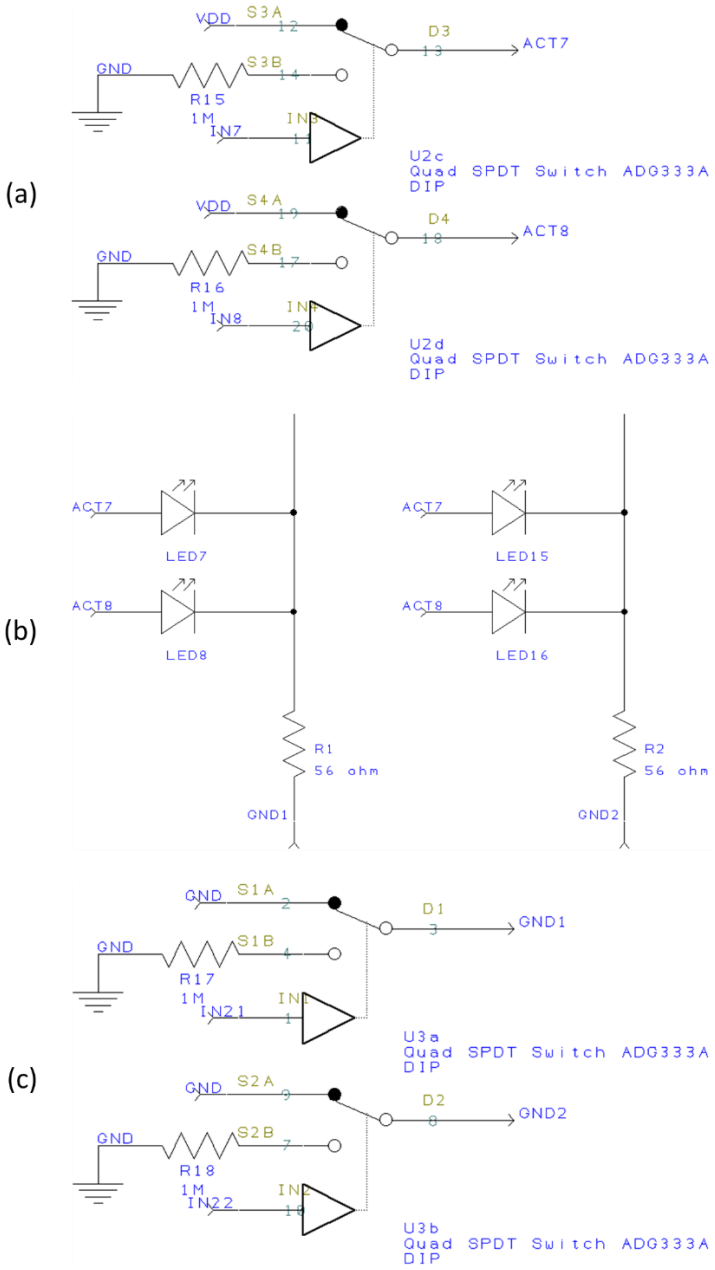

Figure C.12 Part of the schematic for controlling the LED matrix indicator.

C-1-3-2 PCB

(a)

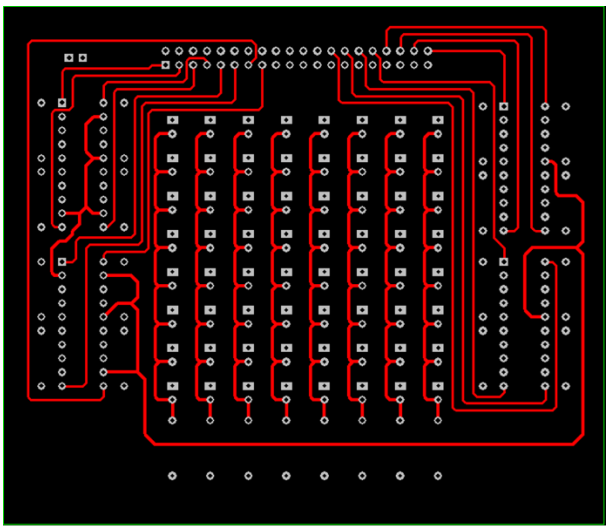

(b)

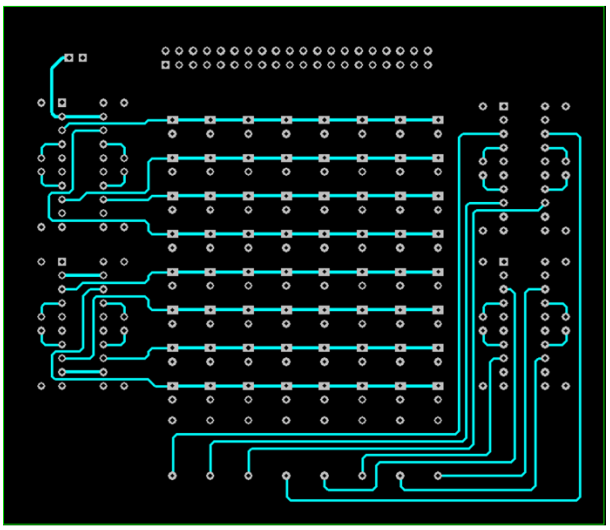

(c)

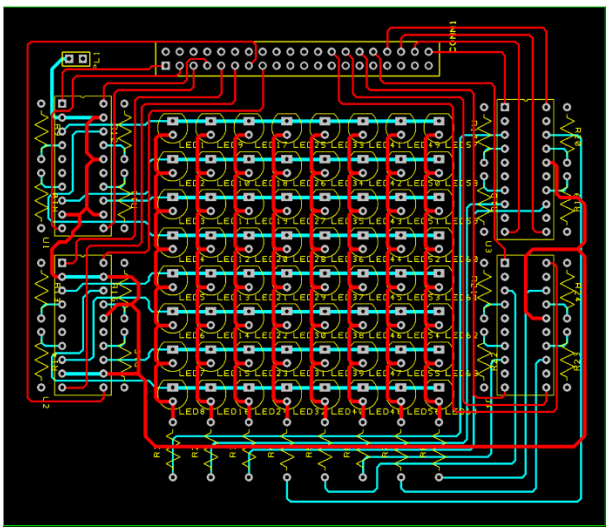

Figure C.13 2-layer PCB layouts of LED indicator for cross-electrode array. (a) Top layer. (b) Bottom layer. (c) Stack-up layout.

C-2 Component Inventory

Table C.1 lists all the electric and mechanical components used for constructing the signal switching electronics. Unit costs are listed as well, including the cost for the PCB fabrication. The total cost (May 2015) is £427.83.

Table C.1 Inventory for all the electronic components in the signal switching electronics.

Category	Component	Part Number	Unit Cost	Unit	Total Cost
PCB Fabrication	PCB Train 4 layer PCB 225mm x 187mm	N/A	£73.08	1	£73.08
FPGA Electronics	XILINX SPARTAN-3A, LCD, VGA, STARTER KIT	HW-SPAR3A-SK-UNI-G	£206.11	1	£206.11
IC	ANALOG DEVICES SWITCH, QUAD, SPDT, 13.5OHM, 20TSSOP	ADG5434BRUZ	£6.47	10	£64.70
IC	MAXIM INTEGRATED PRODUCTS MAX743CWE+ IC, SWITCHING REG, SMD, SOIC16, 743	MAX743CWE+	£11.62	1	£11.62
Resistor	RESISTOR, 56R2, 0.125W, 1%, 1206	MC0125W1206156R2	£0.02	41	£0.92
Resistor	RESISTOR, 1206 1M	MC0125W120651M	£0.01	56	£0.74
Capacitor	PANASONIC CAP, ALU ELEC, 470NF, 50V, SMD	EEE1HAR47SR	£0.15	20	£2.94
Capacitor	AVX 0603 Standard 10nF Ceramic Multilayer Capacitor, 50 V dc X7R Dielectric ±5% SMD	06035C103JAT2A	£0.03	2	£0.06
Capacitor	Panasonic FK SMD 150µF 35 V dc , SMD Aluminium Electrolytic Capacitor, ±20%	EEEFK1V151AP	£0.50	4	£1.98
Capacitor	Kemet ±20% 10µF 16 V dc SMD Tantalum Electrolytic Capacitor, B 125°C T491	T491B106M016AT	£0.35	2	£0.70
Capacitor	Kemet ±10% 2.2µF 20 V dc SMD Tantalum Electrolytic Capacitor, B 125°C T491	T491B225K020AT	£0.21	2	£0.42
Inductor	Bourns PM2120 Series Wire-wound SMD Inductor with a Iron Core, 100 µH ±10% 6.1A Idc	PM2120-101K-RC	£2.19	2	£4.38
Inductor	Murata 2800 Series Wire-wound SMD Inductor 22 µH 3.85A Idc	28223C	£0.60	2	£1.20
Diode	Bourns CD0603-S01575 Switching Diode, 150mA, 100V, 4ns, 2-Pin 0603	CD0603-S01575	£0.05	2	£0.10
LED	Osram Opto LS Q971, CHIPLED 0603 Series Red LED, 11 mcd 160 ° ,2-Pin 0603 SMD	LS Q971	£0.04	2	£0.08
LED	Osram Opto LG N971, CHIPLED 1206 Series Green LED 160 ° ,2-Pin 1206 SMD	LG N971	£0.05	31	£1.64
LED	MULTICOMP LED, 3MM, GREEN, 30MCD, 565NM	HLMP1503	£0.07	64	£4.16
Switch	PCB Slide Switch DPDT On-On 5 A@ 28 V dc Top	5MD1S202AM2QES	£1.17	1	£1.17
Switch	PCB Slide Switch SP On-On 3 A@ 28 V dc Slide	MSS3112D	£2.48	1	£2.48
Connector	HIROSE(HRS) ZX62-B-5PA(11) MICRO USB, 2.0 TYPE B, RECETPACLE, SMT	ZX62-B-5PA(11)	£0.64	1	£0.64
Connector	TE CONNECTIVITY RF COAXIAL, SMA, STRAIGHT JACK, 50OHM	5-1814832-1	£1.21	1	£1.21
Connector	Hirose FX2 Series 1.27mm 100 Way 2 Row Right Angle PCB Socket Surface Mount Board to Board	FX2-100S-1.27DSL(71)	£5.79	1	£5.79
Connector	TE Connectivity AMPMODU Series, 2.54mm Pitch 40 Way 2 Row Straight PCB Header, Solder Termination, 3A	2-826656-0	£1.34	5	£6.72
Connector	40 way IDC bump polarised socket	1-1658527-3	£3.76	6	£22.56
Connector	MULTICOMP ADAPTER, SMA PLUG, BNC JACK, 50OHM	19-29-1 TGN	£4.37	1	£4.37
Connector	TE Connectivity AMPMODU Series, 2.54mm Pitch 3 Way 1 Row Straight PCB Header, Solder Termination, 3A	826646-3	£0.34	1	0.341
Connector	TE CONNECTIVITY / AMP JUMPER, AMP MODU, GREEN, GOLD PLATED	142270-1	£0.45	1	0.45
Cable	Harting 40 Way Unscreened Flat Ribbon Cable, 51.73 mm Width (5 m)	6618297001105	£13.12	0.05	£0.66
Cable	AMPHENOL SPECTRA-STRIP 132-2801-040 RIBBON CABLE, 40WAY (1 m)	132-2801-040	£6.60	1	£6.60

C-3 Electronics Assembly

Figure C.14 and Figure C.15 demonstrate the assembly of the FPGA controlled signal switching electronics for the control of 1-D linear and 2-D crossed-electrode arrays respectively.

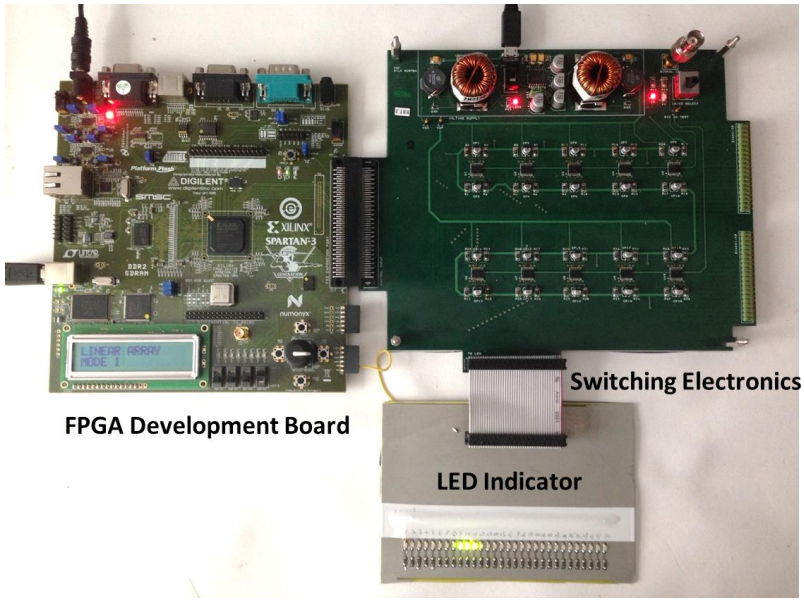

Figure C.14 Signal switching electronics connected with FPGA development board and LED indicator for the control of 1-D linear array.

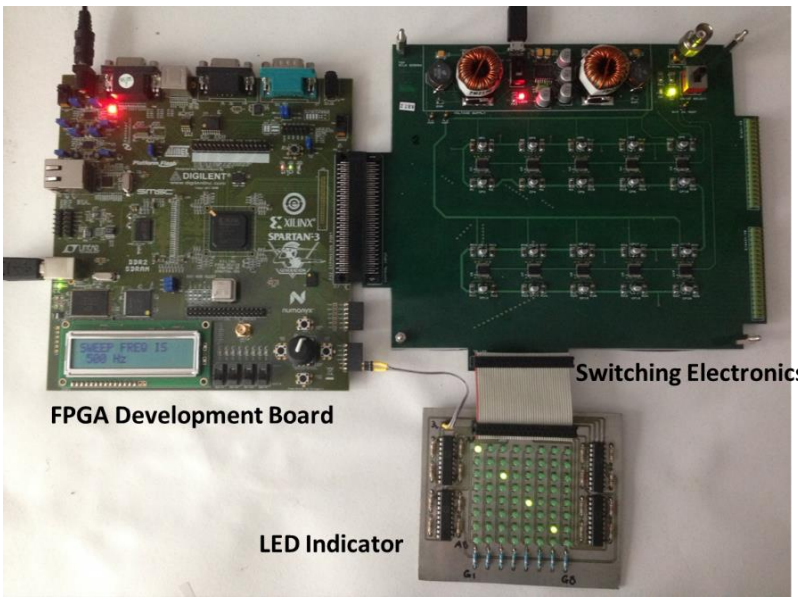

Figure C.15 Signal switching electronics connected with FPGA development board and LED indicator for the control of 2-D crossed-electrode array.

Appendix D Proof-of-principle Study with 2-D Matrix Transducer Array for Particle Manipulation[3]

A 2-D planar array Sonotweezer was constructed with a 2-D matrix ultrasonic array and a glass chamber. The 2-D array was fabricated with thick-film lead zirconate titanate (PZT) as the active material (IKTS-PZ5100, Fraunhofer IKTS, Germany), and the transducers with separated top electrodes and common ground electrode were patterned into a 6 × 6 matrix on an Al_2O_3 substrate by screen printing.

A photograph of the transducer array and an illustration of its layered structure is demonstrated in Figure D.1 (a). For the key layers, the thickness of the PZT, Al_2O_3 substrate and Au electrode are 139 ± 2 μm, 250 μm, and 10 μm, respectively. Each array element has dimension 2 × 2 mm^2, and the element pitch is 2.3 mm. The electrical impedance spectrum of each transducer element in the array was measured in air, with the results shown in Figure D.1 (b) & (c). The smooth Al_2O_3 side of the array was used as the working area.

The impedance spectrum of the combined fundamental thickness extensional resonance frequency of the PZT and the substrate together can be found around 7 MHz, corresponding with an acoustic wavelength of about 200 μm in 20°C water with velocity c_{water} = 1481 m/s. Hence a 100 μm thickness fluid chamber is needed to create a half-wavelength resonance. A glass chamber was prepared with standard microscope glass coverslips to form the fluid carrier layer and the reflector layer, with strips of glass also made with microscope coverslips as the spacers, creating a chamber with a fluid layer with thickness of 110 ± 10 μm. At the fundamental resonance frequency, the electrical impedance for all the elements was around 60 Ω.

[3] The research in this appendix has been submitted to *Ultrasonics* as "Screen-printed Ultrasonic 2-D Matrix Arrays for Microparticle Manipulation ", Yongqiang Qiu, Han Wang, Sylvia Gebhardt, et al., in press.

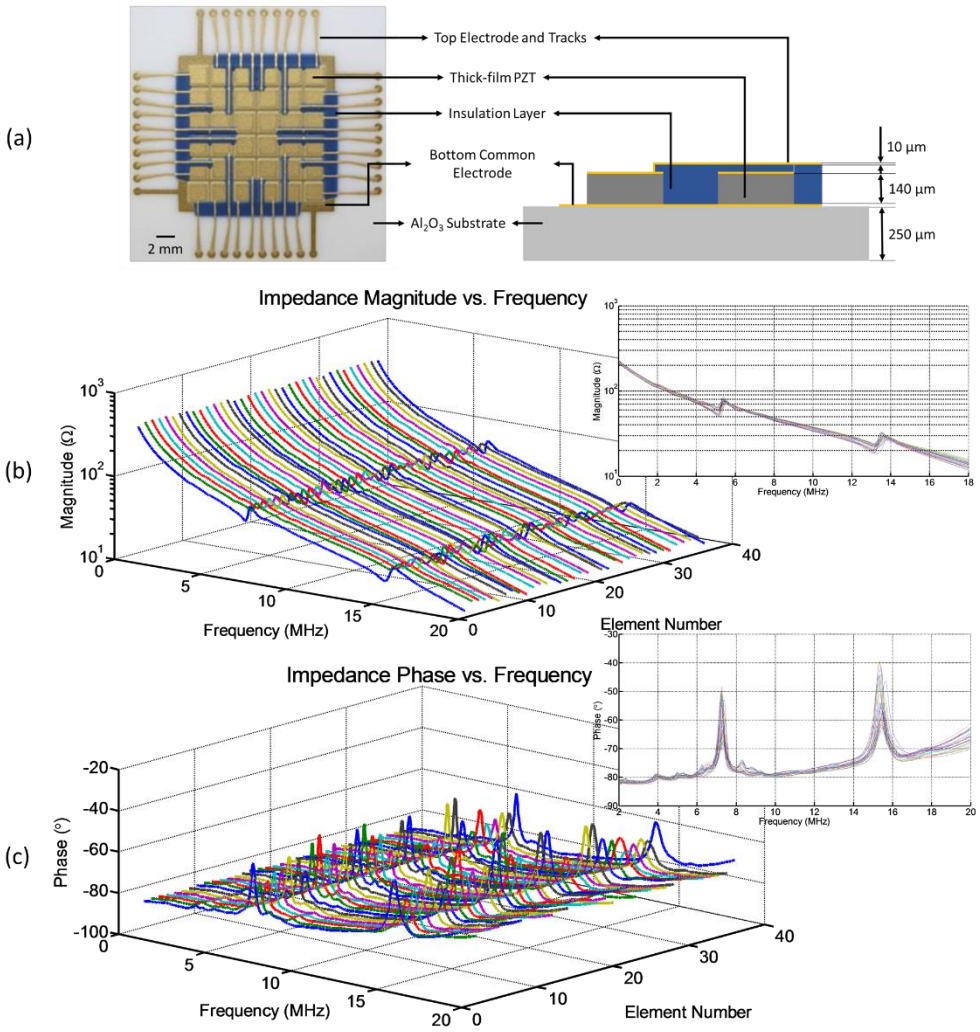

Figure D.1 Impedance spectrum of all 36 transducer elements of the 2-D matrix array. (a) A top view photograph of the 2-D matrix array, and the cross-sectional view of the device layered structure, and the thickness of each layer. (b) and (c) Impedance magnitude and phase spectrum of each transducer element in the array.

In order to address the transducer elements individually, a simple electronic driving adaptor was developed with a spring-probe configuration. Each separate transducer electrode is connected discretely through the electrical fan-out of the thick-film array to a single RF input, which is connected to an external signal source. The common electrode of the transducer array is connected to the analogue signal ground. The signal path of each transducer element is controlled by an individual mechanical slide switch fabricated on a PCB adaptor, and electrical contacts from the PCB to the transducer array were introduced through a group of needle spring probes (261-5159, RS Components Ltd., Northants, UK). The PCB layouts of the driving platform can be found in Figure D.2.

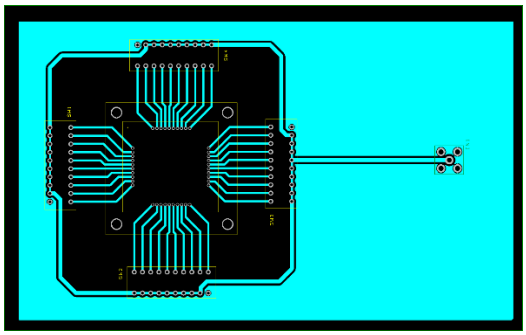

Figure D.2 Single-layer PCB layout for the adaptor for electrical interconnection from the signal source input to the transducer electrode fan-outs through spring probes.

The 2-D matrix array was glued on to a Perspex gasket which serves as a supportive frame to protect the fragile thick-film PZT transducer and also to secure the electrical connection from the transducer element electrode fan-outs to the spring probes. A glass fluid chamber can be coupled on top of the Al_2O_3 layer. A bench-top arbitrary function generator (AFG3101, Tektronix UK Ltd, Berkshire, UK) was used for driving the transducer elements. The experimental setup is shown in Figure D.3 (a). Ø10 µm fluorescent microspheres (Fluoresbrite, Polysciences, Inc., Warrington, PA, USA) were used in the experiments for testing the device. The driving signal from the function generator was a CW sine-wave of 7.6 V_{pp} at 7.258 MHz. Four transducer elements were activated, and the particles were concentrated above the active elements as agglomerates with diameters about 400 µm, as shown in Figure D.3 (b) and (c).

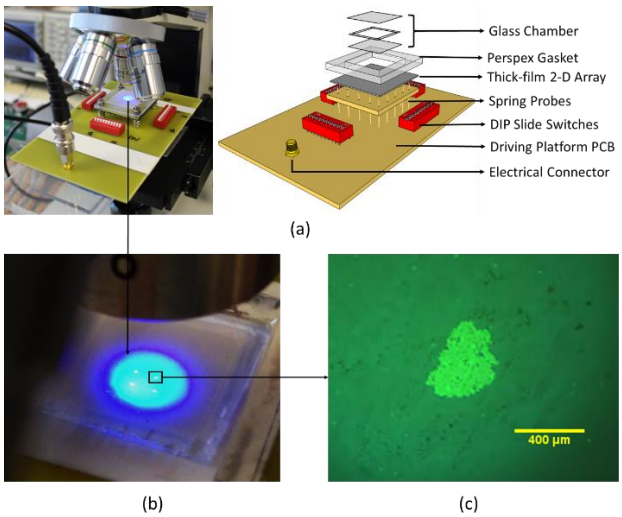

Figure D.3 Experimental setup and results from using the thick-film 2-D array for particle trapping. (a) Demonstration of the 2-D array electronic driving platform and experimental setup. (b) 10-µm polystyrene particles were concentrated into agglomerates over the active elements in the fluid chamber. (c) Micrograph of a single agglomerate.

Although the experiment demonstrated the functionality of the device in terms of particle trapping, the functionality of agglomerate manipulation by switching the elements was restricted. The results are shown in Figure D.4. Video was recorded with a frame rate of 0.04 second/frame (25 fps), and the lateral velocity of the agglomerate was measured as 266 ± 168 μm/s; the lateral manipulation force, balanced with the Stokes' drag, can be calculated as 1.0 ± 0.6 nN. The manipulation step distances are between 1.1 ~ 1.3 mm, which are smaller than the element pitch of 2.3 mm. The main reason is because the chamber lateral dimension (15 × 15 mm^2) is relatively large compared to the fluid thickness (100 μm), so the influence of the adhesive layer roughness introduced during the chamber construction process is large, as it leads to inhomogeneity in the fluid layer thickness. Hence the USW field is largely impaired for generating a $\lambda/2$ pressure nodal plane across the device active area.

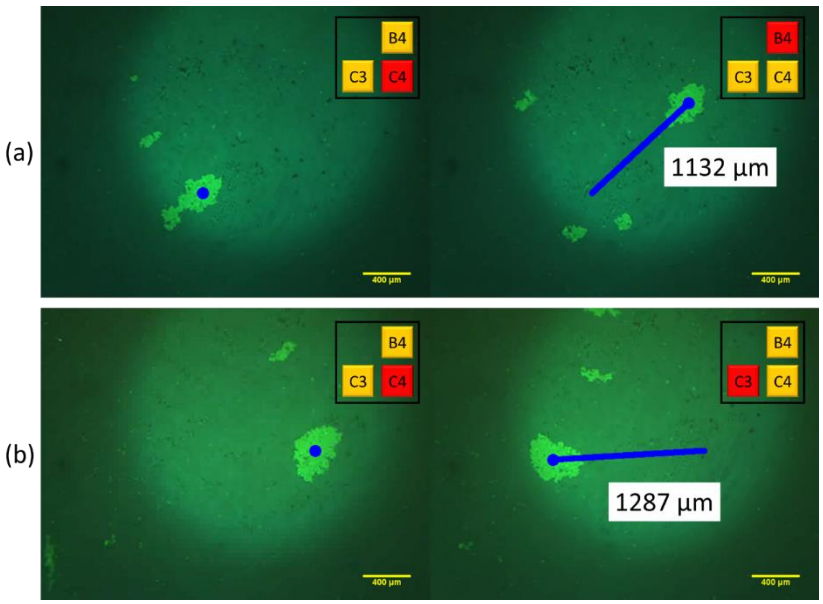

Figure D.4 Micrographs showing the results of manipulating a particle agglomerate with the 36-element 2-D matrix array. The manipulation was controlled by toggling the mechanical switches to active different elements. Ø10 μm particles were firstly concentrated over element C4. (a) The trajectory of the manipulation when element B4 was active. (b) The trajectory of the manipulation when element C3 was active.